FRICTION AND THERMAL BEHAVIOUR IN ELASTOHYDRODYNAMIC LUBRICATION POWER TRANSMISSION CONTACTS

by

Amjad Al-Hamood

Thesis submitted in candidature
for the degree of Doctor of Philosophy
at Cardiff University

Institute of Mechanics and Advance Material

Cardiff School of Engineering

Cardiff University

April 2015

Declaration and Statements

Declaration

This work has not previously been accepted in substance for any degree and is not concurrently submitted in candidature for any degree.

Signed ……..…… (Amjad Al-Hamood) Date…….…….

Statement 1

This thesis is being submitted in partial fulfillment of the requirements for the degree of Doctor of Philosophy (PhD).

Signed ……..…… (Amjad Al-Hamood) Date…….…….

Statement 2

This thesis is the result of my own independent work/investigation, except where otherwise stated. Other sources are acknowledged by explicit references.

Signed ……..…… (Amjad Al-Hamood) Date…….…….

Statement 3

I hereby give consent for my thesis, if accepted, to be available for photocopying and for inter-library loan, and for the title and summary to be made available to outside organisations.

Signed ……..…… (Amjad Al-Hamood) Date…….…….

Summary

This thesis reports experimental and theoretical analyses to study the heat generation and partition between contacting bodies under rolling/sliding elastohydrodynamic (EHL) point contact. A twin disk test rig was re-commissioned and used for the experimental work. 76 mm diameter crowned, super-finished test disks, fixed on parallel shafts, were used in the experimental EHL tests. In each disk, 6 thermocouples were installed to measure the temperature during sliding/rolling contact under EHL conditions. In addition, ceramic washers were fixed on the plane sides of each disk to minimize heat transfer over those surfaces. A Labview data acquisition system was built for acquiring data from the sensors installed on the rig. The EHL experimental results show the fast disk has significantly higher bulk temperature than the slow disk.

A transient two dimensional numerical model was constructed to calculate the average circumferential temperature distribution within the disks using three thermocouples as a boundary condition. The heat partition factor, β, and convection heat transfer coefficient, h, were varied systematically in the model. A linear relationship between β and h_f for the fast disk and 1-β and h_s for the slow disk were obtained. These two linear relations were related together by the variation of h with the rotational speed. Over the approximately steady state condition, the calculated β using this approach was in the range of 0.65 to 0.77 for 32 EHL tests at different loads and sliding speeds. This means that the majority of heat is conducted to the fast disk, which is compatible with the previous findings.

In order to carry out transient modelling, the unloading mechanism was developed to ensure rapid disk separation. This improved the temperature trend in the cooling phase. In addition, a microswitch was used to give accurate monitoring of the disks contacting and separation. The thermocouple arrangement within the disks and their installation technique were assessed and developed. An immersion test in a hot oil bath was used to test the thermocouples dynamic response. This test was modelled, and the results showed significant lag in the measurements. It was concluded that a system identification method is required to identify the dynamic characteristics of the temperature measurement system in order to compensate for time lagging

Extensive studies were carried out to determine the cause behind some of the experimental uncertainties. It was found that the most likely reason behind these uncertainties is the contact pressure variation along the disk-shaft interference fit, which would result in significant thermal conductance variation.

The traction force measurement within the EHL contacts has shown broadly linear increase with increased load at constant sliding speed. This indicates a constant coefficient of friction at constant sliding speed. The results also showed that the coefficient of friction decreases as the sliding speed increases.

Acknowledgments

First of all, all praises and thanks be to Allah for everything, and especially completing this project. I would like to express my deepest gratitude and thanks to my supervisors, Professor Pwt Evans and Dr Alastair Clarke, for their wise advices and continuous encouragement during the time of my PhD study in Cardiff University. I think, I will not forget many of what I have learned from Professor Pwt Evans.

I take this opportunity to thank Dr Khairy Sharif for his help and advice in my research and in having the opportunity to study at Cardiff University. I also must not forget to thank Professor Ray Snidle as he was one of the builders of the tribology labs, especially the test rig that I worked on. I must not forget to thank the department of engineering staff and the workshop members for providing me with the necessary facilities for my research.

I would like to thank the Iraqi Ministry of Higher Education and Scientific Research and Karbala University for the financial support for this study. I also thank the staff of the Iraqi Cultural Attaché in London for their support.

I am also grateful to all PhD student colleagues and friends especially, Hazim, Haider, and Ahmed as we *"Ijazah Dirasia"* spent unforgettable time together in overcoming the difficulties that we faced throughout this challenging period in our lives.

Last but not least, I cannot find words to express my feeling and gratitude to the memory of my mother, and I am in indebted to my father for his continuous support for the whole of my life. I am also thankful to all my family in Iraq especially my brother Ahmed for his great support. I also owe sincere thankfulness to my wife, and thanks to my son Jaafar, and my daughter Jannat.

Contents

Nomenclature

Symbols	Definition	Units
a	minor axis of Hertz elliptical contact	m
A	area	m^2
b	major axis of Hertz elliptical contact	m
C_p	specific heat capacity	$Jkg^{-1}K^{-1}$
E	Young's modules	Nm^{-2}
erf	Error function	---
G	gear ratio	---
Gr	Grashof number	---
h	convection heat transfer coefficient	$Wm^{-2}K^{-1}$
h_f	convection heat transfer coefficients for the fast disk	$Wm^{-2}K^{-1}$
h_s	convection heat transfer coefficients for the slow disk	$Wm^{-2}K^{-1}$
K	thermal conductivity of the test disks	$Wm^{-1}K^{-1}$
K_c	thermal conductivity of the insulating ceramic washers	$Wm^{-1}K^{-1}$
Nu	Nusselt number	---
P	pressure	Nm^{-2}
Q_c	rate of conducted heat	W
Q_e	rate of change in internal energy	W
q_{fr}	frictional heat flux at the EHL contact	Wm^{-2}
Q_g	rate of generated heat	W
Q_r	heat rate transported as a result of disk rotation	W
r	radial coordinate in the thermal model	m
Re	Reynolds number	---
R_i	outer radius of the disk	m
R_o	inner radius of the solution zone	m
T	temperature	^oC, K
t	time	s
T_A	ambient temperature	^oC
u_1	speed of the fast surface	ms^{-1}
u_2	speed of the slow surface	ms^{-1}
u_r	mean entraining speed	ms^{-1}
u_s	sliding speed	ms^{-1}
V	volume	m^3
w	disk width	m
w_c	ceramic washer width	m
z	axial coordinate in the thermal model	m
α	thermal diffusivity	m^2s^{-1}
μ	dynamic viscosity	$m^2\ s^{-1}$

Symbols	**Definition**	**Units**
β	Fraction of heat conducted to the fast surface	---
δ	Radial interface between the shaft and the disk	m
θ	angular coordinate in the thermal model	rad
ν	Poisson ratio	---
ρ	density	kgm^{-3}
χ	The ratio of the convection heat transfer coefficients	---
ω	angular velocity	s^{-1}
suffices	Indicate position of thermocouple according to	---
a b c d e f	Figures 3.7 and 5.17	

Chapter 1:
Introduction and Literature Review

1.1. Introduction

This thesis reports experimental and theoretical analyses on thermal behaviour in point contact thermal elastohydrodynamic lubrication (EHL). This chapter first gives a general overview about the field of tribology and of elastohydrodynamic lubrication. After that, a literature review on the relevant work is discussed. Finally, the aims of the current work are described.

1.2. Tribology

Tribology is "*The science and technology of interacting surfaces in relative motion and the practices related thereto*" as defined first in a Department of Education and Science report (1966). The word *tribology* derives from the Greek word *tribos* which means rubbing. Although the tribology field was defined in 1966, in practice tribology existed a very long time ago. Dowson (1998) presented a very comprehensive historical review on the practical tribology extends to prehistory up to 10^6 years ago (Stone Age), when friction was used for the generation of fire by percussion of flint stones and the rubbing of wood-on-wood.

An interesting insight into tribological development relates to continuous rotary motion, especially the wheel rim tribology and the axle bearing in wheeled vehicles which was also reported in (Dowson, 1998). He mentioned that the archaeological evidence favour Sumer (in Mesopotamia) as the location of the wheel's origin. Figure

1.1 shows disc wheels in a copper model of a Mesopotamian chariot from Tell Agrab, Iraq (2600 B.C.).

Figure 1.1: A copper model for a Mesopotamian chariot from Tell Agrab, Iraq (2600 B.C.), copyright for the image, University of Chicago

Classical tribology involves studying friction, the contact and properties of surfaces, wear and lubrication. More modern tribological topics are: biotribology, nanotribology, and green tribology. Typical details on tribology are available in (Williams, 2005) and (Vizintin et al., 2004).

1.3. Lubrication

Lubrication is essential for most machine elements (that experience relative motion) to maintain functionality, efficiency and service life. The basic idea of lubrication is to place a substance between two rubbing surfaces to reduce friction and wear. The

majority of lubricants are liquids like mineral oils or synthetic esters, but they might be solid like PTFE as used in dry bearings or gas as used in gas bearings.

The contact between solids can be classified as conformal or non-conformal contact. Good examples of conformal contacts are journal bearings and slider bearings. In these bearings, the surfaces make contact with a high degree of geometrical conformity, this allows for carrying load over a relatively large contact area between the surfaces. In the non-conformal contact, the load is carried through a small area of contact such as in roller bearings, cam followers and gears.

Generally, fluid film lubrication of conformal contacts is characterized as hydrodynamic lubrication (HL). Examples of HL exist in journal and thrust bearings where a positive hydrodynamic pressure develops in the lubricant which results in separation of the surfaces. The magnitude of the lubricant pressure is usually less than 5 MPa (Hamrock et al. 2004) which is not enough to cause considerable elastic deformation of the surfaces (usually metals). In hydrodynamic lubrication, the fluid film thickness is generally thick (exceeds 1μm) which prevents the surfaces from making contact. When significant elastic deformation occurs as a result of the lubricant pressure, the lubrication will be categorized as elastohydrodynamic (EHL) lubrication. This is usually associated with lubrication of non-conformal surfaces and is described in the next section.

1.4. Elastohydrodyanmic lubrication (EHL)

If two surfaces (usually non-conformal) are loaded against each other and they are in relative motion with the existence of lubricant, these conditions can lead to the surfaces elastic deformation and separation by the lubricant. This mechanism is known

as *elastohydrodynamic lubrication.* The separation of the contacting surfaces (partially or fully) protects machine element surfaces and reduces the friction significantly. The very useful concept of the EHL is more likely to have appeared accidently than by design, as stated by Gohar (2001) when tribologists observed almost complete lack of wear at lubricated gear teeth.

Prior to the existence of the elastohydrodynamic lubrication concept, Martin (1916) gave a solution to the gear teeth lubrication contact problem using a model based on a cylinder loaded against a plane. Martin imposed rigid surfaces in conjunction with the well-known equation of lubrication developed by Reynolds (1886), incompressible isoviscos fluid was also imposed. The predicted oil film was significantly thin and much smaller than the roughness of the best made gear at the operating loads. This thin lubricant film cannot be considered realistic when observing the long life of running gears without damage which implies full film lubrication. The imposition of rigid surfaces in modelling heavily loaded non-conformal contact was one of limitations in the work of (Martin 1916). Hertz (1881) developed his famous contact theory when he was studying elastic deformation of optical lenses when pressed together. His work was the start of the contact mechanics field, as mentioned by Johnson (1987). Hertz contact theory forms the basis for the today's contact stress and elastic deformation analysis at the loaded non-conformal lubricated contacts.

Alexander Mikhailovich Ertel was the founder of what is called elastohydrodynamics (Popova and Popov 2014). Ertel solved the hydrodynamic lubrication problem using Reynolds' lubrication equation taking into account the combined effect of surfaces elastic deformation (according to Hertz contact theory) and the pressure effects on the viscosity of the lubricant, full film lubrication was predicted. His work was published as the well- known paper (Grubin 1949), as reported by Cameron (1985) and Lugt and

Morales-Espejel (2011). Later on, a full numerical EHL solution for line contact problem was obtained by Dowson and Higginson (1959). Their numerical calculations at heavily loaded contacts gave pressure distributions close to Hertzian and parallel film thicknesses which are similar to Grubin's solution. However, Dowson and Higginson's solutions introduced new characteristic features to the EHL solution at the outlet of the contact, which are the pressure spike and exit film constriction. Subsequently, extensive work has been carried out on the field of EHL regarding different advanced methods of numerical solutions based on the very fast developing computers. In addition different aspects have been taken into account such as the point contact problem, rheological models, surface roughness, thermal effects, as discussed in the review study of the development of the EHL field by Lugt and Morales-Espejel (2011). An anticipation of the future of developments in tribology and especially in the EHL field were presented by Evans and Snidle (2009).

As the current work deals with the temperature rise and heat partition within the EHL contact, the next section will concentrate on these aspects.

1.5. Thermal analysis in EHL

The temperature rise in machine parts due to the relative contact (usually lubricated) is an important factor in the operation of that machine in addition to wear and damage of its parts. Within the elastohydrodynamic lubrication (EHL) contact, the extreme high pressure leads to significant increase in the fluid viscosity in conjunction with elastic deformation of the contacted bodies. This high viscosity fluid within the contact is subjected to shearing and squeezing depending on the relative motion of the contacting surfaces. As a result of this shearing and compressing, heat is generated

within the fluid film and conducted to the solid surfaces in the contacted region. So that it is of considerable interest to study the temperature rise and heat partition in the EHL on the basis of the fluid film.

However, early thermal studies of the contacting bodies were based on dry contact analysis. Before presenting the thermal studies, it is important to classify the solid surface temperature into two components: the steady state or bulk temperature and the transient "flash" temperature that relates to the passage of the solid surface within the contact. Blok (1937) carried out an early work on the temperature rise in dry sliding contact. He considered that if two lubricated surfaces slide over each other with relatively high speed, a high rise in temperature will occur in the actual surface of contact. His work was to investigate the temperature rise in a surface due to stationary and moving heat sources of small dimensions compared to the bodies to which they were applied, which is the case of the semi-infinite body. Different geometries of heat sources with different types of heat distribution were considered, the case of the moving heat source gave an understanding of how the temperature rises in the sliding contacting surfaces.

Later on, Jaeger (1942) set out a general mathematical theory for moving source of heat in a form that can be easily used for particular experimental cases of sliding surfaces. Like (Blok 1937), a semi-infinite solid was imposed. Jaeger introduced exact solutions for the flash temperature in different cases in his work. The shape of the moving source of heat was approximated to either a long narrow strip or rectangular region. In terms of heat strength, uniform strength of the source was taken mainly in addition to brief discussion of variable strength source. The temperature calculation method of Jaeger forms the basis for the majority of gear design methods (Olver 1991). Archard (1959) presented a simple solution for flash temperature, in his work, the

mathematical complexities were reduced by emphasising the relevant physical considerations. The general criteria for evaluating the heat flow for each body was by equating the average temperature in both bodies over the area of contact. For fast moving heat sources, sideways heat flow was neglected as the depth of penetration of heat is small as compared with the contact dimensions i.e. one dimensional heat flow was imposed. Furthermore, he established a method based on the electrical analogy for the calculation of the average temperature in the contact as follows:

$$\frac{1}{\theta_M} = \frac{1}{\theta_A} + \frac{1}{\theta_B}$$

Where θ_M is the average temperature rise in the contact; θ_A is the temperature rise in surface A assuming all the heat flows to it; θ_B is the temperature rise in surface B assuming all the heat flows to it .In his work, he established that two alternative formulae (for high and low speed) can be used to calculate the flash temperatures. The selection of the appropriate formula for a given set of experimental conditions depends on the dimensionless parameter L (the Peclet number) which is a measure of the penetration depth of heat below the surface of contact.

For these dry sliding contact methods, the average or the maximum temperature on the contacting surfaces was assumed to be equal. These assumptions may be accepted in the case of dry contact, but for the lubricated contacts, where an oil film separates the surfaces there is no reason that this must be the case.

(Merritt 1962) carried out an early analytical analysis of thermal lubricated contact based on the fact that the heat is generated within the oil film and the contacted surfaces are not restricted to have the same temperature. He used the Blok model and the solution was based on altering the ratio of conducting heat to each surface. The

results deduced from his analytical analysis showed that the oil film has a highest temperature, the slow surface temperature is lower and the fast disk has the lowest temperature, as shown in Figure 1.2. In this figure, the zz plane in the film has the highest temperature where no heat is conducted through it. Hence the fraction of the generated heat that is conducted to the fast disk is higher than that which is conducted to the slower disk. In addition to his analytical solution, he carried out experimental work on a two disk machine to measure the inner surfaces rim temperature of the disks. The results of the experiments showed that the temperature of the fast disk was higher than the slow disk, which was not consistent with the analytical work. Hence Merritt concluded that "Further work is clearly needed".

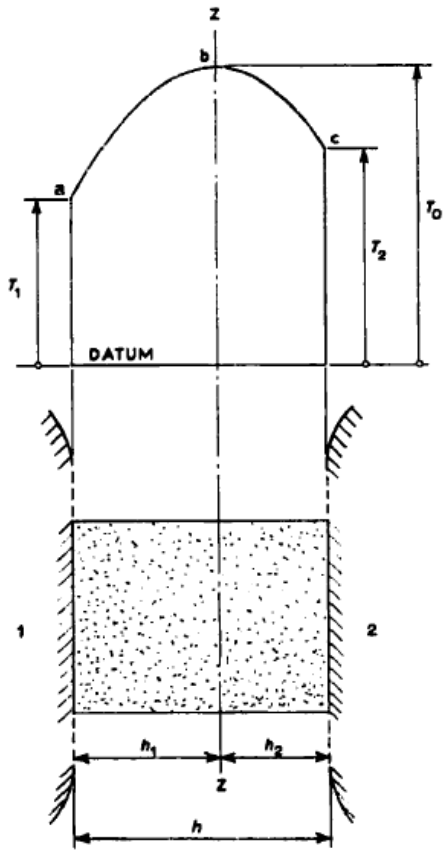

Figure 1.2: The calculated temperature across the oil film, from (Merritt 1962), 1 for the fast and 2 for the slow surfaces.

Later on, Manton et al. (1967) carried out a numerical thermal model considering the EHL problem to predict the temperature of the oil film and the contacting surfaces. The model was based on solving the energy equation in the fluid film. In their study, the case of line contact problem is considered under heavily loaded rolling/sliding conditions where the temperature rise due to contact is significant. Assumptions of Hertzian pressure distribution and constant parallel film were imposed which greatly simplify the numerical solution and are accepted in heavily loaded contact problems. The film thickness was calculated as in (Dowson et al. 1962) which made the shape of the film parallel except for the exit. The model of lubricant viscosity was pressure and temperature dependent and the surface bulk temperature were used as the inlet boundary condition temperature. The oil film and the surface temperatures were then calculated which led to heat partition calculations. These temperatures and assumed shear rates were evaluated for a range of entraining speeds, slide ratios, viscosities and loads. For calculating the heat partition they integrated the temperature rise of the metal components after passing through the contact zone. They deduced that for equal inlet temperatures, the heat flow to the slower surface is higher than the fast surface. Manton et al, compared their theoretical analysis with the experimental work of Merritt (1962) where the fast surface carried more heat. In Figure 1.3, three temperature profiles within the oil film were calculated. Each profile represents different inlet temperatures (80, 90 and 100 ^{o}F) of the fast surface with constant temperature 80 ^{o}F for the slower surface. It can be shown that the apex of the oil temperature is shifted towards the fast surface as its temperature increases, resulting in more heat being conducted to the fast surface than the slower surface which is consistent with the experimental result of (Merritt 1962).

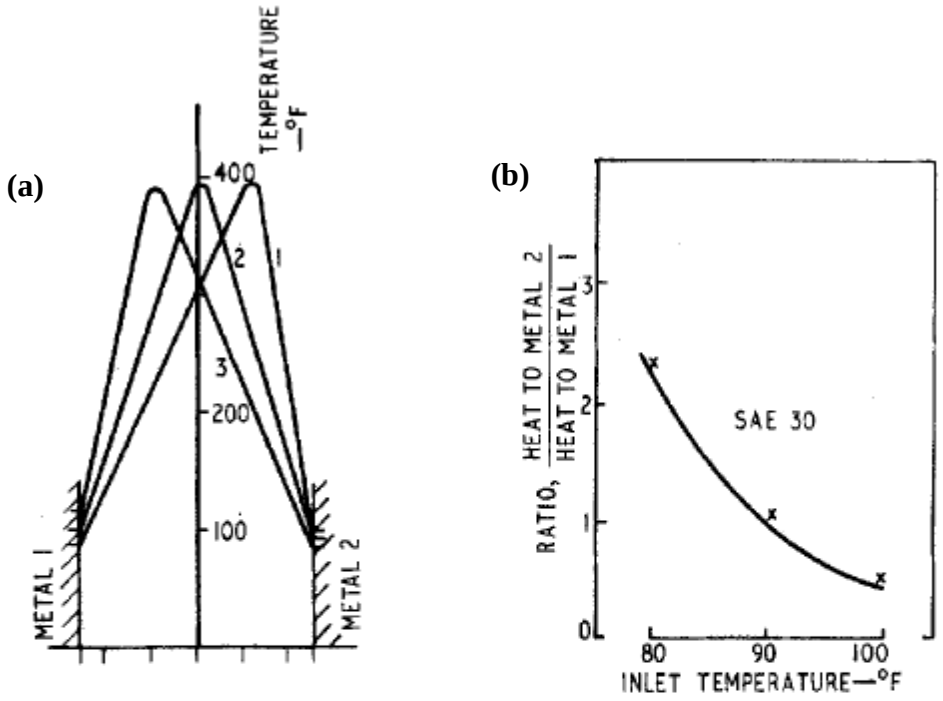

Figure 1.3: Adapted from (Manton et al. 1967), metal 1 is the faster surface, **(a)** the temperature profile at different inlet fast temperature(1for 80°F, 2 for 90°F, 3 for 100°F) with constant 80°F for the slow surface (metal 2). **(b)** the heat partition ratio for the three profiles.

Olver and Spikes (1998) developed a simplified non-Newtonian EHL model which combined the heat transfer effect of the contacting bodies in addition to the lubricant's rheological property variation according to temperature and pressure variation. High fluid film temperature were the common results of their predictions.

Wang and Zhang (1987) developed a more realistic non-Newtonian line contact thermal EHL model which is based on the Reynolds equation, the film shape equation and the energy equation. They concluded that considering both non-Newtonian and thermal conditions in EHL modelling is very important to achieve more reliable results. The subsequent work of (Sadeghi and Dow 1987), (Sadeghi and Sui 1990),

(Sui and Sadeghi 1991), and (Wolff et al. 1992) were similar to the work of (Wang and Zhang 1987) in presenting thermal line contact EHL model on the basis of the Reynolds equation, the film shape equation and the energy equation.

The effect of the roughness of the contacted surfaces were incorporated in the thermal EHL line contact model of (Chang 1992). Simulated (sinusoidal) and measured roughness were used, Chang concluded that the traction is insensitive to the magnitude and the structure of the surface roughness whilst it significantly affects the thermal solution. Real surface roughness also was incorporated in a thermal EHL point contact model by (Zhu and Hu 2001) and (Deolalikar et al. 2008), their models allow for studying the conditions of full film and boundary lubrication, i.e. the heating due to asperity contact in addition to the heat generated in the lubricant were considered. (Horng 1998) studied scuffing failure in rough sliding contacts experimentally using a disk-on-block test rig. He used Blok flash temperature and a criterion for predicting the onset of scuffing failure was proposed. Good agreement was found between the proposed failure criteria and the experimental scuffing data.

A thermal non-Newtonian point contact EHL model was developed in the work of (Sharif et al. 2001) and (Sharif et al. 2004) for modelling the EHL contact in worm gears and in a variable ratio traction drive test rig respectively. The thermal EHL model of Sharif was the basis of the model used by (Clarke et al. 2006) and (Clarke et al. 2007). In these studies, the heat partition between the contacting surfaces in the EHL contact was investigated by adopting different rheological models. The heat partition factor, β that resulted from the EHL model was compared with the factor calculated in (Clarke et al. 2006) by using a two dimensional heat conduction model applied to the experimental work of (Patching et al. 1995). Patching investigated the conditions for scuffing failure of steel disks in the test rig that is used for the current

EHL experimental study. A detailed description of the test rig can be read in section 2.2. The calculated heat partition factor from the experiments of Patching shows that the majority of generated heat within the EHL contact is conducted to the faster disk. This result was the reference for evaluating the realistic rheology incorporated in the thermal EHL model of (Clarke et al. 2006) and (Clarke et al. 2007). Figure 1.4 (a) shows the results obtained by Clarke for the heat partition factor based on the thermal analysis of the disks and single thermocouple temperature recorded by Patching. When plotted against the parameter ΔTu_s, Clarke showed that β followed a trend illustrated by the solid curve. Clarke also calculated the heat partition using an EHL analysis based on different viscosity and non-Newtonian rheological models which are compared with the trend curve of Figure 1.4 (a) in Figures 1.4 (b) and (c).

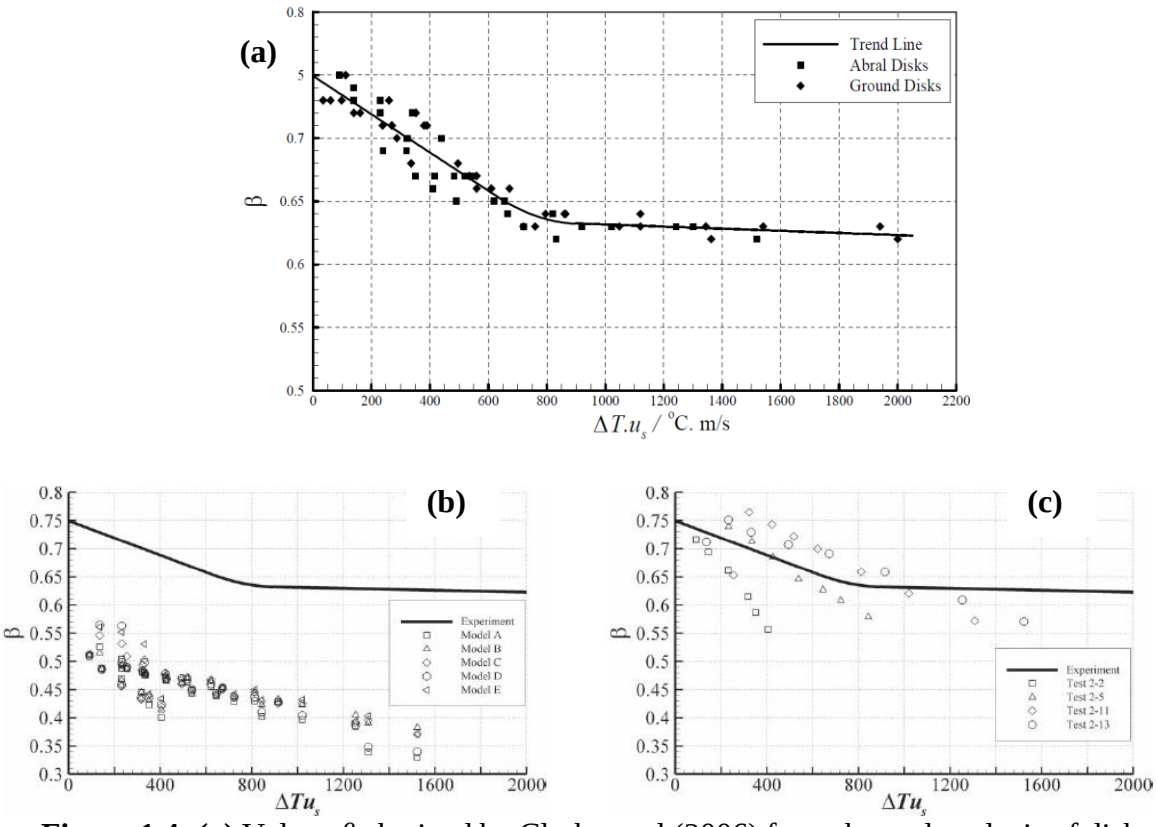

Figure 1.4: (a) Values β obtained by Clarke et al (2006) from thermal analysis of disks in Patching et al (1995), together with comparisons with results from EHL models taken from Clarke et al (2007). **(b)** shows comparisons for rheological models resulting in distributed shear and **(c)** for a limiting shear stress models that results in lubricant slip at or near the high temperature surface.

Later on, Clarke (2009) made extensive development on the test rig used by Patching to evaluate the heat partition in sliding/rolling EHL contact using more reliable techniques. This development was by embedding six thermocouples in each super-finished test disk with the side faces insulated by ceramic washers. More details on this development can be seen in section 2.3.

Kleemola (2010) also used twin-disk machine and real gear test rig for studying the EHL conditions of lubrication in gear contacts. The test devices were developed in conjunction with numerical modelling and this work is published as separate papers as follow. In the work of (Kleemola and Lehtovaara 2006), the test devices were developed to provide continuous variation in loading, rolling and sliding velocities and the inlet oil temperature. A thermocouple was embedded below the surface of one disk to measure the disk bulk temperature. In addition, the grinding process of the test disks was developed to provide grinding direction transverse to the rolling direction together with proper crowning that both correspond to real gear. In (Kleemola and Lehtovaara 2007) a range of tests was carried out on the developed test rig. They detected three different regions in the measured coefficient of friction; linear, non-linear and thermal region. They also found a trend of decreasing friction coefficient with increasing slide/roll ratio. The measured bulk temperature was found to increase as slide/roll ratio increases whilst the measured contact resistance between the disks decreases. Kleemola and Lehtovaara (2008) developed a numerical model to determine the actual viscosity properties and the limiting shear stress of lubricants. The model is an elliptical point contact model which was developed from the numerical line contact model which was used for the calculation of sliding friction in spur gear contacts(Lehtovaara 2002). The two disks were equipped with thermocouples at a location 3 mm below the surface for measuring their bulk

temperatures. The calculated friction coefficient results were generally found to have good agreement with the experimental results. However, the calculated and the measured temperature results have a discrepancy. The fast disk has higher measured bulk temperature than the slow disk which is opposite to the calculated surface temperatures. Kleemola and Lehtovaara (2009) used the twin-disk devices to study the temperature, friction coefficient and lubricant conditions along the line of action in gear contact. The test conditions were adjusted with the modified real gear experiments test rig (Jarvio and Lehtovaara 2002). It was concluded that the twin-disk simulation provides more local information for the friction coefficient, temperature and lubrication conditions than the measurements of the real gear experiments. In the work of (Kleemola and Lehtovaara 2010), the gear lubrication conditions were studied using the modified real gear test rig on the basis of the bulk temperature and contact resistance measurements that were applied to the rig. The gears were polished to 0.05 µm surface roughness and the measurements were carried out in typical gear industry mixed lubrication conditions. Figure 1.5 shows the thermocouple arrangements in the gear teeth.

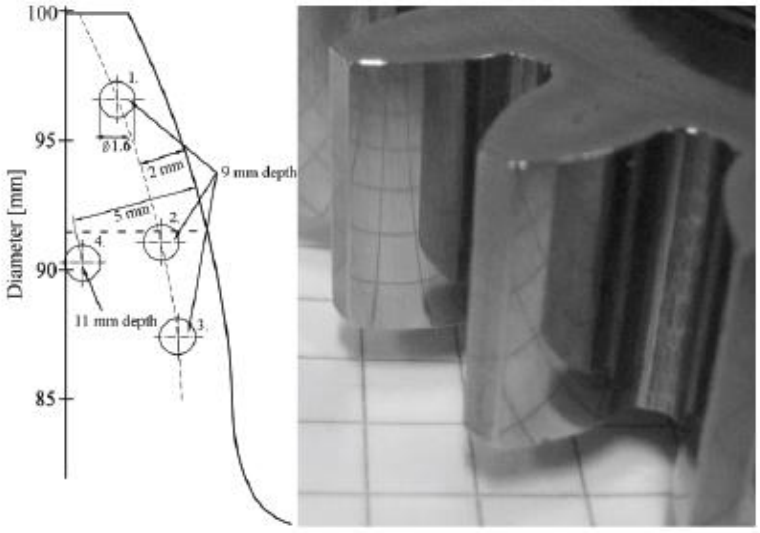

Figure 1.5: The thermocouples arrangement in the spur gear from (Kleemola and Lehtovaara 2010).

Good agreement was found between the measured contact resistance and the corresponding calculated steady state film thickness. The mean coefficient of friction is shown in Figure 1.6 (a) which shows a downward trend as the pitch line velocity increases. Figure 1.6 (b) shows the measured bulk temperature using the four embedded thermocouples for a polished gear test. It can be seen that the location of thermocouples does not give an understanding of how the heat is conducted to the teeth.

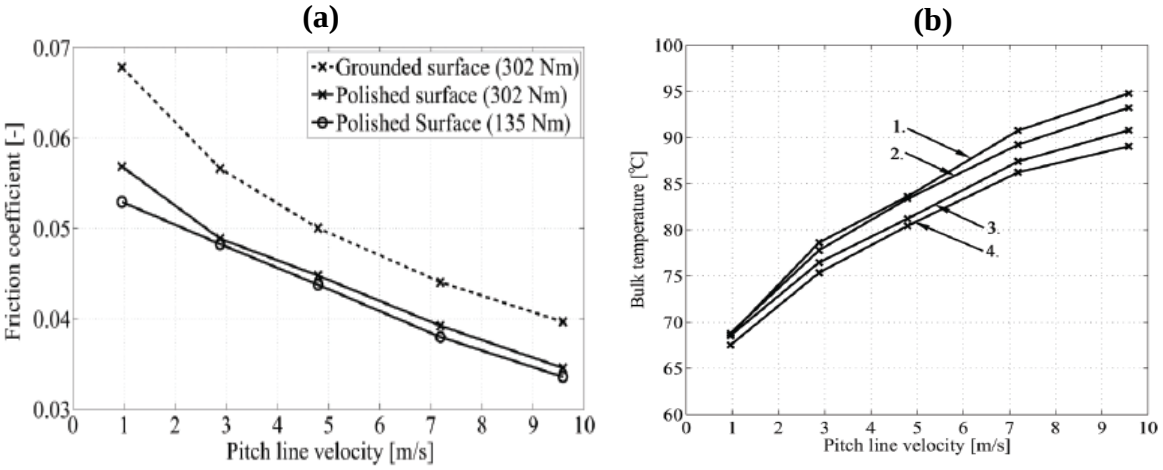

Figure 1.6: The experimental results from (Kleemola and Lehtovaara 2010), **(a)** the coefficient of friction, **(b)** The measured bulk temperature using the four embedded thermocouples.

More recent theoretical work was carried out by Habchi and Vergne (2015) to study the compressive heating/cooling within EHL contacts. Compressive heating is associated with pressure build up in the contact whilst cooling is associated with pressure drop which makes the lubricant acts as a heat sink. A numerical thermal point contact EHL model was used for the calculations under various loads and entraining speed of pure rolling and sliding/rolling conditions. In contrary with the common belief, it was evaluated in most cases that the compressive heating/cooling is less important than the shear heating even under pure rolling. During sliding/rolling

conditions, it was found that the heat generation is governed by shear heating even under the slightest sliding. The ratio of compression to shearing generated heat was found to increase continuously with increased load at a given entrainment speed.

1.6. Insight on temperature measurements in EHL contact

Temperature measurements in tribology are one of more the intractable problems as mentioned by Stachowiak and Batchelor (2004). They listed three of the temperatures that are important to be monitored. These are in ascending order of difficulty:

- The ambient temperature involving the lubricant on the lubricated contact.
- The surface temperature within and adjacent to the region of the dynamic contact.
- The transient temperature rise which is localised on a small area on the heated surface.

In tribology and especially in EHL problems, two major methods for measuring temperature are commonly used which are; thermocouples and infrared temperature mapping, these are reviewed in turn.

1.6.1. Thermocouples

Thermocouples are formed when two dissimilar metals are joined together at a junctions, where heat energy is converted to electric energy directly. More details on the function of thermocouples and their types can be seen in (McGee 1988) and (Bolton 1996). Using thermocouples in tribology problems involves several challenges, for instance, the installation method, the adjacency to the region of concern

and the dynamic response to the highly transient temperature change. Figure 1.7(a) shows a schematic diagram of a conventional thermocouple with the effect of the depth from the surface from (Stachowiak and Batchelor 2004) . The dimensions of the bimetallic junction of the thermocouples is an effective factor in the dynamic response of thermocouples. Some of the limitations that are related to conventional thermocouples are dealt with in special purpose thermocouples, these are described in (Stachowiak and Batchelor 2004), and can be seen in Figure 1.7 (b) and Figure 1.7(c).

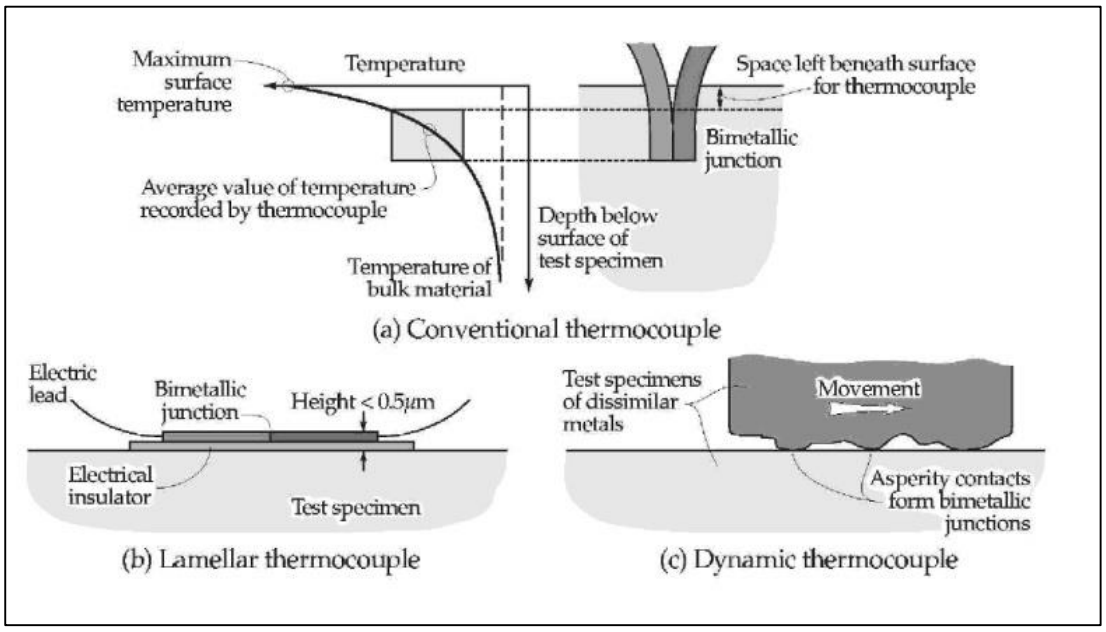

Figure 1.7: Different configurations of thermocouples used in temperature measurements in tribology from (Stachowiak and Batchelor 2004)

The thin film (lamellar) thermocouple shown in Figure 1.7 (b) is produced by coating the test specimen by layers of metal and insulation, the limitation of this type is that it can be easily damaged when subjected to wear . The dynamic thermocouple that is shown in Figure1.7(c) is basically constructed from the contacting metals themselves. Hence the contact temperature is measured directly by measuring the electric potential from the contacting metals. The use of this type is restricted to the limitations of the materials that form the thermocouples.

Dow and Kannel (1979) used the Lamellar thermocouple in a disk machine for measuring the temperature within EHL contact. They concluded that the measured temperature in the contact has an excellent agreement with the calculated temperature based on the measured traction. Henning et al. (1995) had also used a thin (Lamellar) thermocouples in studying the temperature rise in dry sliding contact in a bearing made from thermoplastic polymer. The test was carried out by rubbing a polymer specimen on a flat surface containing a set of the thermocouples. These thin thermocouples were made by depositing vapour of Copper and Nickel on metallic or glass substrates. The formed junctions are of 0.5 to 2 μm and are sandwiched between thin films of hard ceramic to be electrically insulated and protected. Those thermocouples were tested and found to have extremely high response to sudden temperature change. The dynamic thermocouple was used in the work of (Ishikawa et al. 1974) to measure the surface temperature on spur gear teeth. Similarly, the work of (Dinç et al. 1993) used an apparatus involving dynamic thermocouples to measure the contact temperature.

Another useful thermocouple configuration used for surface temperature measurements in tribology is the *trailing thermocouple*. In this technique, a stationary thermocouple is held against the surface of a moving element, it is usually compressed against the surface by means of a spring force. The main feature of this configuration is that there is no need for modifying any of the contacting elements, when the thermocouple is attached onto the surface causes of one or both of these elements. However, the trailing thermocouple cannot be applied to measure the surface temperature at the contact zone between the rubbing surfaces. Another disadvantages of this thermocouple is that in dry surface cases, the measured temperature deviates from the actual surface temperature depending on the compression force. On the other hand when there is a lubricant, it measures the mean value of temperature of the real

surface and the lubricant boundary layer (Iliuc 1980). (Sharif et al. 2004) used a trailing thermocouple to monitor the temperature of the roller in the Torotrack traction rig. The measured temperature from this thermocouple was subject to noise during the tests, however it gave a good indication of the component bulk temperature. A trailing thermocouple was also used by Evans et al. (2008) to measure the mean oil temperature at the contact inlet of rolling ball on a disk rig.

Using the above special purpose thermocouple in tribology does not limit the application of the conventional thermocouples in measuring the temperature of the contacting elements and their ambient temperatures. The low cost, simple structure and reliability are the major features leading to wide use of conventional thermocouples. However, the installation arrangement on the target point, the fixing technique and the junction dimensions still represent challenging problems in using these thermocouples. The following are some examples of applications of the embedded thermocouples in tribological cases. Handschuh and Gargano (2014) studied the behaviour of spur gears under the conditions of loss of lubricants in a simulated aerospace environment. Five thermocouples were embedded in the spur gear at different locations on the web and tooth of the gear as shown in Figure 1.8 from (Handschuh and Gargano 2014).

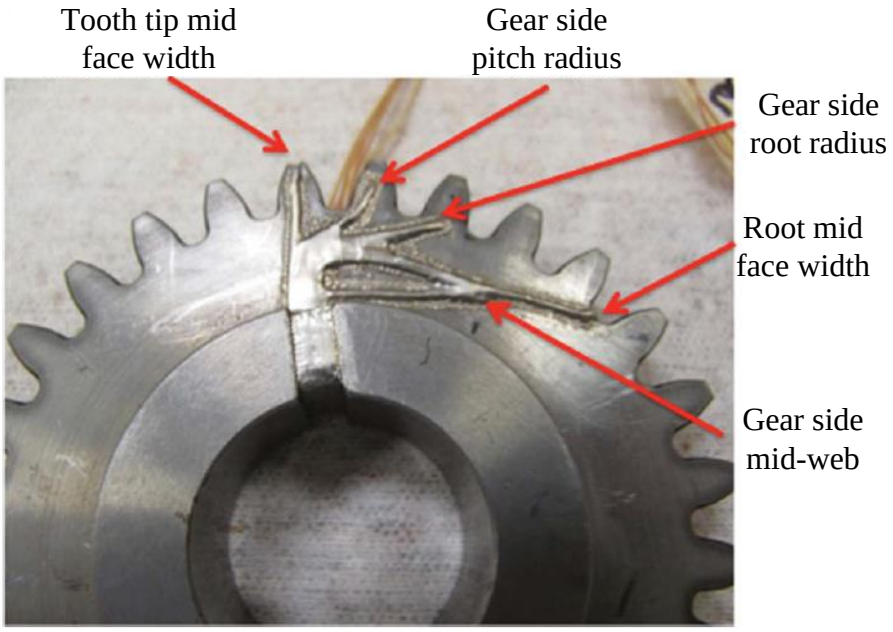

Figure 1.8: The thermocouples arrangement in the spur gear from (Handschuh and Gargano 2014).

Clarke et al. (2014) also used embedded thermocouples at 3 mm below the surface of the disk in twin disk machine. Their work was to study mixed-elastohydrodynamic lubrication using a technique based on electrical contact resistance (ECR). The temperature measured by this thermocouple was important to determine the lubricant viscosity at the entrance of the contact. The thermocouple signal was transmitted through slip rings which are commonly used to transmit data from rotary elements. In the work of (Okamoto et al. 2000), a thermocouple was used to measure the temperature of the bearing outer race in studying the wear and fatigue of engine bearings. Experiments were carried out using a test rig machine in which the conditions of engine bearings were simulated. The experimental results were compared with the EHL calculated results.

1.6.2. Infrared temperature mapping

Turchina et al. (1974) developed a technique for temperature measurement in sliding EHL point contact. This technique is based on measuring the infrared radiation emitted from the contact zone. In their work, modifications were carried out on the equipment that were used for the investigation on the film thickness and traction in (Sanborn and Winer 1971 a) and (Sanborn and Winer 1971 b) respectively. Figure 1.9 shows the experimental equipment used in (Turchina et al. 1974) after development. In this figure the microscope which was used to observe the interference fringe patterns for measuring the film thickness was replaced by an infrared radio- metric detector for temperature measurements.

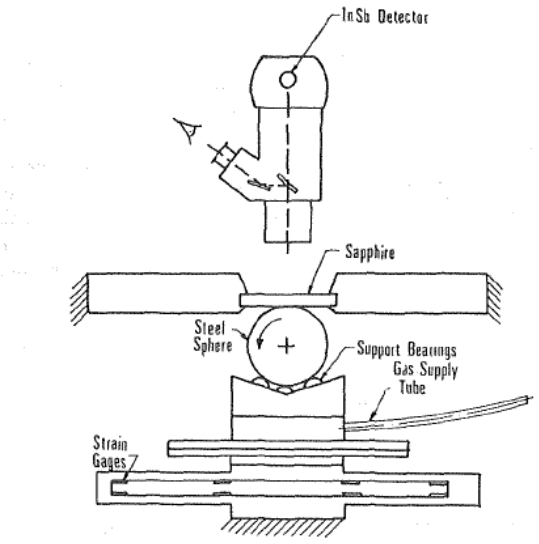

Figure 1.9: the equipment used for measuring the temperature in the EHL sliding contact by using infrared detection technology from (Turchina et al. 1974)

As can be seen from Figure 1.9, the sliding EHL contact is formed between a stationary sapphire plate and rotating steel ball. The experimental devices were set up so as to isolate the components of the radiation of the steel ball, the oil film and the sapphire plate. This then allowed their individual temperatures to be measured rather than the

average temperature of the contact. The lubricant used in this work was a naphthenic mineral oil, the upper sapphire surface was assumed to have the ambient temperature. A particular experimental result has shown a 360 ^{o}C maximum film temperature with a 115 ^{o}C maximum temperature in the steel ball which are both increased by increasing the sliding speed. Their results also have shown that the maximum temperature was located at the contact side lobes where the film thickness is minimum. Later on, Ausherman et al. (1975) had improved the technique for the measurement of temperature distributions in an EHL contact used by Turchina et al. (1974) using two interference filters to separate the individual contributions from the overall infrared radiation. They also achieved detailed mapping of both the ball surface and the fluid temperatures (average temperature through the film thickness). Ausherman et al. (1975) found that the technique that they used were more demanding and reliable than that reported by Turchina et al. (1974). Wymer and Macpherson (1975) also worked on infrared for surface temperature measurements and developed that technique for use in spiral bevel pair. The tool for the measurement of the gear tooth surface temperature was developed and modified. The same technique was also applied within a rolling element bearing for temperature measurements by the inclusion of a sapphire window within the bearing tracks.

(Cann and Spikes 1989) also used IR (infrared radiometry) for measuring the surface temperature profile to use it in determination of the local shear stress across the sliding contact. In their work, the temperature measurements was limited to the metal surface only and no attempt was carried out to measure the lubricant film temperature. A lubricated steel ball sliding against fixed sapphire plate was used in the experimental temperature measurements (pure sliding). The mean shear stress was determined with assumption of equal surface temperature of the contacting bodies in the region of

contact. It was also assumed that all the generated heat is conducted to the contacting surfaces and the heat is generated by shearing only. The temperature profile along the contact was measured for different sliding speeds by using two types of oils.

Glovnea and Spikes (1995) used similar technique to (Cann and Spikes 1989) and made a similar assumption in shear stress determination. However the measuring equipment were developed by replacing the manual mapping by an automatically controlled mapping procedure. This was carried out by using a stepper motor controlled by a microcomputer for scanning the contact zone.

Kim et al. (2001b) were extended the Newtonian numerical solution used in (Kim et al. 2001a) to a non-Newtonian thermal point contact problem, and to compare the results with the experimental work of (Cann and Spikes 1989) which is pure sliding EHL problem. They obtained an overall fair agreement of calculated surface temperature with the experimental results. The best agreement was obtained at the lightest load, and greater discrepancy was found with increasing load. In other words, lower predicted temperatures than the experiment were obtained with higher load.

Spikes et al. (2004) made an extensive development to the temperature mapping techniques described above. These were by extending the previous pure sliding condition to a variable slide/roll contact ratio. In addition, the developed equipment has the ability to measure the temperature of both contacting surfaces whilst the temperature mapping prior to their work were limited only to the steel ball temperature measurement. Figure 1.10 shows the test apparatus used by (Spikes et al. 2004).

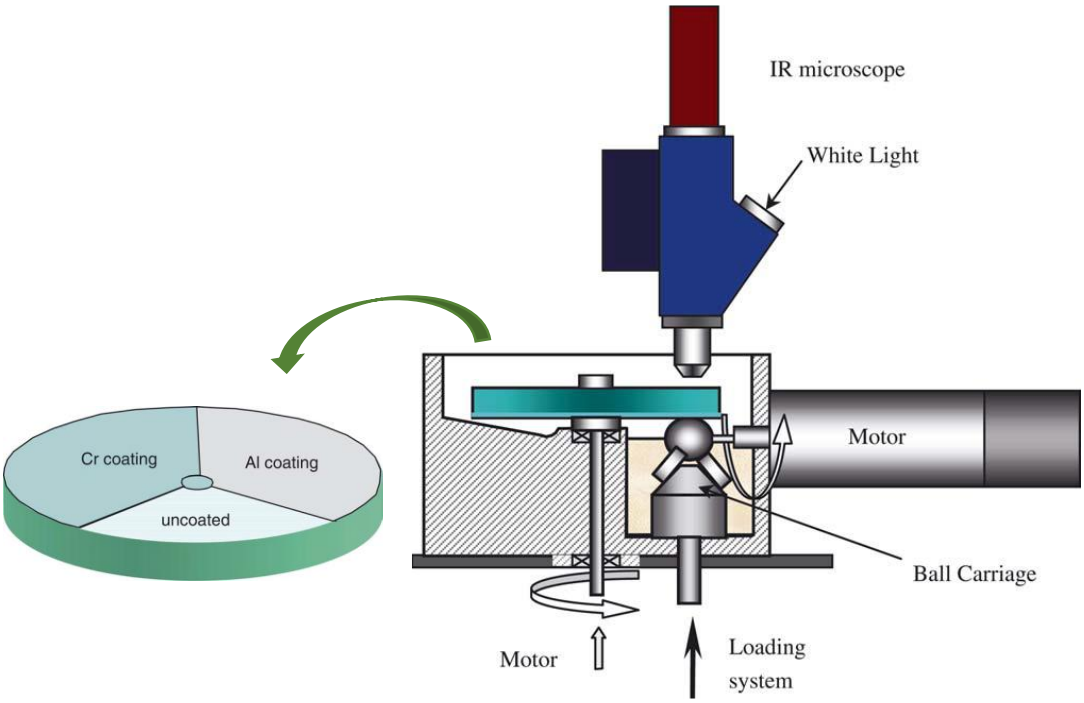

Figure 1.10: The test apparatuses used by (Spikes et al. 2004), adapted from (Spikes et al. 2004)

Figure 1.10 shows that the sapphire surface has the ability to rotate in addition to the steel ball for producing variable slide/roll ratio. Figure 1.10 also shows (on the left) sapphire disk which has coated sectors to achieve the aim of measuring the bulk and surface temperatures of the disk. A typical temperature map for the two contacting surfaces from the work of (Spikes et al. 2004) is shown in Figure 1.11.

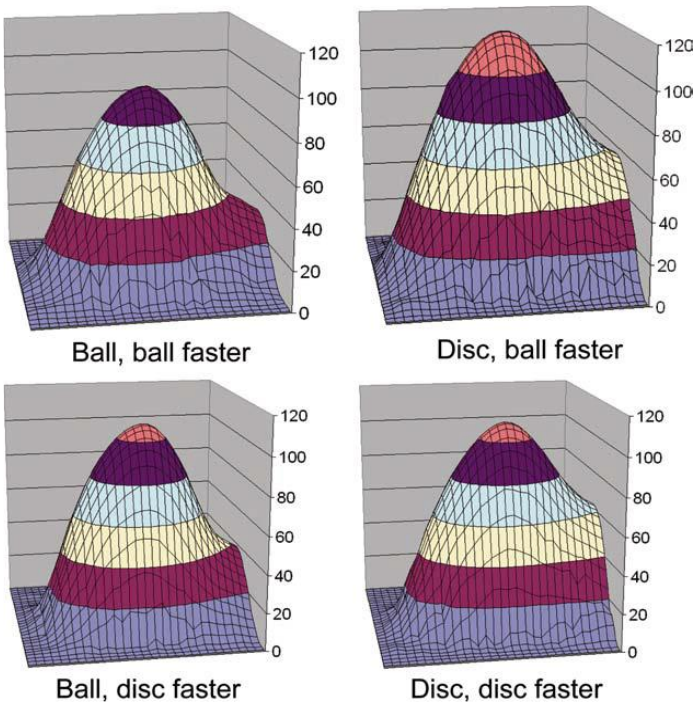

Figure1.11: A typical temperature maps for the contacted surfaces from (Spikes et al. 2004). Sliding speed=1.13 m/s, load =50 N and slide/roll ratio=±1.0

Figure 1.11 shows in the case where the ball is the faster, the disk surface has a higher temperature whilst when the disk is the faster surface, the two surfaces broadly have the same temperature.

Reddyhoff et al. (2009) developed the test apparatus used by Spikes et al. (2004), using a high specification infrared (IR) camera. This provided a full field measurement of the contact instead of scanning by moving the infrared detector over the field. The camera also has higher sensitivity and higher spatial resolution if compared with the previous system. This higher sensitivity allows for larger range of test conditions like loads, speeds and lubricants. In their work, the effect of generated heat due to compression was minimized by subtracting the temperature in pure rolling conditions. Their work was carried out at a single slide/roll ratio of 0.5 and the tests were carried out over a range of entrainment speeds. It was found that the maximum temperature in the faster surface (the disk) is higher than that of the steel ball.

Le Rouzic and Reddyhoff (2013) worked on improving the infrared temperature mapping approach used in (Reddyhoff et al. 2009) for the measurements of rough surface contacts. They were concluded that the infrared microscopy is an active technique for mapping the temperature of the contacted surface and this is enhanced as the camera sensitivity increases. However, at that time time, they found that this technique had two significant restrictions for the use in mapping the rough surfaces: the requirements for an aluminium coated specimen and the diffraction-limited spatial resolution.

1.7. Aims of the current work

Previous work by Clarke et al, summarised in Figures 1.4 (a), (b) and (c), shows that the heat partition generated in an EHL film depends critically on the rheological model used for its analysis. As a result, knowledge of heat partition factor obtained from independent experimentations can provide evidence to enable appropriate rheological models to be determined. Seeking such evidence based on robust experimentations was underlying objective of this research.

The principle aim of this project is to study the temperature rise, heat partition and friction within EHL point contacts. A test rig for this purpose was available and needed to be re-commissioned and developed for obtaining EHL experimental results. An investigation on uncertainties associated with the experimental results was also to be carried out. A numerical thermal model for the test disks would be built and examined with corresponding theoretical models. Optimization methods would be developed for more reliable heat partition results by modelling the experimental EHL tests. Finally, the experimental and modelled results would be compared with the previous

experimental results and with the results obtained from numerical thermal point contact EHL model.

Chapter 2:
A Test Rig for the Experimental Investigation of EHL Point Contact

2.1. Introduction

In this chapter, the test rig that is used for the investigation of heat partition in EHL contacts is fully described. A general background about the history and development of this rig is given in sections 2.2 and 2.3 which summarize the work of previous contributions. The process of re-commissioning the rig for use in the experimental program that was carried out in this project is described in sections 2.4 to 2.10. The re-commissioning process included the instrumentation and calibration of the sensors for building the data acquisition system.

2.2. Description of the test rig

2.2.1 General overview

The test rig was originally constructed to investigate scuffing failure of surfaces, under conditions of sliding speed and load typical of those found in gas turbine gearing. It was designed for a Rolls-Royce/SERC co-funded project (Patching 1994), for the aim of reproducing the conditions found in gas turbine engine gearing and to study scuffing failure. The rig is a two disk machine which simulates rolling/sliding power transmission contacts under EHL conditions. The two experimental disks in contact are considered as equivalent rollers that represent gear teeth under similar gear

circumstances in terms of load, rolling and sliding speed. This allows the study of EHL contacts without the complications of varying load and kinematics which occurs in gears, cams, and roller bearing etc. The test rig was designed to provide high speed disk rotation up to 12000 rpm, with adjustable gear ratio giving slide/roll ratios of up to 1.3. The disks are crowned to give a self-aligning point contact. The original specification of the two disk machine is outlined in Table 2.1 from (Patching 1994).

Table 2.1: The initial specification of the Two-Disk Machine from (Patching 1994)

Sliding speed	Up to 23 m/s
Maximum Hertzian contact Pressure	Up to 1.7 GPa
Oil feed temperature	Up to 200 ^{o}C
Lubricant	Mobil Jet II synthetic (ester-based) gas turbine lubricant
Disk Material	Case-carburised alloy steel to Rolls-Royce specification 6010
Heat treatment	Case-carburized, hardened and tempered to Rolls-Royce specification (RPS371)
Disks surface finish	Final Grinding to 0.4 µm Ra, transverse to direction of rolling/sliding

Figure 2.1 is a general view of the test rig, whilst Figure 2.2 shows the layout of the test rig. Figure 2.3 is isometric drawing of the test head and Figure 2.4 shows the layout of the test head.

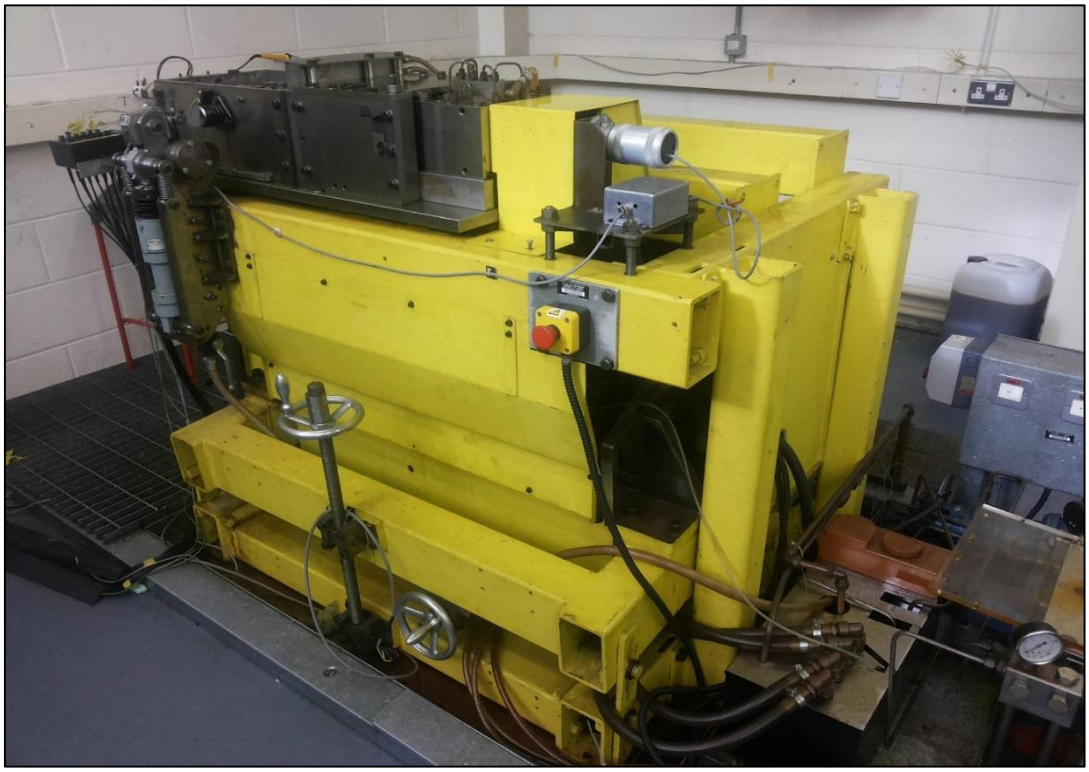

Figure 2.1: Photograph showing general view of the test rig

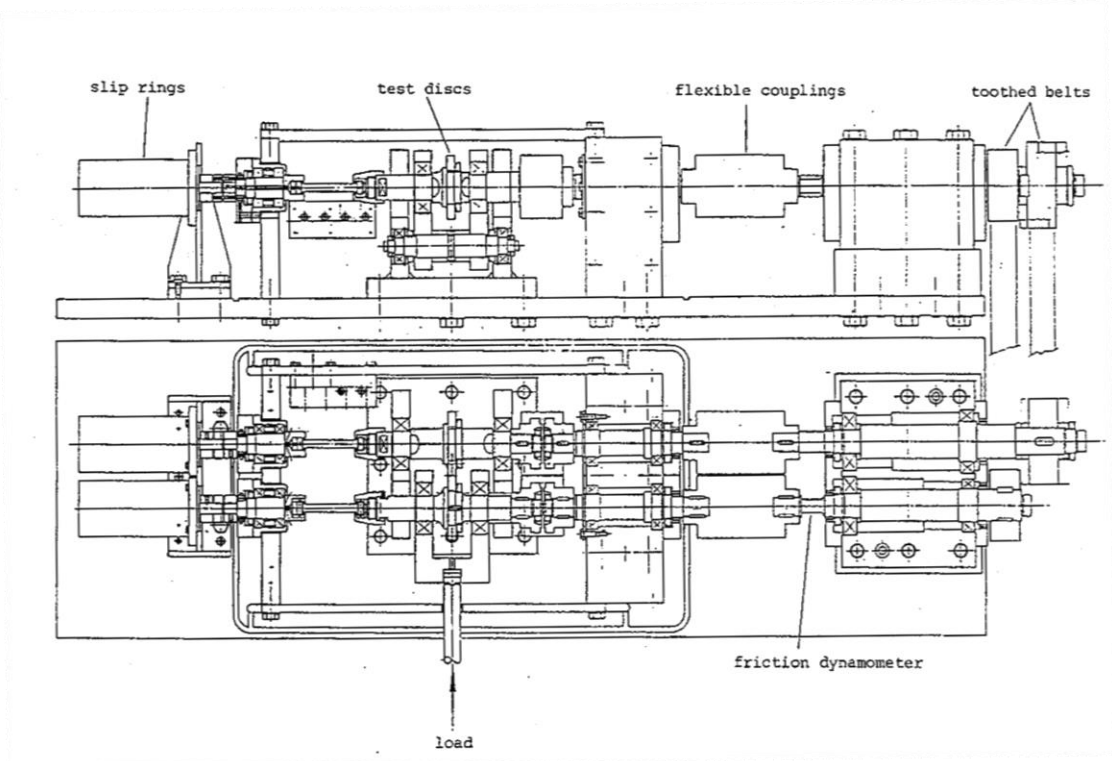

Figure 2.2: Section and plan drawing of the rig showing the test disks and shafts, the drive path and the loading arrangements from (Patching 1994)

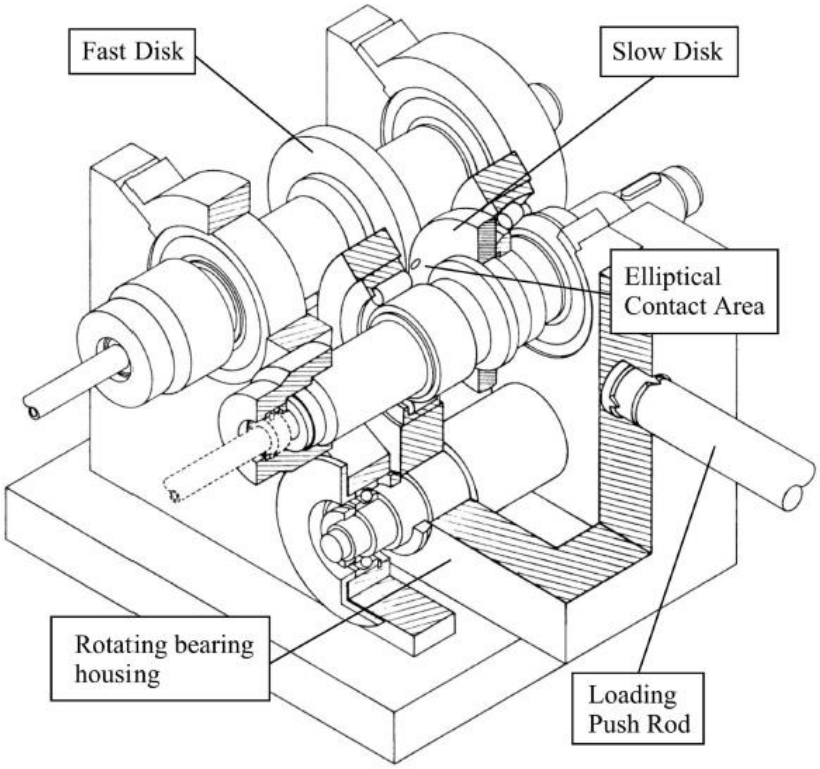

Figure 2.3: Isometric view of the test head from (Clarke 2009)

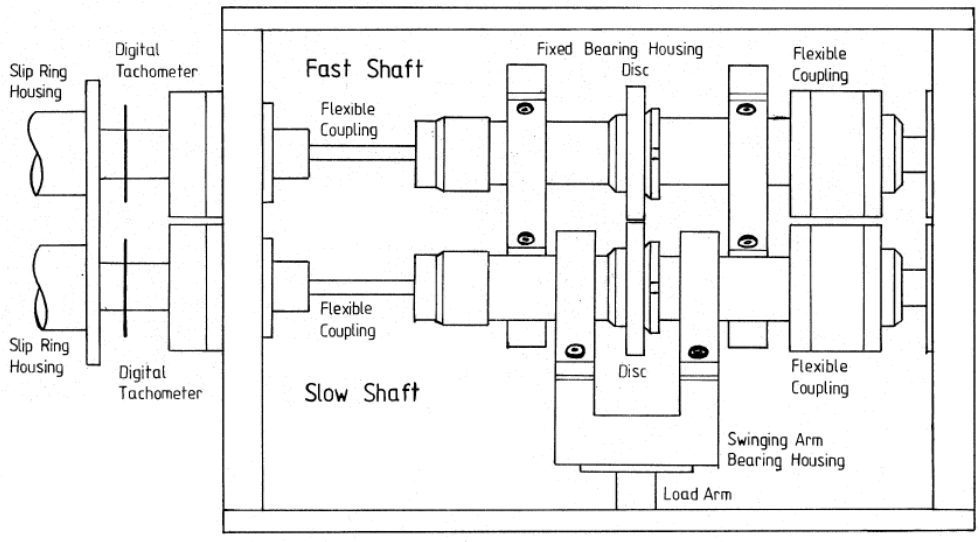

Figure 2.4: Layout of the Test Head from (Patching 1994)

The rig was designed to operate at relatively high speed, accordingly the test disk shafts are supported by rolling element bearings. There are double row spherical roller bearings at one end of each shaft, which provides both radial and axial restraint. The other end of each shaft is supported by cylindrical roller bearings which restrain in the radial direction only. This support configuration gives high radial load capacity with allowance for axial thermal expansion.

The shafts are made from EN36C steel, case hardened to 680 Hv (Clarke, 2009). They are finish ground between dead centres to ensure a high degree of concentricity. The disks are pressed onto the shafts with a high diametral interface fit of a range (15 to 25) μm and secured by locking nuts. The shafts have long axial holes with cross-drilled radial holes for feeding thermocouple wires from the test disks to the slip rings at the end of each shaft.

The rig is powered by a fixed speed AC motor via an 18.5 kW TASC eddy current variable speed coupling, which drives the splitter gearbox via a toothed belt and pulleys. The two output shafts of the splitter drive are also connected to the test shafts via toothed belts and pulleys. The maximum speed of the TASC unit is 2800 rpm. The belt drive ratio between the test shafts and the output shafts of the splitter gearbox controls the speed in each test shaft which is designed to allow a maximum fast shaft speed of 12,000 RPM, corresponding to a disk surface of 47.88 m/s. Different combinations of pulleys are available to allow having test shaft speed ratios between 1 (pure rolling) and 5. The shafts rotate in opposite directions which makes the surfaces of the contacted disks move in the same direction. The following is a kinematic analysis of two surfaces undergoing rolling/sliding relative motion. The surface speed of each disk is u_1 and u_2 respectively, so that the sliding speed is

$$u_s = u_1 - u_2 \tag{2.1}$$

The mean entraining velocity (the rolling velocity) is defined as

$$u_r = \frac{u_1 + u_2}{2} \tag{2.2}$$

Hence the slide/ roll ratio is written as

$$\frac{u_s}{u_r} = \frac{2(u_1 - u_2)}{(u_1 + u_2)} \tag{2.3}$$

Writing equation (2.3) in terms of the effective gear ratio, *G*, between the shafts gives:

$$\frac{u_s}{u_r} = \frac{2(G - 1)}{(G + 1)} \tag{2.4}$$

The pulley configurations in the current work were chosen to give a 4.24 gear ratio and therefore the slide /roll ratio is 1.24.

2.2.2 The test disks and the insulating washers

The test disks fitted to the rig are of standard geometry used in the disk machines at Cardiff University. They are crowned with radius 304.8 mm (12") and their main diameter is 76.2 mm (3"). Figure 2.5 shows the geometry and dimensions of the disks. This geometry forms an elliptical dry Hertzian contact between the disks with aspect ratio of 3.91. The larger axis of the contact (the major axis) is parallel to the disk axis and the direction of the entraining speed is parallel to the smaller axis (minor axis). The disks were made from a case-carburising Nickel-Chromium alloy steel provided by Rolls-Royce to their specification RR6010. The composition of this alloy is given in Table 2.2.

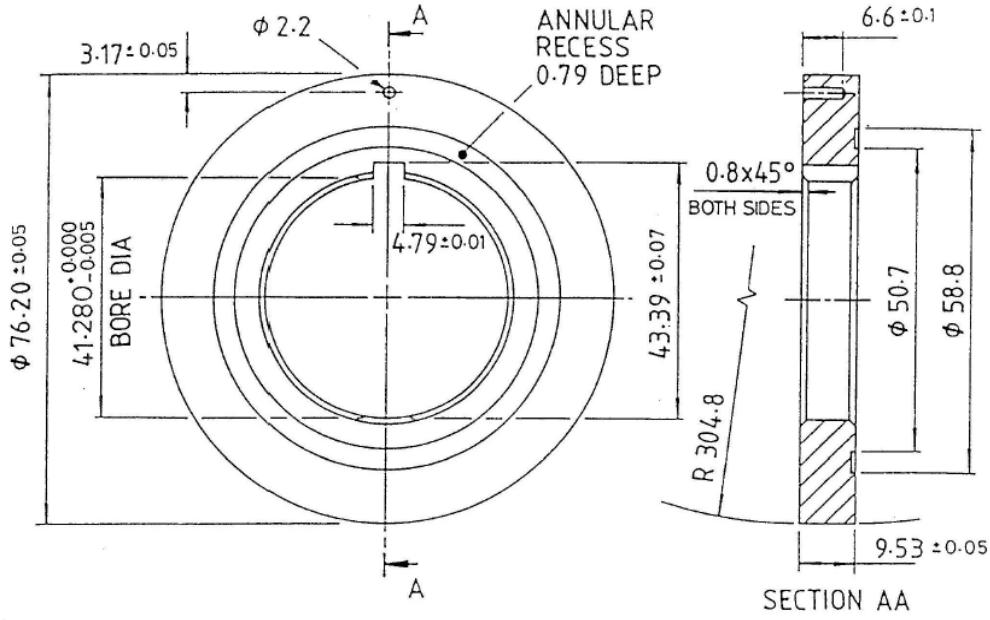

Figure 2.5: The initial design of the test disks from (Patching 1994), all dimensions in mm

Table 2.2 Composition of RR6010 Steel (%mass)

Element	C	Si	Mn	P	S	Ni	Cr	Mo
Max	0.18	0.35	0.55	0.015	0.012	4.30	1.40	0.30
Min	0.14	0.10	0.25	0.00	0.00	3.80	1.00	0.20

The heat treatment process of the disks is outlined in Table 2.3 which is a typical aerospace specification. Following heat treatment, the disk surfaces were ground and super-finished to a typical roughness (Ra) of 0.04 μm.

Table 2.3: The heat treatment specifications of the test disks from (Patching 1994)

- Normalise @ 930 ºC ±10 ºC for 3 hours ±15 minutes
- Harden @ 850 ºC ±10 ºC for 3 hours ±15 minutes
- Temper @ 530 ºC ±10 ºC for 3 hours ±15 minutes
- Carburize @ 927 ºC ±10 ºC to yield a carburized case depth (RC 50) of 0.036 to 0.042 inch, with a surface carbon (second 0.002" cut) of 0.65 to 0.95% Carbon
- Cool to room temperature after carburising
- Stress relieve @ 566 to 621 ºC for 4 hours ±15 minutes, then air cool
- Harden @ 788 to 829 ºC for 30 minutes, then oil quench (24 to 60 ºC)
- Subzero treat, within 60 minutes of quenching, for 3 hours minimum at -79 ºC or lower
- Temper @ 160 ºC ±5 ºC for 3 hours ±15 minutes
- Final carburized surface hardness to be HRC 60 to 63
- Case depth (HRC 50) to be 0.036 to 0.042"
- RC 60 depth to be 45% of 0.036" (0.016" of case)
- Core hardness to be HRC 36 to 41

2.3. Background

As mentioned previously, the test rig used to carry out the present experimental work was originally constructed to investigate scuffing failure of surfaces, under conditions of sliding speed and load typical of those found in gas turbine gearing. The original scuffing tests had been carried out by Patching (1994). In those tests, the scuffing failure in the running disks was detected after applying a series of loads on the contact region which is under EHL conditions. The friction force between the surfaces in the EHL point contact and the bulk temperature within the disks were recorded on an analogue chart recorder during the tests for a series of increasing loads. The tests were ended by unloading the disks when scuffing failure was detected: the scuffing being indicated by a sudden increase in noise, friction and disk temperatures which is shown in Figure 2.6 from (Patching 1994).

Figure 2.6 provides example records of the temperatures for both slow and fast disks, the friction force generated in the contact is also recorded. These data are recorded versus time (which increases from right to left in this chart) for a series of increasing load stages. There are seven load stages in this figure. In each load stage, the temperature increases gradually until reaching (or approaching) steady state at the end of that load stage. The friction force decreases slightly before the end of each load stage. This behaviour might occurs as a result of a running in process in the disks surfaces during loaded rotation. The running in process leads to smoother surfaces, consequently, the friction force reduces. During the last stage of the test, the steep increase in the recorded quantities (temperature and friction) indicates scuffing occurring in the contacting surfaces. Subsequently, the disks were unloaded, and thus lead to a sharp fall in the recorded data.

The most surprising aspect of Figure 2.6 is the higher temperature recorded for the fast disk and lower temperature for the slow one. The temperature might be expected to be higher in the slower disk for two reasons. Firstly, the previous theoretical analysis concluded that the largest amount of heat in the EHL contact is conducted to the slower surface. Secondly, the fast disk loses more heat by convection during the test because it runs with higher speed, and as a result, the forced convection heat transfer is increased with increasing speed.

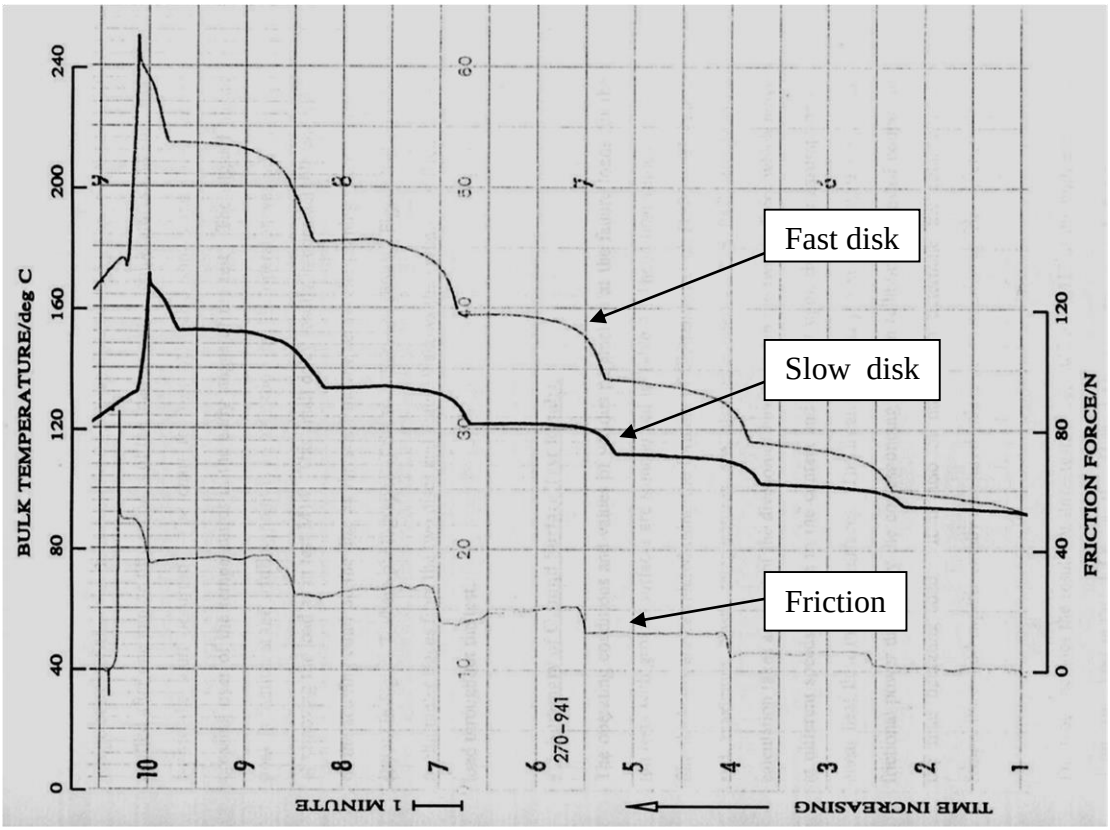

Figure 2.6: A chart for typical scuffing tests (adapted from Patching, 1994). Note that the time increases from right to left in this chart record

This unexpected temperature behaviour in the test disks led Clarke et al. (2006) to investigate the heat partition between two surfaces in EHL contact. They used the scuffing results to study the thermal analysis and the heat partition between two surfaces undergoing EHL point contact phenomenon. In that study, the results from a thermocouple embedded 3.2 mm below the surface in each disk was applied to a two dimensional bulk temperature conduction numerical model. Each shaft and its disk were considered as a single body in that thermal analysis. Previous empirical relations from the literature were used to provide the convection heat transfer coefficients used in the model.

Type J thermocouples are used in the test disks for the previous work and also for the research repeated in this thesis. The temperature measurements are in the range 15 to 230 ^{o}C. The Type J thermocouples used had a range of -75 ^{o}C to 250 ^{o}C with an uncelebrated accuracy of ± 2.5 ^{o}C.

Subsequently, Clarke (2009) made extensive modifications to the disks and the data acquisition system of the rig. The modified test rig was used to carry out a series of experiments for studying the heat partition and thermal analysis in EHL point contacts. In this program of work, each disk was fitted with six thermocouples in two rows of three, located at radial positions 3 mm and 6 mm below the running surfaces of the disks. The thermocouples were located at different circumferential positions so that they were not in an axial straight line, in order to minimise any disruption caused to conduction in the disks.

The other important modification was fixing ceramic insulating washers on both sides of each disk to control and minimize convection heat losses from the side face of the disks. Figure 2.7 shows the test disks after the modifications made by Clarke (2009). The figure shows the disks as fixed on the shafts and two ceramic washers are fitted to the side faces of each disk. Attachment is by means of M3 bolts as can be seen on the slow disk in the photograph.

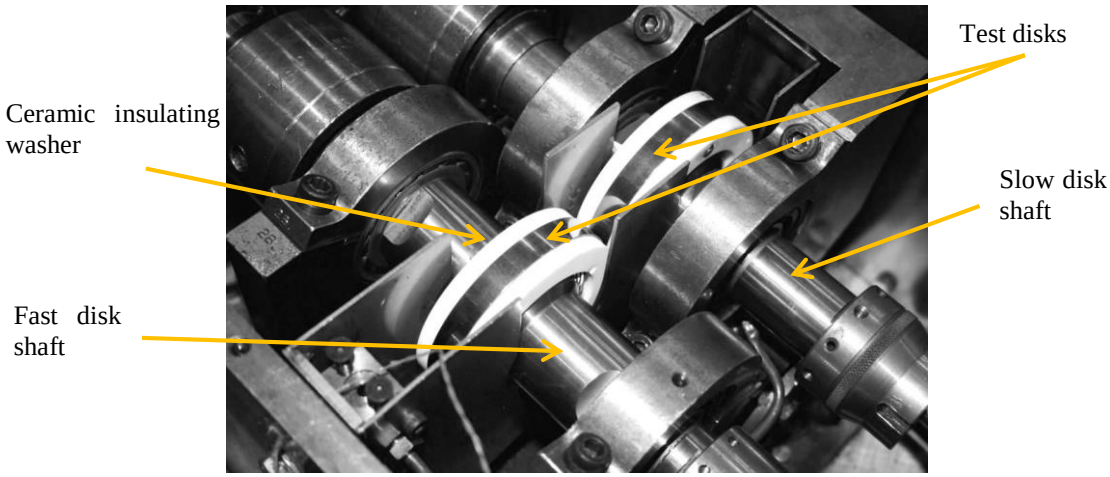

Figure 2.7: Photograph showing the test head after the modification, from (Clarke 2009)

Figure 2.8 is a schematic section of the disk and shaft configuration showing the positions of the six thermocouples embedded in the disk. Each of these rows has a central thermocouple and one on either side approximately 2 mm from the side surface. They are at least 9 mm on length apart in the circumferential direction

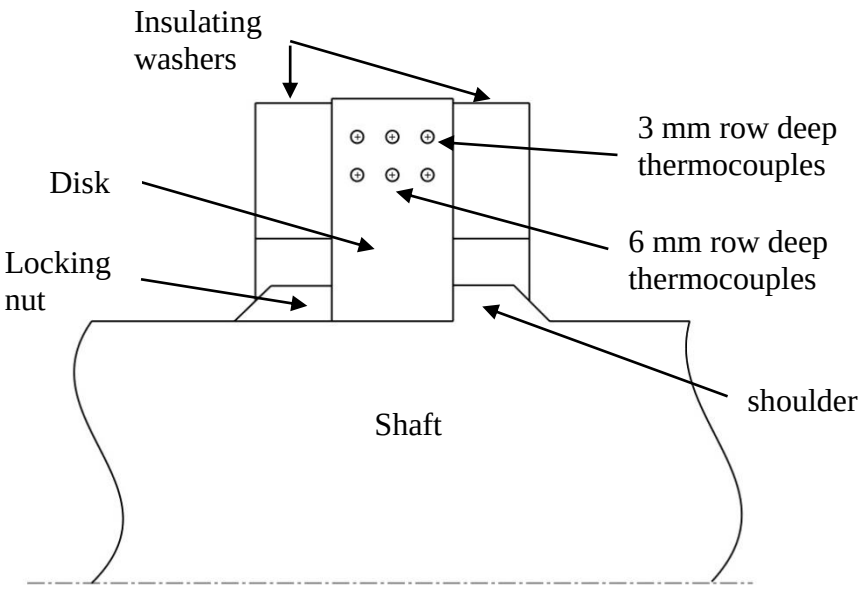

Figure 2.8: Section showing the modifications made by Clarke (2009)

The insulating washers are intended to control the heat flow in the radial direction. Thus, the temperatures recorded by the six thermocouples in each disk are appropriate for the disk thermal modelling.

The outside diameter of the washers is 76 mm which is slightly smaller than the disk outside diameter (76.2 mm). This is to ensure that each washer will not come into contact with its counterpart on the other disk. The test disk is sandwiched by two washers using machine screws. The bolt head and the nut are sited in counterbored holes through the washer. Figure 2.9 shows one of the ceramic insulating washers

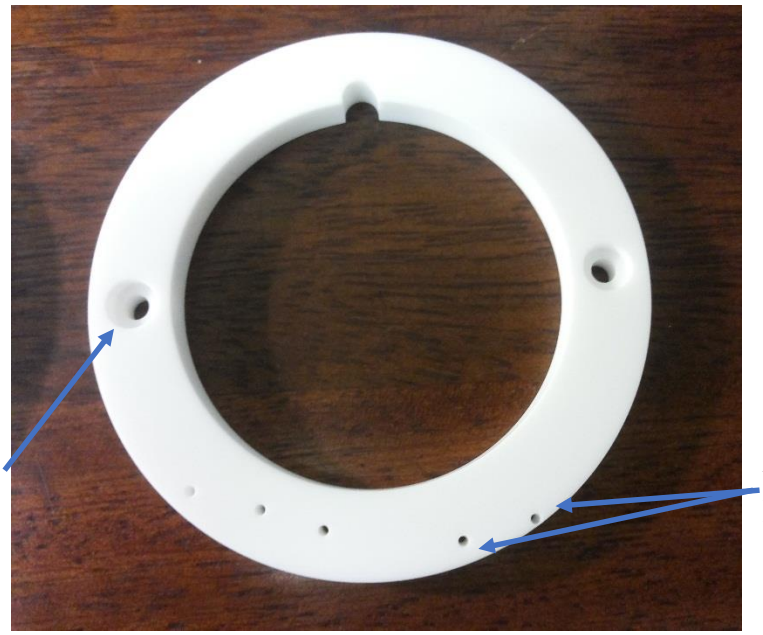

Figure 2.9: Photograph shows one of the ceramic washer insulators

The insulating washer was manufactured of ceramic material (Macor), see appendix A. This material is machinable with normal metalworking tools to high tolerances. The continuous working temperature is up to 800 ^{o}C, and it has a low

thermal conductivity of 1.46 Wm^{-1} K^{-1} ,. The coefficient of thermal expansion of this material is $9.3x10^{-6}$ K^{-1} which is approximately similar to that of the steel ($12.6x10^{-6}$ K^{-1}). In fact, thermal expansion was the crucial factor used to select this material in this work since Clarke (2009) faced problems with PTFE washers. The PTFE has a high thermal expansion ($230x10^{-6}$ K^{-1}) which led to thermocouple damage during heating as a result of the very big difference in expansion between the disk and the PTFE washers.

A two dimensional transient heat conduction model was developed by Clarke (2009) to model the disk bulk temperature distribution. The solution was carried out for a two dimensional generating plane. The inner row of thermocouples were used as a boundary condition for the problem, whilst the outer row was used to match the possible solution. The temperature distribution was calculated using a range of values for convection heat transfer coefficient and the heat partition factor β. The most acceptable values of those coefficients were those which minimized the error between the calculated temperature and the temperature recorded by the outer row of thermocouples.

A range of EHL tests was carried out after the new development. During each test, the disks were run at a particular speed with a 4.2 speed ratio, then the disks were loaded together in rolling/sliding condition causing the disk temperatures to rise due to frictional heating at the contact. This loading was continued until approximately steady temperatures were recorded by the thermocouples; at which time the disks were unloaded. The recorded data from those tests were used in solving the numerical model to find heat partition factor β and the heat transfer coefficients for both disks. A transient model of the temperature distribution in each disk was run using a range of fixed values for the heat partition factor, β, and the heat transfer coefficient, h. Each

disk was analysed independently and the values of β and h were selected to obtain the best fit to the measured temperature over the whole experiment, i.e. for both the heating and cooling phases. The best fit was obtained from an error measure that was minimised for the β, h combination selected, however the minimum point was not clear cut

A series of tests was carried out for a range of loads and running speeds using a constant slide / roll ratio of (1.24). The results of these tests are shown in Table 2.4.

Table 2.4: The heat partition results of the tests carried out by Clarke (2009)

Test	Sliding Speed m/s	Load N	β	$1-\beta$
A1	10	850	0.10	0.30
A2		1460	0.65	0.35
A3		1850	0.80	0.35
A4		2320	0.95	0.45
A5		2850	0.60	0.40
A6		3450	0.55	0.40
B1	13	850	0.45	0.35
B2		1460	0.70	0.35
B3		1850	0.70	0.40
B4		2320	0.55	0.45
B5		2850	0.35	0.35
C1	16	850	0.40	0.35
C2		1460	0.60	0.40
C3		1850	0.40	0.40
C4		2320	0.45	0.40
C5		2850	0.40	0.45
D1	20	850	0.40	0.50
D2		1460	0.40	0.40
D3		1850	0.40	0.40
D4		2320	0.40	0.40

As the disks were analysed independently, the values of β and 1-β obtained from the disk analyses of each experiment were not constrained to add to unity. Such a property was seen as a measure of the overall accuracy and is not apparent in the results obtained as given in Table 2.4

It can be seen that consistent results were obtained for the slow disk, but for the fast disk the results were inconsistent.

Subsequently, a short investigation of the possible sources of error in the results was carried out by Voller (2010). The main issues he worked on are discussed in sections 2.3.1, 2.3.2 and 2.3.3

2.3.1. Cooling of the slip rings

The thermocouple signals are transferred from the rotating shaft to the data acquisition system through slip rings. It is known that the voltage produced by a thermocouple is very small, and it will be subject to noise from the slip ring's sliding contact. Voller (2010) found that the heat generated in the slip rings during running was increasing the amount of noise. Since the slip rings for the fast disk have a higher sliding speed and are thus heated more, the error resulting is greater than that in the slow shaft slip rings. A new slip ring casing developed especially for that type of slip ring was fitted which promoted good circulation of the cooling air around the rings, reducing the errors as far as possible.

2.3.2. Improving the unloading phase

Voller (2010) found that the disks were not separated sufficiently when the load was removed in the cooling phase. This potentially allowed some direct heat transfer between the unloaded disks in the contact zone which might be a source of error in the results. To solve that, the gap between the disks in the unloading stage was increased from 0.7mm to 1.2mm by modifying the stop behind the swinging yoke. In addition, it was found that it was important to pull back the slow disk to actively separate the disks when the load was removed.

2.3.3. Cleaning the slip rings

Finally, Voller (2010) found a further technique to reduce noise in the temperature signals. While running the rig without loading the disks, fluctuation in the measured temperature was noticed. It was clear that this fluctuation was not a real external temperature change. An investigation into cleaning procedures was developed to clean the slip rings using a solvent degreaser. That cleaning led to reduced noise levels on the slip ring channels.

2.4. Data acquisition and control System

The instrumentation of the test rig is classified into the control and the data acquisition of the desired physical quantities. The driver unite speed and the contact load are controlled and the disk temperatures, the ambient temperature, the disk speed and the load and friction in the contact area are measured. Table 2.5 gives details of the

instrumented quantities as input and output and their type. Figure 2.10 shows a schematic of control and data acquisition system of the rig as modified and developed by the author.

Table 2.5: The instrumented quantities in the test rig

Physical Quantity	Signal Type	Description
Disk Temperatures (12 channel)	Thermocouple analogue input	J-Type Thermocouple (6 for each disk)
Ambient and Oil Jet Temperature (16 channels)	Thermocouple analogue input	J-Type Thermocouples installed in selective places around the disk and in the oil jet.
Applied Load	Analogue Voltage Input	Load Cell
Load Status	Digital Voltage Input	Microswitch
Friction	Analogue Voltage Input	Strain gauge torque transducer
Fast Disk Speed	Digital Input	Optical Sensor
Slow Disk Speed	Digital Input	Optical Sensor
Motor Speed Control	Analogue Output	Control the TASC drive unit
Load Control	Analogue Output	Control hydrodynamic proportional valve

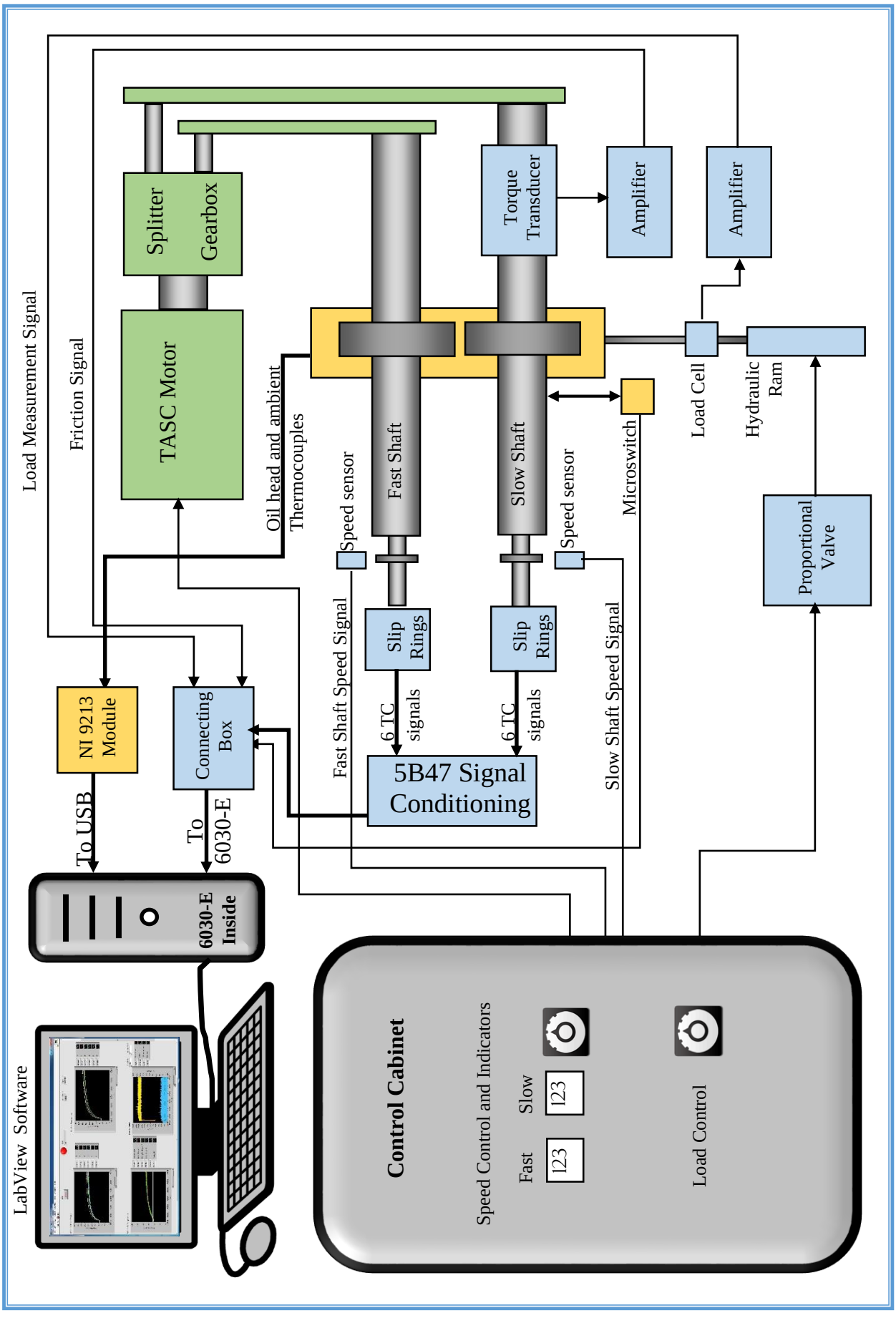

Figure 2.10: Schematic of the test rig control and data acquisition system as developed from the version used by Clarke (2009)

As shown in Figure 2.10, the control cabinet includes speed and load control. The speed of the test disks is controlled by a rotary potentiometer on the control cabinet which controls the TASC Eddy Current drive unit coupling between the motor and the splitter gear box. The speed of each disk is indicated by two digital displays on the control cabinet. The load is also controlled by a rotary potentiometer on the control cabinet which controls a proportional valve that applies the desired load by varying pressure in the hydraulic ram. The measured data from the test rig is acquired using LabView software installed on the computer. The labview software logs the data using a data acquisition card (National Instruments 6030-E) which is fixed inside the computer to serve as the interface between the computer and the electronic instruments fitted to the rig. This card is 16 bit resolution and has 16 analogue input channels. 14 channels are used for the 12 disk thermocouples, the load measurement and the friction measurement. It also has 8 digital Input/Output channels. One is used for indicating the status of loading and unloading of the disks by receiving a digital signal from a microswitch as explained in section 5.3. The components of the instrumentation system are now explained in turn. The NI 9213 module shown in Figure 2.10 was built-in in the acquisition system during the current work for further temperature measurements, this is described in section 5.8.

2.5. NI Labview data acquisition software

The data acquisition software was written in National Instrument Labview SP1 2011 which is compatible with the National Instruments 6030E data acquisition card. This software displays and stores the data that is received from the various sensors fitted on the test rig. In general, the Labview software consists of two parts; the "Front

Panel" which is the user interface and the "Block Diagram" which is a constructive code that controls the user interface. The user interface ("Front Panel") developed in this work for data acquisition from the test rig is shown in Figure 2.11.

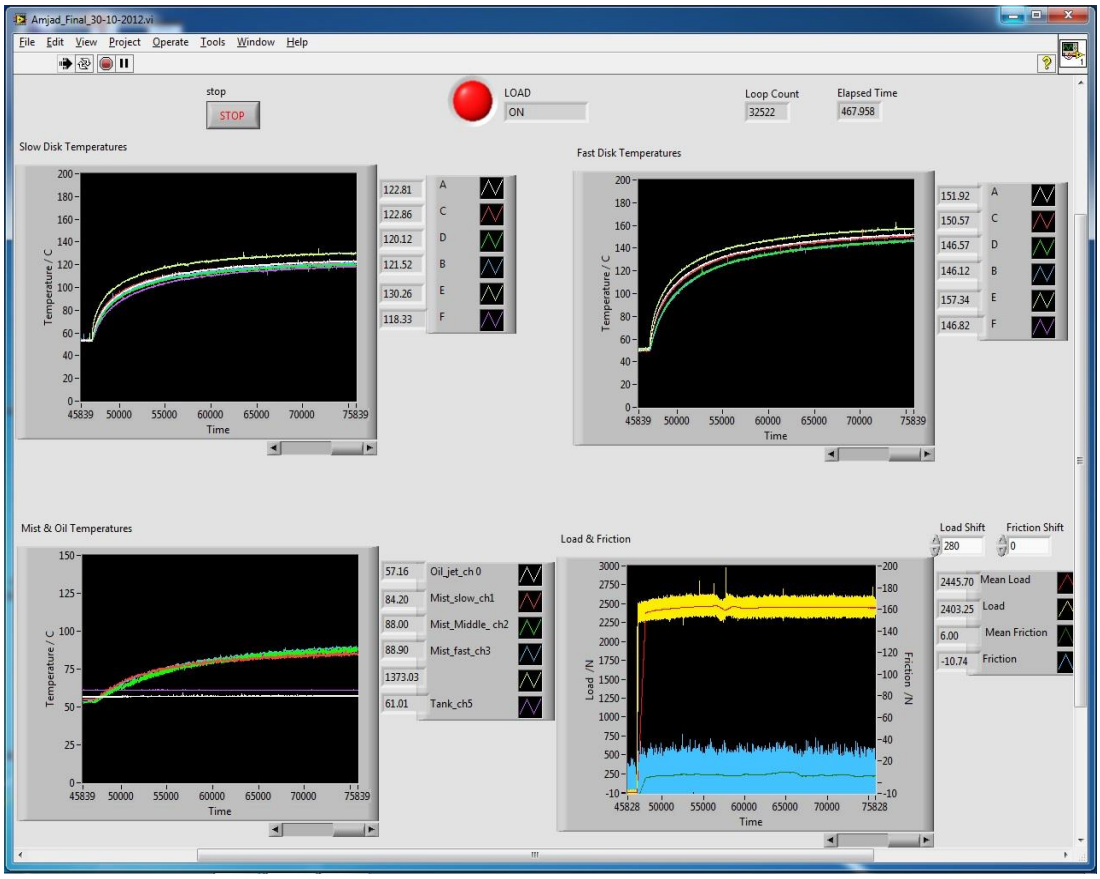

Figure 2.11: The front panel of the NI LabVIEW software used in this work

Figure 2.11, shows that the four charts that display the slow disk temperatures, the fast disk temperatures, the oil and ambient temperatures and the load and friction. In addition, in front of each chart, the instantaneous numerical value of each parameter is displayed in a digital indicator for accurate observations. The elapsed time and number of loops of data logging are also displayed in digital indicators. To avoid disks

being damaged by un-expected loading, the load status when loading and unloading is displayed using on/off and green colour bulb indicator.

The data logging frequency is 75 Hz. This is important in capturing the very rapid temperature changes at the beginning of the heating and cooling phases during the EHL test. The acquired data are displayed as mentioned previously, and at the same time they are written to a spread sheet external file which is used later for data input in the thermal numerical model.

2.6. Thermocouples installation, instrumentation, and calibration

The thermocouples used in this work are of J-type (iron/constantan), in order to be compatible with the already installed instrumentation. Extensive investigation was carried out by Clarke (2009) to find the best way of installing the thermocouples in the disks. It is important that the installation method of thermocouples achieves high thermal conductivity between the thermocouple itself and the surrounding measured area. On the other hand, electric connectivity should be eliminated specially if using multiple thermocouples on electrically conductive material, which is the case in the test disks. It was concluded that ceramic cement which has high thermal conductivity and is electrically insulating is the most efficient material for thermocouple mounting in the disks.

In terms of the thermocouple signal conditioning, 5B-series modules manufactured by Analog Devices are used for signal conditioning in the test rig. These modules are designed so that one module only conditions one signal as they feature galvanically isolated input and output. The modules are plug-in and they are slotted in backplanes which offer channel to channel isolation. Figure 2.12 shows the series of modules used

in the test rig, slotted into the 16-channel backplanes, and connected to the thermocouples.

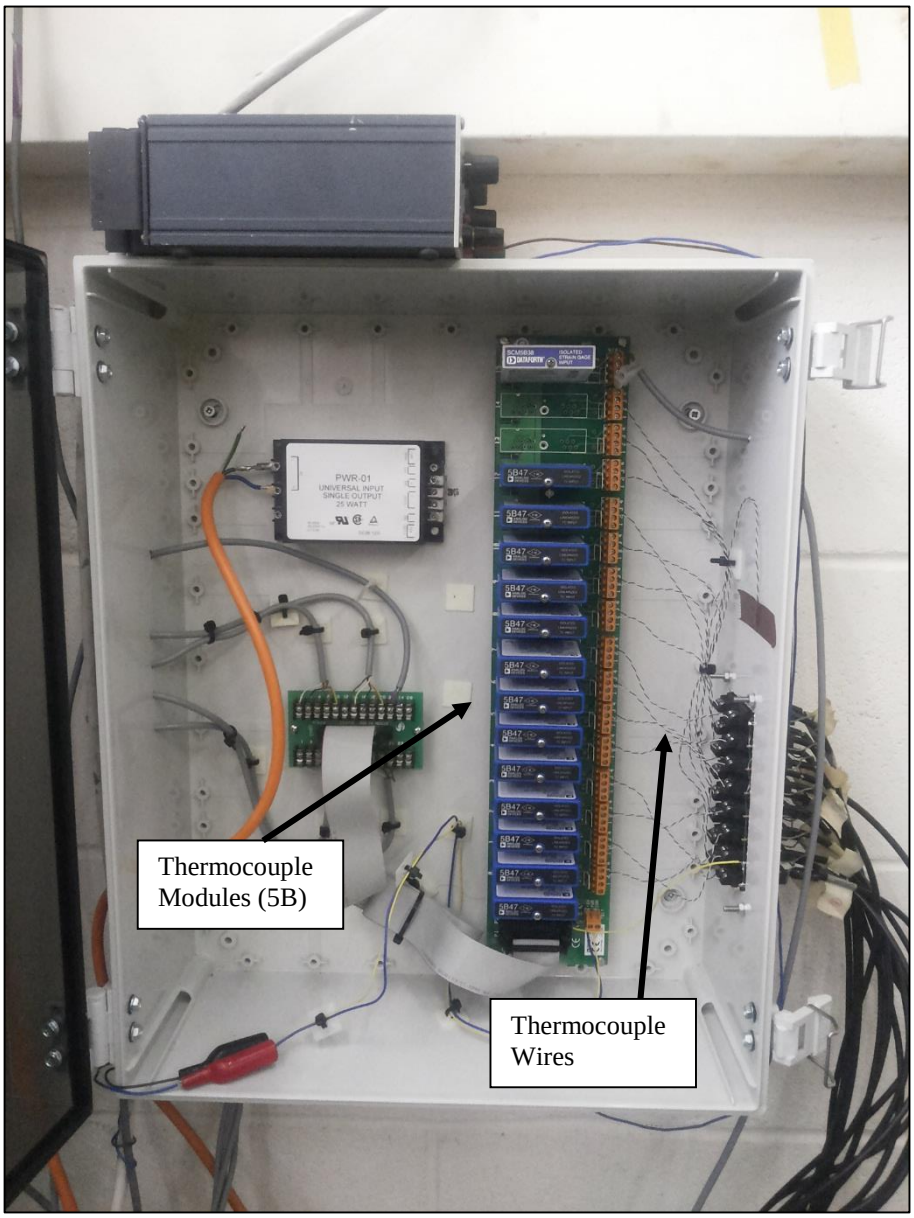

Figure 2.12: The series of 5B Modules used for thermocouple signal conditioning in the test rig

The thermocouples fitted to the test disks were carefully calibrated to improve measurement accuracy. In general, calibration can be defined as a process, carried out

under specified conditions, to establish the relationship between the indicated values measured by the instrument and the corresponding known values measured by an already calibrated device.

The fitted thermocouples in each test disk were calibrated in a temperature controlled oven. Figure 2.13 shows a schematic diagram of the thermocouple calibration process and Figure 2.14 is a photograph of the calibration arrangement and equipment. The oven used is insulated which is important in achieving a steady state temperature environment.

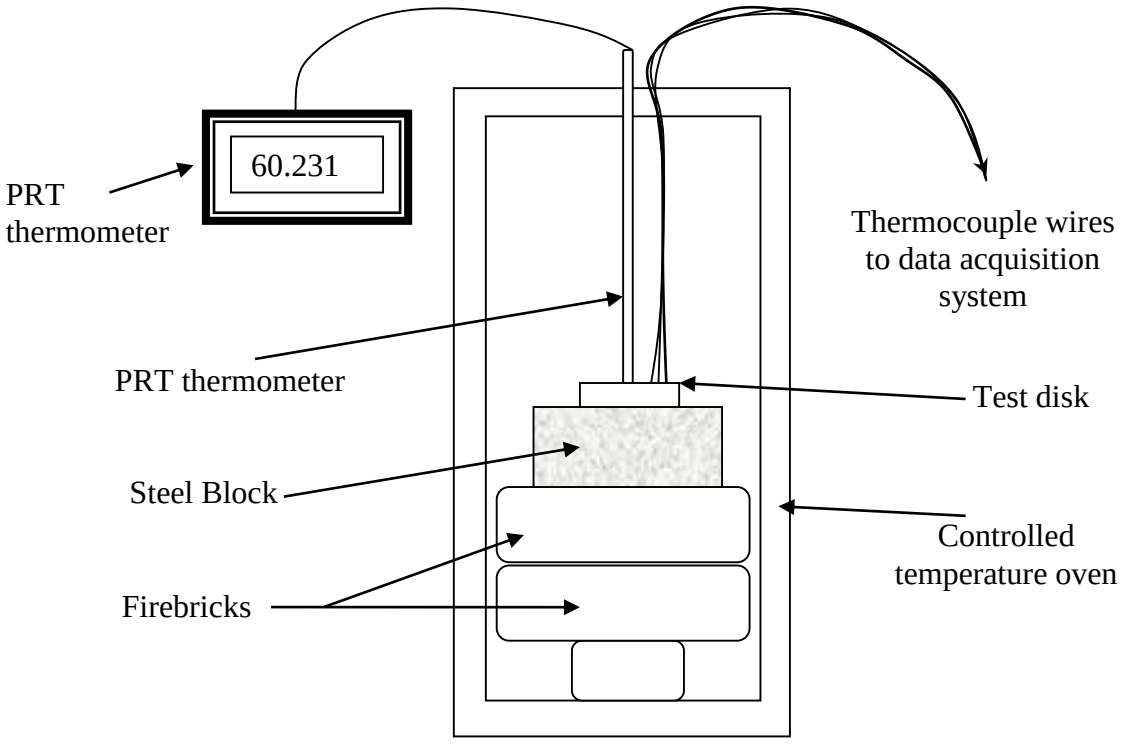

Figure 2.13 Schematic diagram of thermocouple calibration

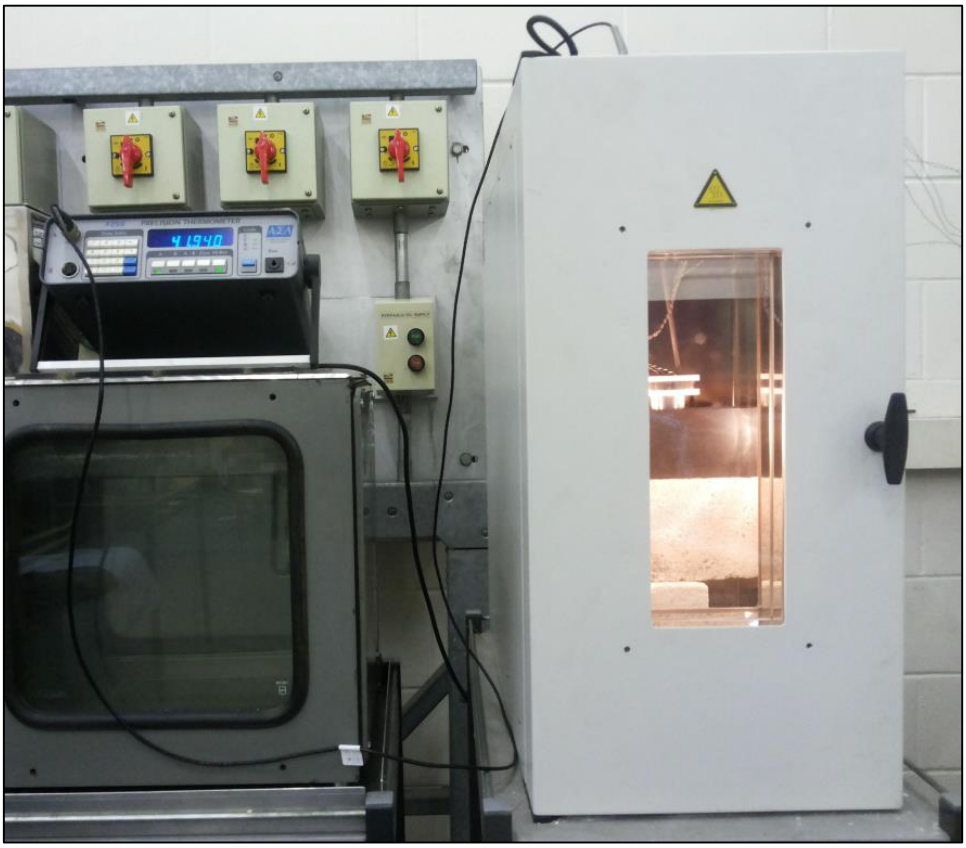

Figure 2.14: Photograph of thermocouples calibration

Each disk (with the 6 fitted thermocouples) was calibrated individually. The disk was placed on a large steel block giving it a large thermal mass to reduce temperature fluctuation in the disk. The disk and the steel block were placed on fire bricks to keep the disk in the centre of the oven and directly in front of the fan, which maintained efficient temperature control. The lowest fire brick was smaller in size to allow effective air circulation inside the oven as the suction opening is at the oven's base.

The reference temperature for the calibration process was measured by a calibrated Platinum Resistance Thermometer (PRT) which is of high accuracy with maximum error of ±0.1 ºC. The thermometer's probe was inserted in the oven through an opening and was kept in contact with the test disk as shown in Figures 2.13 and 2.14. The

thermocouple leads were fed through a small opening in the oven roof and connected to the data acquisition system through the same connection path as used when the disks are fixed in the test rig. Keeping the same connection path is important so that any source of systematic error caused by the connections, the wires, the slip rings and any part of the data acquisition system is included in the calibration.

The calibration procedure was carried out by setting the temperature of the oven to a specific value. The PRT thermometer and the Labview software were observed until steady state conditions were reached. This took a time of at least one hour depending on the target temperature. Once steady state was achieved, the thermocouple temperatures were recorded for a one minute period. The average value of each thermocouple temperature was calculated and recorded against the PRT reading at that time. This process was carried out for target temperatures in the range 20^{o} C to 160 ^{o}C in 20 ^{o}C steps, covering the expected temperature range within the disks during the EHL experiment.

A typical calibration set of thermocouple measurements against the PRT measurements is shown in Figure 2.15. In this figure, a least squares trend line was established for the temperature readings with a coefficient of determination (R^2) of 0.991 and a standard deviation of 0.53 ^{o}C.

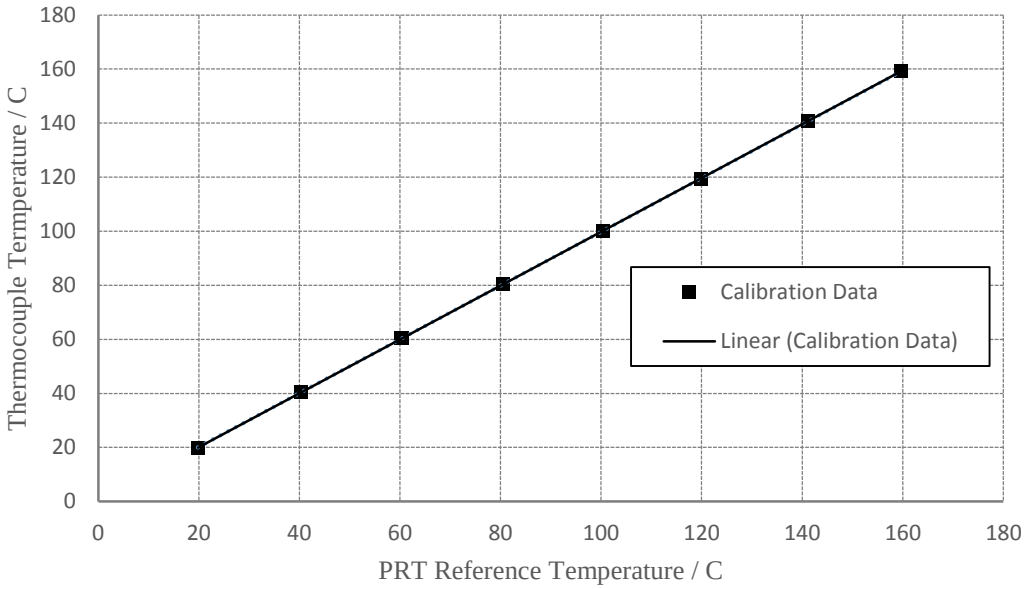

Figure 2.15: The calibration data for thermocouple ***a*** of the fast disk

The linear trend line of the calibration data in Figure 2.15 was evaluated for all 12 thermocouples. The equations of these lines were included in the Labview data acquisition software. This leads to instantaneous correction of the raw temperature during the EHL tests.

The thermocouple calibration process was assessed by making a comparison between the raw and calibrated data. The error between the raw thermocouple reading and the reference temperature for 288 calibration items (for 12 thermocouples, 8 temperature stages, and 3 repeats of the calibration readings) are shown in the histogram in Figure 2.16 (a). Figure 2.16 (b) shows the histogram of the thermocouples error after processing using the calibration curves. It is shown that the accuracy is improved and the error distribution is moved towards the lower error. Table 2.6 shows some statistics for the error of the data prior and after calibration.

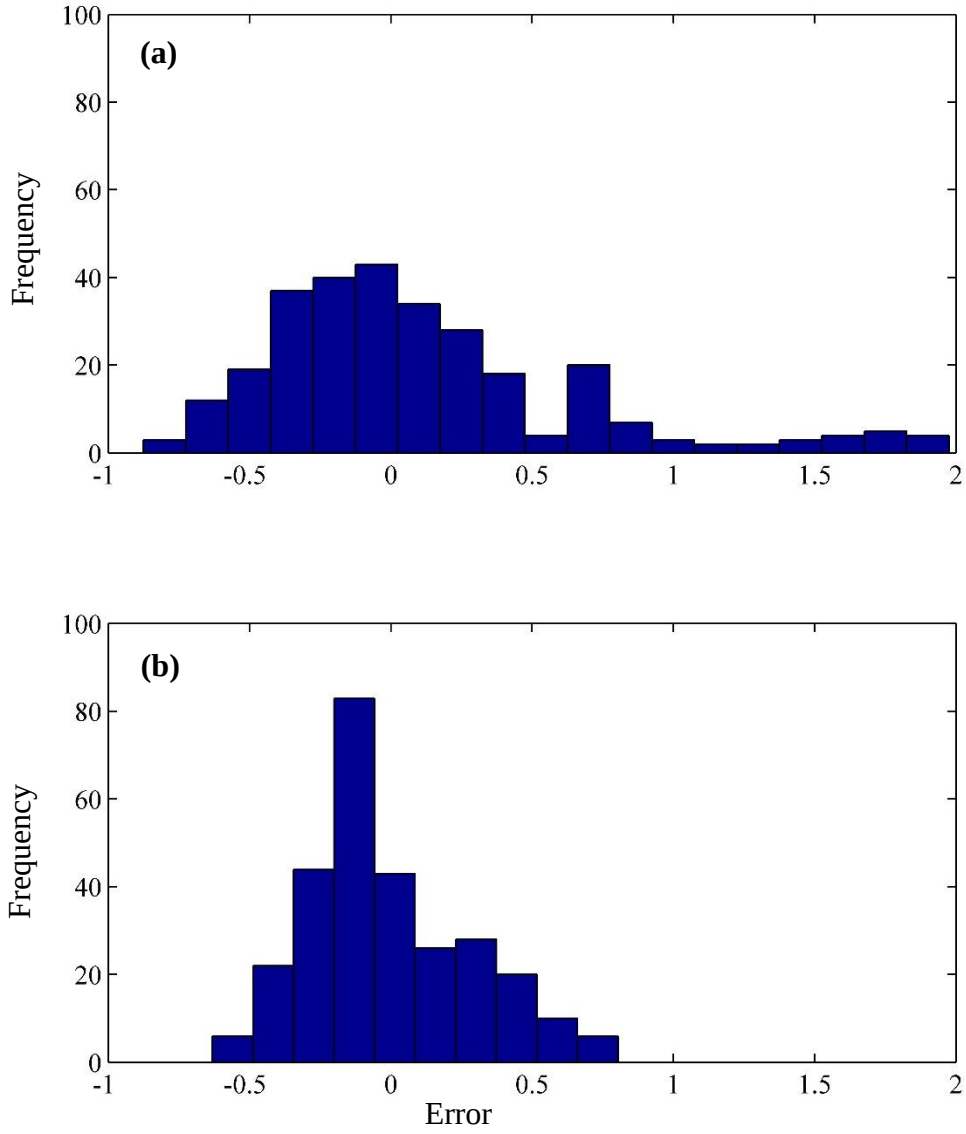

Figure 2.16: Thermocouple calibration histograms; (a) Error frequency for the raw data, (b): Error frequency for the calibrated data

Table 2.6: A statistical comparison between raw and calibrated data of thermocouples

Statistics	Raw Data	Calibrated Data
Maximum error	1.9	0.8
Summation of the absolute error	117.0	66.5
Average of the absolute error	0.40	0.23
Standard deviation	0.56	0.29

2.7. Loading mechanism

In this rig, the disks are loaded by a hydraulic mechanism. This mechanism includes a hydraulic ram, a bell-crank lever and a push rod as shown in Figure 2.17. The load is applied by the hydraulic ram via the bell-crank to the push rod which is connected to the swinging yoke that supports the slow disk shaft. The contact between the bell crank and the push rod is through a load cell which is used for load measurement, while the contact between the push rod and the yoke through crossed knife-edges to ensure that the line of action of load always passes through the point contact between the disks. The hydraulic oil is pressurized by a pump and controlled by a variable pressure valve. In the current work, the maximum applied load is 2320 N which corresponds to a 1.4 GPa maximum Hertzian pressure for the test disks.

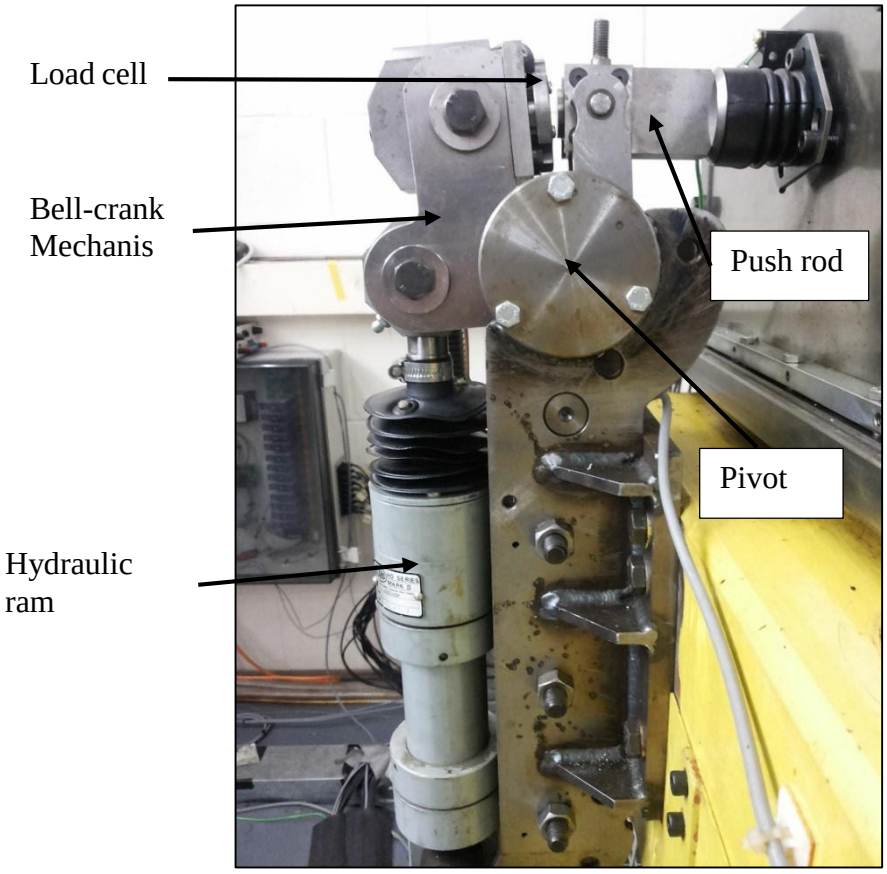

Figure 2.17: The hydraulic loading mechanism

2.8. Load cell calibration

The applied load on the contact area is measured by a load cell which is connected to an amplifier-indicator unit. This is connected to the data acquisition system, which logs the load continuously during the tests and writes the load values to a spreadsheet together with the temperature measurements which are logged at the same times. The output signal from the load cell is 0-10V DC and is proportional to the applied load. Figure 2.18 shows the load cell with the bell with the bell crank lever retracted.

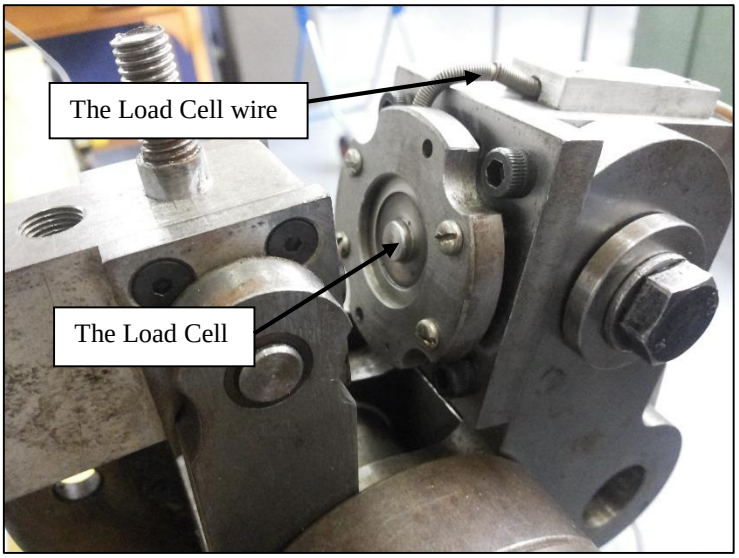

Figure 2.18: The load cell

For the calibration process, the hydraulic actuator was disconnected from the bell-crank mechanism which allows the bell crank to rotate through 90°. The cell was calibrated by applying a range of accurately measured weights suspended on a lever in order to apply known forces to the load cell. The lever is hinged on a bracket made for the calibration process and is accurately counterbalanced as shown in Figure 2.19. The range of weights used was selected to cover the expected range of loads for the planned EHL tests.

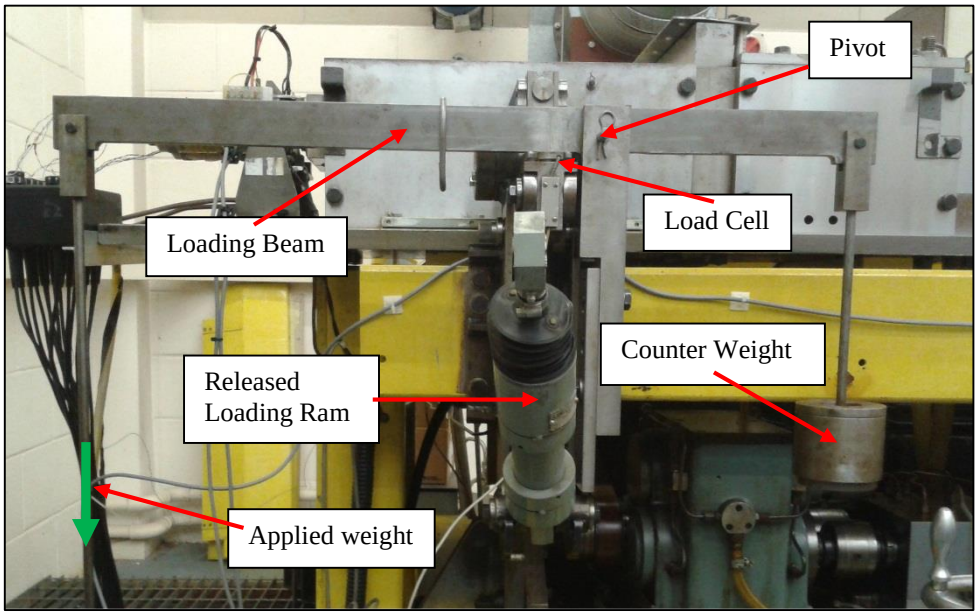

Figure 2.19: Calibration of the Load Cell

The calibration process was repeated three times and a very good linear relation between the load and the measured voltage was found on each occasion with coefficient of determination (R^2) of 0.999. Figure 2.20 shows the calibration curve for the mean of three calibration processes and a linear least squares fit with a coefficient of determination (R^2) of 0.999 and a standard deviation of 8.3×10^{-4} V. However, this relation was found to have a significant shift in intercept between calibrations. This is shown in Figure 2.21 where the two best fit lines having the biggest shift can be seen to be shifted by an amount of approximately 100N. The shift is thought to be the result of drift in the electrical circuity.To solve this problem, an adjustable load shift was built in the Labview data acquisition system. This load shift is set before applying the load in the test to make the initial load become zero. It is important to note that whilst the intercept shifted, the slope of the calibration curve remained constant between calibrations, hence the fundamental load/voltage characteristic of the load cell was not affected. The experiments were run at a nominally constant load with the value

recorded throughout. When the load was removed at the end of the experiment, the measured value returned to zero indicating that there was no change in the offset during the experiment.

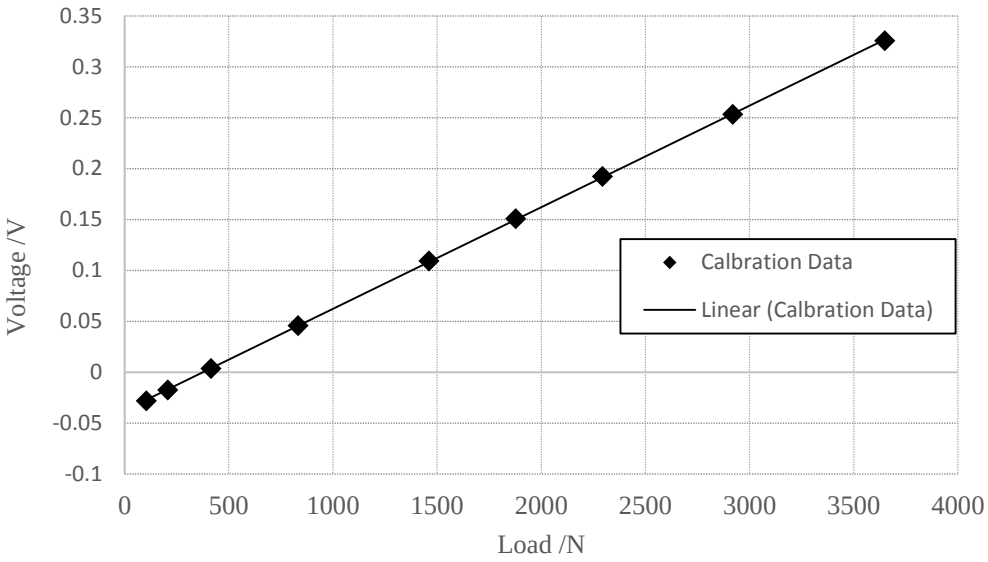

Figure 2.20: Calibrations Curves for the mean of three calibration processes.

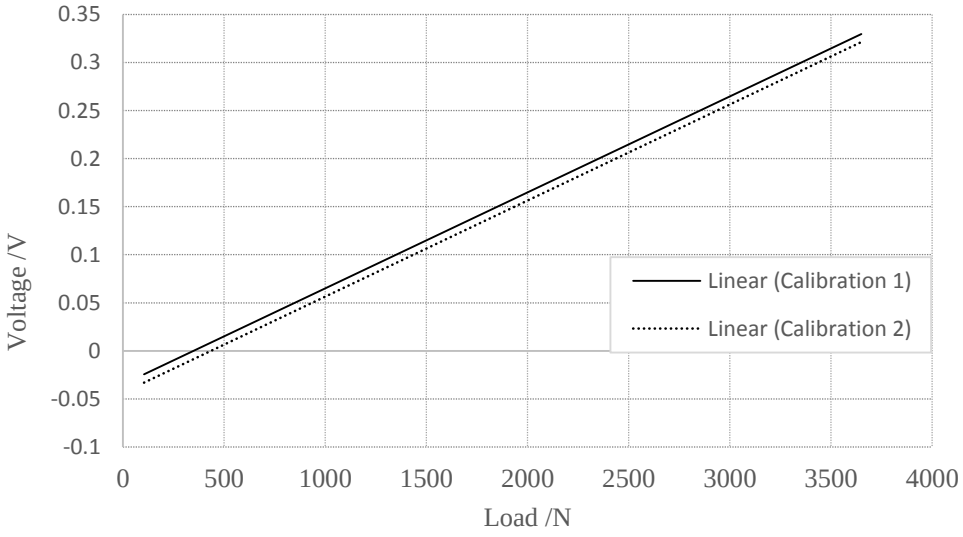

Figure 2.21: The calibration curves of two calibration processes of the load cell at different calibration times showing shift in intercept

2.9. Friction transducer calibration

The friction transducer consists of a reduced section in the slow speed shaft that is fitted with strain gauges that allow the torque in the shaft to be measured. The strain gauges are connected to a strain-gauge amplifier using slip rings, which is then connected to the data acquisition system (which is described in section 2.4). The amplifier is fitted to the 16 channel 5B system.

In order to calibrate the friction transducer, a dead weight loading arm as shown in Figure 2.22. was clamped to the pulley of the slow speed shaft with the toothed drive belt disconnected. The other end of the slow speed shaft was clamped inside the test head to prevent it from rotating during calibration. In this configuration, a series of known torques can be applied to the slow shaft by adding accurately measured weights to the loading arm so as to obtain the measured torque response from the friction transducer which is situated in the shaft between the fixed end and the loading arm.

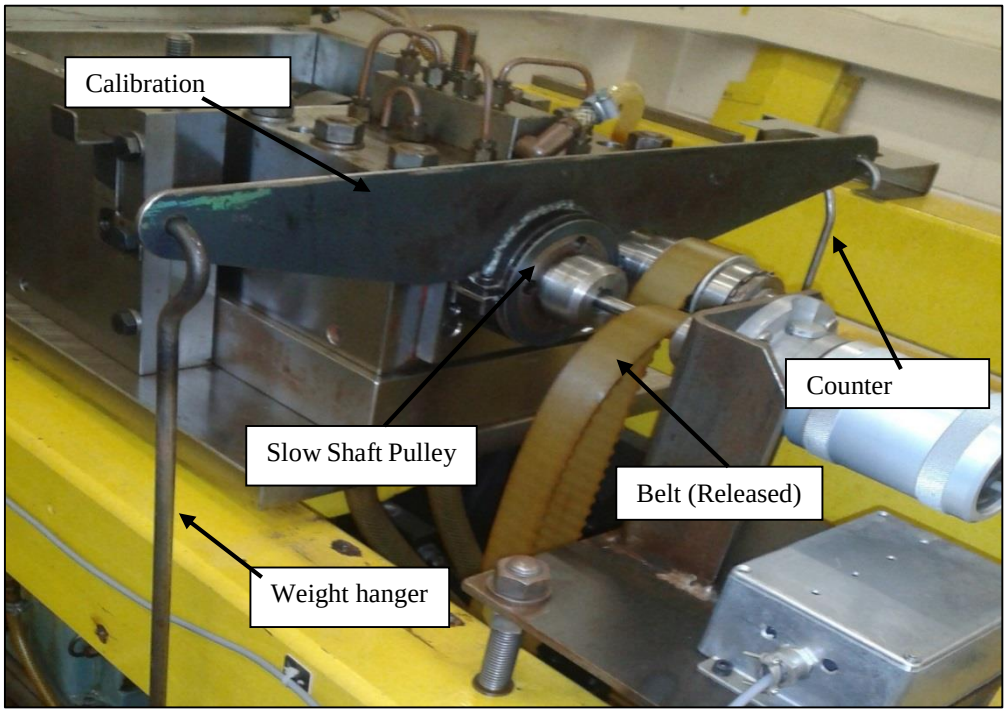

Figure 2.22: Calibration of the friction transducer

After balancing the loading arm, a series of masses were applied on the weight hanger producing known torques on the shaft. The range of masses was selected to cover the expected range of friction force in the EHL tests. The voltage from the friction transducer was logged at each applied torque step producing the data for the relation between the voltage and the applied friction force. This linear relation was built into the Labview data acquisition system to convert the measured voltage into the measured friction force during the experiments.

The calibration process was repeated three times for more consistency, the linear least square fit of the mean of these calibrations was used for constructing the best fit calibration curve that is shown in Figure 2.23 having a coefficient of determination (R^2) of 0.999 and a standard deviation of 5.4×10^{-4} V. As in the load cell calibration, it was found that there was a small amount of shift in the intercept values when the process was carried out at different times. This offset value was dealt with by configuring a manually adjustable friction shift in the Labview system which was adjusted prior to carrying out each experiment (when the shafts are stationary) to remove any zero-offset in the data. The friction force was maintained throughout each experiment and the value recorded when the load was removed was checked and again returned to zero.

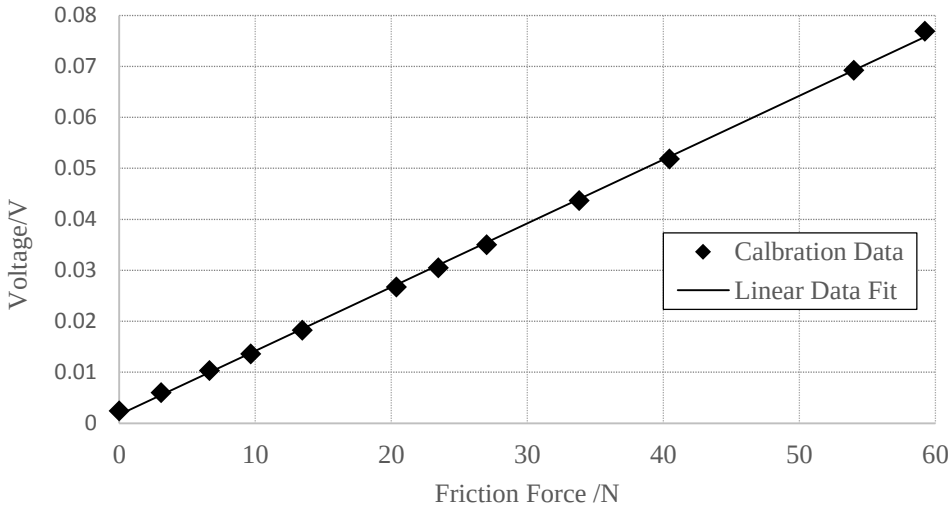

Figure 2.23: The calibration curve of the friction transducer based on the mean of three calibration processes.

2.10. Bearing friction measurement

As described in the previous section, a friction transducer is fitted to the slow shaft to measure the friction force. In fact, the measured friction force is not only the traction force, but also includes the bearing friction and windage losses as a result of the shaft rotation. Figure 2.24(a) shows a schematic of the shaft arrangements with the bearings and their directions of rotation. It is vital to determine an accurate value of the contact friction force which is used in calculating the frictional heat generated at the EHL point contact. Figure 2.24(b) shows the torques acting on the slow shaft, including the EHL friction torque and the bearing and other loss torques which act in the opposite direction. Thus, the actual EHL torque is the sum of that measured by the transducer and the bearing friction torque. It should be noted that in the slow shaft, the torque due to traction at the EHL contact acts in the same direction as the shaft rotation. In the fast shaft the traction acts in the direction opposite to the rotation of the shaft.

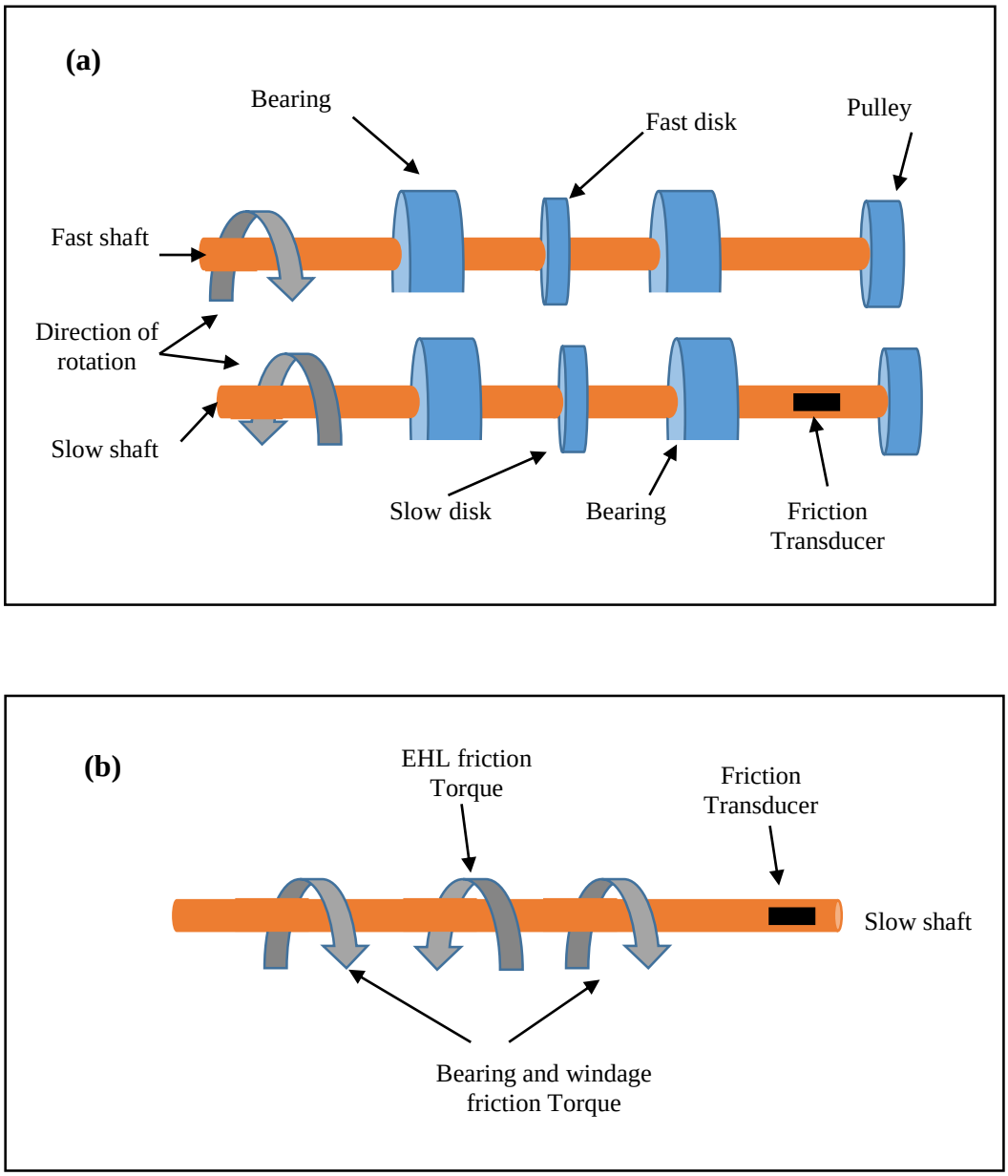

Figure 2.24: Bearing friction measurment; (a) Shafts and bearings layout, (b) Torques on the slow shaft

An experiment was carried out to measure the bearing friction torque in order to be able to add it to the quantity measured by the friction transducer. First of all, the coupling at the fast shaft was disconnected between the driving pulley and the fast shaft to allow the fast shaft to rotate freely. The disks were loaded and the shafts rotated together in pure rolling. In that state, the friction torque measured by the

friction transducer represents the total bearing friction torque for both shafts as there is no relative velocity between the disks i.e. no sliding and no contact friction. Because the bearings in both shafts are identical, the measured torque was divided by two before adding it to the total frictional torque.

The frictional bearing torque is influenced by both the load applied to the bearing and the rotational speed. The bearing friction was measured over the range of loads and speeds encountered in the real EHL tests. The shafts were run at 774 rpm, 1005 rpm, 1238 rpm and 1546 rpm. These slow shaft speeds give sliding speeds of 10 ms^{-1}, 13 ms^{-1}, 16 ms^{-1} and 20 ms^{-1} respectively sliding/rolling experiments at the rig slide/roll ratio. At each speed condition, the load was varied from 800 N to 2320 N which is the full range of load in the EHL tests. Figure 2.25 shows 4 families of friction force data corresponding to the speed range described fitted by linear best fit for use as friction transducer measurement corrections in order to obtain an accurate EHL contact friction force.

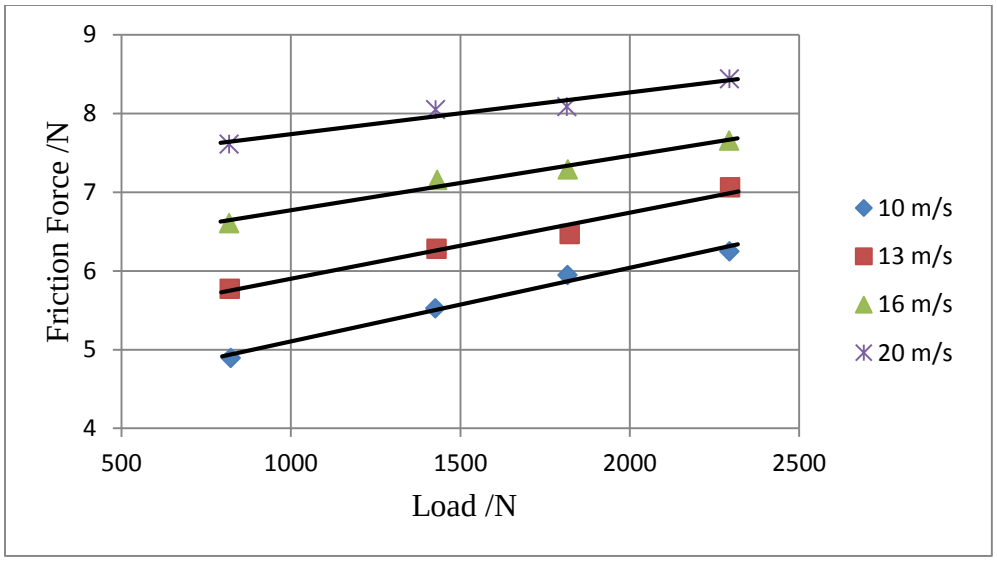

Figure 2.25: The measured friction force due to the bearings and windage

2.11. Shaft speed sensors

The test disk speed is measured by optical speed sensors, which are fitted on the rig outside the test head to measure the speed of each shaft. These sensors feature an infrared emitting diode, and infrared sensor encased in a black thermoplastic casing facing each other as shown in Figure 2.26. A slotted trigger disk is fitted to each shaft which interrupts the infra-red beam emitted by the diode and received by the sensor. During the shafts rotation, 120 5V TTL square wave are generated from each sensor per revolution where the trigger disks have 120 slots .The signal from the sensors is processed in the control cabinet and the test disk speed is shown in the display unit.

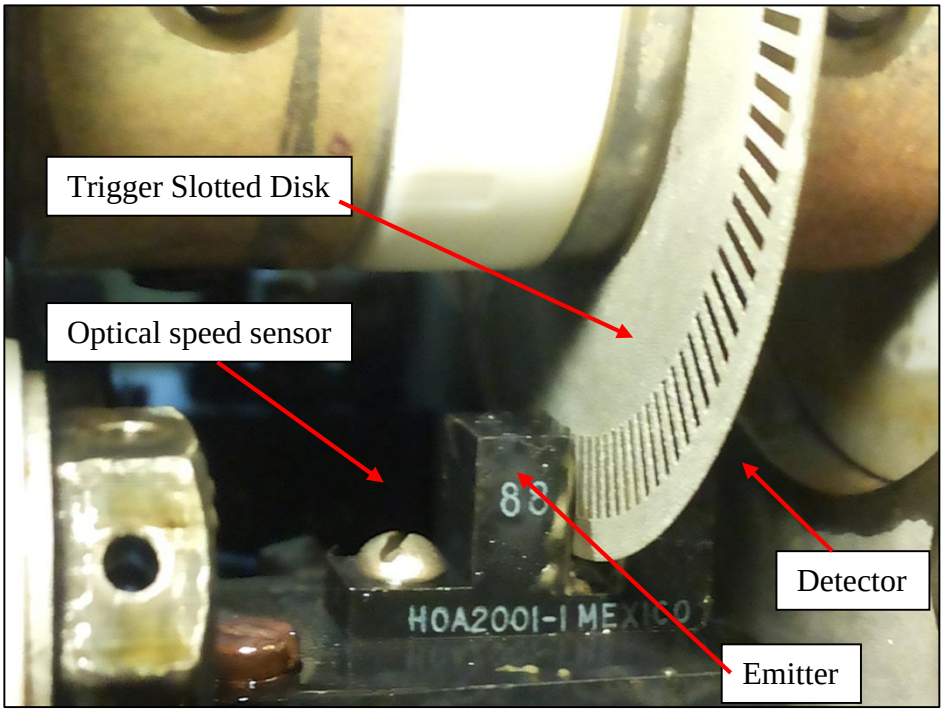

Figure 2.26: Test Disk speed measuring configuration

Chapter 3:
Theory and Formulation of Numerical Model for Thermal Analysis of the Test Disks

3.1. Introduction

In this Chapter the formulation of the governing differential equations of the temperature distribution in the test disks is derived, and a numerical solution using a finite difference formulation is outlined. The solution process including the details of the computing program developed is also described.

During EHL contact, sliding and rolling of the contact surfaces leads to heat generation within the lubricant film. The majority of this heat is partitioned between the contact surfaces. The heat absorbed by the oil film is neglected because it has a very small mass flow rate within the region of contact. The fraction of the heat dissipated within the oil film that is convected away from the contact by the oil flowing through the contact is estimated as being between 1/500 and 1/1200 as discussed in the extract from the author's publication (Al-Hamood et al. 2015) that is included in Appendix B. In this study, it is assumed that the heat conducted to the surfaces is the total heat generated multiplied by the heat partition factor, β for the fast surface, and by (1- β) for the slow surface. β is an important experimental factor which can be regarded as a property for the EHL contact condition and can be compared with that obtained theoretically in a detailed EHL thermal analysis.

3.2. The governing partial differential equation

The model formulation is started from the derivation of the partial differential equation that governs the temperature distribution within the disks. A cylindrical coordinate system (*r, θ, z*) is used as it is appropriate for the test disks. Accordingly, an element of the disk is considered as shown in Figure 3.1 which has dimensions *δr, δz, rδθ* . The disk's material is assumed to be homogenous and isotropic, which means that the material properties such as thermal conductivity, density and specific heat capacity at every position and direction are the same within the disks.

The element in Figure 3.1 is considered fixed in space, and the disk material passes through during rotation, with the axis of rotation coincident with the Oz axis. The centre of the control element is located at (*r, θ, z*)

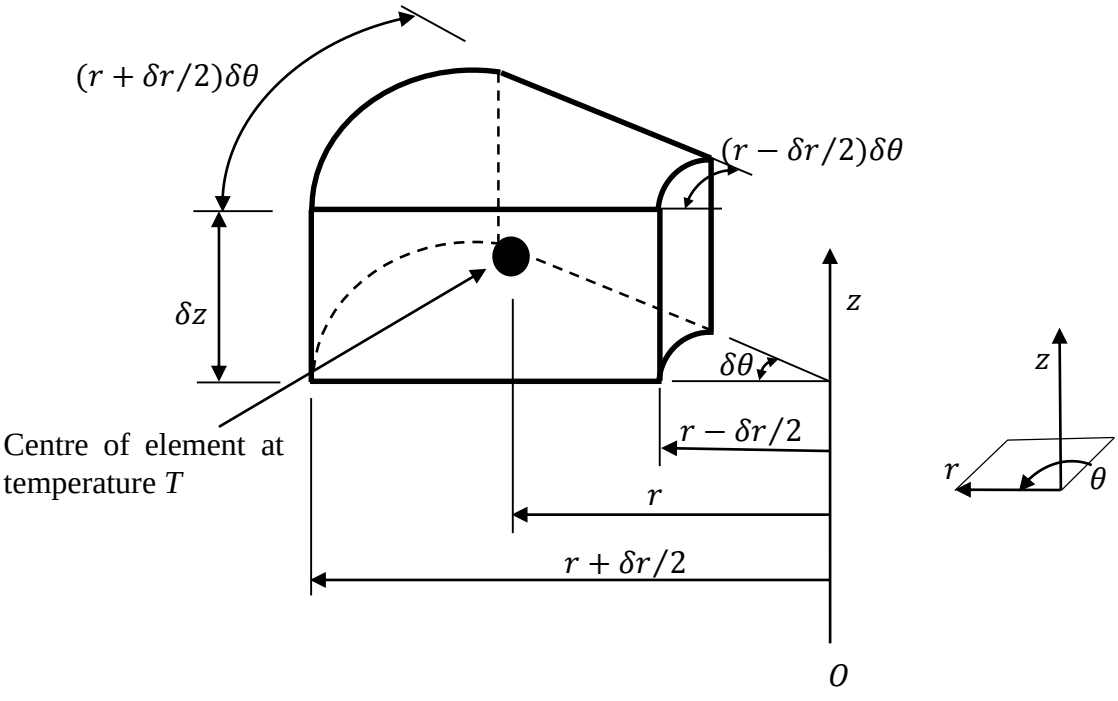

Figure 3.1: Control element of the disk

Considering the material in the control volume at time *t* as the material system, the rate of increase of the energy in the material system is made up of two parts: (i) the rate of increase of energy in the fixed control element, and (ii) the rate at which energy is leaving the control element due to material motion.

In other words, the thermal energy balance of the control element, at time *t* may be written as:

$$\left[\begin{matrix}\textbf{Net heat rate}\\ \textbf{conducted in}\end{matrix}\right] + \left[\begin{matrix}\textbf{Rate of heat}\\ \textbf{generated inside}\end{matrix}\right] = \left[\begin{matrix}\textbf{Rate of change in}\\ \textbf{internal energy}\end{matrix}\right] + \left[\begin{matrix}\textbf{Net heat rate transported out}\\ \textbf{as a result of disk rotation}\end{matrix}\right]$$

Which is based on the conservation of energy, and may re-written as:

$$dQ_c + dQ_g = dQ_e + dQ_r \tag{3.1}$$

The terms of equation (3.1) are derived in detail through the following sections

3.2.1. Total energy conducted into and out of the control element

According to Fourier's law of heat conduction, see (Holman, 2010) the time rate of conducted heat transfer in the *x* direction is:

$$Q_c = -KA\frac{\partial T}{\partial x}$$

Where

Q_c is the heat transfer time rate

K is the thermal conductivity of the material

A is the area of the cross section that the heat flow perpendicularly

$\frac{\partial T}{\partial x}$ is the temperature gradient along the direction of heat flow

(The minus sign indicates that conduction is from high to low temperature).

3.2.1.1. Conduction in radial direction

The conducted heat flow in the radial direction across the element face at $r - \frac{\delta r}{2}$ can be written as

$$dQ_{r-\frac{\delta r}{2}} = -K\left(\left(r - \frac{\delta r}{2}\right)\delta\theta\delta z \frac{\partial T}{\partial r}\Big|_{r-\frac{\delta r}{2}}\right)$$

$$= -K\left(\left(r - \frac{\delta r}{2}\right)\delta\theta\delta z\right)\frac{\partial}{\partial r}\left(T - \frac{\partial T}{\partial r}\frac{\delta r}{2}\right)$$

Simplifying gives

$$= -K\left(\left(r - \frac{\delta r}{2}\right)\delta\theta\delta z\right)\left(\frac{\partial T}{\partial r} - \frac{\partial^2 T}{\partial r^2}\frac{\delta r}{2}\right) \quad (3.2)$$

In the same manner, the conduction across the face at $r + \frac{\delta r}{2}$ may be written as:

$$dQ_{r+\frac{\delta r}{2}} = -K\left(\left(r + \frac{\delta r}{2}\right)\delta\theta\delta z\right)\left(\frac{\partial T}{\partial r} + \frac{\partial^2 T}{\partial r^2}\frac{\delta r}{2}\right) \quad (3.3)$$

3.2.1.2. Conduction in the axial direction

The conducted heat flow in the z direction across the element face at $z-\frac{\delta z}{2}$ is

$$dQ_{z-\frac{\delta z}{2}} = -K(r\delta\theta\delta r)\frac{\partial T}{\partial z}\Big|_{z-\frac{\delta z}{2}} = -K(r\delta\theta\delta r)\frac{\partial}{\partial z}\left(T-\frac{\partial T}{\partial z}\frac{\delta z}{2}\right)$$

$$= -K(r\delta\theta\delta r)\left(\frac{\partial T}{\partial z}-\frac{\partial^2 T}{\partial z^2}\frac{\delta z}{2}\right) \quad (3.4)$$

Also, conduction at $z+\frac{\delta z}{2}$ is given by

$$dQ_{z+\frac{\delta z}{2}} = -K(r\delta\theta\delta r)\left(\frac{\partial T}{\partial z}+\frac{\partial^2 T}{\partial z^2}\frac{\delta z}{2}\right) \quad (3.5)$$

3.2.1.3. Conduction in the circumferential direction

The heat flow in the circumferential direction across the element face at $\theta-\frac{\delta\theta}{2}$

$$dQ_{\theta-\frac{\delta\theta}{2}} = -K(\delta z\delta r)\frac{\partial T}{r\partial\theta}\Big|_{\theta-\frac{\delta\theta}{2}} = -K\left(\frac{\delta z\delta r}{r}\right)\frac{\partial}{\partial\theta}\left(T-\frac{\partial T}{\partial\theta}\frac{\delta\theta}{2}\right)$$

$$dQ_{\theta-\frac{\delta\theta}{2}} = -K(\delta z\frac{\delta r}{r})\left(\frac{\partial T}{\partial\theta}-\frac{\partial^2 T}{\partial\theta^2}\frac{\delta\theta}{2}\right) \quad (3.6)$$

Similarly, at $\theta+\frac{\delta\theta}{2}$ the heat flow is

$$dQ_{\theta+\frac{\delta\theta}{2}} = -K(\delta z\frac{\delta r}{r})\left(\frac{\partial T}{\partial \theta}+\frac{\partial^2 T}{\partial \theta^2}\frac{\delta\theta}{2}\right) \quad (3.7)$$

3.2.1.4. The net conducted heat into the control element

Adding equations 3.2 to 3.7 together gives the net rate of heat conduction into the control element,

$$dQ_c = Kr\delta r\delta\theta\delta z\left[\frac{1}{r}\frac{\partial T}{\partial r}+\frac{\partial^2 T}{\partial r^2}+\frac{\partial^2 T}{\partial z^2}+\frac{1}{r^2}\frac{\partial^2 T}{\partial \theta^2}\right] \quad (3.8)$$

3.2.2 Net heat rate transported out of the control element as a result of disk rotation

To consider flash temperature effects in the disk, its rotation needs to be taken into account. The energy equation is developed here including this term for completeness although it is used in simpler form presented in section 3.4 for this thesis. The energy change of the fixed control element due to disk rotation is represented by passing the disk material through that element instantaneously.

The solid mass flow rate entering the control element in the circumferential direction may be written as:

$$\dot{m}_{in} = \rho v_{in} dA \quad (3.9)$$

And the solid mass flow rate leaving the element is:

$$\dot{m}_{out} = \rho v_{out} dA \quad (3.10)$$

where v_{in}, v_{out} are the velocities perpendicular to the surfaces at $\theta - \delta\theta$ and at $\theta + \delta\theta$ respectively.

Now, the rate of energy transport into and out of the element is written as respectively

$$(Q_r)_{in} = e_{in}\dot{m}_{in} \tag{3.11}$$

$$(Q_r)_{out} = e_{out}\dot{m}_{out} \tag{3.12}$$

where e_{in} , e_{out} are the specific energy (energy per unit mass) entering and leaving the control volume respectively.

Therefore the change in element energy due to disk rotation is:

$$dQ_r = e_{out}\dot{m}_{out} - e_{in}\dot{m}_{in} \tag{3.13}$$

Noting: $\dot{m}_{out} = \dot{m}_{in} = \omega r \rho \delta r \delta z$.

Substituting in equation (3.13) gives

$$dQ_r = \omega r \rho \delta r \delta z \, \Delta e \tag{3.14}$$

Substituting for Δe in equation (3.14) gives

$$dQ_r = \omega r \rho \delta r \delta z C_p (T|_{\theta+\frac{\delta\theta}{2}} - T|_{\theta-\frac{\delta\theta}{2}})$$

where C_p is the specific heat capacity of the disk material. The temperature on the element face at $\theta \mp \frac{\delta\theta}{2}$ may be written as

$$T|_{\theta+\frac{\delta\theta}{2}} = T + \frac{\delta\theta}{2}\frac{\partial T}{\partial\theta}\bigg|_{\theta} + \frac{\delta\theta^2}{8}\frac{\partial^2 T}{\partial\theta^2}\bigg|_{\theta}$$

$$T|_{\theta-\frac{\delta\theta}{2}} = T - \frac{\delta\theta}{2}\frac{\partial T}{\partial\theta}\Big|_{\theta} + \frac{\delta\theta^2}{8}\frac{\partial^2 T}{\partial\theta^2}\Big|_{\theta}$$

Therefore, making the above substitution for the temperature leads to equation (3.15)

$$dQ_r = C_p\rho\omega r\delta r\delta\theta\delta z\frac{\partial T}{\partial\theta} \tag{3.15}$$

3.2.3. Rate of change in internal energy

The change in internal energy for the solid disk see (Holman 2010) in the control volume at time *t* is

$$dQ_e = \rho V C_p\frac{\partial T}{\partial t} \tag{3.16}$$

Substituting for the element volume gives,

$$dQ_e = \rho(r\delta\theta\delta r\delta z)C_p\frac{\partial T}{\partial t} \tag{3.17}$$

3.2.4. Internal heat generation

In the case of the control element considered, no heat is generated internally, such that

$$dQ_g = 0 \tag{3.18}$$

3.2.5. Overall governing partial differential equation

Substituting equations 3.8, 3.15, 3.17 and 3.18 into equation 3.1 gives the overall partial differential equation of the temperature distribution within the disk

$$Kr\delta r\delta\theta\delta z\left[\frac{1}{r}\frac{\partial T}{\partial r}+\frac{\partial^2 T}{\partial r^2}+\frac{\partial^2 T}{\partial z^2}+\frac{1}{r^2}\frac{\partial^2 T}{\partial \theta^2}\right]$$

$$= C_p\rho\omega r\delta r\delta\theta\delta z\frac{\partial T}{\partial\theta}+\rho(r\delta\theta\delta r\delta z)C_p\frac{\partial T}{\partial t}$$

Simplifying gives

$$\alpha\left[\frac{1}{r}\frac{\partial T}{\partial r}+\frac{\partial^2 T}{\partial r^2}+\frac{\partial^2 T}{\partial z^2}+\frac{1}{r^2}\frac{\partial^2 T}{\partial \theta^2}\right]=\omega\frac{\partial T}{\partial\theta}+\frac{\partial T}{\partial t} \tag{3.19}$$

Where $\alpha=\frac{K}{\rho C_p}$ which is called the thermal diffusivity (m^2/s), (Holman 2010)

Equation (3.19) represents the overall partial differential of the temperature distribution at any time within the disks material.

3.3. Finite Difference Numerical Method

3.3.1. Introduction

The mathematical formulation of the majority of scientific problems involves rate of change with respect to independent variables, which leads to the governing equations being partial differential equations (PDEs). Most of those partial differential equations cannot be solved using analytical solution, therefore, numerical methods are used to find an approximate solution to those PDEs. The finite difference method (FDM) is

one such solution method, in which the approximation is established at discrete values of the independent variables and all partial derivatives terms are replaced by discrete differences. Turning to the overall partial differential equation (3.19), no analytic solution is available to solve it including the problem's boundary conditions and so FDM is used for this aim. Accordingly, the temperature derivatives are replaced with finite-sized differences at nodes in particular locations on a solution mesh. Thus, the problem is reduced to a system of linear equations representing the temperatures at each node in the mesh which can be solved using an iterative technique. The fundamentals of the finite differences in this chapter are based on (Croft et al. 1977) and (Smith 1985).

3.3.2. Finite difference approximation to derivative

Consider a function *f(x)* as shown in Figure 3.2, if *f(x)* and its derivatives are single-valued, finite and continuous function of *x*, then by Taylor's theorem(Smith 1985),

$$f_{(x+\Delta x)} = f_{(xo)} + \Delta x f'_{(xo)} + \frac{(\Delta x)^2}{2!} f''_{(xo)} + \frac{(\Delta x)^3}{3!} f'''_{(xo)} \ \ldots. \tag{3.20}$$

$$f_{(x-\Delta x)} = f_{(xo)} - \Delta x f'_{(xo)} + \frac{(\Delta x)^2}{2!} f''_{(xo)} - \frac{(\Delta x)^3}{3!} f'''_{(xo)} \ \ldots. \tag{3.21}$$

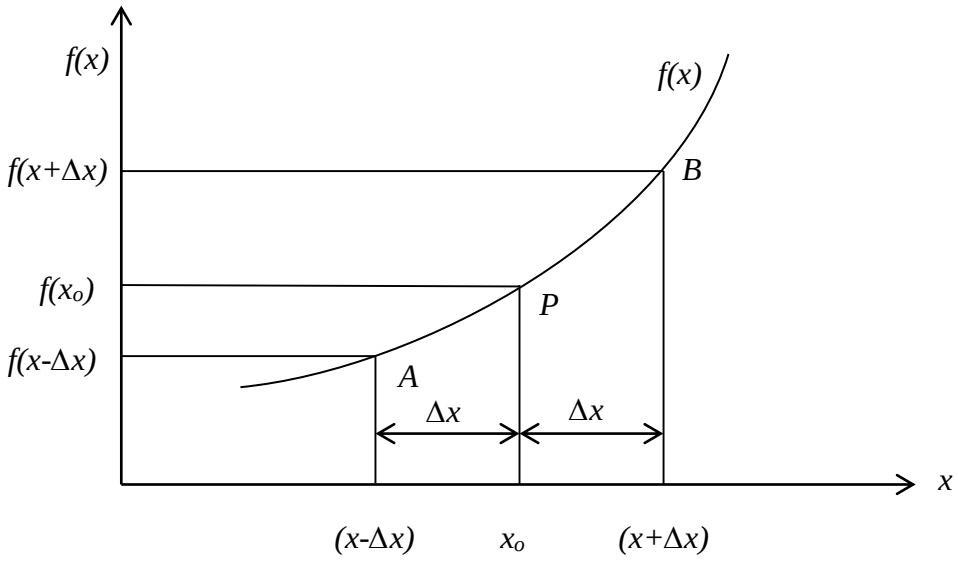

Figure 3.2: Finite differences formulation

Adding equations (3.20) to (3.21) gives

$$f_{(x+\Delta x)} + f_{(x-\Delta x)} = 2f_{(xo)} + (\Delta x)^2 \; f''_{(xo)} + O((\Delta x)^4) \; \ldots$$

Where $O((\Delta x)^4)$ is the terms containing fourth and higher powers of Δx which assumed to be neglected if compared with lower power of Δx. Accordingly:

$$f''_{(xo)} = (\frac{d^2 f}{dx^2})_{x=x_o} \simeq \frac{1}{(\Delta x)^2}\{f_{(x+\Delta x)} - 2f_{(xo)} + f_{(x-\Delta x)}\} \qquad (3.22)$$

Noting that equation (3.22) has a trunction error of order $(\Delta x)^2$ on the right hand side.

Now by subtracting equation (3.21) from equation (3.20) and neglecting the terms of order $(\Delta x)^3$ gives:

$$f'_{(xo)} = (\frac{df}{dx})_{x=x_o} \simeq \frac{1}{2\Delta x}\{f_{(x+\Delta x)} - f_{(x-\Delta x)}\} \qquad (3.23)$$

Again, equation (3.23) of an error order of $(\Delta x)^2$. This equation approximates the slope of the tangent at the point of interest *P* by points after *B* and before *A*. This is called the central difference approximation. Alternatively, the first order derivative can be evaluated by using forward point *B* or backward point *A* with the point of the interest *P* giving forward difference or backward difference formulae respectively. The forward and backward difference equation is derived immediately from equations (3.20) and (3.21) respectively by neglecting the terms having $(\Delta x)^2$ and higher:

$$f'_{(xo)} \simeq \frac{1}{\Delta x}\{f_{(x+\Delta x)} - f_{(xo)}\} \qquad \text{Forward difference} \qquad (3.24)$$

$$f'_{(xo)} \simeq \frac{1}{\Delta x}\{f_{(xo)} - f_{(x-\Delta x)}\} \qquad \text{Backward difference} \qquad (3.25)$$

The error in equations (3.24) and (3.25) is of order Δx which means that the central difference formulation is more accurate than the forward and backward formulation, and hence in the formulation used in this work.

3.4. Transient two dimensional bulk temperature model

3.4.1. The simplified partial differential equation

Provision of holes for thermocouples in the disk involves a manufacturing process which was hole spark erosion in this case. It was crucial to avoid weakening or affecting the running surface of the disk by the thermocouple's holes, remembering that the disks are designed to carry high periodic load during the EHL tests. With these limitations, the thermocouples were installed at 6 mm, 3 mm, and 1.25 mm below the surface, this is discussed in section 5.6. At these depths, the thermocouples are not

expected to experience temperature changes at the frequency of rotation and can only measure the average temperature in the circumferential direction.

The distance to which temperature rise penetrates below the surface depends on the duration of application of the heat source. In the test disks analysis, this duration depends on the disk speed and the width of the contact zone. The following analysis is to evaluate the depth of temperature rise penetration in the test disks for the range of loads and speeds used in the EHL tests as they pass through the contact. The contact zone is considered as fixed in space and a point *p* on the surface of the disk passes through that zone as shown in Figure 3.3. It is clear that the central point *P* indicated in the figure will experience the longest heating time.

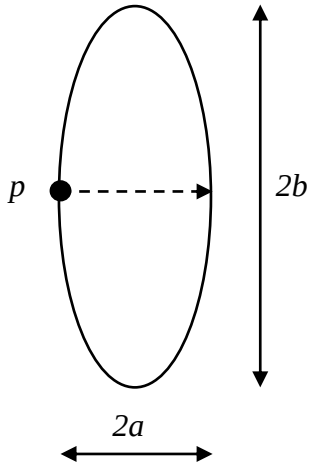

Figure 3.3: Hertz contact zone through which surface points pass and experience surface heating

The temperature of the point rises as it enters the zone, and heat continues to penetrate below that surface point for as long as it remains in the contact zone. For analysing this scenario, consider the solution of the transient semi-infinite solid (Holman 2010).This model is derived for a semi-infinite body as shown in Figure 3.4

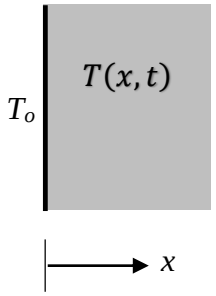

Figure 3.4: Semi-infinite body

This body is assumed to be at initial temperature T_i, when the surface temperature is suddenly changed and maintained at temperature T_o. The one dimensional transient heat conduction is:

$$\frac{\partial^2 T}{\partial x^2} = \frac{1}{\alpha}\frac{\partial T}{\partial t}$$

x in this case in represents *radial* distance below the disk surface.

The boundary and initial conditions are:

$T(x,0) = T_i$

$T(0,t) = T_o \quad for\ t > 0$

The temperature at any time and distance from the surface is given by:

$$T(x,t) = T_o + (T_i - T_o)\ erf\frac{x}{2\sqrt{\alpha t}} \tag{3.26}$$

Where *erf* is the Gauss error function (Holman 2010).

Now at any depth and time $T(x,t)$ is considered as not being affected by the temperature rise, so that it stays at the initial temperature if

$$T(x,t) = T_i = T_o + (T_i - T_o)\, erf\, \frac{x}{2\sqrt{\alpha t}}$$

Simplifying gives

$$erf\, \frac{x}{2\sqrt{\alpha t}} = 1$$

From the tabulated results of the error function, erf, this occurs when

$$\frac{x}{2\sqrt{\alpha t}} = 3.6$$

$$x = 7.2\sqrt{\alpha t} \qquad (3.27)$$

Equation (3.27) gives the heat penetration depth as function of time and material properties. For a given time of passage through the contact, point at depth greater than the value of *x* given by equation (3.27) will remain at unchanged initial temperature. The longest residence time of a point in the contact zone is at the slowest speed and highest load which gives the largest Hertzian contact dimensions. Within the range of EHL tests in this work, 774 rpm is the slowest speed and 2320 N is the highest load. Figure (3.5) is a plot of equation (3.27) over the range of time for passage of a point through the contact zone for the EHL test range used in the experiments. It therefore shows the maximum heat penetration depth for these conditions.

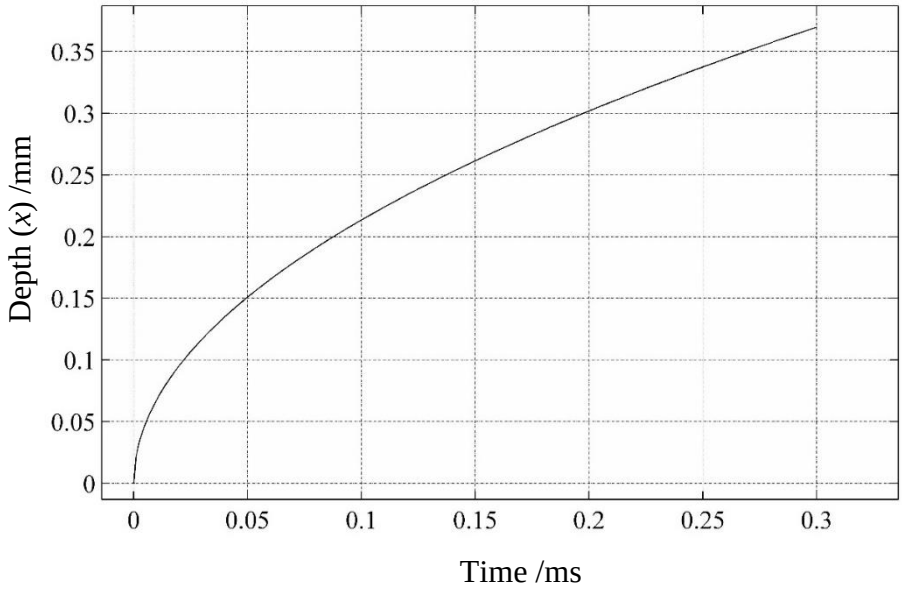

Figure 3.5: The transient heat penetration depth in the test disks

Figure 3.5 shows that the maximum flash temperature penetration is lower than 0.4 mm for the range of speed used. This value is less than the closest thermocouple to the surface which has 3mm or 1.25 mm in the development carried out in this work. This conclusion was also reached by (Clarke 2009) using a transient numerical model and (Qiao 2005) who considered a constant heat flux applied at the surface of a semi-infinite solid.

In summary, the arrangement of the thermocouple positions was designed on stress considerations and the technical wiring issues and they are not subjected to variation of temperature in the circumferential direction. Uniform thermal behaviour in the circumferential direction of the disks is therefore assumed and the problem is reduced to a two dimensional transient conduction model. The general partial differential equation (3.19) can then be written as:

$$\frac{\partial T}{\partial t} = \alpha \left[\frac{1}{r}\frac{\partial T}{\partial r} + \frac{\partial^2 T}{\partial r^2} + \frac{\partial^2 T}{\partial z^2} \right] \tag{3.28}$$

To solve equation (3.28) numerically by using the finite difference method, two main approaches are available: the explicit and the implicit methods, these are considered in the next sections

3.4.2 The explicit solution method

In order to use this method to solve equation (3.28), the time derivative is converted to forward difference approximation. The temperature of an individual mesh point at a time step is expressed in terms of the temperature at the same point and at its neighbouring mesh points at the previous time step, which are known values. The temperature at all mesh points is calculated for the present time step in this way and the solution continues forward in time. This method is simple but it suffers from time step restriction in terms of stability. Therefore, the time step and mesh steps should be related according to the criteria necessary to achieve stable solution as discussed in e.g. (Smith 1985)

$$0 < \frac{\alpha k}{h^2} \leq 0.5$$

Where

k is the time step

h is a spatial step

Accordingly, fine spatial meshes lead to very small time steps and long computational time. As a result of this restriction, this method is not considered as the most efficient way for the numerical solution of the present problem.

3.4.3. Crank-Nicolson implicit method

This method was proposed by Crank and Nicolson (Smith 1985) and is stable regardless of the value of the time step. In this method, the time derivative is formulated by central difference approximation calculated at the time midway between the previous time step and the present time step. Also, the spatial derivative terms on the right hand side of equation (3.28) are formulated using finite difference approximations at the previous time step and the current time step (where the temperatures are unknown). As a result, a set of equations are developed in terms of temperatures at each mesh point which must be solved simultaneously using a solution technique. In summary, the Crank-Nicolson method is unconditionally stable and more accurate as it uses central difference approximations and this method is used in the numerical solution in this work.

The finite difference formulation is outlined in Figure 3.6. It shows a schematic diagram of the mesh layout for the two dimensional bulk temperature equation.

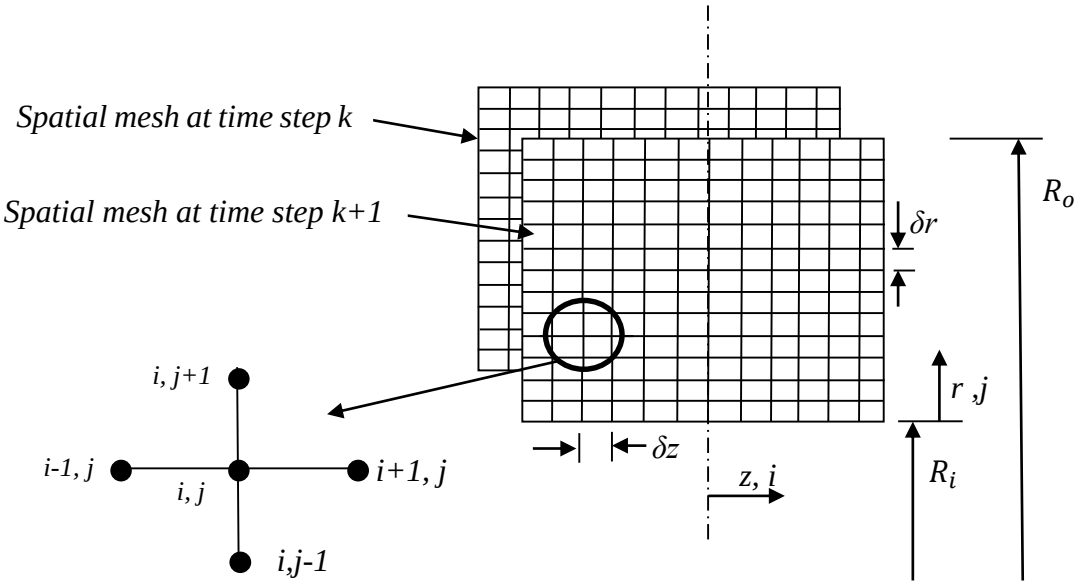

Figure 3.6: A schematic diagram of the finite difference mesh for the considered region within the disk

By using the Crank-Nicolson method, equation (3.28) becomes

$$\frac{T_{i,j}^{(k+1)} - T_{i,j}^{(k)}}{\delta t} = \frac{1}{2}\left(\alpha \left[\frac{1}{r}\frac{\partial T}{\partial r} + \frac{\partial^2 T}{\partial r^2} + \frac{\partial^2 T}{\partial z^2} \right]_{i,j}^{(k+1)} + \alpha \left[\frac{1}{r}\frac{\partial T}{\partial r} + \frac{\partial^2 T}{\partial r^2} + \frac{\partial^2 T}{\partial z^2} \right]_{i,j}^{(k)} \right) \tag{3.29}$$

The spatial finite difference terms can be written as

$$\frac{\partial T}{\partial r} = \frac{T_{i,j+1} - T_{i,j-1}}{2\delta r}$$

$$\frac{\partial^2 T}{\partial r^2} = \frac{T_{i,j+1} + T_{i,j-1} - 2T_{i,j}}{\delta r^2}$$

$$\frac{\partial^2 T}{\partial z^2} = \frac{T_{i,j+1} + T_{i,j-1} - 2T_{i,j}}{\delta z^2}$$

And

$$(r = R_i + j\delta r)$$

Substituting for these spatial terms and for $(r = R_{in} + j\delta r)$ into equation (3.29) gives

$$\frac{2}{\alpha}\left(\frac{T_{i,j}^{(k+1)} - T_{i,j}^{(k)}}{\delta t}\right) =$$

$$\left[\frac{T_{i,j+1} + T_{i,j-1} - 2T_{i,j}}{\delta r^2} + \frac{T_{i,j+1} - T_{i,j-1}}{2(R_i + j\delta r)\delta r} + \frac{T_{i,j+1} + T_{i,j-1} - 2T_{i,j}}{\delta z^2}\right]^{(k+1)}$$

$$+ \left[\frac{T_{i,j+1} + T_{i,j-1} - 2T_{i,j}}{\delta r^2} + \frac{T_{i,j+1} - T_{i,j-1}}{2(R_i + j\delta r)\delta r} + \frac{T_{i,j+1} + T_{i,j-1} - 2T_{i,j}}{\delta z^2}\right]^{(k)}$$

Collecting like terms together gives an equation of the form

$$T_{i,j}^{\,k+1} - [AT_{i,j+1} + BT_{i,j-1} + CT_{i+1,j} + DT_{i-1,j}\,]^{k+1} = [\mathrm{E}\,T_{i,j} + AT_{i,j+1} + BT_{i,j-1} + CT_{i+1,j} + DT_{i-1,j} + \mathrm{F}]^{\mathrm{k}} \quad (3.30)$$

Where

$$A = \frac{s+j+1/2}{2(s+j)(\varphi+\gamma+1)}$$

$$B = \frac{s+j-1/2}{2(s+j)(\varphi+\gamma+1)}$$

$$C = D = \frac{\gamma}{2(\varphi+\gamma+1)}$$

$$E = \frac{\varphi-\gamma-1}{\varphi+\gamma+1}$$

$$F = 0$$

$$s = R_i/\delta r$$

$$\varphi = \frac{\delta r^2}{\alpha\delta t}$$

$$\gamma = \frac{\delta r^2}{\delta z^2}$$

3.4.4. Boundary nodes

The solution region for the two dimensional bulk temperature distribution is the region JKLM shown in Figure 3.7. In this figure, the applied boundary conditions for the numerical solution are outlined and they will be explained in the following sections.

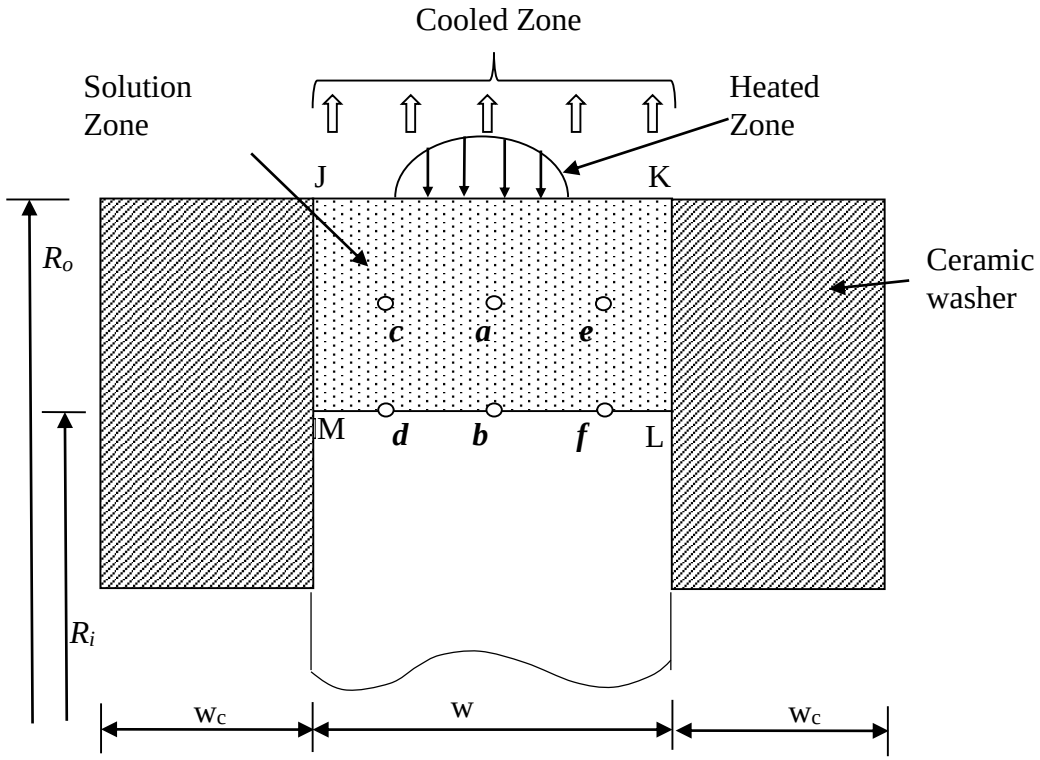

Figure 3.7: The transient two dimensional model of the test disks during EHL experiment. Equation (3.28) is solved over the region JKLM and positions of thermocouples are indicated by ***a, b, c, d, e*** and ***f***

3.4.4.1. The outer radius boundary condition

The outer surface of the disk is represented by the line JK as the problem is reduced to a two dimensional problem as mentioned previously. On this boundary, part of the frictional heat which is generated within the EHL point contact is conducted to the disk within the Hertzian contact width. On the other hand, heat is transferred from this face to the surrounding by forced convection as a result of the disks rotation. Hence

the energy balance at this boundary is considered to eliminate the temperature at the non-existent point (*i, j+1*) in equation(3.30) as follows

$$K\frac{\partial T}{\partial r} = K\frac{T_{i,j+1} - T_{i,j-1}}{2\delta r} = q_{fr} - h\left(T_{i,j} - T_A\right) \tag{3.31}$$

Where *K* is the disk's thermal conductivity, q_{fr} is the frictional heat flux conducted to each disk, *h* is the forced convection heat transfer coefficient and T_A is the temperature of the surroundings. Making $T_{i,j+1}$ the subject of equation (3.31) and substituting into equation (3.30) makes coefficient *A*=0 and modifies the values of *B* to *F*. The value of the heat transfer coefficient h will be discussed later in section 3.5. The frictional heat flux q_{fr}, is applied over the running track on the disks surfaces which is created by the contact zone during rolling/sliding motion between the disks, and has the Hertzian contact width. The flux distribution over the width is assumed to be proportional to the contact pressure which has semi elliptic form. The value of q_{fr} is obtained by integrating the flux in the circumferential direction over the contact area. This leads to the result:

$$q_{fr} = 1.5\bar{q}\left(1 - \frac{z^2}{b^2}\right) \qquad \text{on } z \leq \pm b \tag{3.32}$$

$\bar{q}$ is the portion of the total generated frictional heat that flows to each disk. This total heat is the frictional power dissipation within the contact that is equal to Fu_s where *F* is the measured frictional force and u_s is the sliding speed. The thermal analysis of the disks during EHL contact is carried out on the assumption that a proportion of the total heat flows to one of the surfaces and the rest of that heat flows to the other surface. Consequently, in this study, β is imposed as the proportion of the total heat flowing

into the fast disk and (1-β) is the corresponding portion for the slow disk. $\bar{q}$ for each disk becomes:

$\bar{q} = \frac{\beta F u_s}{4\pi b R_o}$ for the fast disk

$\bar{q} = \frac{(1-\beta) F u_s}{4\pi b R_o}$ for the slow disk

Where R_o is the outer radius of the disks.

According to the above formulation, the total power dissipation is partitioned between the disks and distributed in parabolic form in the axial direction and uniformly around the whole of the running track in the circumferential direction.

During the numerical solution analysis of the disks, they were treated individually. The value of β and 1- β is nominated in a range of (0 to 1) in 0.1 steps for each disk until the calculated temperatures match the temperature measured by the thermocouples ***a, c*** and ***e***.

3.4.4.2. Inner radius boundary condition

In this section, the temperature distribution along the boundary line ML shown in Figure 3.7 is constructed. At this radial position R_i (6 mm below the surface) three thermocouples are installed at positions labelled ***d***, ***b*** and ***f*** in the figure. ***d*** and ***f*** are installed in holes 2mm deep from the respective sides of the disk. Thermocouple *b* is installed at the centre. The temperature is recorded continuously during the experiment by those thermocouples for their particular positions. In order to represent the temperature distribution to be used as a boundary condition along line ML, two

formulae where chosen to represent the temperature distribution at this surface. The first option uses a fourth order polynomial distribution imposed along the disk width which as function of z:

$$T(z) = Az^4 + Bz^3 + Cz^2 + Dz + E \tag{3.33}$$

The coefficients A-E are determined by imposing the three thermocouples values ($T_{\boldsymbol{d}}$, $T_{\boldsymbol{b}}$, and $T_{\boldsymbol{e}}$) and by making the slope of the function equal to zero at both surfaces where the ceramic insulators are fixed, i.e. assuming zero heat flow in z direction at these surfaces, which is not unreasonable given the very low conductivity of the insulators.

The second option uses a 2nd degree polynomial with non-zero slope at the surfaces:

$$T(z) = Az^2 + Bz \quad + C \tag{3.34}$$

The coefficients *A*, *B* and *C* are determined by applying the three thermocouple readings (***d, b***, and ***e***) as boundary conditions. Figure 3.8 shows the two options for imposing the boundary temperature distribution for a typical experiment of the fast disk.

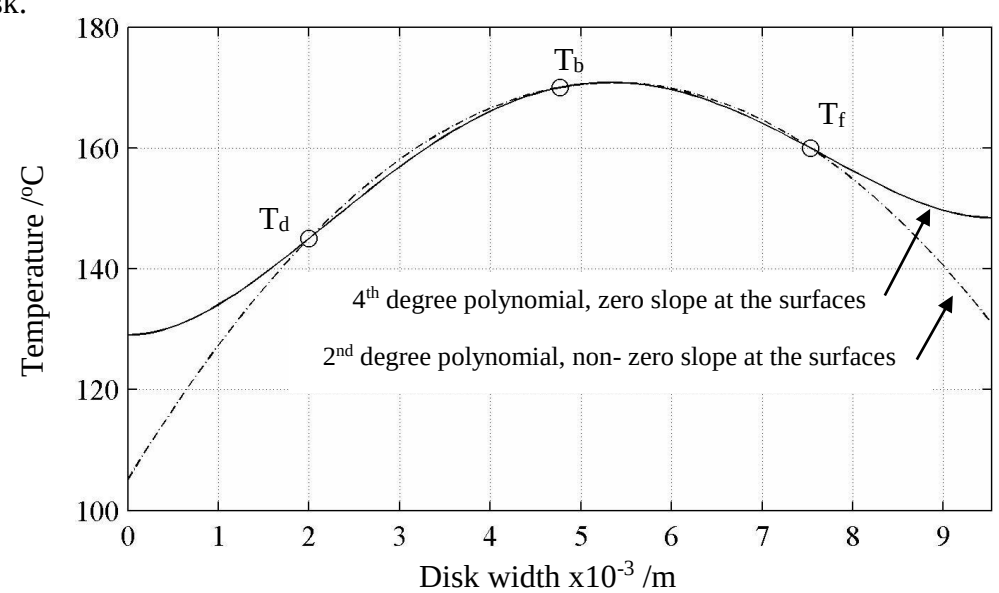

Figure 3.8: Two imposed temperature distribution at the inner radius of the test disk based on three thermocouples readings at that radius

3.4.4.3. The insulated faces boundary conditions

Both side faces of the disks are insulated by ceramic washers as mentioned in section 2.3. The lines JM and KL in Figure 3.7 represent these faces. At these boundaries the temperature terms $T_{i+1,j}$ at KL and $T_{i-1,j}$ at JM in equation (3.30) must be eliminated. The heat balance at this boundary states that the conducted heat from the disk surface must be equal to the conducted heat through the insulation washers. At these boundaries, the temperature is considered equal for both the disk and the insulation, whereas, the outer face temperature for the insulation is considered equal to the ambient temperature T_A which is measured by thermocouples installed in the enclosure of the disks. Accordingly, the heat balance equation at the face KL becomes:

$$-K\frac{\partial T}{\partial z} = -K\frac{T_{i+1,j} - T_{i-1,j}}{2\delta z} = K_c\frac{(T_{i,j} - T_A)}{w_c}$$

where w_c is the ceramic washer width. Re arranging this equation and substituting in equation (3.30) will eliminate $T_{i+1,j}$. Using the same heat balance at the face JM leads to an equation that can be used to eliminate $T_{i-1,j}$ in equation (3.30).

3.5 Numerical Solution

The solution area JKLM described in Figure (3.7) is divided into a uniform rectangular grid with n x m nodes based on the dimensions of that area. In addition an appropriate time step is selected according to the spatial mesh. The nodes on the boundary ML were specified as boundary values where time varying values were given by the thermocouple measurements and use of equation (3.33) or equation (3.34). The remaining n × (m-1) nodal values were linked by the n × (m-1) equations of the form

of equation (3.30). This set of simultaneous equations were solved using Jacobi iteration at each time step and by using the previous time step solution, where the first temperature distribution is imposed as a uniform temperature which is achieved when the disks are left running under no load in the temperature controlled lubricating oil.

During the EHL experiments, the data are recorded in a spread sheet file including the disks' temperature measurements, the oil temperature and the ambient temperature in addition to the friction and load measurements. These data were curve fitted using the Matlab curve fitting Toolbox to remove the noise from the measurements, then the full set of fitted data was written to data file.

For the numerical finite difference solution, a Fortran90 code was written which reads the experiment data file and uses it during the solution. For each experiment, the solution is carried out for each disk individually and the output data written to external files. The analysis was carried out over a range of (β,h) values over the range ($0.1 \leq \beta \leq 1$) and ($100 \leq h \leq 1200$ $Wm^{-2}K^{-1}$). Figure 3.9 shows a flow chart for the Fortran 90 code used in the numerical solution.

The calculations used to obtain the results were carried out with the finest mesh considered in the meshing tests of section 3.6.1 i.e. mesh IV of Table 3.1. They were carried out on an Intel Core i7-2600 CPU @ 3.40 GHz using the LINUX operating. The transient analysis for the loading phase of the experiment was obtained in 100 seconds run time for each individual (β, h) combination

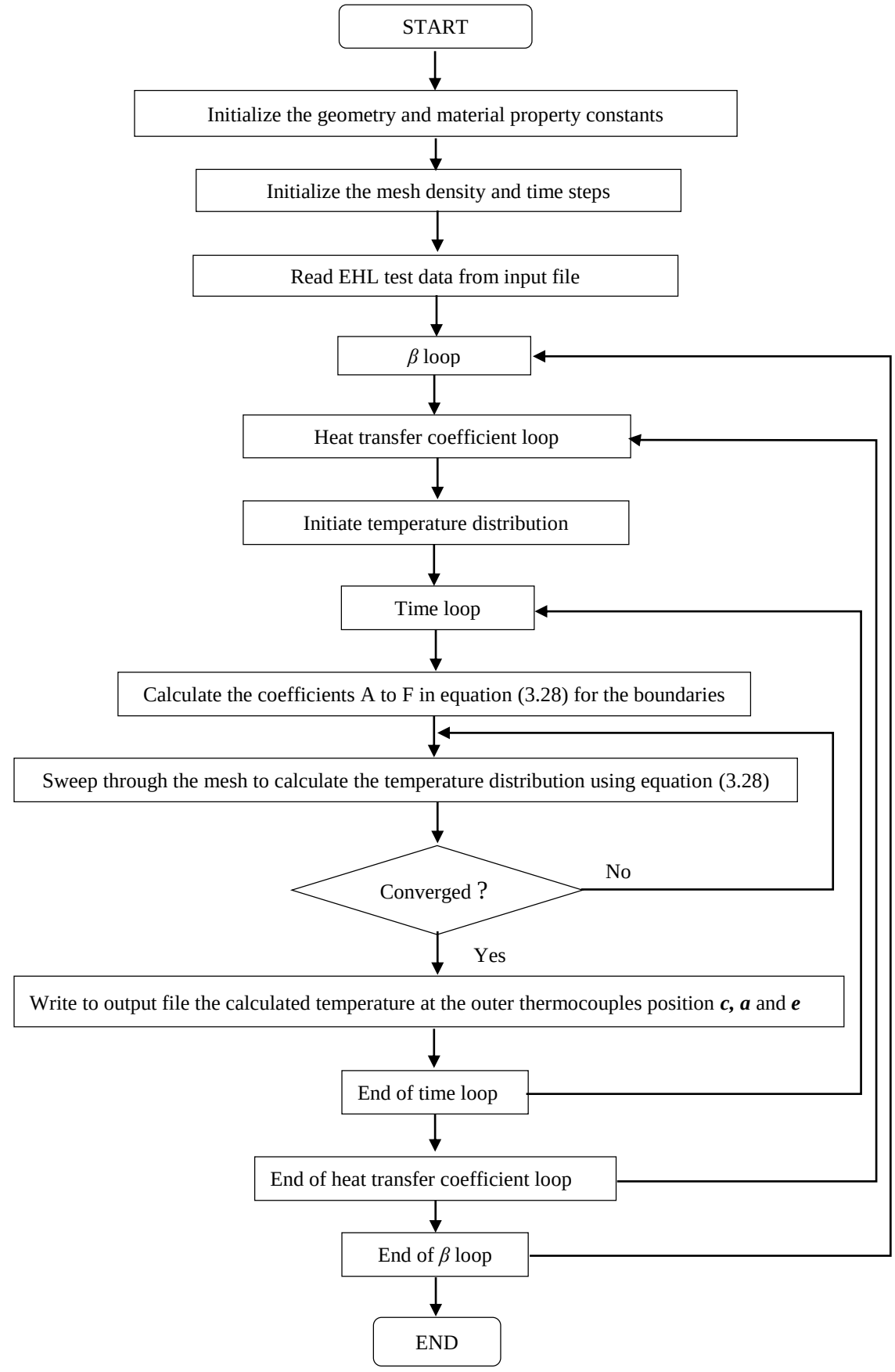

Figure 3.9: The flow chart of the two dimensional transient model.

3.6. Numerical model test and validation

Before applying the formulated model to the real experimental EHL tests, different mesh densities and time increments were tested in order to evaluate the proper values. In addition, different methods were used to check the validity of theory and the numerical formulation of the thermal numerical model. This validation also helped to determine the appropriate spatial mesh density and time increments in terms of the desired accuracy and calculation time. The validation is based on comparing the results of the numerical model with an available analytical model using some approximations. The models which are used for the validation are the transient model and the steady state model.

3.6.1. Meshing test

The solution zone was meshed using different mesh densities and time increments. The mesh is designed to have approximately the same mesh spacing in both the *z* and *r* direction. Four sets of mesh densities from coarse to fine were tested and used in the model. For each spatial set, the appropriate time increment was determined. A test case using conditions of constant heat flux over the running track was imposed, and the inner radius temperature was kept at 20 ^{o}C. For each particular mesh set, the temperature trace for different time increments was tested until a smooth unchanging curve obtained. Figure 3.10 a shows the calculated temperature at specific mesh point using two different time increments (1s and 0.04 s) for a specific mesh spatial mesh density (9x13). The figure shows clearly that 0.04 s time increment gives a smooth temperature trace, and smaller time increments will not give better results in terms of

this work. Figure 3.10 (b) shows the percentage error between the two curves according to the formula:

$$error = \frac{T_{0.04} - T_{1.00}}{T_{0.04}} * 100 \tag{3.35}$$

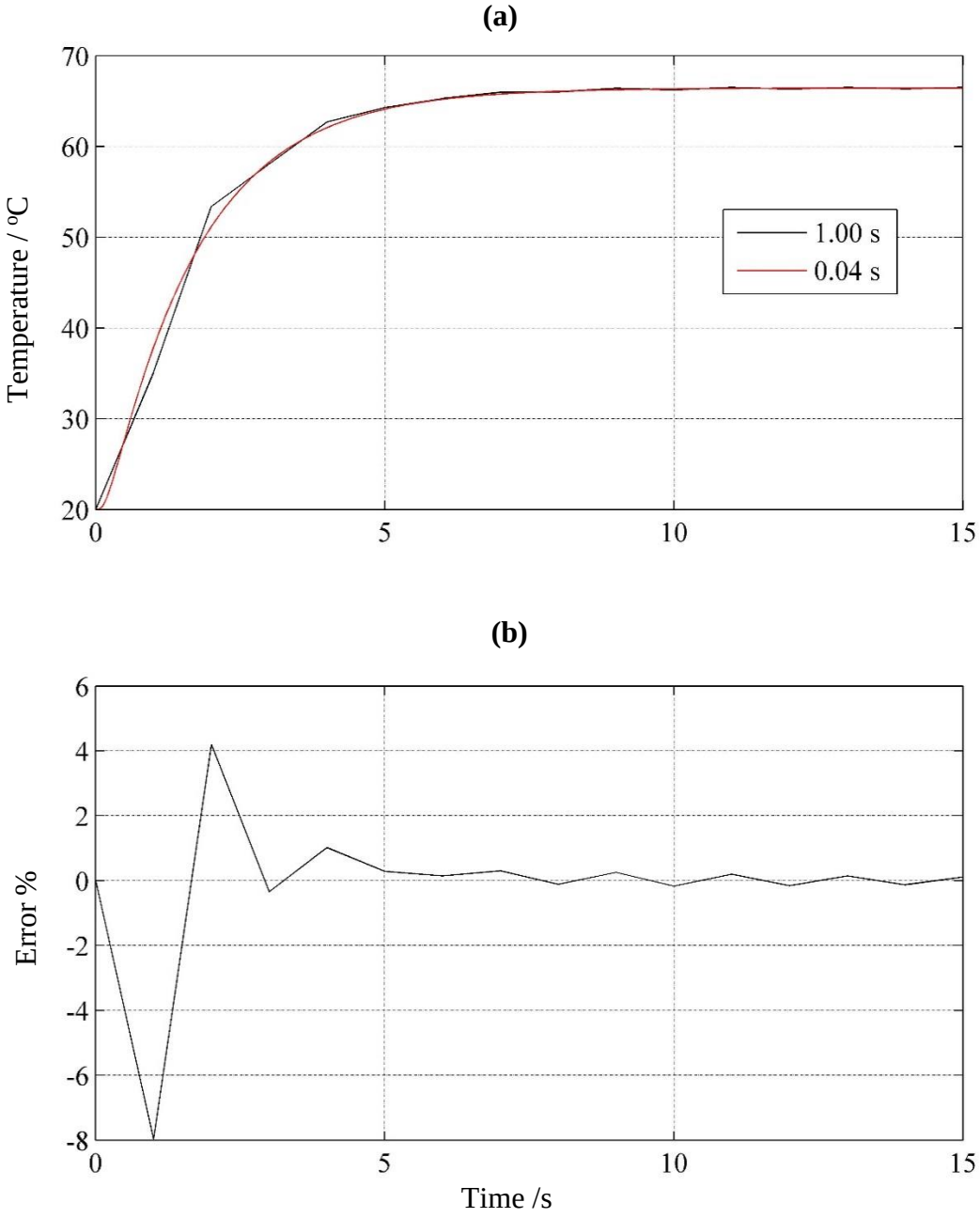

Figure 3.10: Testing the proper time increment for (9 x13) mesh density: **(a)** the temperature trace, **(b)** the error between them according to equation (3.35)

Then a set of mesh densities was tested using the procedure illustrated in Figure 3.10, and the proper time increment for each mesh density was evaluated. Table 3.1 shows the mesh densities and the appropriate time increments for each of them.

Table 3.1: The mesh densities tested in this work and the proper time increments

Mesh set	Nodes in r direction	Nodes in z direction	Time increments /s
I	9	13	0.040
II	17	27	0.010
III	33	53	0.005
IV	65	105	0.001

Table 3.1 shows the range (coarse to fine) of spatial mesh and the corresponding time increments, these sets will be used in the numerical analysis for modelling the EHL tests. Each of those sets gives good agreement when compared with each other. Figure 3.11 shows the comparison between set I and set IV for the central node in the mesh which represents the position of thermocouple ***a***. Figure 3.11 (a), is the temperature trace and Figure 3.11 (b), is the deviation between them according to the formula:

$$error = \frac{T_{IV} - T_I}{T_{IV}} * 100 \tag{3.36}$$

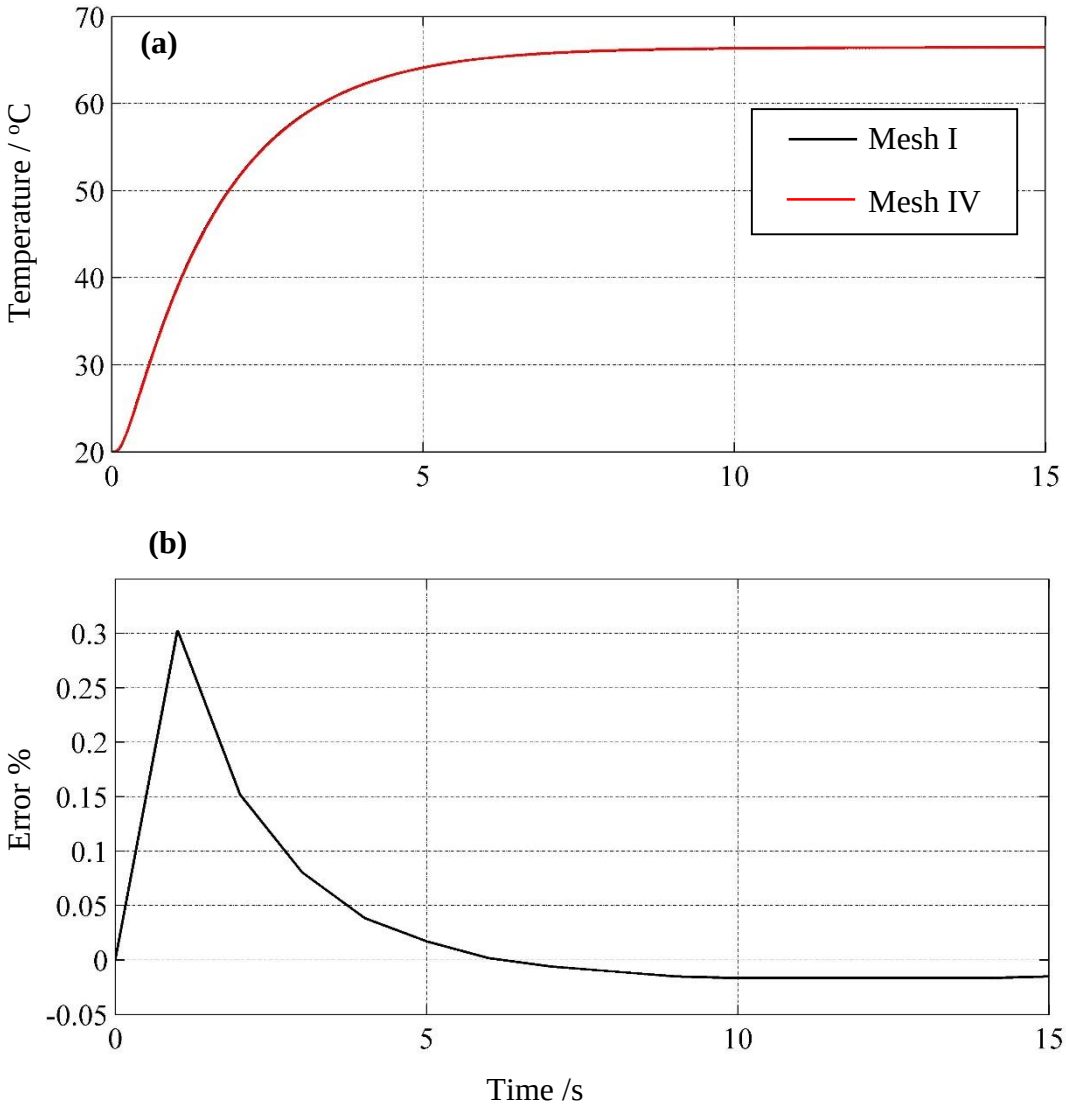

Figure 3.11: Comparison between mesh I and mesh IV at the central mesh node; **(a)** Calculated temperature at the node within the disk, **(b)** The error between the two meshes.

An extensive mesh test was carried out with the aim of checking the validity of the model for different spatial mesh and time increments. In this investigations the temperatures at the position of each mesh point of the coarsest grid was obtained for each of the other grids tested for all time steps. Note that the number of nodes in *z* direction was changed from 13 to 14 nodes for mesh I in order to be able to make direct comparisons at the same spatial positions. Detailed comparisons were made for

the results at particular times in the analysis. The times chosen were 2, 4, 8, and 15 s which cover the interval of Figure 3.11. The finest mesh set was selected as the reference case for the other sets. Table 3.2 shows the maximum percentage error according to the formula:

$$Max\ error = \left| \left(\frac{|T_{IV}(i,j) - T_{set}(i,j)|}{T_{IV}(i,j)} \right) * 100 \right|_{maximum}$$

Table 3.2: The maximum percentage error between mesh densities as compared with IV set

Mesh set	Time at which the comparison evaluated /s			
	2	4	8	15
I	0.567	0.130	0.024	0.015
II	0.142	0.046	0.025	0.021
III	0.078	0.032	0.021	0.017
IV	0.000	0.000	0.000	0.000

Table 3.3 shows the mean percentage error between meshes at different specific times according to the formula:

$$Mean\ Error = \frac{\sum |T_{IV}(i,j) - T_{set}(i,j)|}{\sum T_{IV}(i,j)} * 100$$

Table 3.3 : The average percentage error between mesh densities as compared with IV set

Mesh set	Time at which the comparison evaluated /s			
	2	4	8	15
I	0.480	0.112	0.020	0.012
II	0.121	0.039	0.021	0.017
III	0.067	0.027	0.018	0.014
IV	0.000	0.000	0.000	0.000

The results in Tables 3.2 and 3.3 shows small errors in all cases which will not influence the efficiency of the model in the actual experiment calculation in terms of the intended results. They also shows that the biggest differences occur during the initial highly transient phase with much reduced differences as the steady state conditions is approached at t=15 s.

The above mesh tests were carried out using an ideal problem with constant heat flux on the whole surface and zero thermal conductivity of the insulating ceramic washers. Now these meshes are also tested and compared using a real EHL test. This means that the heat flux was applied at the contact zone in parabolic form, with the side insulation allowing a small amount of heat conduction in the axial direction. The outer radius boundary was subjected to heating and cooling as described in section 3.4.4.1. In addition, the temperatures at the inner radius of the solution zone are variable according to the thermocouple measurements at that level.

The first important issue is the heat flux distribution. As described in section 3.4.4.1, the heat flux that is applied to the surface within the contact zone is assumed to be a parabolic distribution (equation (3.32)) as a result of the Hertzian semi elliptic pressure distribution. Applying this relation to discrete nodes on the surface leads to a loss of part of the value of the applied heat, as shown in Figure 3.12.

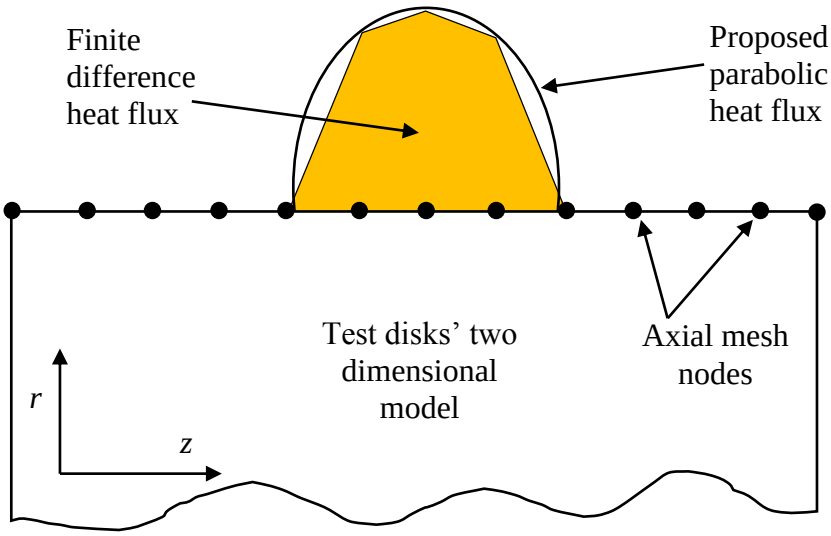

Figure 3.12: The heat flux formulation in the contact zone according to the proposed parabolic formula and the finite difference mesh

This effect depends on the mesh density in the axial direction, in addition it depends on the Hertzian major dimension which depends on the applied load. To treat the effect of the heat lost by this discretization, a correction factor was calculated for each mesh density and for all the load stages used in the EHL tests. Table 3.4 show the correction factors for all load stages and mesh densities.

Table 3.4: The correction factor for heat loss resulted from finite difference meshing

	Load /N	850	1460	1850	2320
	Hertz dimension ***b*** /m	0.00125	0.00150	0.00162	0.00175
Mesh in axial direction n	13 (I)	1.0667	1.0667	1.0667	1.0667
	27 (II)	1.0286	1.0159	1.0159	1.0101
	53 (III)	1.0051	1.0039	1.0031	1.0025
	105 (IV)	1.0013	1.0010	1.0008	1.0007

More investigations were carried out using data from the real EHL problem at time stages; 125 s, 250 s, 600 s, and 1000 s as shown in Figure 3.13. They include the rapid transient states and the approximately steady state period. Noting that Figure 3.13 shows the calculated temperature versus time at 3 mm below the surface at the centre of the two dimensional solution zone.

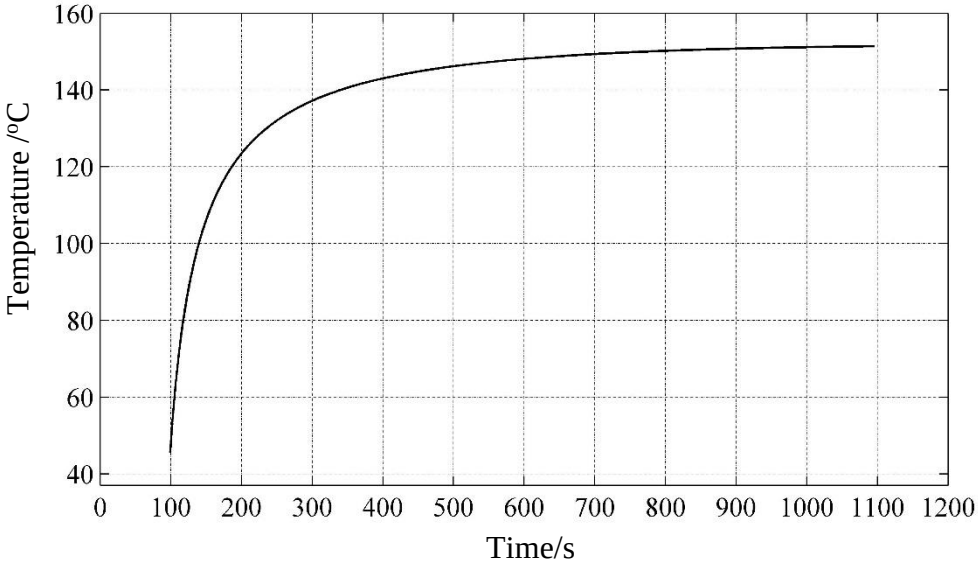

Figure 3.13: The transient calculated temperature at the centre of the two dimensional solution zone for real EHL test

The results of comparison between the mesh tests are shown in Tables 3.5 and 3.6 which gives the maximum error and the mean error respectively.

Table 3.5: The maximum percentage error between mesh densities as compared with mesh set IV

Mesh set	Time at which the comparison evaluated /s			
	125	250	600	1000
I	5.015	3.641	3.177	3.111
II	0.498	0.356	0.337	0.341
III	0.709	0.509	0.385	0.381
IV	0.000	0.000	0.000	0.000

Table 3.6: The average percentage error between mesh densities as compared with mesh set IV

Mesh set	Time at which the comparison evaluated /s			
	125	250	600	1000
I	0.379	0.242	0.231	0.230
II	0.141	0.095	0.020	0.016
III	0.102	0.059	0.026	0.024
IV	0.000	0.000	0.000	0.000

In Table 3.5, the maximum error is high for set I which is not acceptable in terms of accurate solution. This error is caused by coarser resolution of the contact zone width in mesh set I. However this error is concentrated near the contact zone at the surface, Figure 3.14 shows the maximum error contours for all mesh sets. It can be seen that the error concentration occurs near the contact zone, which means the outer rows thermocouple positions is out of the significant error zone except for mesh I.

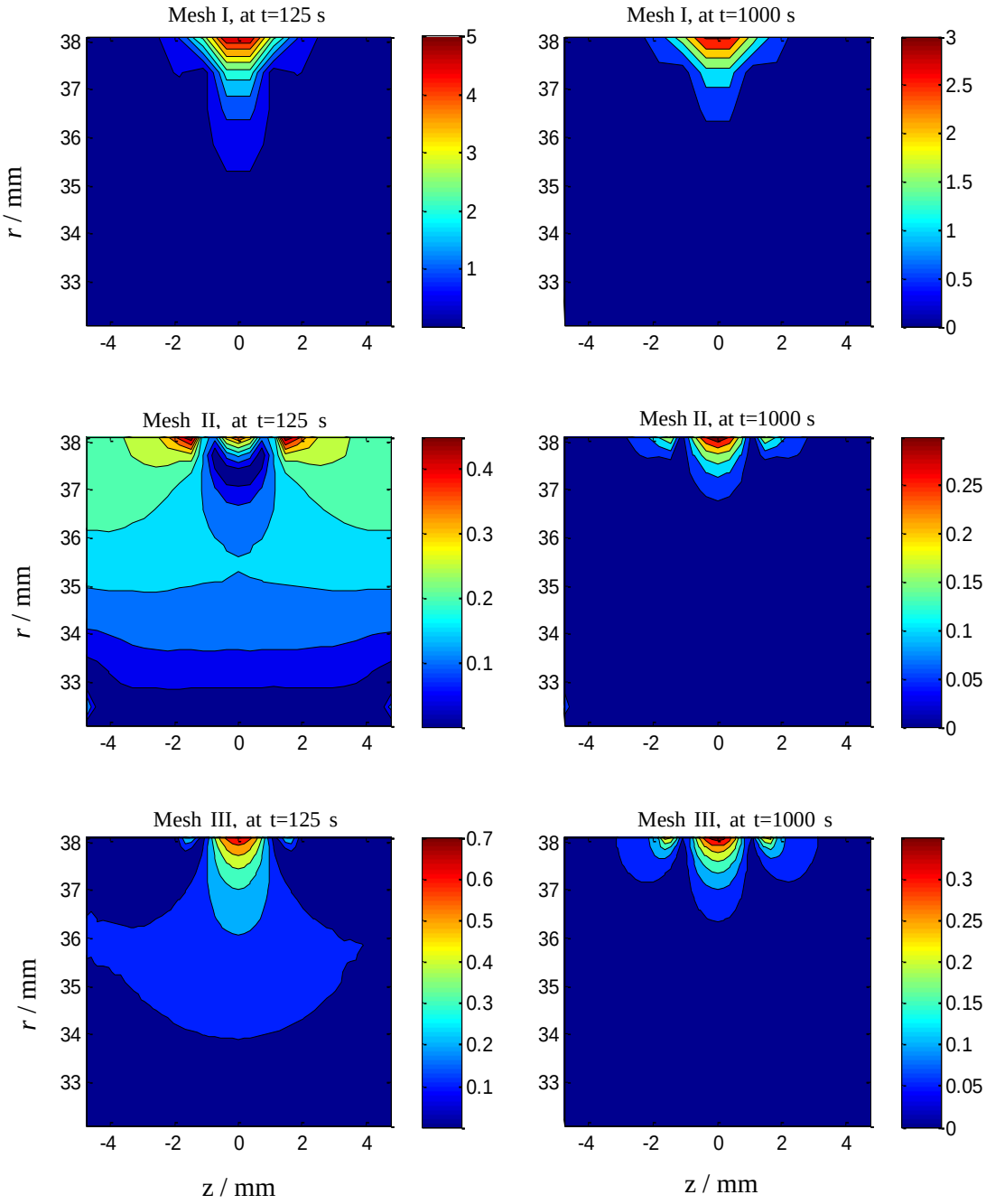

Figure 3.14: The error contour for the mesh densities as compared with set IV at 125 s and 1000 s time of real D4 EHL experiment

3.6.2. Transient state validation

In this section, the model is compared with the analytic solution of the transient semi-infinite solid (Holman 2010) described in section 3.4.1 by using equation 3.26:

$$T(x,t) = T_o + (T_i - T_o)\, erf \frac{x}{2\sqrt{\alpha t}}$$

The analysis based on the derived numerical mode will be conducted on one disk calculation and compared with the above analytical model. A large outer radius (2m) is imposed and the insulation washers were assumed ideal (i.e. zero thermal conductivity). These two assumptions assume that the material below the disk surface (at the very large radius) behaves like the material near the surface in the semi-infinite solid. An initial temperature of 20 ^{o}C was specified for both models and suddenly changed surface temperatures of 160 ^{o}C were imposed. The boundary temperatures at the inner radiuses were kept at 20 ^{o}C as it is far from the surface. A range of mesh density and time step increments were tested for the model. Figure 3.15 (a) shows the change in temperature 3 mm below the surface for the time after sudden temperature change at the surface for both models. Figure 3.15 (b) shows the percentage error between the analytic and numerical models obtained from the formula:

$$error = \frac{T_{analytic} - T_{numeric}}{T_{analytic}} * 100 \qquad (3.33)$$

Figure 3.15 presents very good agreement between the models. In addition, the amount of error is acceptable for the analysis used in this study. It also was found, for those conditions, that the temperature only penetrates to 230 mm depth below the surface for the time interval shown. Therefore the assumption of constant inner radius temperature (1968 mm below the surface) is acceptable.

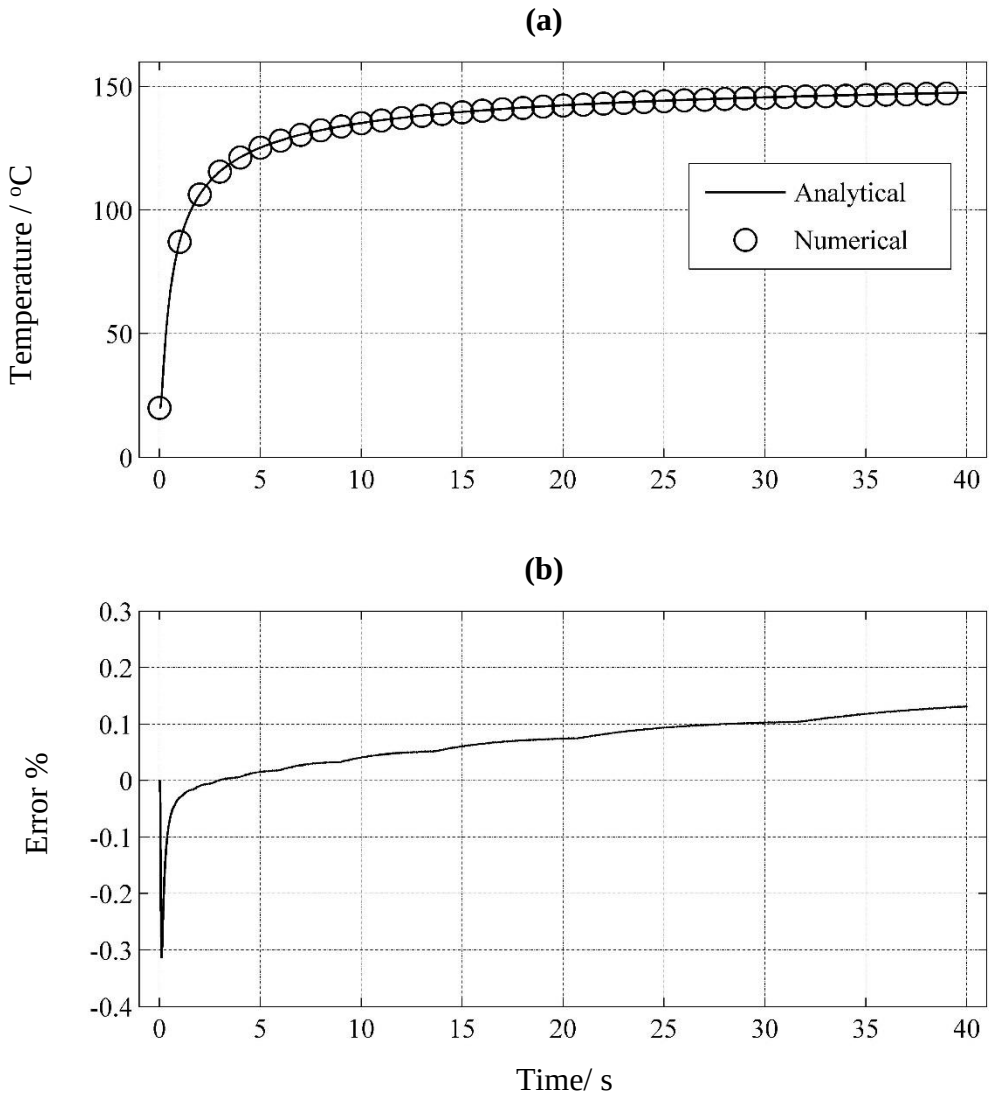

Figure 3.15: The validation of the numerical model at the transient state; **(a)** :temperature versus radius for analytical and numerical solutions 3mm below the surface, **(b):**the error percent in equation (3.33)

3.6.3. Steady state validation

In this section, an analytical steady state model is used to test the derived numerical model. In this analysis, the assumption of ideal insulations is imposed as in section 3.6.2. The whole running track is assumed to be subjected to uniform steady heat flux (rather than the parabolic heat flux over the contact zone) and heat also leaves the disk by convection. The energy equation per unit width at steady state may written as:

$$Q_{flux} = Q_{convection} + Q_{conduction}$$

Simplifying gives

$$2\pi r_{out} H_{flux} = 2\pi r_{out} h(T_{out} - T_A) + Q_{conduction}$$

Where

H_{flux} represents the conducted heat to the disk which is distributed uniformly over the running track.

T_{out} is the temperature of the running track

T_A is the ambient temperature

Thus,

$$Q_{conduction} = 2\pi r_{out} H_{flux} - 2\pi r_{out} h(T_{out} - T_A) \quad (3.34)$$

According to Fourier's law of conduction

$$Q_{conduction} = -KA\frac{dT}{dr}$$

This equation may rewritten as

$$dT = \frac{Q_{conduction}}{-2\pi rK} dr$$

This can be integrated along the solution zone in the disks

$$\int_{T_{in}}^{T} dT = \int_{r_{in}}^{r} -\frac{Q_{conduction}}{2\pi K}\frac{dr}{r}$$

After integration and simplification

$$Q_{conduction} = \frac{2\pi K(T - T_{in})}{ln\,(r/r_{in})} \tag{3.35}$$

See Holman (2010) for example.

Substitute equation (3.35) into equation (3.34) to obtain

$$\frac{2\pi K(T - T_{in})}{ln\,(r/r_{in})} = 2\pi r_{out} H_{flux} - 2\pi r_{out} h(T_{out} - T_a)$$

Simplifying gives

$$T = \frac{T_{in} + \left(H_{flux} - h(T_{out} - T_a)\right) r_{out} ln\,(r/r_{in})}{K} \tag{3.36}$$

Equation (3.36) represents the temperature at any radius.

Now, substitute for $r = r_{out}$ in the equation (3.36) to find T_{out}

$$T_{out} = \frac{r_{out} h T_a + \frac{K}{ln\,(r_{out}/r_{in})} T_{in} + r_{out} H_{flux}}{h r_{out} + \frac{K}{ln\,(r_{out}/r_{in})}} \tag{3.37}$$

Equation (3.37) gives the running track temperature which should be calculated and substituted in equation (3.36) to calculate the temperature at any radius analytically.

Figure 3.16 (a) shows the temperature versus the disk radius at steady state for the analytical and numerical models, and Figure 3.16 (b) shows the percentage error between the exact and the numerical solution according to the formula;

$$Error = \frac{T_{f.d} - T_{exact}}{T_{exact}} * 100 \tag{3.38}$$

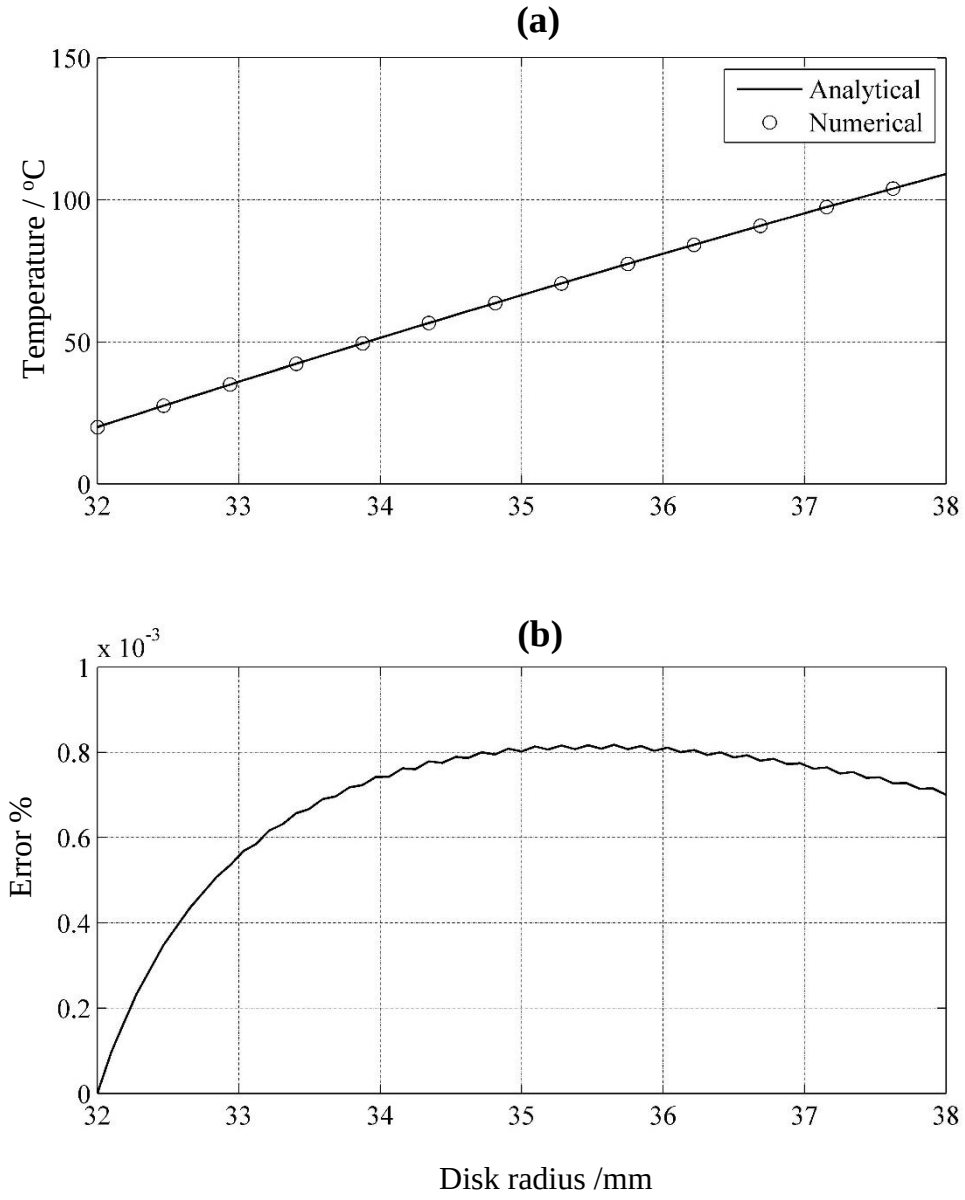

Figure 3.16: The validation of the numerical model at the steady state; **(a)** temperature versus radius for analytical and numerical solutions, **(b):**the error percent in a (equation (3.38))

The tests confirm that the numerical model has been correctly implemented as far as can be determined by comparison with problems having analytical solutions. Variation with respect to *z* has not been tested in this way as a suitable analytic solution was not identified, however the *z* variation is restricted to the calculation term where it forms part of a Laplacian expression.

Chapter 4:

Methodology of Modelling the EHL Tests

4.1. Introduction

In this chapter, the methods of modelling the EHL disk tests carried out using the test rig described in chapter two are described in detail. During the EHL disk tests, the results were logged, including the temperatures, friction force, and load, described in detail in section 2.4. The thermal response of the disks is modelled using the numerical model described in chapter three, following the methodology described in this chapter.

During the EHL tests, the disks are in loaded contact with full film lubrication and heat is generated within that film as a result of sliding and rolling between the contacting surfaces which results in shearing of the lubricant film. This heat is partitioned between these surfaces according to heat partition factor β which is the notation adopted for the proportion of heat conducted to the fast disk. Accordingly, $1-\beta$ is the fraction of the total heat conducted to the slow disk. The amount of heat that leaves the contact by means of the lubricant is neglected as the lubricant mass flow through the contact is small. On the other hand, the rotating test disks loose heat by forced convection heat transfer to the surrounding environment. This occurs through the oil jets that supply the contact zone and the oil mist that surrounds the disks as it rotates in the surrounding air. It is to be expected that the forced convection heat transfer coefficient is speed dependent and therefore that each disk has a different heat transfer coefficient as they are rotating at different speeds.

In summary, the heat partition factor β and the convection heat transfer coefficient for each disk are unknown. Methods of modelling should be used to evaluate these unknown factors which lead to a complete thermal analysis of the test disks. The ultimate objective is to link the results of that thermal analysis to a thermal lubrication analysis of the EHL point contact, and through this to be able to judge the most realistic rheological model. by consideration of the thermal behaviour of the lubricant film in terms of heat partition.

Two approaches to this problem are considered. One is to model the heat flow in the disk pair at the near steady state conditions and establish the heat transfer coefficients from speed dependence given in the literature. The other is to model the cooling phase to obtain a heat transfer coefficient from the observed temperature decay when the heat source is removed. Both methods were considered and the first was adopted to produce the results given. The rapid transient changes during initial cooling were found to present obstacles to the use of the second approach.

4.2. Data noise removal

In general, noise is a common problem in the experimental data which is caused by a range of reasons and conditions. In this work, the acquired data suffer from fluctuating noise around their real value. This type of noise affects mainly the recorded temperature measurement by the thermocouples fitted in the test disks. The reasons behind this type of noise are electrical as the data is acquired by electronic hardware devices which are subjected to electrical noise from other devices in the laboratory and in general surroundings. Furthermore, slip rings are known to potentially cause noise on the signals which they are used to transmit.

As outlined previously in section 2.5, a LabView data acquisition software code was constructed specially for this project. One option considered was to build a filter into the software to remove the noise from the data instantaneously during running of the rig. This would reduce the size of the output data file considerably but it would potentially distort the very rapid change in data at load removal which was thought to be important in the simulation. Therefore, it was decided to record all the acquired data in its raw form so that the necessary filtering could be applied to the raw data post-test. This approach allowed the filtering method to be developed and its effect on subsequent modelling to be assessed.

In the method adopted, the experimental data was filtered using regression analysis, in order to fit smooth curve to the discrete experimental data. This regression process was conducted using the Matlab curve fitting toolbox. The toolbox includes applications and functions to perform data surface and curve fitting processes. It provides two different environments to use. One of these is interactive environment using the Curve Fitting application which is shown in Figure 4.1.

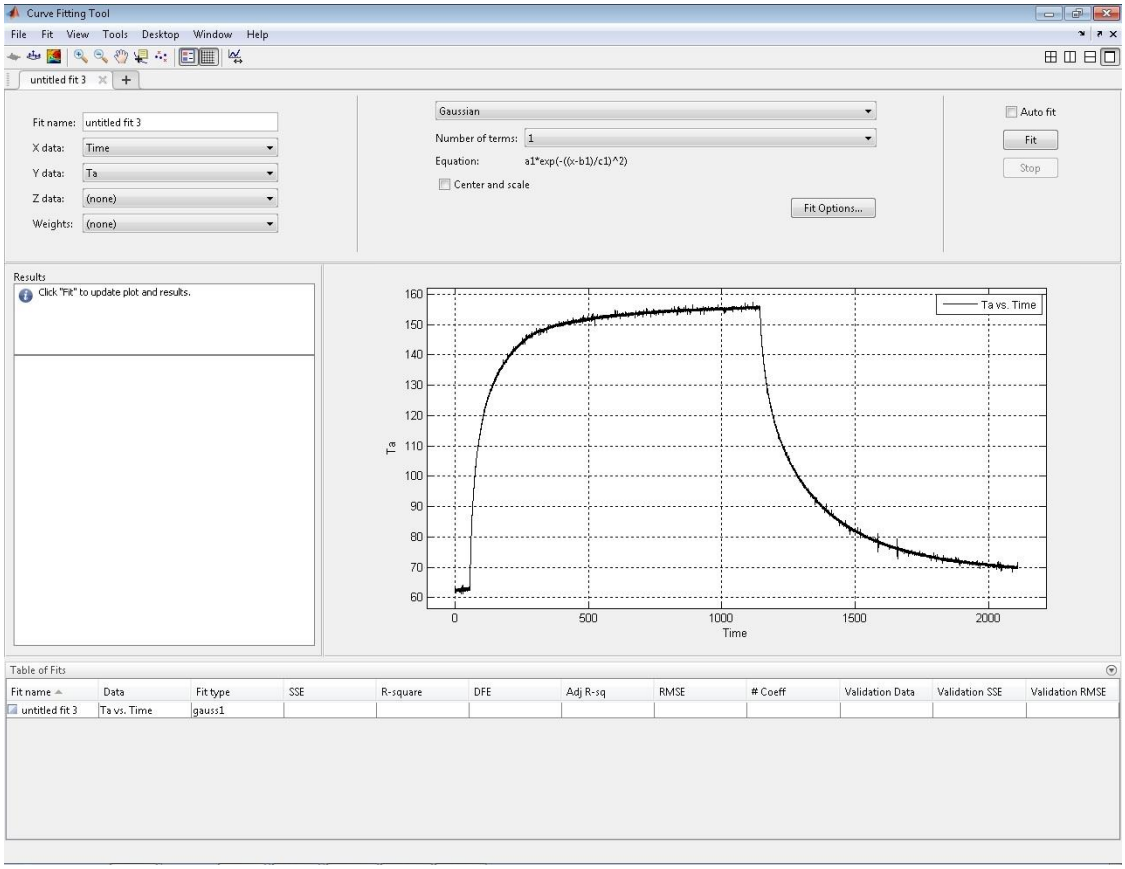

Figure 4.1: Matlab Interactive curve fitting toolbox.

Figure 4.1 shows the temperature data of a thermocouple from the EHL disk test which has been imported for the purpose of the curve fitting process. The data in this figure appears to have a thick line, but this due to the noise levels in the raw data. The other environment which the toolbox provides is the programmatic environment which involves writing Matlab code. The general steps in both methods are the same and are explained in turn.

The first step in the curve fitting process is to import the experimental data into the Matlab workspace. Each thermocouple's temperature data versus time is processed separately as shown in Figure 4.1. Following this, the data is partitioned into multiple segments so that each can be curve fitted individually as it is difficult to evaluate a function which represents the whole interval of the experiment due to the load removal

that occurs at around 1150 s. In general, the data is divided into the heating and the cooling phases. Sometimes, each of those phases are subdivided to two pieces if the overall fit obtained is weak. The second step is to exclude any obviously out-lying data points. After this pre-processing, a range of built-in mathematical functions is examined by the toolbox which uses the least squares method to evaluate the most appropriate function for representing the raw data. The visual assessment is the first step in selecting the best fitted function where they are plotted against the raw experimental data, the residuals also are observed visually. Beyond this assessment, the toolbox provides a range of statistical measures of quality of fit for curve fitting (Matlab curve fitting toolbox user's guide).

Figure 4.2 shows functions fitted to the experimental data imported and shown in Figure 4.1. These data were curve-fitted in two phases, cooling and heating. Figure 4.3 shows part of Figure 4.2 in greater detail.

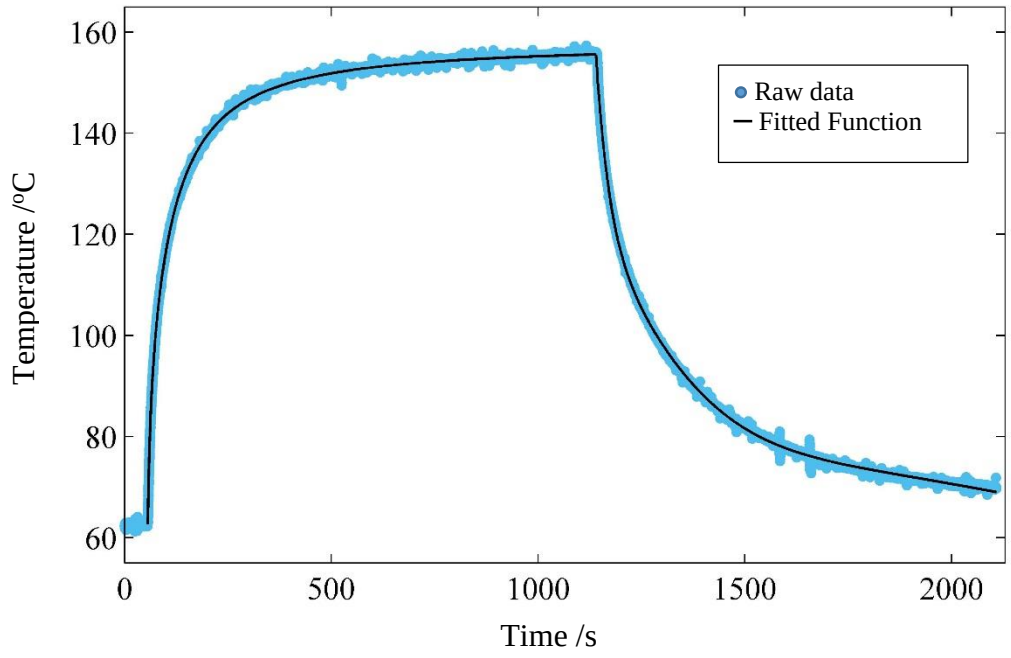

Figure 4.2: An example of data curve fitting using the Matlab curve fitting toolbox

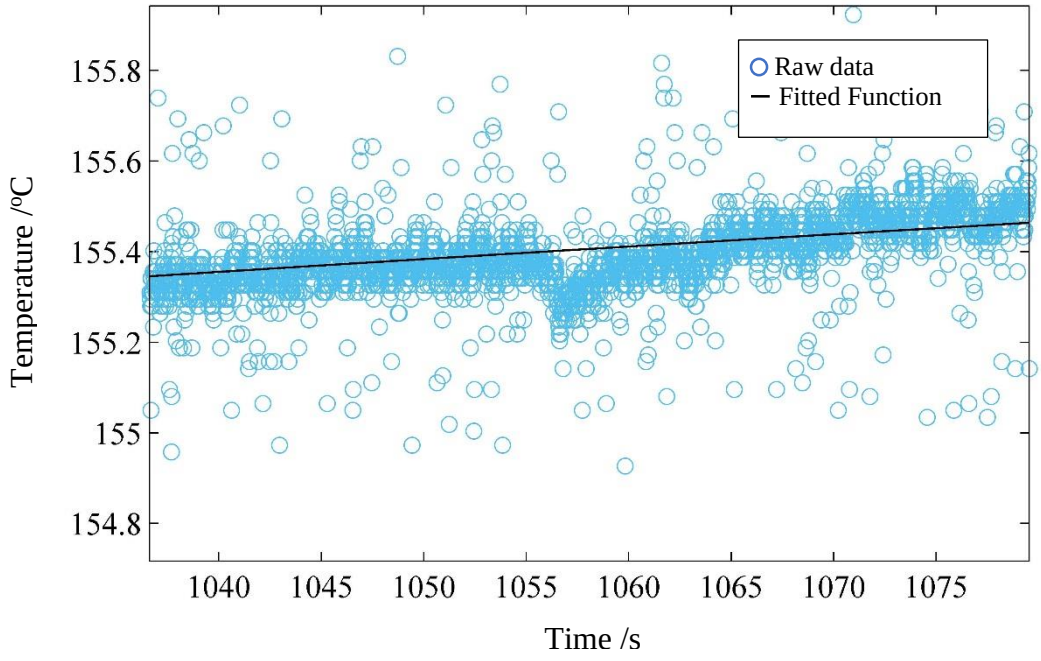

Figure 4.3: A detailed view of Figure 4.2 to show in details the raw data and fitted functions

For the heating zone, the fitted function shown in Figure 4.2 takes the general form

$$f(x) = \frac{p_1x^5 + p_2x^4 + p_3x^3 + p_4x^2 + p_5x + p_6}{x^5 + q_1x^4 + q_2x^3 + q_3x^2 + q_4x + q_5}$$

Where

p_1=185 p_2=465.8 p_3=-4.467x10^5 p_4=-2.313x10^4 p_5=-1029 p_6=-27.03

q_1=18.45 q_2=-164.2 q_3=-1.57x10^5 q_4=6.06x10^4 q_5=2304

With coefficient of determination of the fit, R^2= 0.999.

For the cooling phase the fitted function took the general form

$$f(x) = a_1 \exp\left(-\left(\frac{x-b_1}{c_1}\right)^2\right) + a_2 \exp\left(-\left(\frac{x-b_2}{c_2}\right)^2\right) + a_3 \exp\left(-\left(\frac{x-b_3}{c_3}\right)^2\right)$$

Where

a_1=159.1 b_1=1072 c_1=850.9 a_2=83.94 b_2=199.5 c_2=229.1 a_3=38.55 b_3=540.5 c_3=191.4

with coefficient of determination of the fit, R^2= 0.928.

4.3. Error minimization at steady state

After filtering the experimental data, the new filtered data is written to an external file which is ready for simulation by the two dimensional transient numerical model. As described previously in section 3.5, each disk is simulated individually starting from uniform initial temperature distribution, which is achieved by running the unloaded disks under the heated oil feed. A range of simulations are carried out with each simulation being produced for assumed fixed values of parameters β and h. The values used for the convection heat transfer coefficient h covered the range of $100 \leq h \leq 1200$ $Wm^{-2}K^{-1}$ in steps of 100 $Wm^{-2}K^{-1}$. The range of h was selected by Clarke (2009) to cover the range of heat transfer coefficients for the shaft speeds used, as predicted using heat transfer data in the literature. This range was further extended by Clarke (2009) to account for the wide range of β values considered in his analysis. The values used for heat partition factor covered the range $0.1 \leq \beta \leq 1$ with a step of 0.1. This means that data were modelled 120 times over the experiment time interval using the curve fitted data for the inner position thermocouples as boundary conditions for each disk. In these analyses, the calculated temperatures at the positions of the outer row thermocouples were written to an output file. These data were used to evaluate the heat transfer and the heat partition coefficients by minimization of the deviation between the calculated and the experimental data at the positions of the outer row of

the thermocouples. Figure 4.4 presents the measured and calculated temperature at the position ***a*** thermocouple for different sets of (h_f, β) of the fast disk.

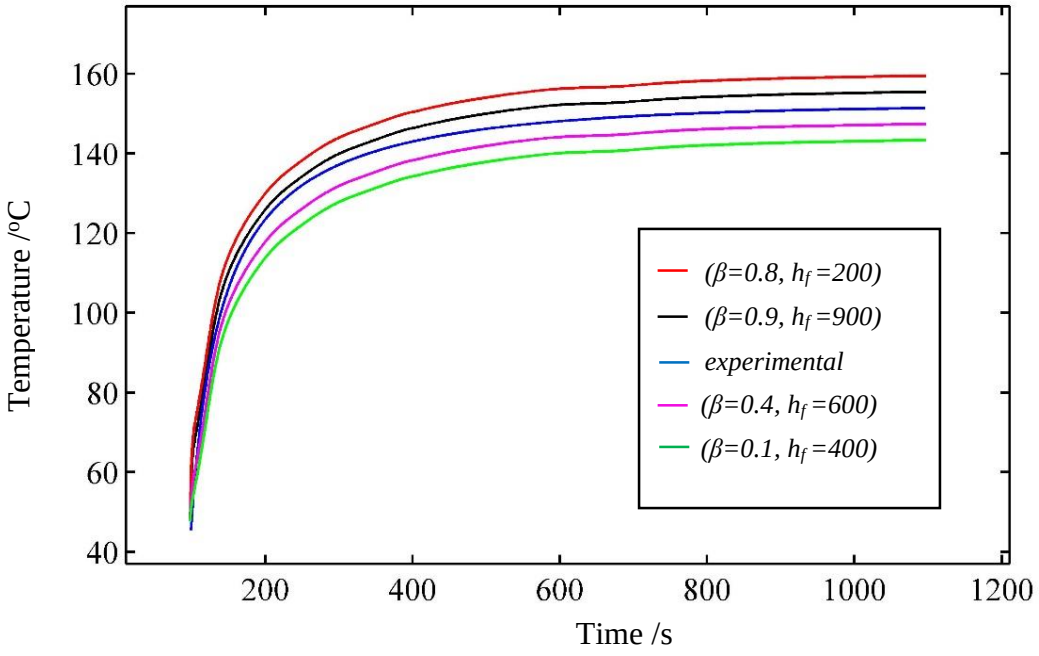

Figure 4.4: The calculated temperature at the position of thermocouple ***a*** for the fast disk for different values of the pair (β, h_f)

In this section the data are simulated over the heating phase only and the error evaluation is carried out over the last 150 seconds of the heating phase which represents approximately the steady state EHL point contact. The error criteria used for optimization is as following:

$$\varepsilon = \frac{1}{n}\sum_{1}^{n}\left(\frac{2\varepsilon_a + \varepsilon_c + \varepsilon_e}{4}\right)$$

Where, ε_a, ε_c, and ε_e are the absolute value of the difference between the calculated and measured temperature at the thermocouple positions ***a***, ***c***, and ***e*** respectively, and *n* is the number of data points over the last 150 seconds of the heating phase. It can be

noticed that thermocouple position ***a*** has double weighting in evaluating the error as it is at the centre of the disk, which is subjected to less measurement distortion when compared with the other sided thermocouples (***c*** and ***e***). The use of double weighting for the central temperatures at thermocouple ***a*** also ensures that this temperature has equal weighting in the error calculation as the two side thermocouples (***c*** and ***e***). Figure 4.5 shows the error contours for the fast disk plotted over the β, h_f parameter space used for error evaluations.

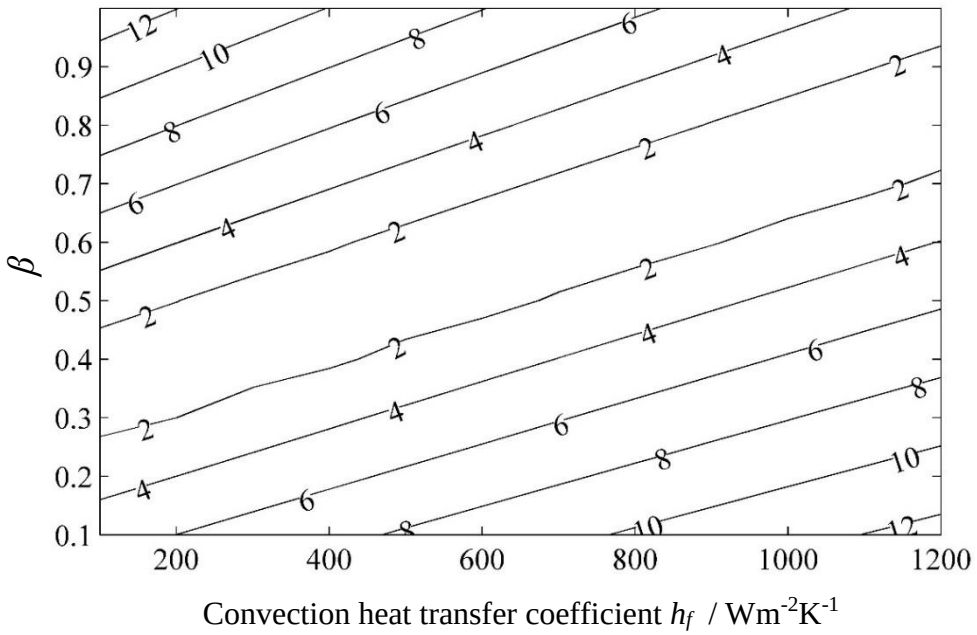

Figure 4.6: The calculated error ε over the last 150 second of the steady state for the fast disk

It can be seen in Figure 4.5 that the contours of error consist of broadly parallel straight lines and the minimum error is enclosed by contours having a narrow range of β and h_f. Similarly, the slow disk error ε is shown in Figure 4.6, which again shows similar features to Figure 4.5, ie, the minimum error occurs along a line that is enclosed by a narrow range of $1\text{-}\beta$ and h_s

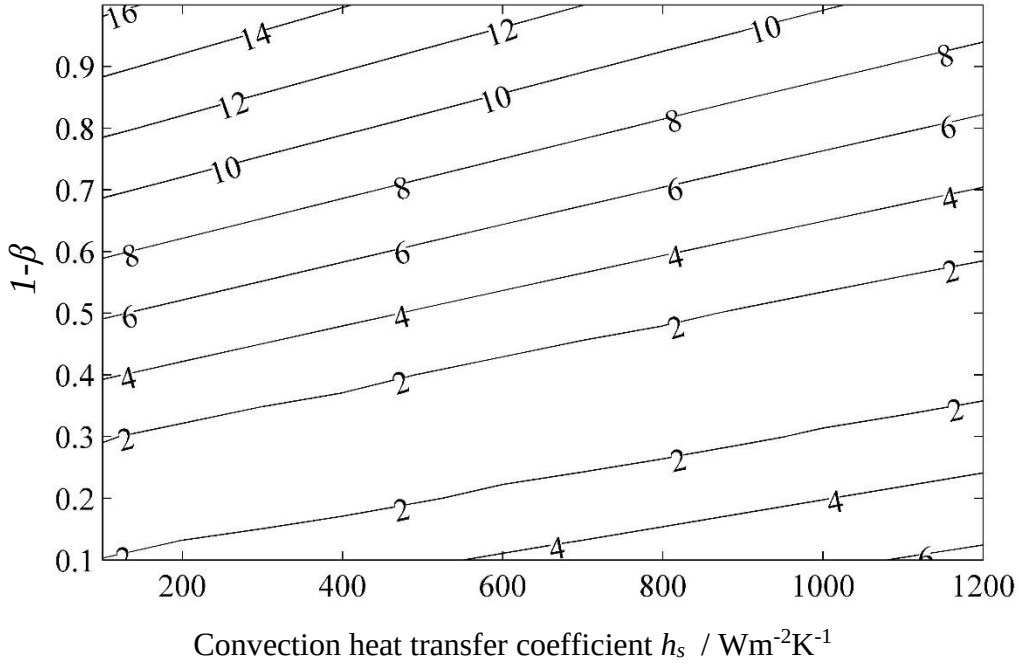

Figure 4.6: The calculated error ε over the last 150 second of the steady state for the slow disk

Both figures shows that the minimum error can be obtained over a range of β values provided that the h values are adjusted accordingly. Figure 4.7 and Figure 4.8 show the error data on the contour map for the fast and slow disks respectively with the error values shown for each β, h combination analysed

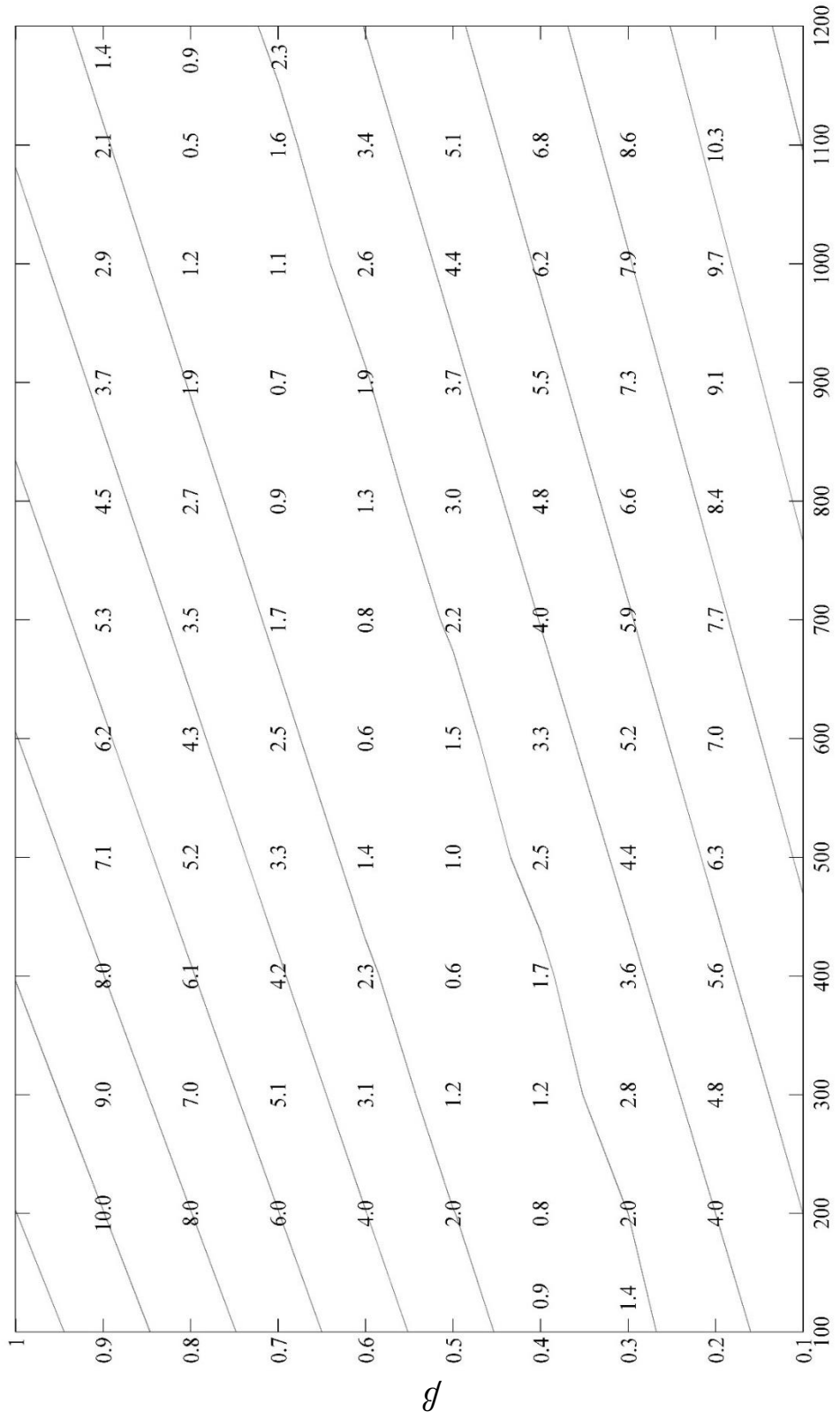

Figure 4.7: The error values ε in addition to the contoures for the fast disk

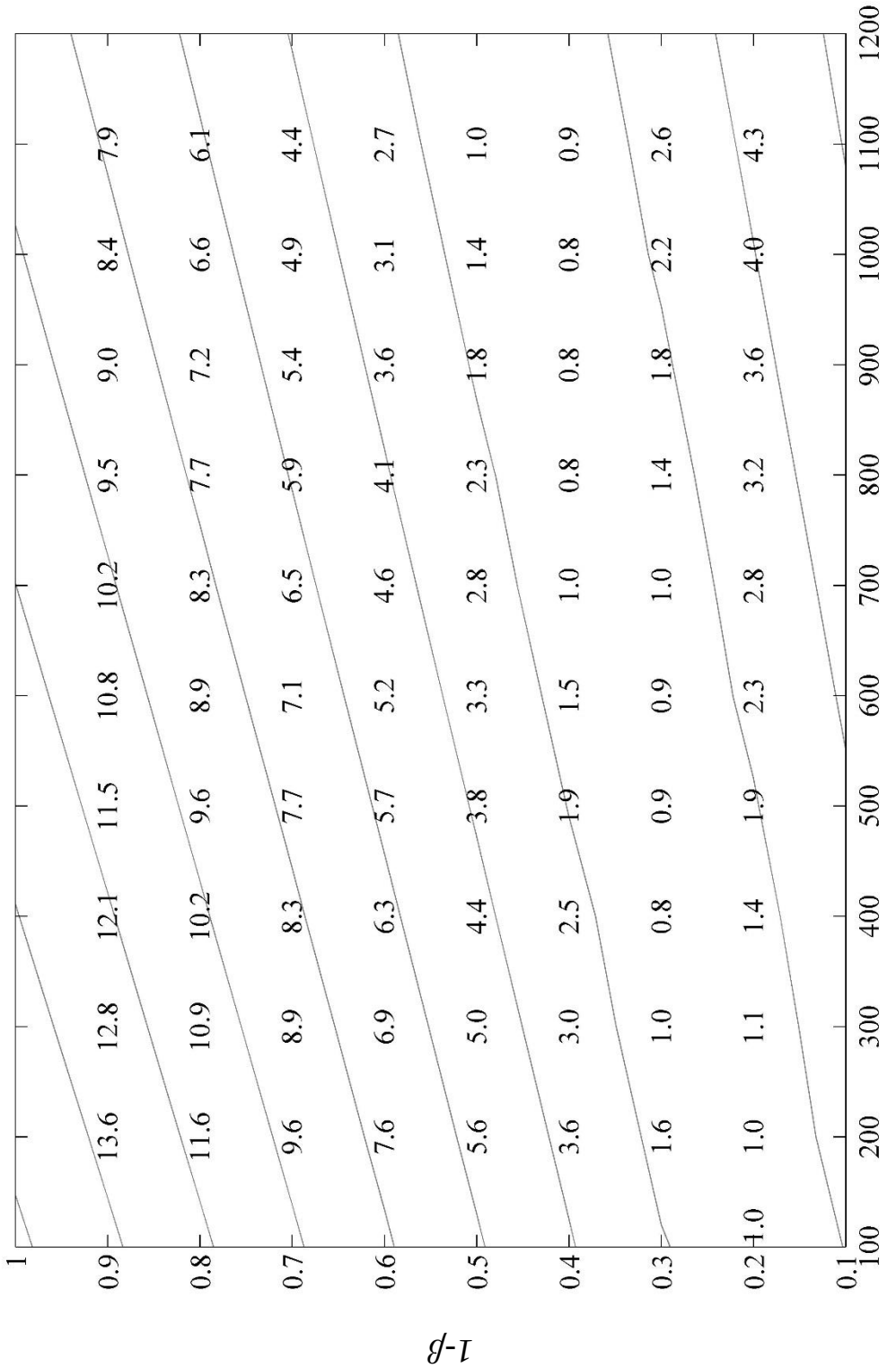

Figure 4.8: The error values ε in addition to the contoures for the slow disk

As can be seen in Figures 4.7 and 4.8, there is no clear position with a local minimum error, rather there is a straight line between the 2°C contours on which the actual β h combination can be expected to occur. It is also un reliable to evaluate the heat partition factor β and the heat transfer coefficient h for both disks based on minimum between the calculated and experimental temperature at the positions of the outer row thermocouples.

The most likely reason behind this uncertainty in finding the minimum error was experimental data uncertainties. Consequently, further investigations were carried out to improve the methodology of finding the minimum error. Fictitious experimental data were generated by solving the thermal model for specific values of β=0.7 and h_f =900 $Wm^{-2}K^{-1}$ to produce a data set from the calculated transient temperatures at the thermocouple positions. This should remove the uncertainties due to experimental error. The new generated data depend to some extent on the lower row thermocouple readings that represent the temperature distribution at the inner radius of the solution zone. Figure 4.9 shows the error map for the fast disk based on the fictitious generated data. As can be seen in Figure 4.9, zero error is achieved at (β=*0.7* and h_f =900 $Wm^{-2}K^{-1}$) which were assumed to be the solution. However, when observing the error values bounded by the 2 °C contours, the results based on the generated data do not provide a regular trend along the contours. The minimum error contours can be seen to form very long inclined ellipses in the β h plane, and although the correct error value of zero is obtained at the β h_f point, the approach is unable to determine the minimum error positions accurately when the data includes experimental error. The long elliptical error contours are a feature of the problem and not caused by uncertainties.

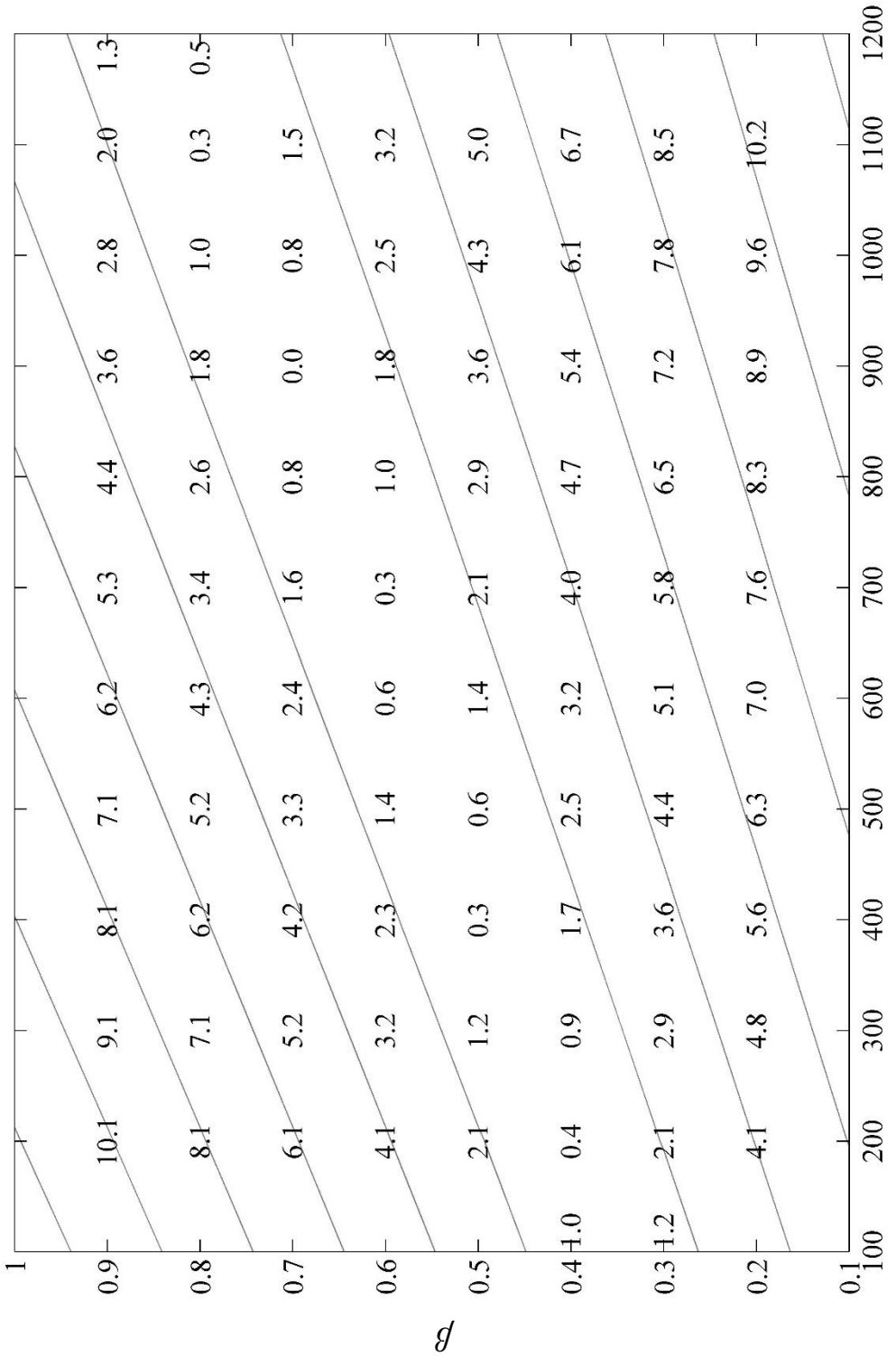

Figure 4.9: The error values ε in addition to the contoures for the fast disk

As a result, the minimum error is established along a line that is parallel to the general contour lines (i.e. the major axis of the long ellipses, which may be slightly curved). This line relates β and h_f for the fast disk and $1\text{-}\beta$ and h_s for the slow disk in a linear relationship and the solution should be a point on each of these lines.

More investigations were carried out to clarify the linear relation between the heat partition factor β and the convection heat transfer coefficient h_f for the fast disk, and the corresponding relation between $1\text{-}\beta$ and h_s for the slow disk. This process was carried out by curve fitting the error along lines of constant β and constant h_f . Figure 4.10 shows an example of fitting error values versus β for constant h_f =800 $Wm^{-2}K^{-1}$. In this figure, it can be seen that the minimum error corresponds with β=0.67 approximately, while the minimum error point corresponds to β=0.7. As a result a computer code was written to find the minimum error according to the fitted function.

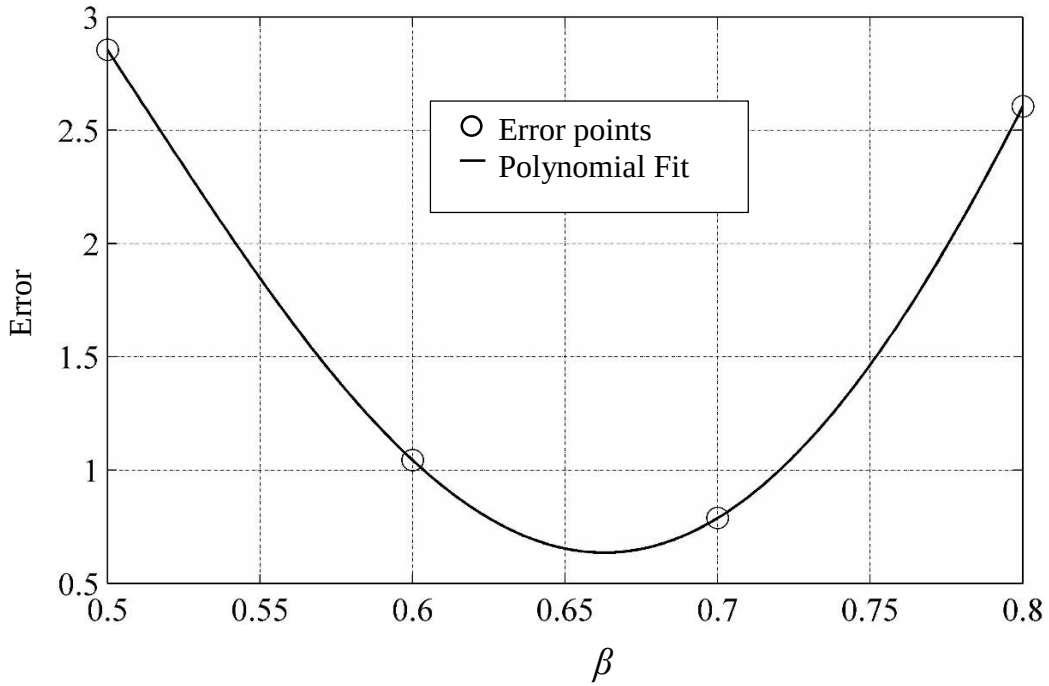

Figure 4.10: Evaluating the minimum error by fitted function for particular value of h_f =800 $Wm^{-2}K^{-1}$

The locus of these minimum errors are plotted on the original error contour as shown in Figure 4.11 for the fast disk and Figure 4.12 for the slow disk. It can be seen in these figures that the points of minimum error closely follow a linear relationship.

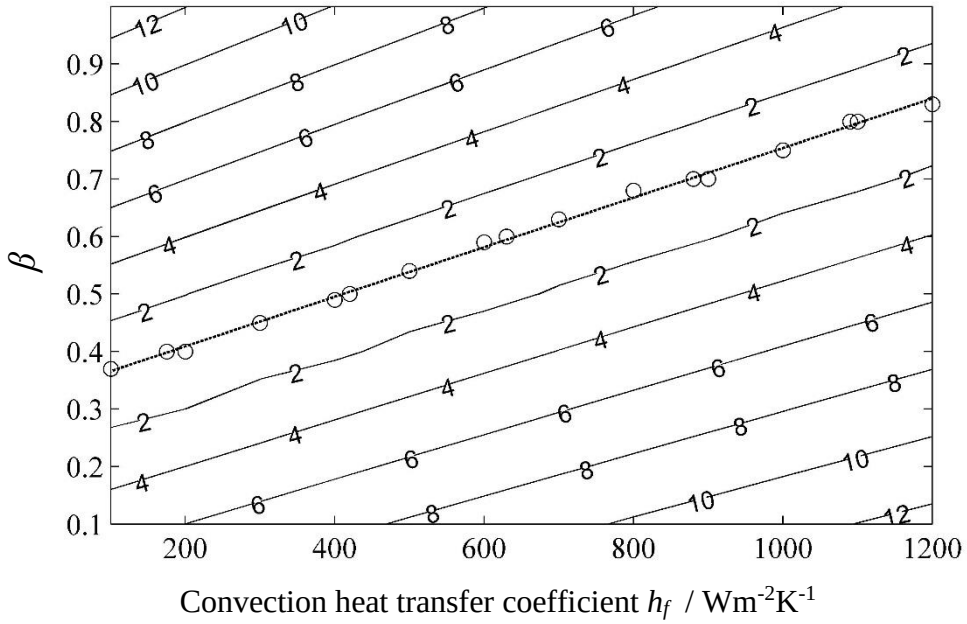

Figure 4.11: Determination the line of minimum error by least square fit for the points of minimum error for the fast disk

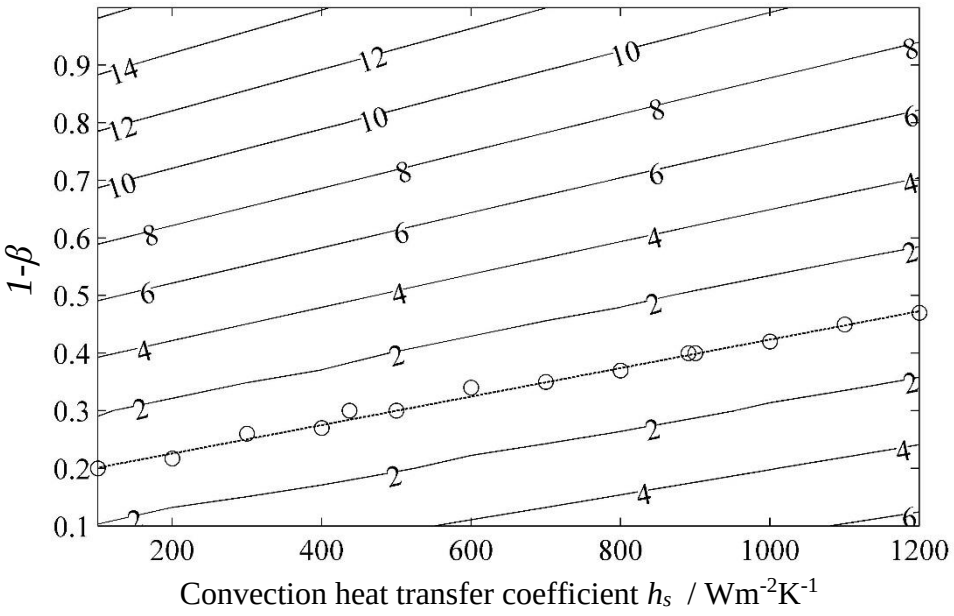

Figure 4.12: Determination the line of minimum error by least square fit for the points of minimum error for the slow disk

In spite of the fact that these lines of minimum errors narrow the solution to this extent, the need for finding a unique solution point on this line remains. The temperature distribution within the disk is governed by the flow of heat into the disk at the contact and the rate of heat removal at the surface. Consequently, the temperature distributions obtained are different at any assumed point on this line. Figures 4.13 and 4.14 show the calculated temperature distributions using values of β and h_f at the extremes of the line of minimum error in Figure 4.11; Figure 4.13 for $\beta = 0.37$, h_f=100 $Wm^{-2}K^{-1}$ and Figure 4.14 for $\beta = 0.83$, h_f=1200 $Wm^{-2}K^{-1}$.

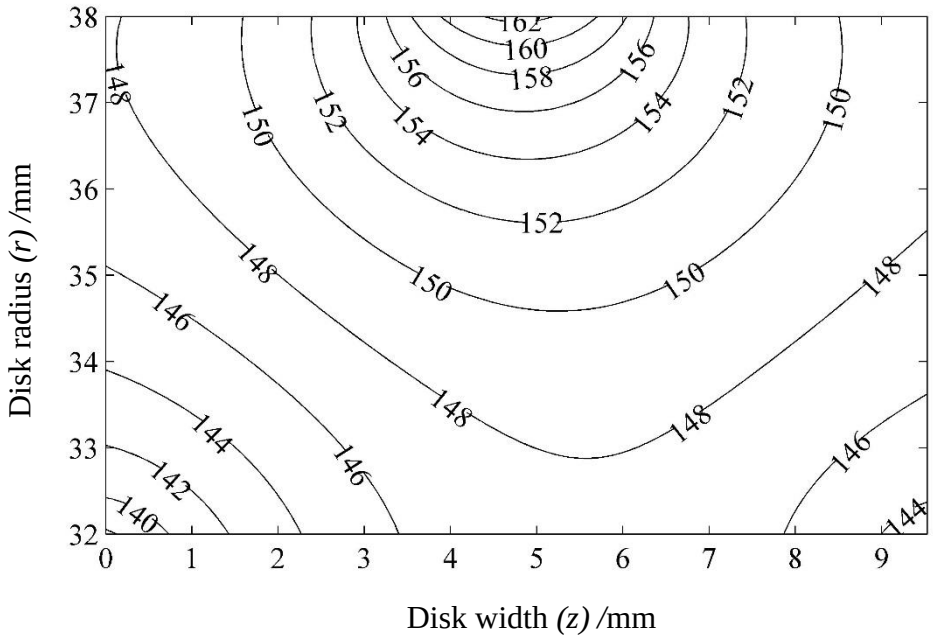

Figure 4.13: The two dimensional temperature distribution (in ^oC) within the fast disk at the end of the steady state based on $\beta = 0.37$, $h_f = 100$ / $Wm^{-2}K^{-1}$

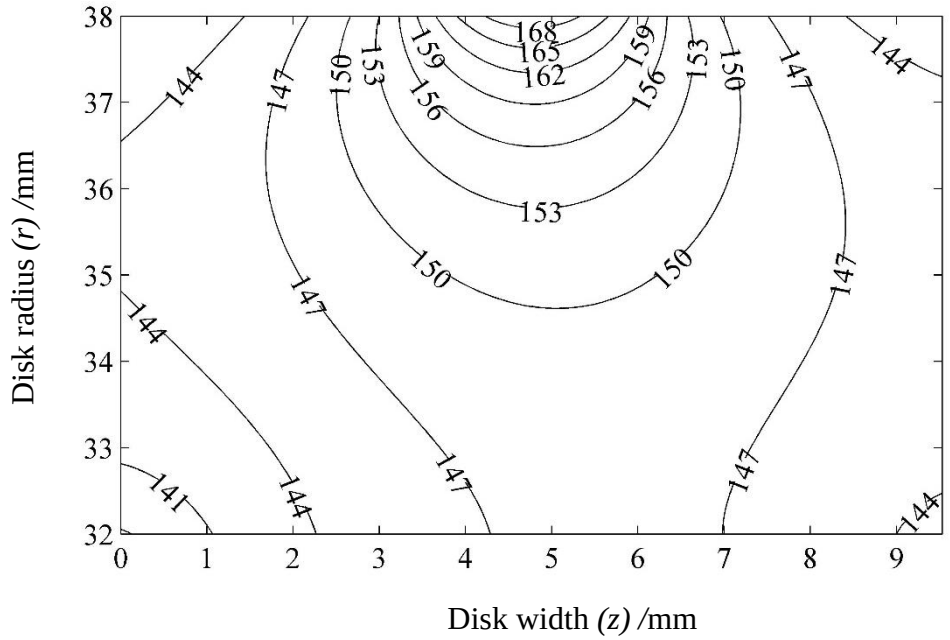

Figure 4.14: The two dimensional temperature distribution (in ^{o}C) within the fast disk at the end of the steady state based on $\beta = 0.83$, $h_f = 1200$ / $Wm^{-2}K^{-1}$

These evaluations at the extremes of the line of minimum error show that the temperature distribution near the heated surface is sensitive to the β , h_f values selected. In Figure 4.13 the temperature near the contact zone is 162^{o}C while it is 168^{o}C at the same place for the values of β , h_f used for Figure 4.14. This phenomenon is due to the fact that the error is minimised at the 35 mm radius and the temperature at the inner radius is the same. Hence the temperature distribution bounded by the region ($32 \leq r \leq 35$) mm is the same along the line of minimum error while the outer region is not. This also means that the additional part of the heat conducted to the disk for the high temperature case also leaves the disk surface by convection in the model before reaching the thermocouples.

As with the fast disk, the slow disk evaluation at the extremes of the line of minimum error presents two different temperature distributions which have a temperature difference of approximately 4^{o}C near the contact zone below the surface while the temperature distribution bounded by the region ($32 \leq r \leq 35$) mm are the same. This is

shown in Figures 4.15 and 4.16 which are the results for $1-\beta = 0.2$, hs=100 $Wm^{-2}K^{-1}$ and $1-\beta = 0.48$, hs=1200 $Wm^{-2}K^{-1}$ respectively.

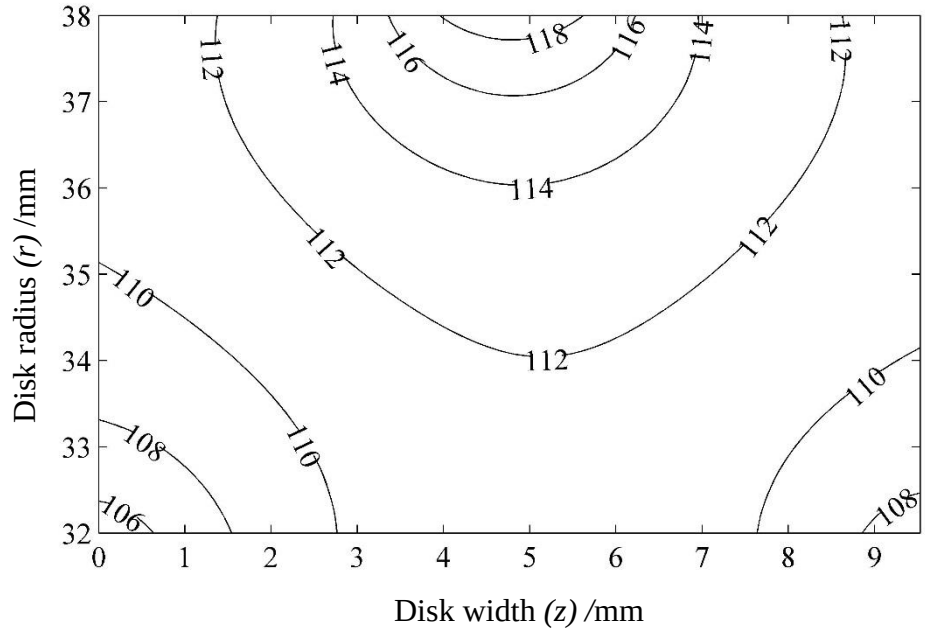

Figure 4.15: The two dimensional temperature distribution (in ^oC) within the slow disk at the end of the steady state based on $1-\beta = 0.2$, $h_s = 100$ / $Wm^{-2}K^{-1}$

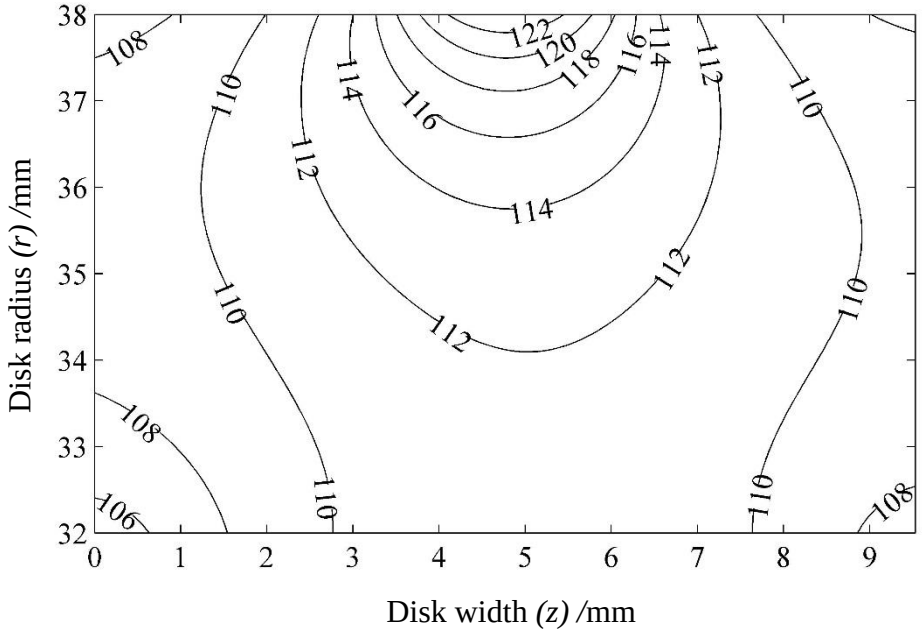

Figure 4.16: The two dimensional temperature distribution(in ^oC) within the slow disk at the end of the steady state based on $1-\beta = 0.48$, $h_s = 1200$ / $Wm^{-2}K^{-1}$

Now when considering Figures 4.11 and 4.12, it is apparent that the (β, h_f) parameters for the fast disk and (1-β, h_s) parameters for the slow disk are clearly related in a linear manner that correspond to the lowest values of ε in the analysis. These can be expressed as

$$\beta = A + Bh_f \tag{4.1}$$

$$1 - \beta = C + Dh_s \tag{4.2}$$

Accordingly, it is possible to identify the value of β by introducing the relationship that can be expected to exist between h_f and h_s. for the fast and the slow disk respectively

Several studies have been carried out to evaluate the heat transfer from horizontal rotating cylinder as it is one of the important heat transfer engineering problems. Anderson and Saunders (1953), Dropkin and Carmi (1957), Cardone et al. (1997), and Özerdem (2000) carried out experimental programmes to study convection heat transfer from horizontal cylinders rotating in quiescent air. From all of those experimental studies, the following relation was evaluated:

$$Nu = E(Re)^n \tag{4.3}$$

Where

Nu is the Nusselt number $= \frac{hd}{K}$

Re is the Reynolds number $= \frac{\rho v d}{\mu}$

E is a constant

n is the power of *Re*

h is the convective heat transfer coefficient

K is the thermal conductivity of the fluid

ρ is the fluid density

v is the effective velocity

d is the disk diameter

μ is the dynamic viscosity of the fluid

Equation 4.3 can be written for both fast and slow disks:

$$h_f = E\frac{k}{d}\left(\frac{\rho d}{\mu}\right)^n (u_f)^n \tag{4.4}$$

$$h_s = E\frac{k}{d}\left(\frac{\rho d}{\mu}\right)^n (u_s)^n \tag{4.5}$$

Taking the ratio of these two equations gives

$$h_f/h_s = \left(u_f/u_s\right)^n = \chi \tag{4.6}$$

Solving equations (4.1) and (4.2) using equation (4.6) gives an expression for β

$$\beta = \frac{\chi\, BC - AD}{\chi B - D} \tag{4.7}$$

Values of power *n* obtained in the literature vary between 0.571 (Özerdem 2000) and 0.8 (Cardone et al. 1997) and the generally accepted value is 0.667 (Dropkin and Carmi 1957), which is the value used for the current calculations. The coefficients A to D in equation (4.7) are obtained from the linear relationship of the line of minimum

error for both the fast and the slow disk, and the speed ratio for the experiment is 4.24. Using these values gives χ=2.62 and β=0.73.

The sensitivity of the results for β to the power n used in this method of solution were tested for the range reported in the literature. The sensitivity of β for the range of n values is shown in Figure 4.17, it can be seen that the effect of n values in this range is very limited.

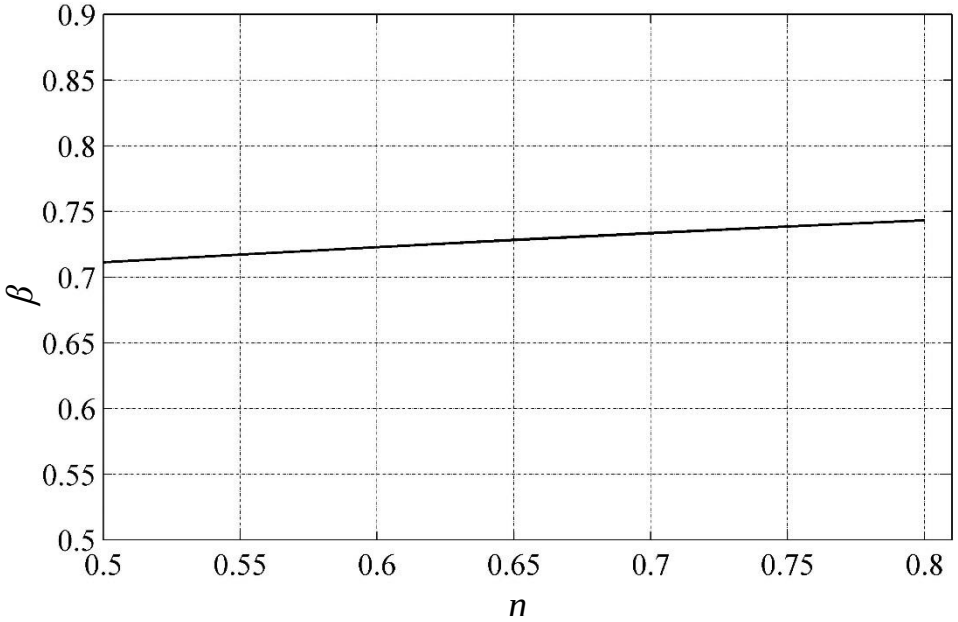

Figure 4.17 The sensitivity of β over the probable range of the power parameter n in equation (4.7)

4.4. Error minimization at transient state

In this section, the numerical analysis of the model is applied over the cooling phase for the period immediately following the unloading the disks to evaluate the convection heat transfer coefficient. When this coefficient is determined, the heat partition factor β can determined according to the linear relationships obtained in the previous section. This approach would allow each disk to be analysed individually to

obtain the value of β. Comparison of the values obtained for the two disks would provide a check of the accuracy of the evaluation.

As described previously, the disks are loaded and heated via the dissipated heat within the EHL point contact. The load was maintained for sufficient time to allow approximately steady state temperatures to be achieved. In section 4.3, the error optimization was carried out over the last 150 seconds of the heating phase which is approximately at steady state. The reason behind concentrating on this zone is to ensure minimum change in the problem conditions and parameters, i.e. the heat partition factor and the convection heat transfer coefficient. In addition the analysis of the experimental EHL tests were planned to be linked to a steady state thermal numerical EHL point contact model, available within the research group. In this section, the cooling phase analysis was focused on the time immediately following unloading of the disks so that the temperatures were not significantly altered and the heat transfer coefficient remained unchanged.

A key aspect of the cooling phase solution is that no heat partition factor β is involved in the error optimization which is different from the steady state optimization solution. Accordingly, the convection heat transfer coefficient is the only variable that should be varied to obtain minimum error in the comparison with the outer row thermocouple measurements. However, the limitations in this analysis is its reliance on the initial temperature distribution that itself depends on β and h which are not defined. Nevertheless, the steady state solution has shown that the β and h values lie on a straight line of minimum error, the values of the pair of β and h on that line determine the temperature distribution at the end of the steady state which will be the initial conditions of the cooling phase. Figure 4.18 shows the temperature versus time at the position of thermocouple ***a*** for three (β, h_f) pairs located at the beginning, middle,

and the end of the minimum error line of Figure 4.11. Note that the surface temperature calculated for each of these cases is different but that the each minimum the error between model and experiment at thermocouple ***a.*** The figure shows that the value of β, h_f pair govern the cooling temperature trace clearly while they are almost identical in the steady state interval (note that a small shift of less than 1 ^{o}C is applied to superimpose them at the steady state interval for clear comparison on the cooling phase). This is because the line of minimum error has small but finite error.

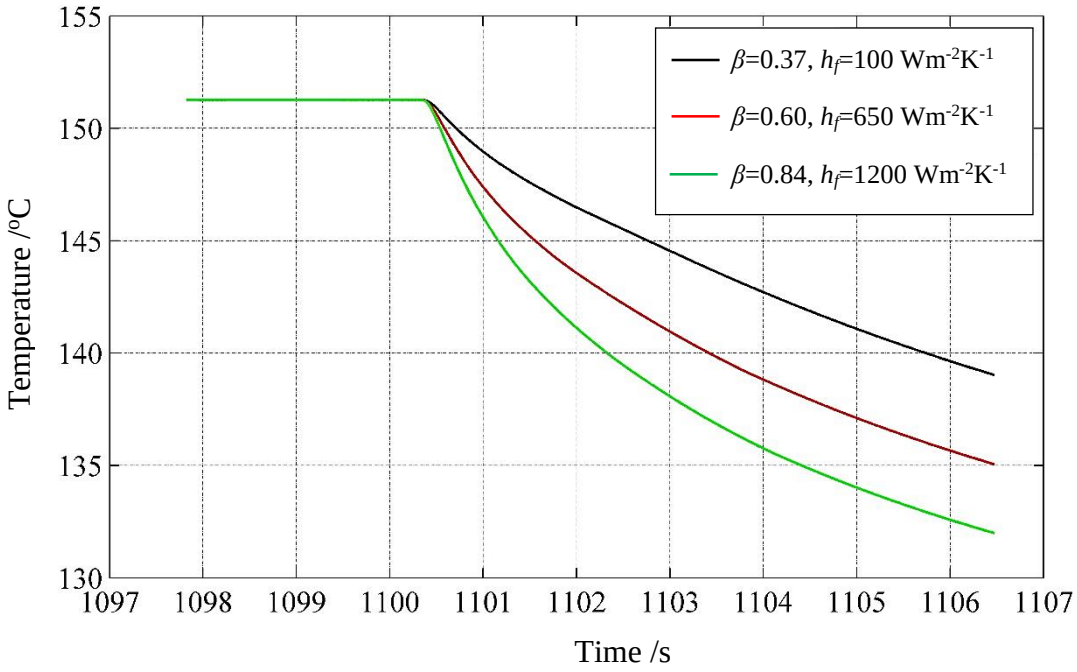

Figure 4.18: The effect of the value of β chosen from the line of minimum error, it shows the effect over the end of the heating (approximatlysteady state) and the starting of the cooling phase.

Now, these different calculated temperature traces based on different values of pairs of β, h_f , are matched with the experimentally measured temperatures. This is shown in Figure 4.19 (a). It can be seen in this figure that none of these calculated temperature traces can match the trend of the experimental data. The main incompatibility in the trend is that the calculated temperature drops sharply at the start of the cooling phase

when compared with the experimental measurements which have a delayed response. Figure 4.19 (b) shows the slope of these curves which clearly displays the inconsistency between the theoretical and the experimental data.

The start of the cooling stage in this analysis is indicated by the load cell when it shows a very rapid load drop. At the time of load drop, the friction force used for representing the generated heat is set to zero in the model to start the cooling stage calculations. The load cell signal is more clear cut in indicating the time at which the load is removed as the friction measurement is subjected to a higher level of electrical noise. The filtered friction force is used for the analysis is shown in Figure 4.19 (c)

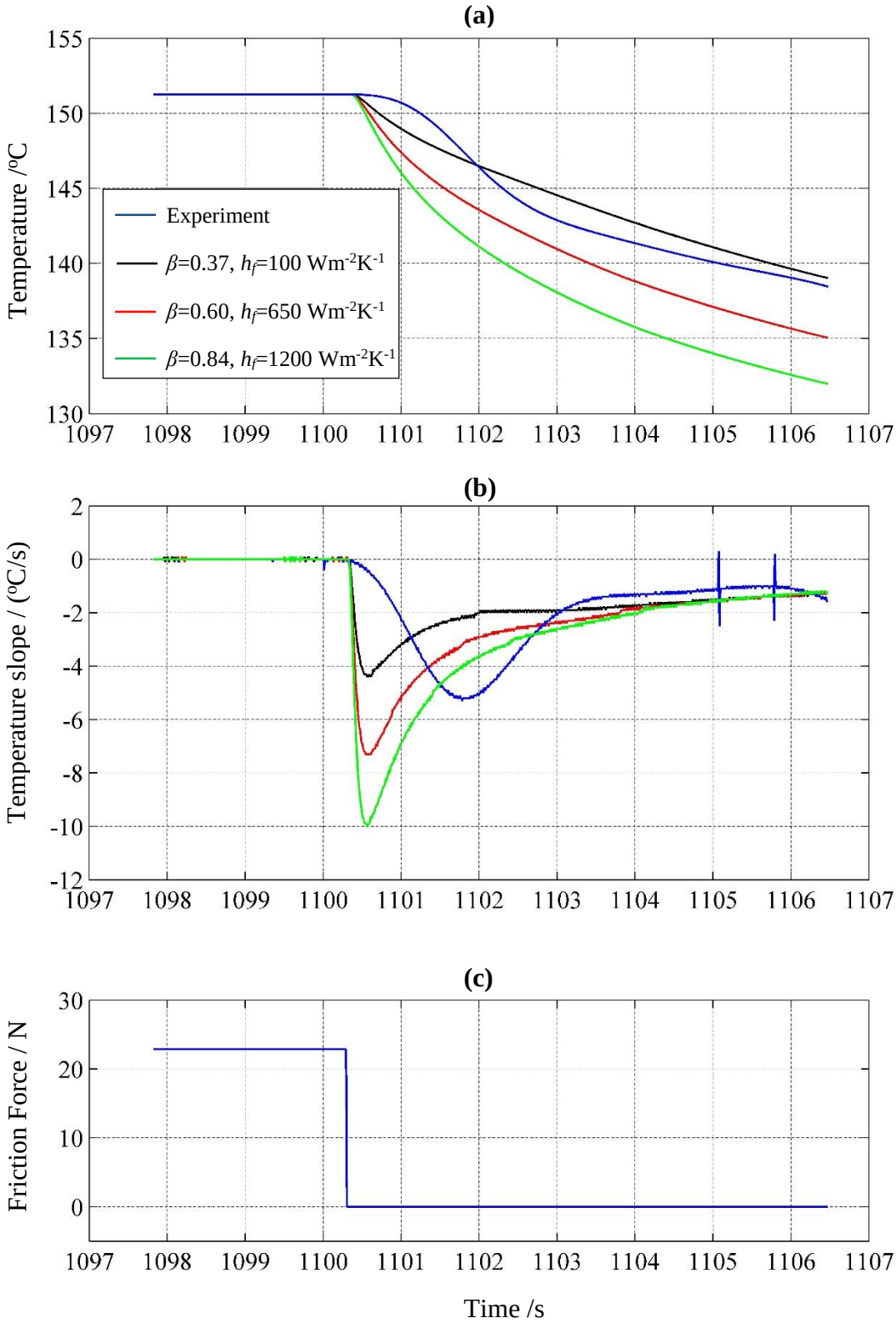

Figure 4.19: (a) The temperature for different values of β along the line of minimum error as compared with the experimental data in ***a***, **(b)** the slopes of the temperature in ***a***, **(c)** the friction force used in the model.

The trend inconsistency that appears in Figure 4.19 was investigated firstly in terms of unloading mechanism. As described previously in section 2.7, the loading mechanism consists of a hydraulic ram that pushes the load only in the direction of the loading. The unloading process occurred when releasing a manual valve in the hydraulic network fixed on the control cabinet. As a result, this type of mechanism does not allow for the disks to separate quickly when unloading takes place, so that, the separation between the disks may not increase as rapidly as the indicated pressure drop, resulting in a gradual decrease in the thermal interaction between the disks. This may lead to a more gradual decrease in the measured temperature as compared with the theoretical analysis. To eliminate this possible reason for the inconsistency of results, design changes for improving the unloading mechanism were carried out and is described in section 5.2.

Before the un-loading mechanism improvement was implemented, a numerical investigation was carried out by replacing the step drop in the friction force by a ramped friction force, to examine the effect on the temperature response at the beginning of the cooling phase. Figure 4.20 shows the results obtained when the friction force is reduced linearly from its steady state value to zero over 1.5 s time. In part a of this figure, the temperature trends are very consistent especially over the time 1100.7 to 1102.5 s. In part (b), the slopes also shown good consistency. These results make improving the unloading mechanism a possible step in improving the cooling phase calculation and including it in the overall analysis.

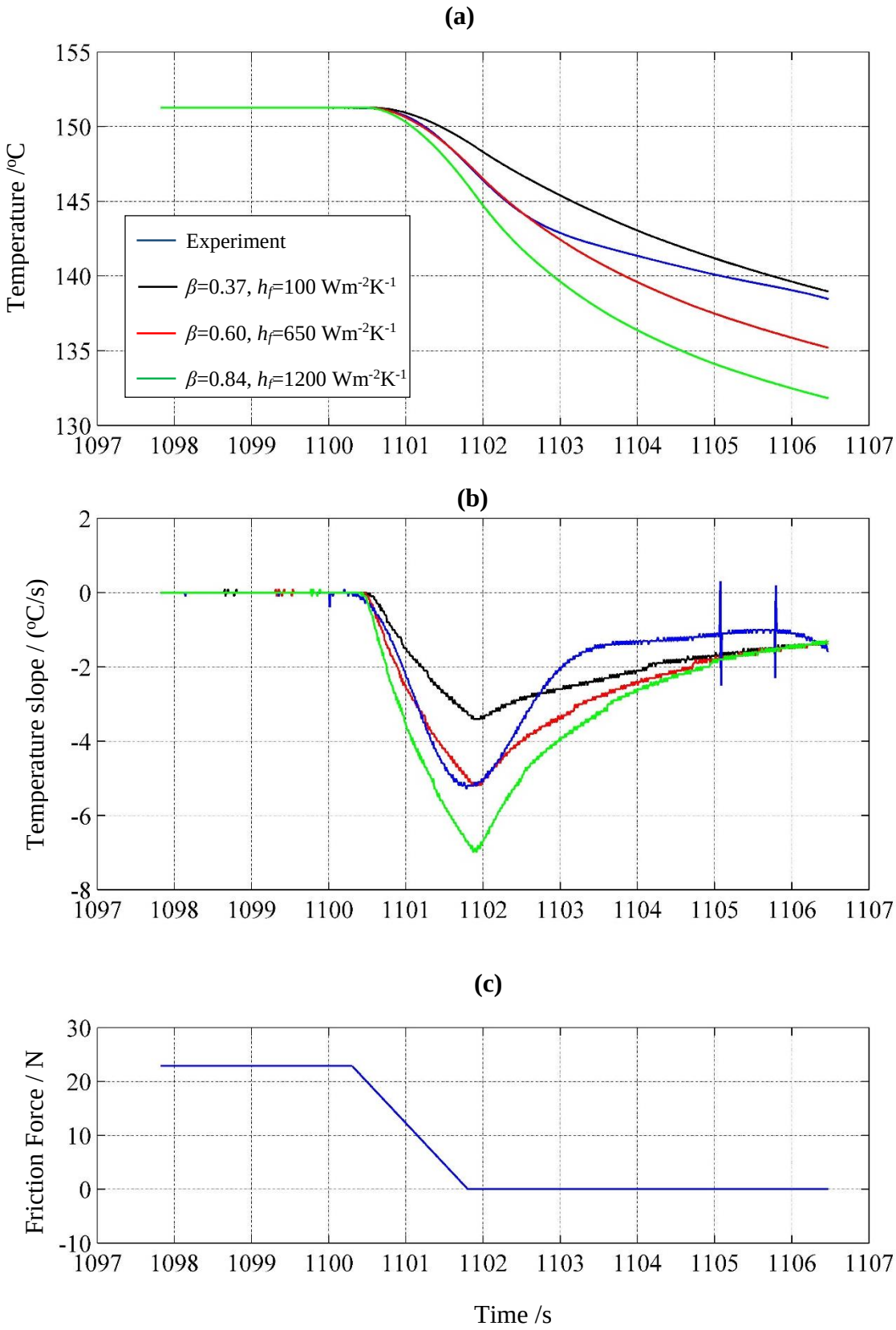

Figure 4.20: (a) The temperature using ramped friction force for different values of β along the line of minimum error as compared with the experimental data in ***a***, **(b)** the slopes of the temperature in ***a***, **(c)** The assumed friction force used in the model.

To sum up, two techniques were discussed in this chapter for obtaining the heat partition in the experimental EHL tests. The first technique is based on error minimization at the steady state conditions. The second is based on the error optimization over the transient state just after unloading of the disks. These methods have initiated needs for developing the test rig, and this will be discussed in the next chapter.

Chapter 5:
Test Rig Development

5.1. Introduction

This chapter reports the developments that were carried out on the test rig. These developments were generally introduced according to difficulties, which were raised during the establishment of the EHL test modelling methodology. The unloading mechanism development, the disk separation monitoring, and thermocouple installation and dynamic response are reported in this chapter. It also covers the redesigning of the thermocouple arrangements within the disks in addition to involving new hardware for further temperature measurements in the test rig.

5.2. Improvement of the unloading mechanism

In this section, the loading mechanism is investigated and improved in order to ensure rapid disk separation in the unloading process. The reason behind this aim is that the numerical simulation of the experiments is established based on instantaneous disk separation at the time of unloading. The effect of gradual separation of the disk was examined in section 4.4, where it was concluded that more gradual disk separation might be one of the causes of the temperature incompatibility trend as compared with the numerical model. Furthermore, it was established from the results of repeat experiments reported by Voller (2010) that pulling the yoke which supports the slow shaft bearings during unloading to force disk separation made the results of the temperature measurement more consistent. Ideally, when the disks are isolated the

heat generated in the contact zone becomes zero instantaneously, and the disk separation is sufficient to ensure that no heat is transferred between the disks within that zone.

In order to make the unloading process as rapid as possible, an investigation was carried out on the hydraulic loading arm during loading and unloading. The hydraulic system used in the rig is uni-directional which provides pressure in the direction of loading only. Hence, it is necessary to provide an opposite force to retract the mechanism as quickly as possible.

A simple experiment was carried out by hanging weights on a temporary rod fixed through the end of the loading arm as shown in Figure 5.1. This configuration represents a pre-load opposing the hydraulic pressure effect. The experiments establish that including a pre-load in this way leads to a rapid retraction of the mechanism, and is much more consistent and effective than pulling the push rod back manually using the method implemented in the previous tests.

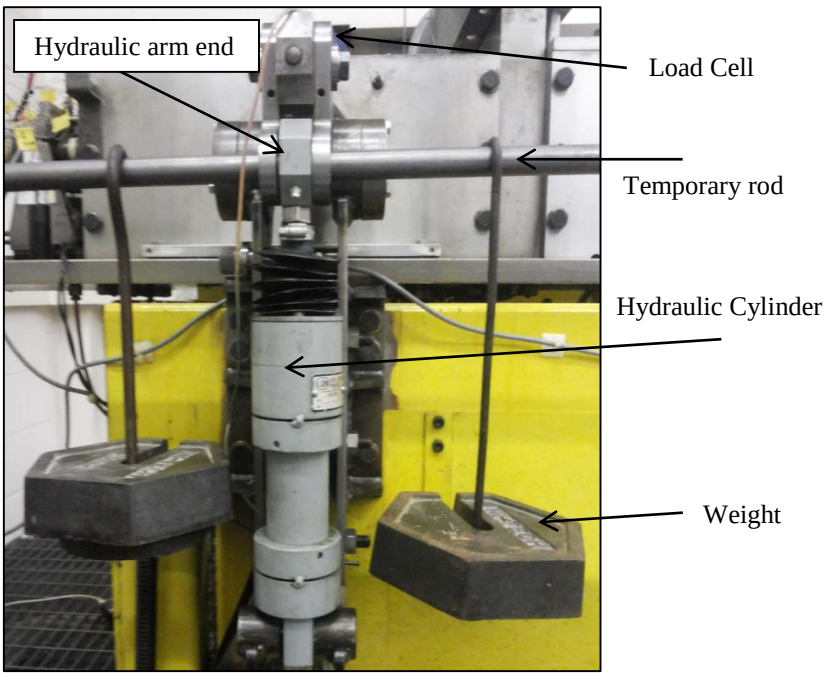

Figure 5.1:A photograph of the simple experiment for the investigation of applying a pre-load force to the hydraulic ram to move it in reverse direction during un-loading.

It was determined that a total pre-load force of about 200 N was sufficient to achieve a rapid retraction of the mechanism. Since the load applied to the contact is measured by a load cell fitted to the crank-bell mechanism which shown in Figure 5.1, the pre-load overcome by the hydraulic force does not influence the load in the experiment.

Weights were used to determine the effective level of pre-load required, and subsequently two springs with suitable brackets were designed to provide the force for the cylinder. This arrangement was chosen for two reasons. Firstly the arrangement is more compact and does not require a large space around the cylinder for the weights. Secondly, the spring force becomes zero when they return to their original length which means that the loading arm is not subject to the pre-load when the cylinder is retracted. This was seen to be a much more attractive option than using weights. The springs and their brackets are shown in Figure 5.2.

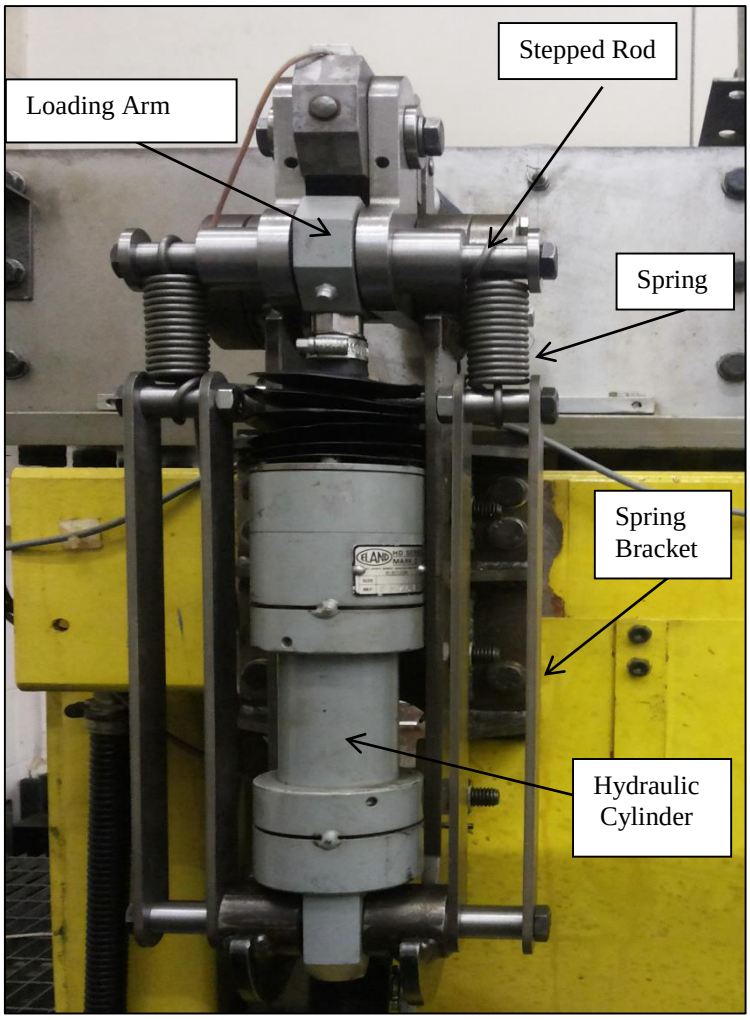

Figure 5.2: The hydraulic cylinder with springs for reversing the motion during unloading

During the experimentation used to determine the optimal pre-load, a further significant issue was noticed in the unloading process. This was the time lag in removing the hydraulic load due to the location of the unloading valve which was built in to the control cabinet of the rig. Hydraulic connection from this dump valve to the rig was through long small diameter steel pipes and flexible hoses. The need for the hydraulic fluid to flow along this path to allow the ram to retract caused a significant delay in cylinder retraction. To solve this problem, a new dump valve was fixed near to the cylinder feed positions shown in Figure 5.3. The new valve provides a flow path

directly to the oil tank by a short hose and it is used for loading and unloading while the original valve on the control cabinet is left in the loading position permanently.

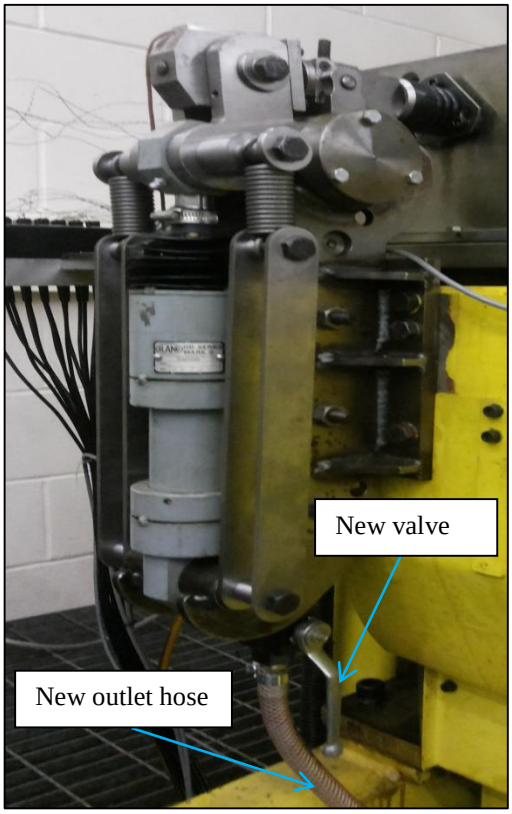

Figure 5.3: The new valve and the outlet hose which exhaust the oil directly to the oil tank

A schematic diagram of the hydraulic loading circuit in the test rig is shown in Figure 5.4 including the new modification.

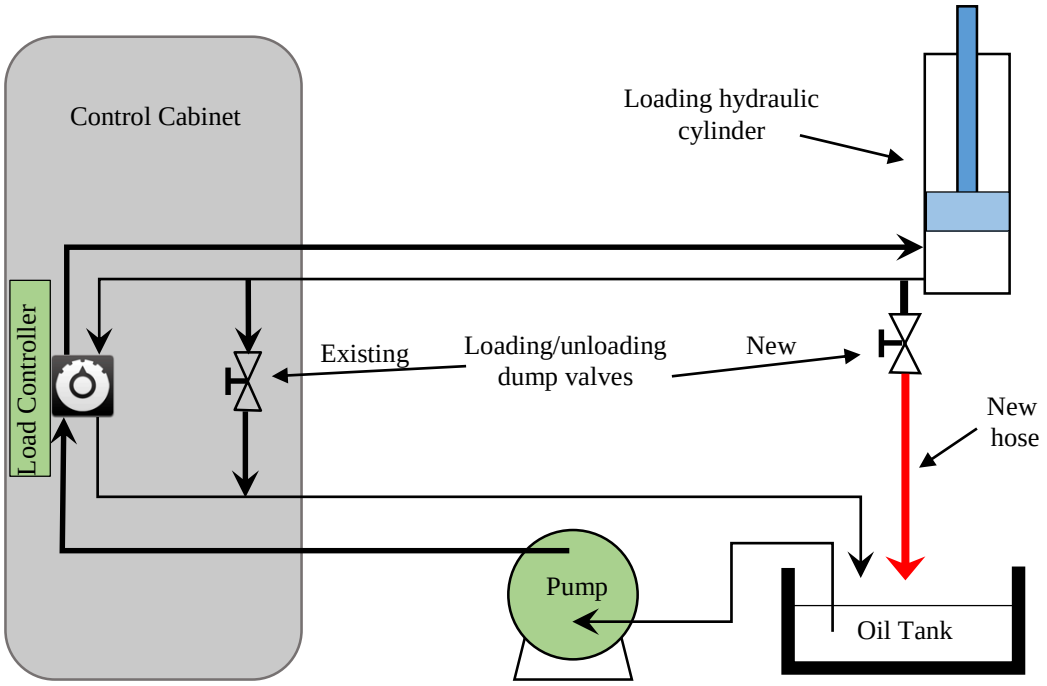

Figure 5.4: schematic diagram of the hydraulic loading network

5.3. Disk contact-separation monitoring

In the numerical model of the experiments it is essential that the time of applying and removing the load is determined accurately, especially when modelling the starting of the cooling phase described in section 4.4. Previously, this time was indicated by changes in the load cell signal which measures the load applied to the disks. When the load is applied or removed, a rapid change in the load cell reading is observed and the time of this rapid change is used in the model. Figure 5.5 (a) shows the temperature measured by thermocouple ***a***, Figure 5.5 (b) shows the load which measured by the load cell and Figure 5.5 (c) shows the projection of the load on the temperature in the large scale detail inset on the figure. At the beginning of the loading phase, a rapid

change in the load occurs and the temperature is seen to rise from that time. Consequently, at the beginning of the un-loading phase both the load and the temperature drop with a time lag in the temperature change as shown Figure 5.5 (c).

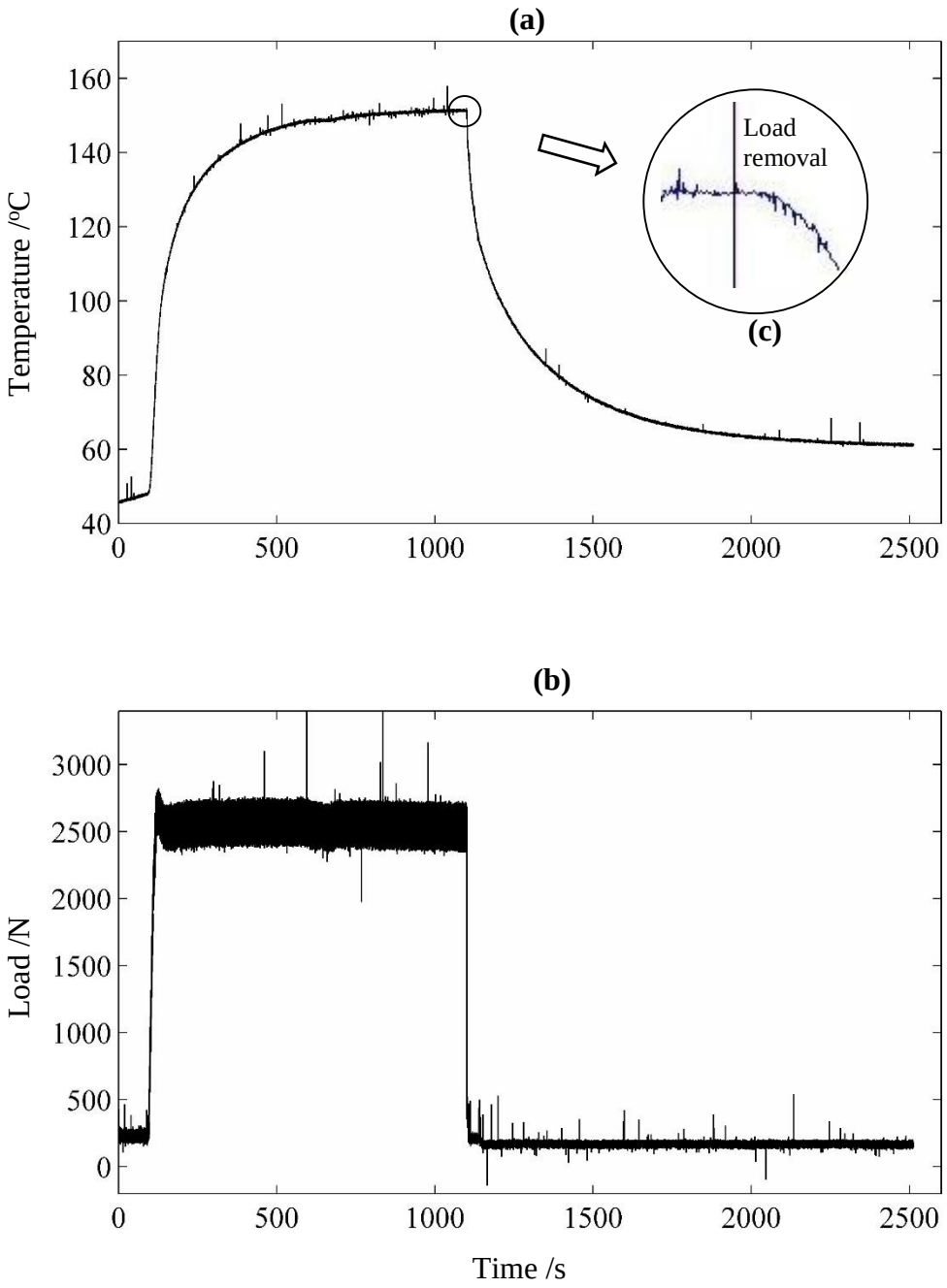

Figure 5.5: Show the importance of unloading monitoring. **(a)** Thermocouple ***a*** temperature, **(b)** load, **(c)** large scale detail of the of load removal point and on temperature.

During the numerical analysis of the unloading phase (section 4.4), it was found that the load cell readings cannot be considered definitive in this regard. The load cell identifies the time at which the hydraulic pressure is removed but not necessarily the time over which the loading mechanism retracts and the disk contact is removed.

With the aim of determining the accurate time of contact of the disks and subsequent contact removal, a microswitch was used to indicate the motion of the yoke which supports the slow disk bearings. The microswitch was supplied with a roller end which was removed and replaced by a threaded brass block fitted with a small bolt to increase its length to be fitted in the rig and allow its effective length to be finely adjusted. Figure 5.6 shows the microswitch before and after modification.

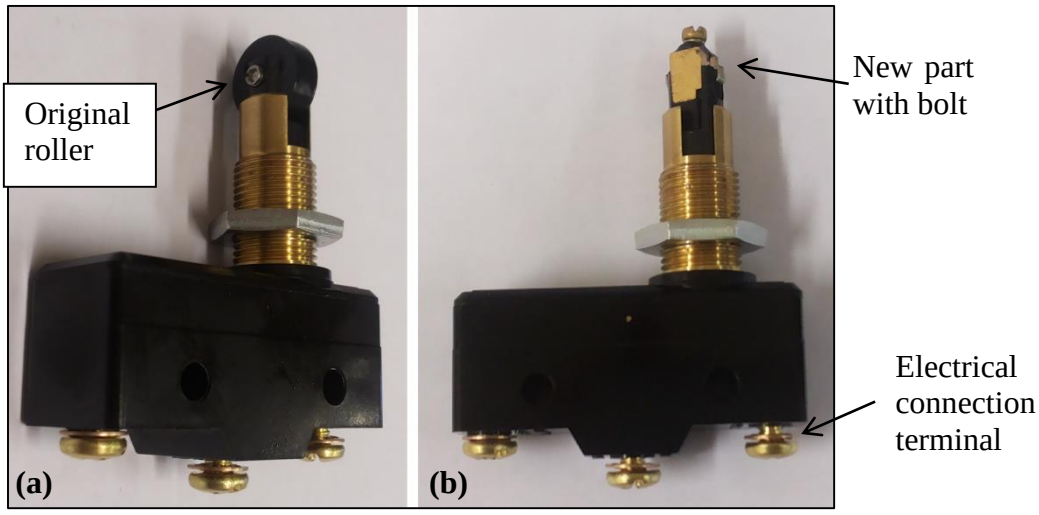

Figure 5.6: Microswitch used for monitoring loading and unloading of the disks, **(a)** before modification, **(b)** after modification

The microswitch is connected electrically to one of the digital channels in the PCI card to log the yoke position together with the other data logged. It was mechanically fixed through a hole in the side of the test head enclosure to touch the yoke as shown in

Figure 5.7. The clearance for indicating the motion was adjusted using a feeler gauge to approximately 0.15 mm.

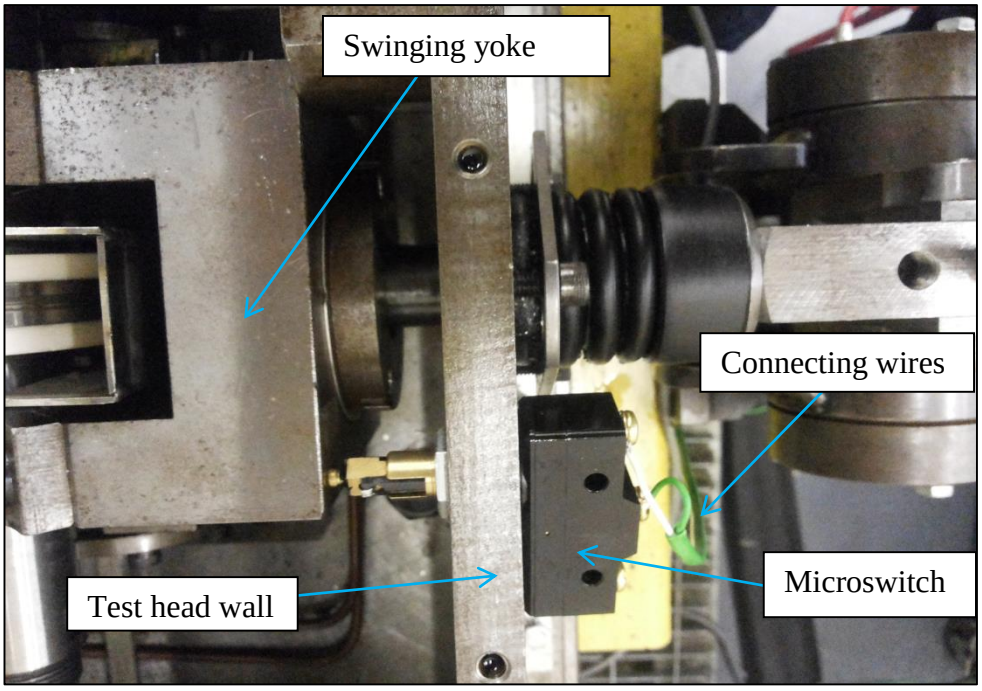

Figure 5.7: Photograph shows the assembled microswitch used to monitor loading and un-loading.

The digital readings of the microswitch is included in the Labview software, it read either 1 which refers to disks in contact and 0 for out of contact. This digital reading is written in the results file which is used later in the simulation for start of each loading and unloading phase. The microswitch reading is also displayed as text and a bulb indicator (red for loading and green for unloading) on the front panel of the LabVIEW software. These indicators give more functionality to the data acquisition system of the test rig, and are important in safety and test disk protection if an unexpected loading or unloading occurs.

After these improvements, the temperatures measured by thermocouple ***a*** are shown in Figures 5.8 and 5.9 for the fast and slow disks respectively, parts (a) and (b) show the measurement before and after the improvements respectively

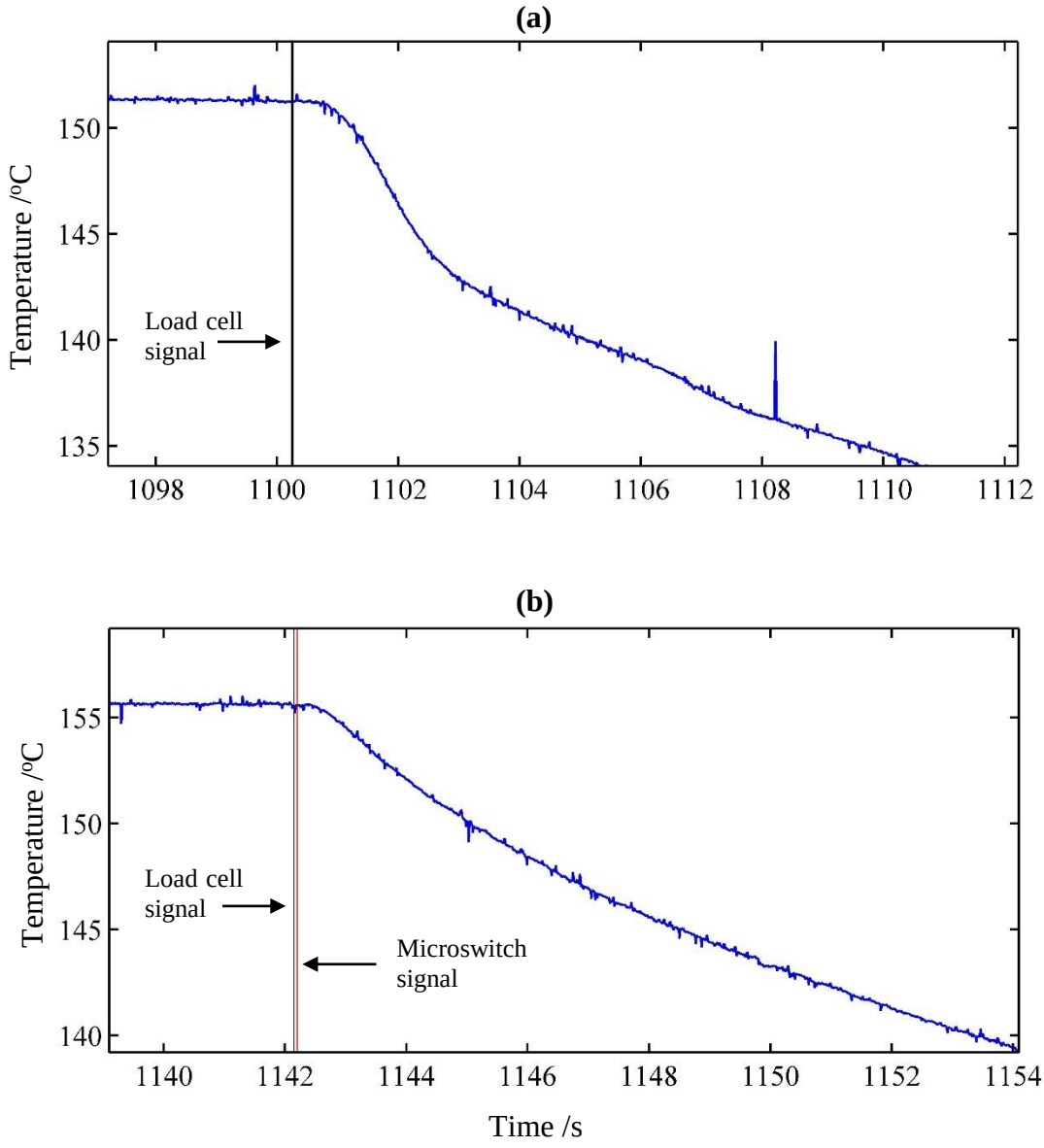

Figure 5.8: The effect of the unloading improvements on the temperature measurements trend for the fast disk, **(a)** before the improvements, **(b)** after the improvements

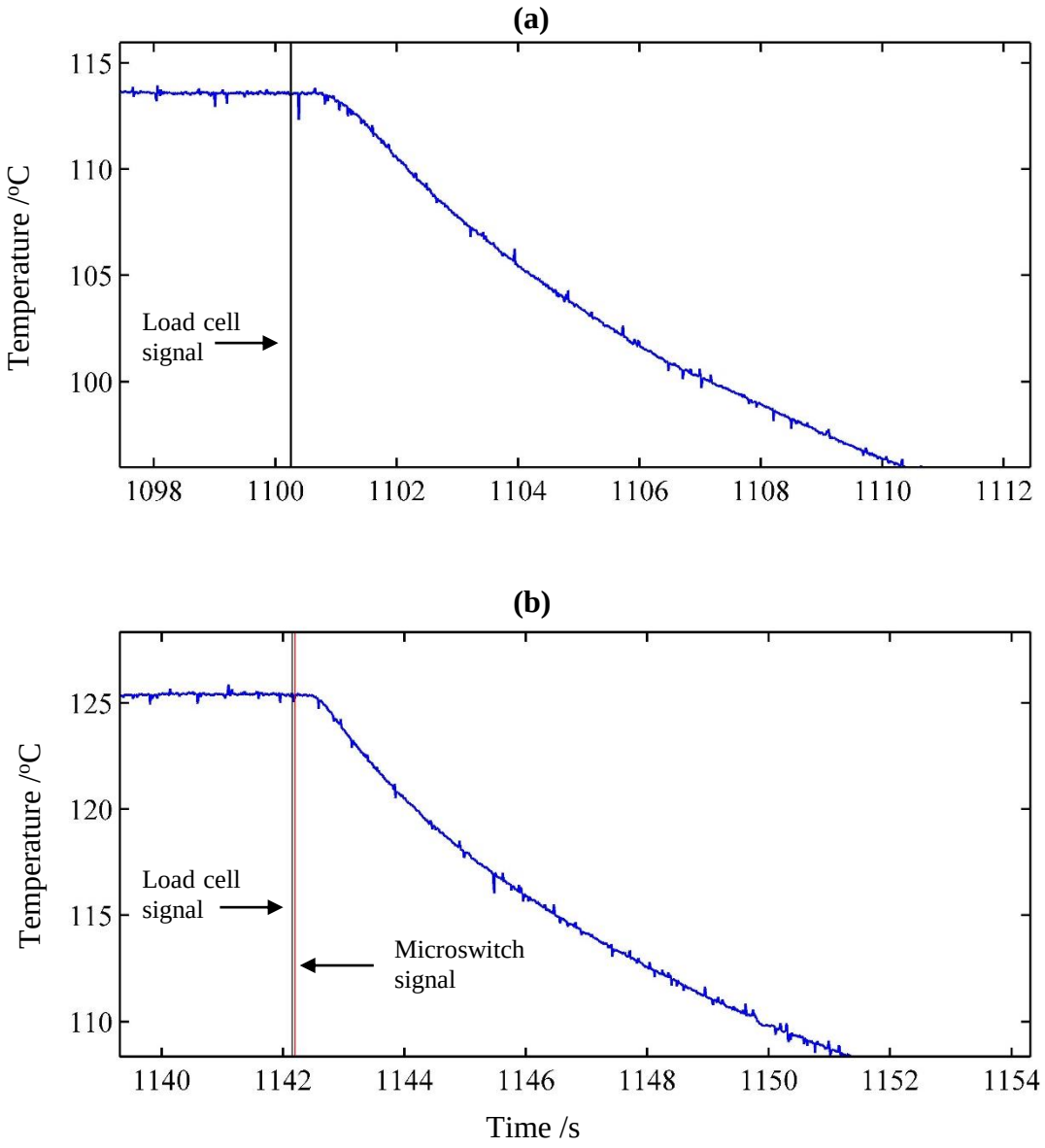

Figure 5.9 The effect of the unloading improvements on the temperature measurements trend for the slow disk, **(a)** before the improvements, **(b)** after the improvements

In part (b) of these figures, an accurate time of disk separation is indicated by the recently installed micrswitch. The signals of the microswitch and the existing load cell show only 0.05 s of time difference in indicating disk separation in parts (b). However, this does not mean that the load signal in parts (a) indicates the disk separations with this sort of precision because the rapid unloading mechanism had not developed at the time that the data for part (a) was obtained. Determining an accurate time of disk

separation is crucial in the cooling phase simulation as it is the starting time of the cooling phase

By comparing the measurements before and after these developments, a shorter time lag in the temperature drop is observed than was the case before the developments. This might be due to the rapid disk separation achieved in addition to the possible effect of the thermocouple installation technique developed which is described in the next section.

Another important observation from comparing part (a) and (b) in Figures 5.8 and 5.9 is that the trend of thermocouple measurement at the beginning of the unloading phase is much improved. It can be seen that the trend before the developments has two distinct cooling phases (which is particularly noticeable in Figure 5.8 (a)), whilst after the developments, it follows a more continuous smooth trend. A possible explanation for this achievement might be that previously, the disks were separated by only a very small gap for about 1 second after unloading starts. This small gap allows for direct heat transfer between the disks in addition to the normal convection of heat to the ambient surroundings. Therefore for the fast disk, the cooling rate is higher in the first part of cooling as the heat is convected to the ambient and to the slow disk, whilst after full disk separation, it is only convected to the ambient surroundings.

5.4. Thermocouple installation developments

The thermocouple installation approach plays an important role in the accuracy of the temperature measurements acquired in the test rig. In other words, it is essential that each individual installed thermocouple measures the temperature at its intended location in the disk, and their transient response should follow as closely as possible

the rapid temperature change occurring at their location during the EHL experiments. In addition, the temperature distribution and heat flow within the disk should ideally not be distorted as a result of the thermocouples fitted. And finally, performance sustainability under dynamic conditions and environmental circumstances is also required.

The thermocouples used in this rig are of J type (iron – constantan) which has 0.2 mm diameter wires that are welded together creating an approximately 0.4 mm diameter thermocouple junction. It is known that the smaller the thermocouple mass the better time response (Bentley 1995), which is an important feature in measuring the steep temperature changes immediately following the disk unloading.

As in the work of Clarke (2009), the thermocouples were fitted in the test disk at the end of blind holes where the end of those holes are the desired location for the temperature measurements. A CC-high temperature cement produced by the Omega Company was used for potting the thermocouples in the holes. This cement is electrically insulating and thermally conductive and is designed especially for thermocouple installation. It consists of a catalyst liquid and powder that are mixed together to create the cement. Full details of the CC high temperature cement is available in appendix C.

A series of holes of various diameters were drilled in a metal test specimen for both skill training and in order to investigate the optimal hole diameter for thermocouple installation. It was found that 1.3 mm diameter holes are the best option for this particular combination of cement and thermocouple size based on experimentation over a period that allowed installation skills to be developed. During the installation, the thermocouple was pushed to ensure its tip was in contact with the disk at the hole

end, to try to ensure that there is a minimum cement between the disk material and the thermocouple. Care was also taken to ensure that the hole was filled with cement to support and secure the thermocouple.

In addition to the previous investigations, more work was carried out to examine the effect of installation method on the time response of the installed thermocouple. A two part disk was manufactured for this purpose which is shown in Figure 5.10. When assembled, this disk has 76.2 mm outside diameter and 9.53 mm width which is corresponds to the actual test disk dimensions. It includes five thermocouples installed on a pitch circle 3mm below the outer cylindrical surface midway between the side faces. Three of these thermocouples were installed in 1.3, 2.2 and 3 mm diameter holes respectively using the CC-high temperature cement. The other two thermocouples were installed by clamping their tips by assembling the two parts of the disk without any cement, which eliminates any possible delay in the heat transfer between the disk and the thermocouple tips. These two thermocouples represent the ideal installation as no cement surrounds their tip and the physical clamping should ensure they are in good thermal contact with the disk itself.

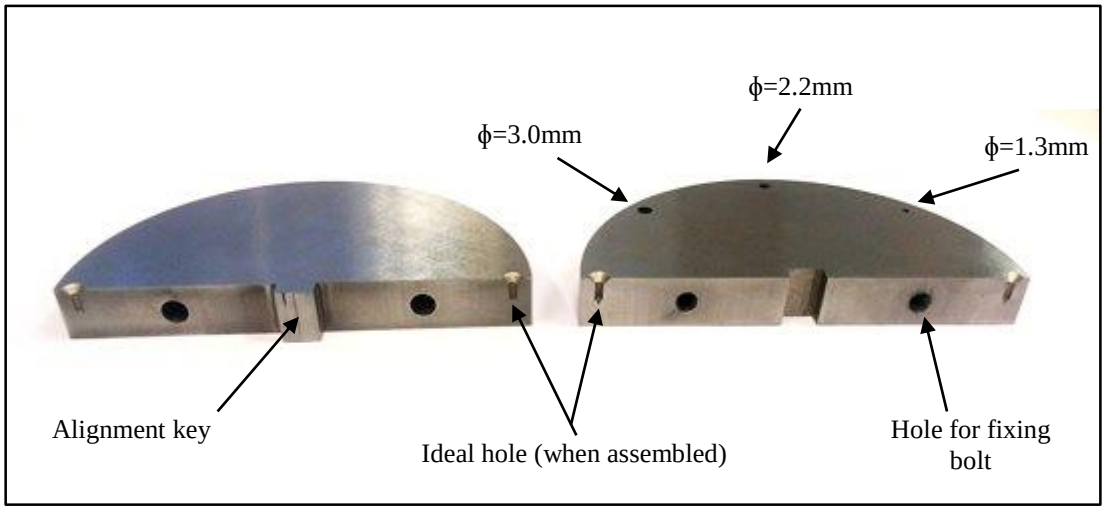

Figure 5.10: The two parts disk used for investigation the dynamic response of thermocouples corresponds to their installation

Figure 5.11 shows in detail the positions at which the ideal thermocouples were installed. In the right hand part, a small notch can be seen whilst it is flat on the left hand side, the thermocouple tip is pinched between this notch and the flat surface when the disk parts are assembled.

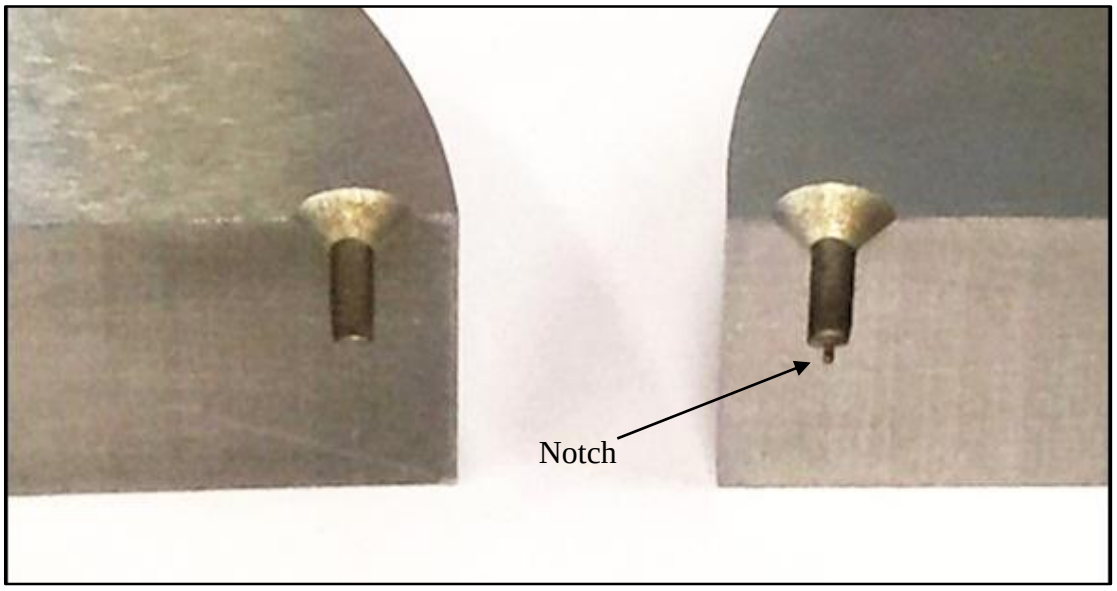

Figure 5.11: Detailed view of the ideal thermocouples locations

Figure 5.12 shows the two part disk after assembly and installation of the five thermocouples. This disk will be used to investigate the effects of cement and hole diameter on the response of the thermocouples compared with ideally installed thermocouples.

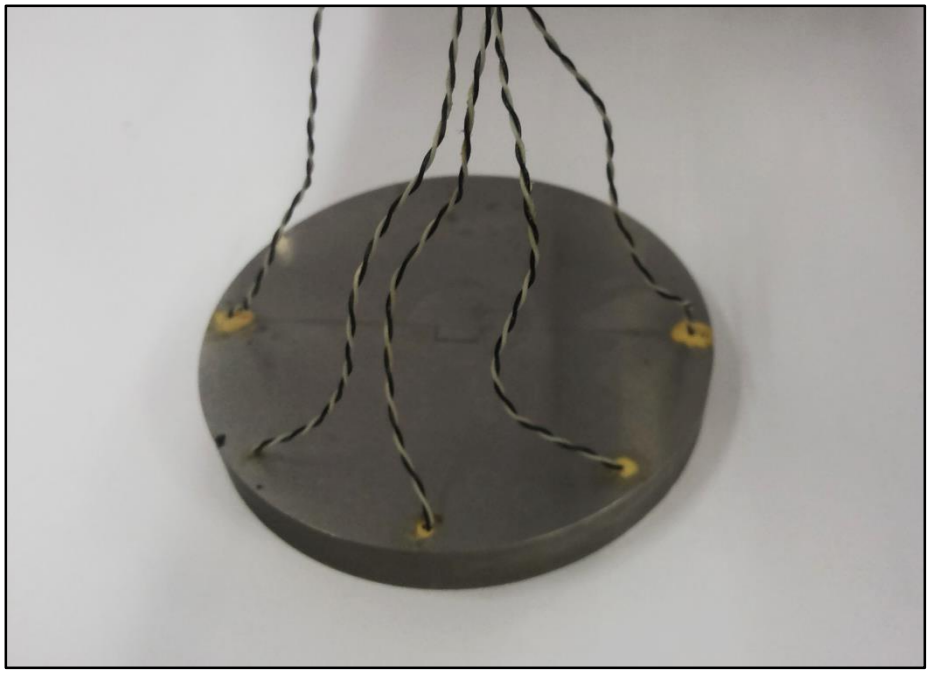

Figure 5.12: The assembly of the two parts disk after the thermocouples installation

Before using this disk in experiments, it was calibrated using a controlled temperature environment oven and a reference temperature measured by a PRT thermometer in the same way as the test disk calibration, described in section 2.6. The temperature was varied between of 20^{o}C and 80^{o}C in 20^{o}C steps. This range was selected as the planned experiment was immersion of the disk stabilized at the lab ambient temperature into a hot water bath held at a temperature of 80^{o}C. Figure 5.13 is a photograph showing the experiment of rapid immersion of the two part disk having approximately 16^{o}C initial temperature into the 80^{o}C water bath for testing the thermocouple response to rapid temperature change.

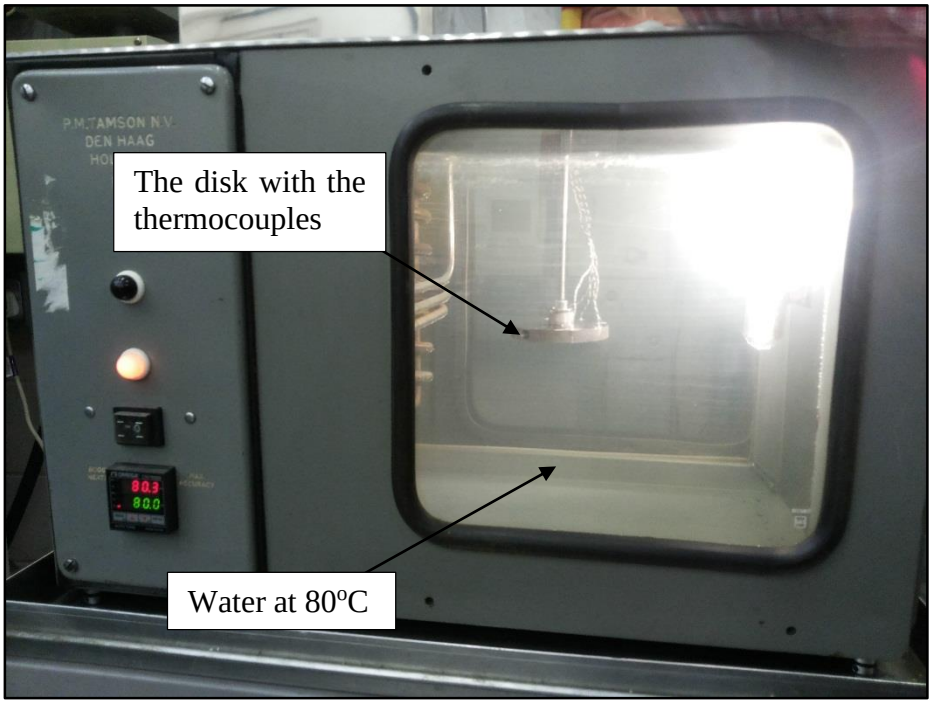

Figure 5.13: The water bath used for examining the dynamic response of the thermocouples according to their installation

The temperature traces measured by the five thermocouples for the experiment described above are shown in Figure 5.14.

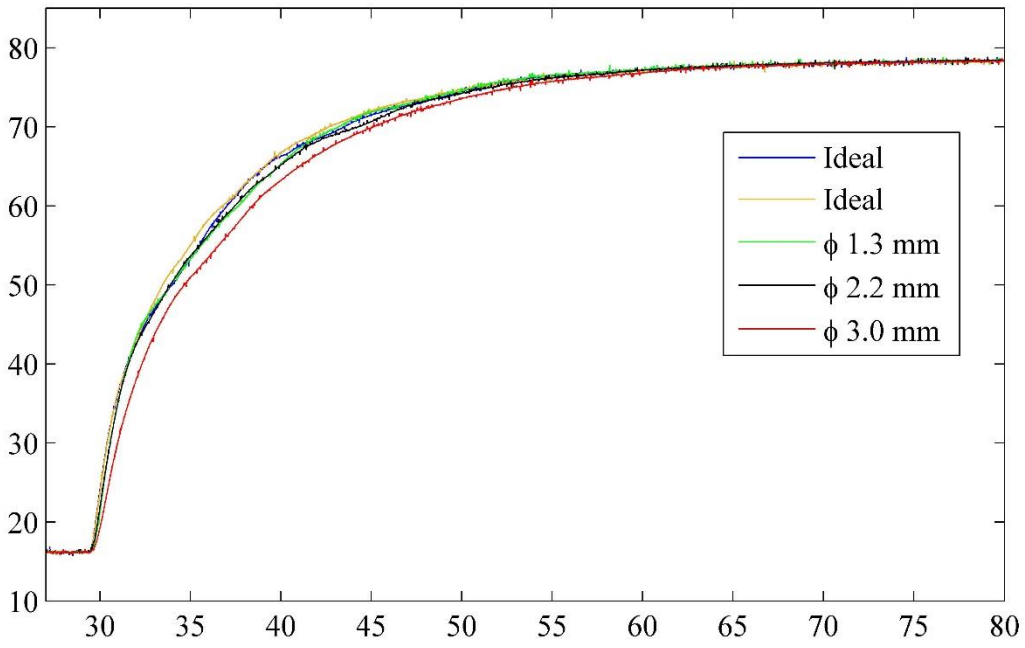

Figure 5.14: The temperature measured by the five thermocouples during immersion the two parts disk in water bath at 80ºC

It can be seen that the thermocouples mounted in the 1.3 mm and 2.2 mm diameter holes show consistent transient response when compared with the ideal thermocouples. However rather than the thermocouple mounted in 3 mm diameter hole gives a considerable lag in the transient response in comparison with the other four thermocouples. It was concluded from the above experiment that the thermocouples installed in the 1.3 mm and 2.2 mm diameter holes give acceptable transient response in terms of the experiment conditions. Also, from the installation experiments with cement, it was concluded that the minimum hole diameter of 1.3 mm gives a good thermocouple installation for these particular thermocouples. Therefore, the 1.3 mm diameter hole was used in installing the thermocouples in the actual test disks for use in the EHL experiments.

5.5. Thermocouple position improvements

The thermocouple positions within the test disks was described in section 2.3. These thermocouples were installed into two radial rows, 3mm and 6mm below the outer surface. The inner row thermocouples (6 mm below the surface) were used to define the boundary condition for the two dimensional solution zone at that radius. On the other hand, the outer row thermocouples (3 mm below the surface) were used for error minimization individually and as in combination in the numerical modelling in order to determine the heat partition.

In this section, the thermocouple locations are considered and improved in order to improve the results of the EHL tests. The boundary condition thermocouples were maintained at their original positions but an investigation was carried out to redesign the outer row thermocouple locations. Using the previous numerical calculation in

section 4.3, the radial temperature variation is plotted in Figure 5.15 for the fast disk at the end of the heating phase (approximately steady state). In this figure, the temperature at the two faces ($z=\pm w/2$, w is disk width) and the centre of the disk ($z=0$) is shown along the disk radius within the solution zone. The lower radius $r=32$ mm is a boundary condition provided by the inner row of thermocouples fitted to a second order polynomial function, while the higher radius $r=38$ mm is the outer surface disk which is subjected to both heating and cooling during the EHL experiments. The three thermocouples used for error minimization are installed at $r=35$ mm, (one in the centre and 2 mm below the surface of each side face).

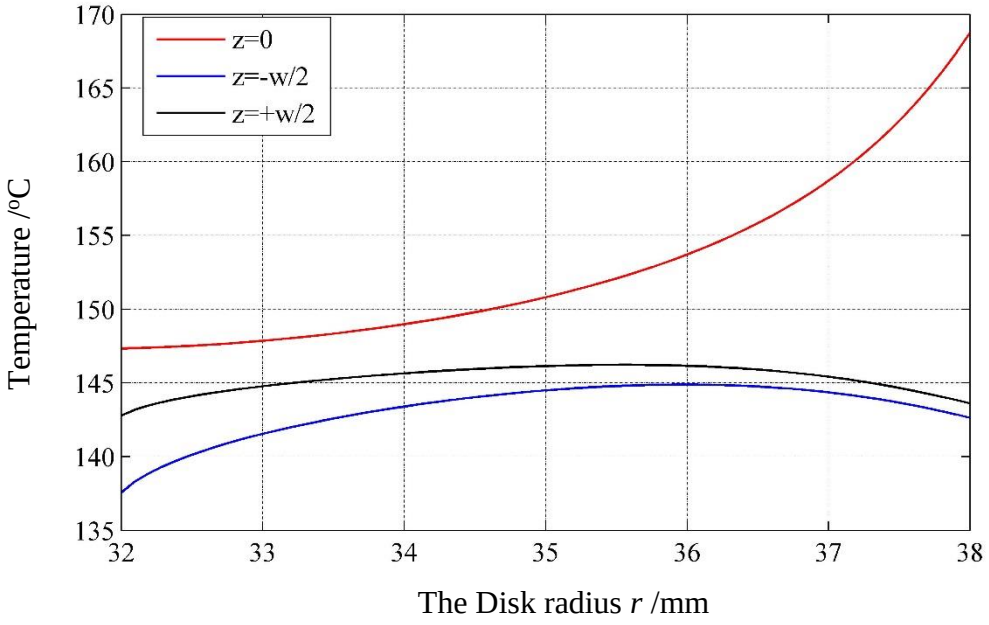

Figure 5.15: The temperature along the radius for the fast disk at steady state D4 EHL experiment at the two sides and the centre of the disk

It can be seen in Figure 5.15 that both disk faces show broadly similar trends. They have a maximum temperature located between 35 mm and 36 mm radius which then decreases slightly up to the surface, while the temperature at the centre increases continuously as the radius increases along the region. Accordingly, the middle of the

solution zone within the disk ($z=0$) has the maximum temperature variation, especially close to the surface. Therefore installing additional thermocouples in the centre close to the surface will increase the range of temperature variation that can be used for error minimization in order to enhance the solution determination.

Now when considering the transient solution outlined in section 4.4 (in which the model was applied to the data at a rapid temperature change just after unloading the disks) it was identified that the temperature measurement system has an amount of lag in following the theoretical model during the rapid temperature change. It was concluded that in order to benefit from the data in the period of rapid temperature change, it was necessary either to develop the measurement system or identify the mathematical relationship between the actual metal temperature and the lagging thermocouple temperature, as measured.

Regarding the measurement system development, the work carried out on the thermocouple installation in the previous section and the unloading mechanism development in section 5.2 represent the achievable improvement within the scale of this project. With respect to the identifying the mathematical relation, it is necessary to consider the inner row thermocouples used as boundary conditions in the numerical modelling.

As long as these measurement are steady state, they do not include the lag effect which occurs during rapid temperature changes. In other words, when the disks are unloaded, they start to lose heat and the temperature starts to fall at first at the largest radius and then progress towards the smaller radius and eventually reaching the radius of the inner row thermocouples (6 mm below the surface). At this time, the numerical solution will start to include a boundary condition (the temperature measurement at 6 mm below

the surface) involving response lag. Thus, the analysis of the highly transient state is reliable only up to the time when the temperature starts to change 6 mm below the surface which is a very short time.

Accordingly, for this short time, the temperature change 3 mm below the surface is insufficient for solution discrimination. Therefore positioning a thermocouple closer to the surface is important in transient state error minimization. Figure 5.16 shows the temperature change at three levels below the running surface; 1.25 mm, 3 mm and 6 mm when unloading occur at time 1243.28 s and up to the time prior to temperature change at 6 mm below the surface.

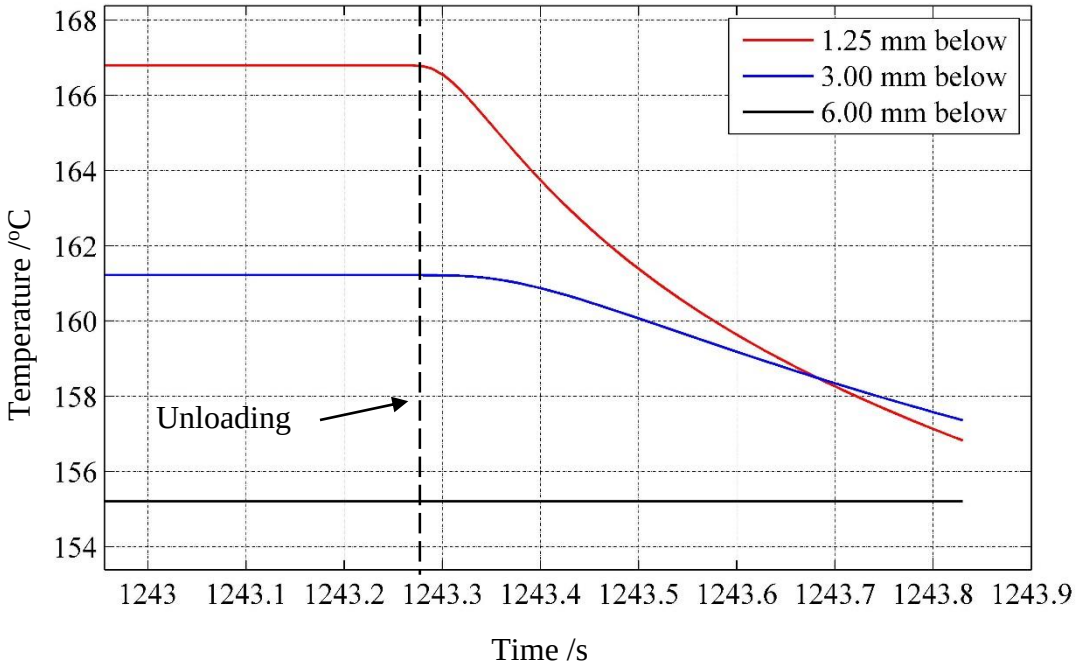

Figure 5.16: Showing the temperature variation at the centre of two levels below the running surface for the fast disk during unloading up to the time before the 6 mm level temperature starts to change

It can be seen that at 1.25 mm below the surface, the temperature variation is higher than that at the 3 mm depth which is where the thermocouple ***a*** was located by Clarke (2009).

In summary, according to both steady state and transient analyses, it is beneficial to install a thermocouple closer to the running surface on the centre line of the disk. Since each slip ring only has sufficient channels for six thermocouples, one of the outer thermocouples ***e***, 3 mm below the running track, will be moved to a new position closer to the surface on the centre-line of the disk.

5.6. Thermocouples arrangement in the test disks

According to the investigations implemented in the previous section, it was decided to relocate one of the side outer row thermocouples to a new position close to the surface along the centre of the disk, in order to give better temperature discrimination. However, these disks are subjected to high load on a small contact area during the EHL experiments. Accordingly, the disk material near the contact zone undergoes high stresses that should be taken into account when forming a new thermocouple hole.

The new planned holes in the test disks should be below the point at which sub-surface plastic yielding is expected to occur. Plastic yielding of ductile material is usually assessed according by Tresca's maximum shear stress criterion, the maximum shear stress occurs at a distance *z* below the surface given by

$$z \cong a\left(0.7929 - 0.3207\frac{a}{b}\right) \tag{5.1}$$

where

a is the minor elliptical dimension of the contact area.

b is the major elliptical dimension of the contact area.

To calculate the minimum distance below the surface at which a thermocouple hole can be safely positioned. The maximum planned load for the EHL tests in this study was 2320 N which produces Hertz dimensions of $a=0.45$ mm and $b=1.75$ mm. According to equations (5.1), if yield occurs it will be at a distance of ($\boldsymbol{z \simeq 0.32}$ **mm**) below the surface. So that, any hole in the disk should be below this distance (after factorized by safety factor).

It was decided to position the new hole at a centre of 1.25 mm below the surface with a diameter of 1.3 mm (likewise all other holes) by considering a safety factor of 2 approximately. The new two dimensional thermocouple arrangement is shown in Figure 5.17 and the detailed engineering drawing is shown in Figure 5.18.

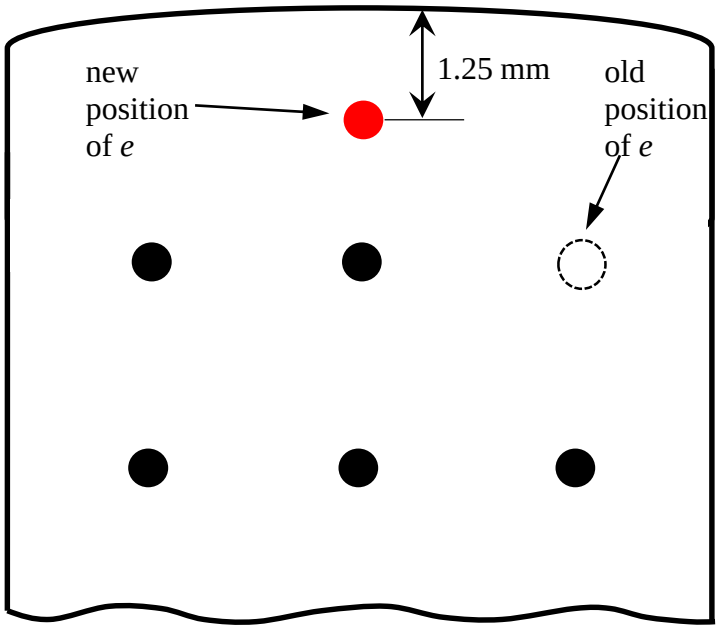

Figure 5.17 : The two dimensional new arrangment of the thermocouples installed in the test disk

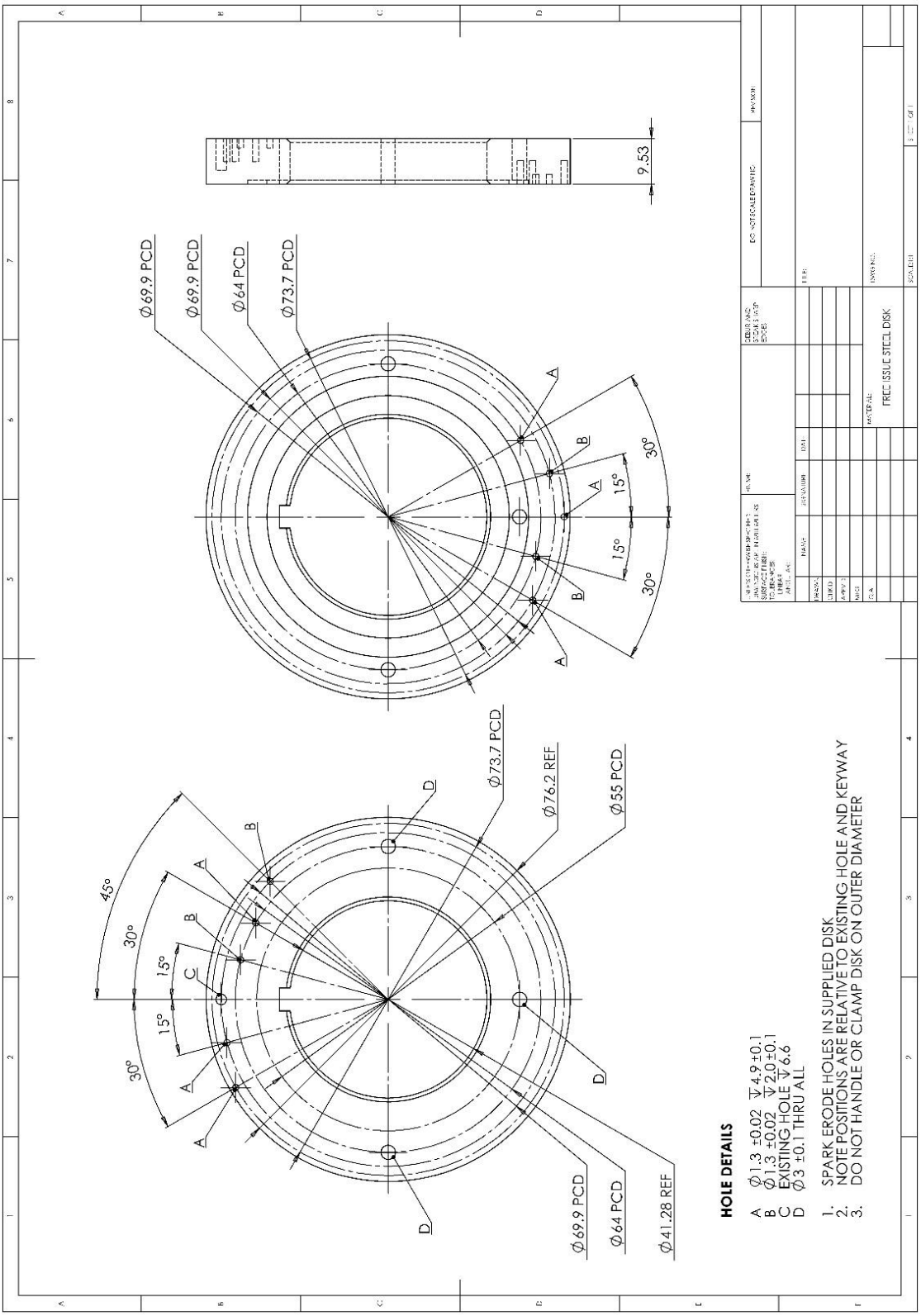

Figure 5.18: Detailed drawing showing the test disks including the new holes arrangement

The disk's material is hardened and cannot be drilled with traditional drilling methods and so the holes were created by spark erosion. Before that, the disk's surface roughness was measured in two directions (axial and circumferential), together with accurate measurements of the main disk radius and the crowning radius. This surface measurement process was carried out using Taylor Hobson Talysurf series 2. Figure 5.19 shows the measurement setup of the test disk in the circumferential direction.

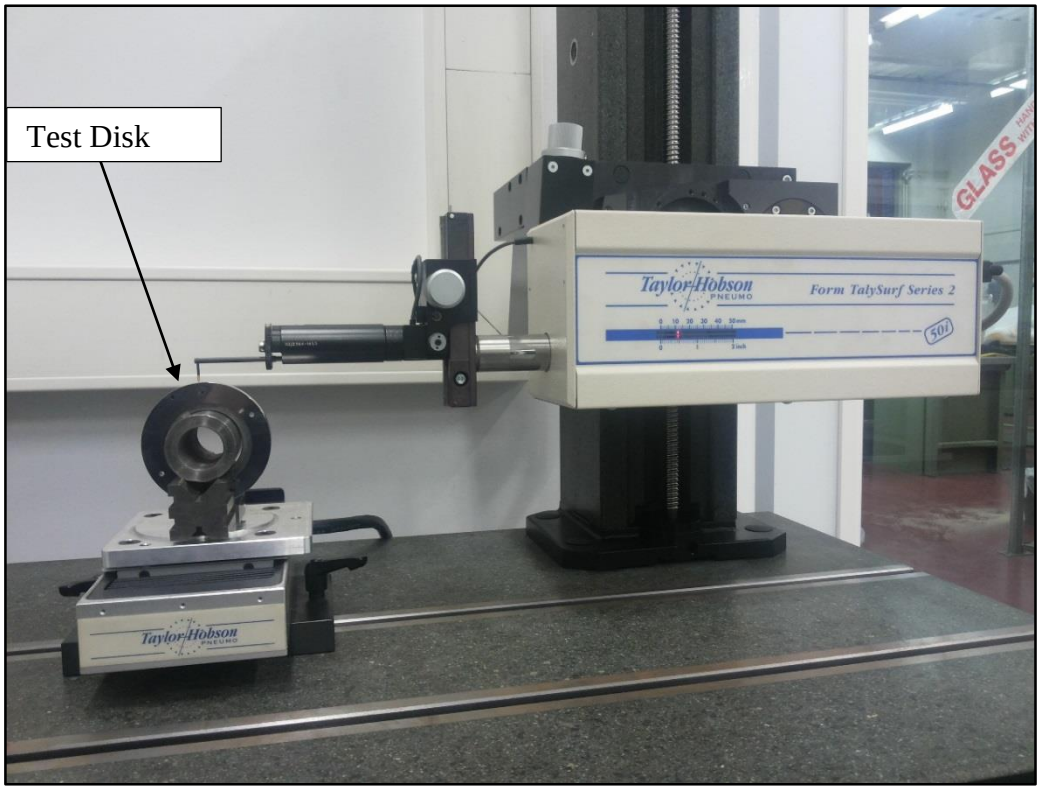

Figure 5.19: The surface roughness measurement of the disk using Taylor-Hobson Talysurf

The acquired profile data were then filtered using Taylor Hobson software in order to separate form, waviness and roughness and to compute the average roughness *Ra*. Figure 5.20 shows a typical roughness profile for one of the test disks (super-finished) which was then installed in the test rig. For this case the *Ra* is 0.032 µm. Figure 5.21 is a photograph showing the mirror like surface of the super-finished disk.

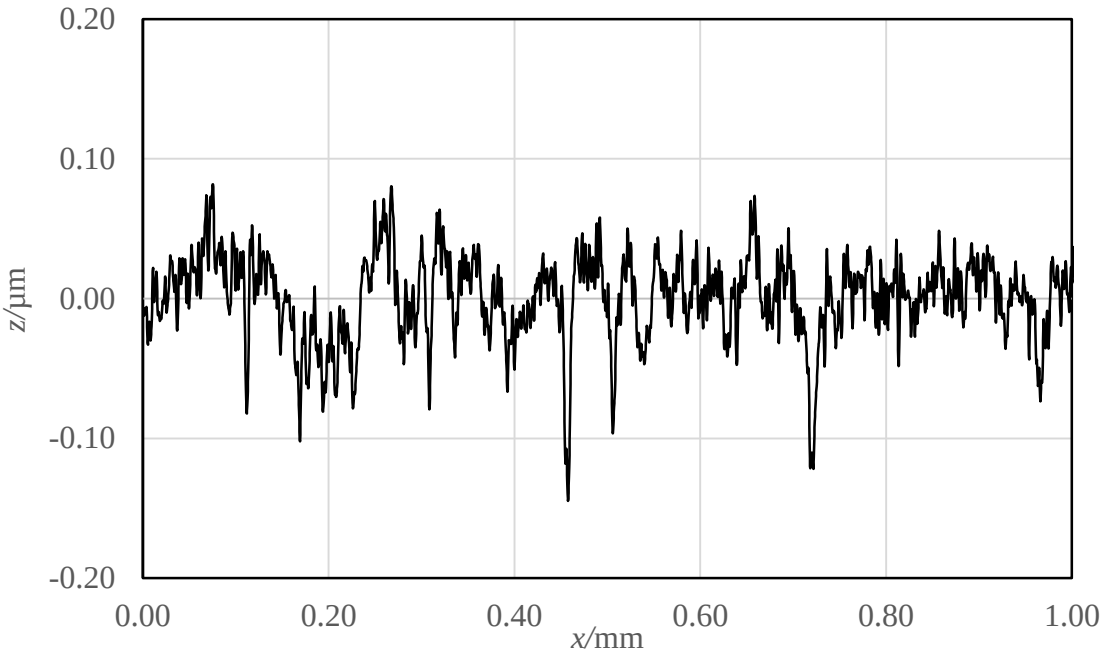

Figure 5.20: The circumferential surface roughness profile for the typical super finished test disk prior to installation in the test disk

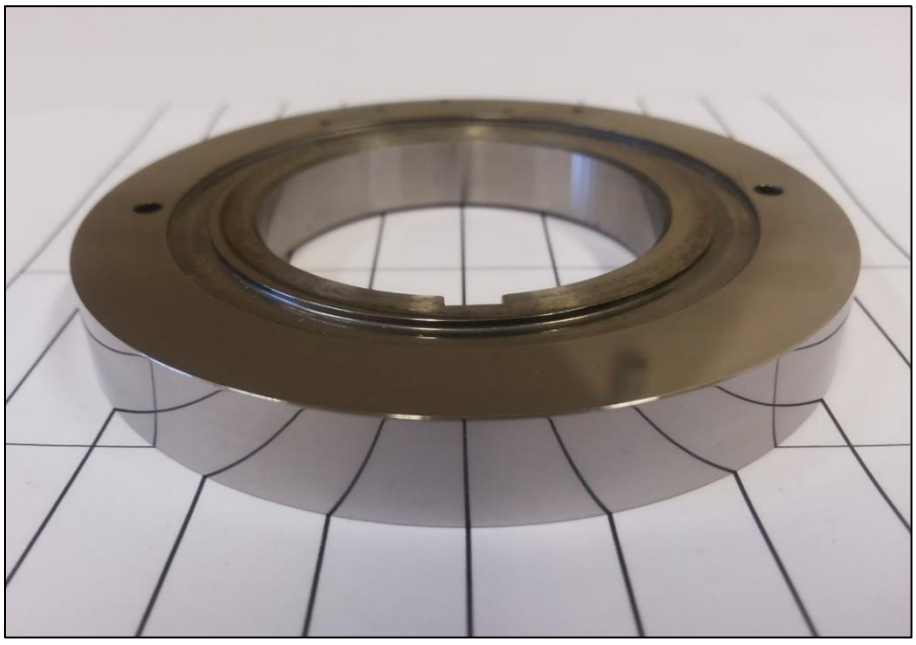

Figure 5.21: Photograph showing the mirror like surface of the super-finished test disk

5.7. The dynamic response of the installed thermocouples

After installing the thermocouples and the insulation washers on the test disks, they were calibrated in a controlled temperature environment oven as described in section 2.6. Prior to installing the test disks in the test rig, it was decided to carry out immersion tests in a high temperature environment to study the dynamic response of the installed thermocouples. The objective of these immersion experiments was to observe the response of all thermocouples together, and identify any variation due to the individual manual installation and manufacturing aspects. Furthermore, the results of these tests may be linked to numerically simulated cases, which can lead to evaluating a mathematical formulation of the thermocouple lag response, which was encountered in modelling the starting of the cooling phase described in section 4.4.

The thermocouples were connected to their relevant physical channels which were the same channels used during calibration and when installed in the test rig. Secondly, additional PTFE insulation disks were manufactured for the purpose of the immersion tests. These disks shown Figure 5.22 were designed to insulate the rest of the disk planer faces that were not insulated with the ceramic washers.

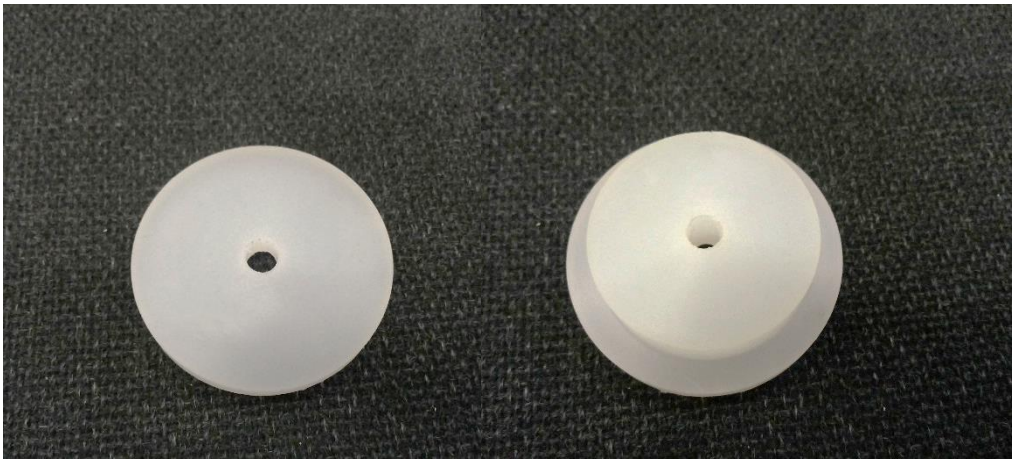

Figure 5.22: The temporary PTFE insulation washers fitted on the disks to use in the immersion tests

Accordingly, when these washers are fitted, all the disk surfaces (even the inner annular surface) are insulated except for the outer annular surface which experiences heat input during the tests. Figure 5.23 shows the PTFE disks when assembled to the test disks.

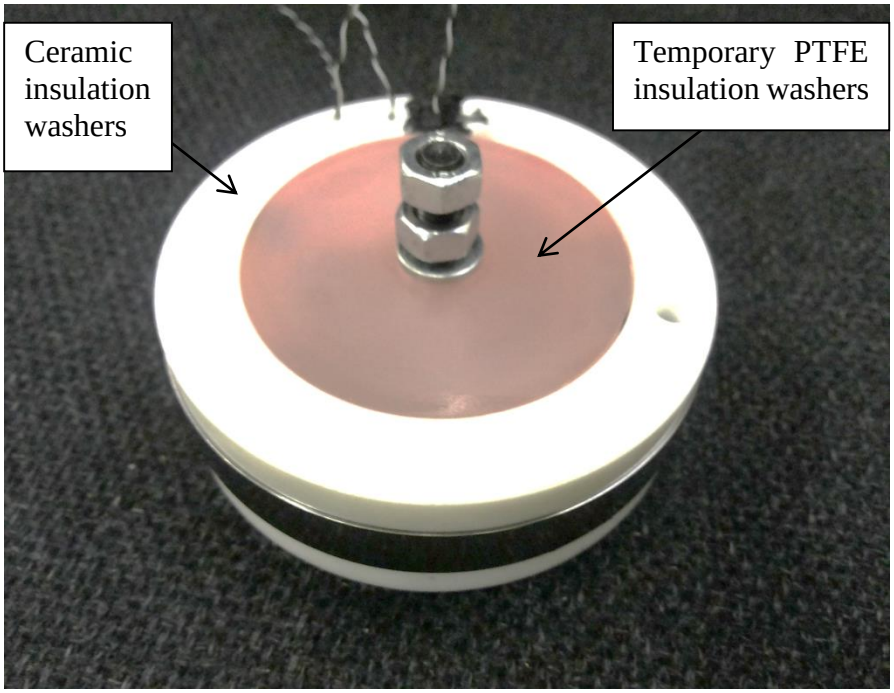

Figure 5.23: The test disk after fitting the insulations for preparing to the immersion test

There were two main reasons for incorporating this additional insulation, the first is to let the heat flow through the disks in the radial direction only, which enables consequent response of the thermocouples that are at different radial levels to be assessed and the second is to simplify their mathematical modelling in order to analyse the results of the tests.

The immersion tests were planned to be implemented using the oil tank which supplies the test head oil in the rig during the normal EHL experiments. The oil temperature was adjusted to around 110 ^{o}C, and the heaters and stirrers were turned on until the oil

temperature reached steady state. Afterwards, the heaters and the stirrers were turned off to obtain stagnant oil, this to ensure natural convection heat transfer to the disk surfaces which is modelled more simply. Then the disk was immersed horizontally and kept inside the oil until the measured disk's temperatures reached the steady state. Figure 5.24 shows the temperature for the thermocouples 1.25 mm, 3 mm and 6 mm below the surface at the disk centreline.

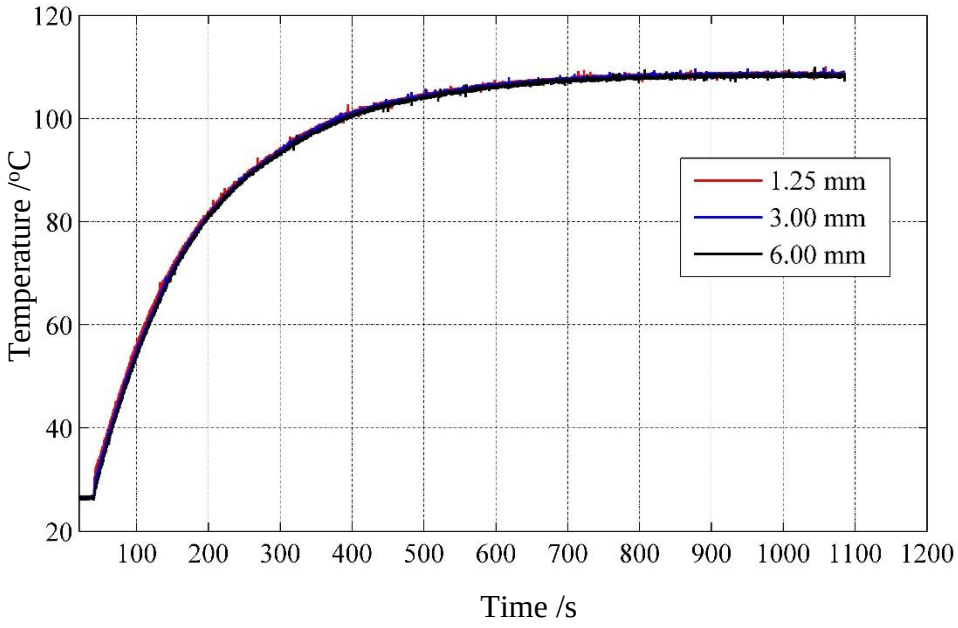

Figure 5.24: The immersion test results which shows the temperature measured by the central thermocouples at three levels below the surface

It can be seen in Figure 5.24 that the three temperatures have an initial value of 26 °C approximately which rise to 108 °C after immersion. Figure 5.25 shows the first 100 s time of the experiment shown previously in Figure 5.24.

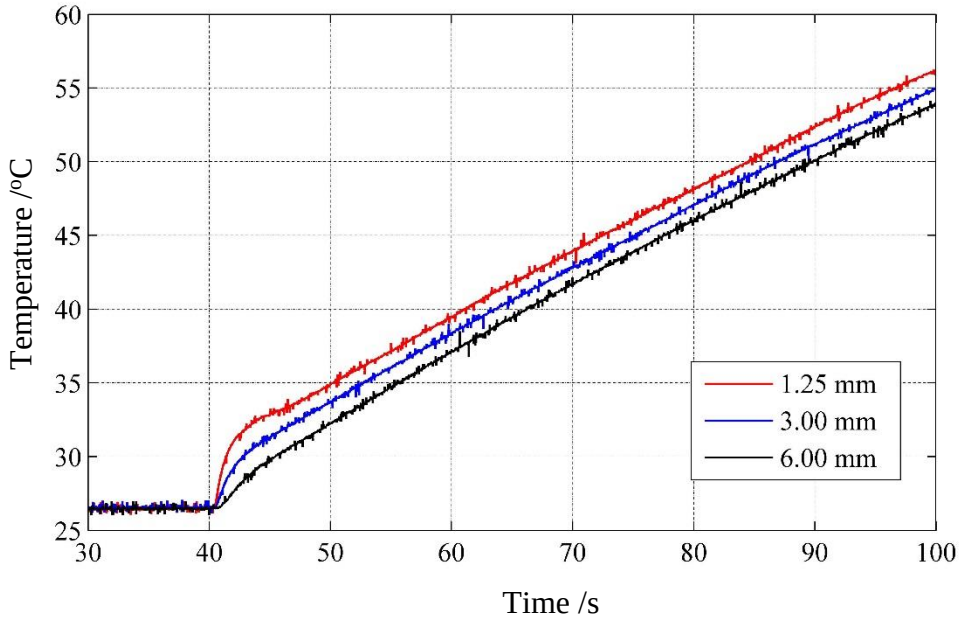

Figure 5.25: Focus part of Figure 5.24

The thermocouples can be seen to respond consistently the thermocouples in relation to their distance from the heated surface. It may be seen that during the time range from 41 to 44 s, the temperature rises more sharply than that in the subsequent time especially for the thermocouple located 1.25 mm below the surface. A possible explanation for this trend is that at the moment of the disk immersion, the disk is moving relative to the oil such that forced convection heat transfer occurs while after the disk is held stationary in the oil, the disk is heated by natural convection in which less heat is transferred.

A range of immersion tests were carried out on both disks and the response of the six thermocouples in each disk was examined. The results of these immersion tests have shown a consistent dynamic response of all the thermocouples in terms of the installation and the thermocouple manufacturing.

Despite the consistency of the dynamic response of the installed thermocouples, the influential lag in the dynamic response discussed in section 4.4 necessitated further investigations to determine the nature of the lag of response that all thermocouples follow. This does not appear by comparing their measured response as they are all subjected to lagging. The experiments were modelled numerically to evaluate the likely temperature response at the thermocouple locations regardless of any expected practical source of response lag. A one dimensional radial numerical model was applied to these experiments by assuming ideal insulation on the side faces and the inner annular face. The heat is transferred from the hot oil to the disk through the outer annular surface by a natural convection process. In this process, the heat transfer coefficient should be identified within the numerical modelling. Therefore, a function for representing the average natural heat convection coefficient with the conditions of the immersion test (Holman, 2010) was used

$$\overline{Nu}_f = 0.59(Gr_f Pr_f)^{0.25} \tag{5.2}$$

The subscript f indicates that the dimensionless group numbers $(\overline{Nu}_f, Gr_f \text{ and } Pr_f)$ are evaluated at the film temperature, which is the average temperature between the fluid bulk temperature and the wall temperature.

Another important issue in linking the theoretical model to the experimental immersion test is the identifying the time of the instant at which the test disk was immersed in the hot oil. Accordingly, two indicators were used for this aim, the first is the microswitch that is connected to the data acquisition system and used originally for indicating loading and unloading the disks. It was disassembled from the rig temporarily and used in these immersion tests by pressing it manually at the instant of immersion. For more certainty in identifying the time of immersion, the second

indicator was a free thermocouple which was fixed on the disk in order to measure ambient temperature adjacent to the disk. The temperature measured by this free thermocouple indicates clearly when the disk is immersed in the oil. Figure 5.26 shows the immersion test temperature at 3mm below the surface together with the numerical model results, it involves the convection heat transfer coefficient calculated according to equation (5.2).

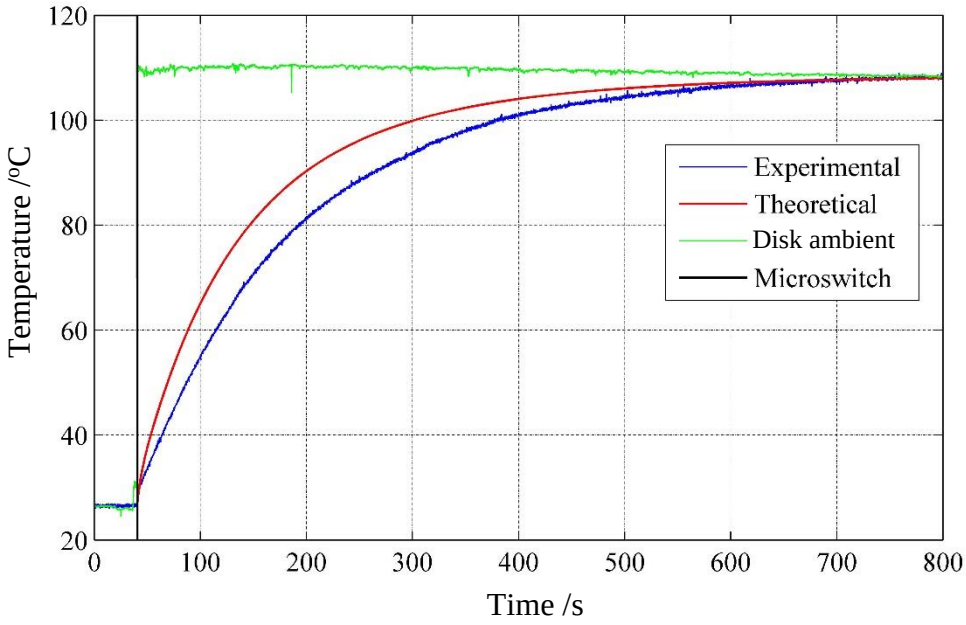

Figure 5.26: The immersion test temperature at thermocouple ***a*** and the relevant calculated temperature

Figure 5.26 also shows the free thermocouple and the microswitch indicators which are used to indicate the immersion time. It was important to identify this time by these indicators since the objective of these experiment is studying the dynamic response. Both indicators gives good agreement and so can be relied on. The results of this analysis suggest that in general, there is a clear lag in the response of the measured temperature as compared with the theoretical simulation. If this result is confirmed, that means there is one or more element in the measurement system which contributes

to this lag of response. Regardless of the cause of this lag, it is crucial to ensure that the modelling of the immersion test is reliable, especially the mathematical formula used in the calculation of the convection heat transfer coefficient (equation (5.2)).

In order to confirm the fact that the measurement system of temperature involves some source of inaccuracy that leads to lag in the dynamic response, it was decided to use alternative mathematical functions for heat transfer coefficient from the literature, which can be used for the immersion experiment case. Holman (2010) derived an equation for the local free convection heat transfer coefficient for a vertical flat plate.

$$Nu_x = 0.508Pr^{1/2}(0.952 + Pr)^{-1/4}Gr_x^{1/4} \tag{5.3}$$

And the average heat transfer coefficient (Holman 2010)

$$\bar{h} = \frac{4}{3}h_{x=L}$$

Equation (5.3) is derived for vertical flat plate, however the vertical cylinder can be treated as a vertical flat plate in the free convection when (Holman 2010):

$$\frac{D}{L} \geq \frac{35}{(Gr_L)^{1/4}}$$

This condition is satisfied in the immersion tests experiments.

Another empirical equation for representing the convection heat transfer coefficient that is given by Holman and attributed to (Churchill and Chu 1975) is:

$$\overline{Nu} = 0.68 + \frac{0.670\,Ra^{1/4}}{[1 + (0.492/Pr)^{9/16}]^{4/9}} \tag{5.4}$$

The previous three various models were used for modelling the immersion test. In addition to using a range of models for the heat transfer coefficient, the oil temperature was altered for the immersion tests to ensure more certainty. Figures 5.27 (a) and (b) show the modelling of immersion tests of oil temperature at 69 ºC and 138 ºC respectively. Both figures include the models 1, 2 and 3 based on equations (5.2), (5.3) and (5.4) respectively in representing the convection heat transfer coefficient.

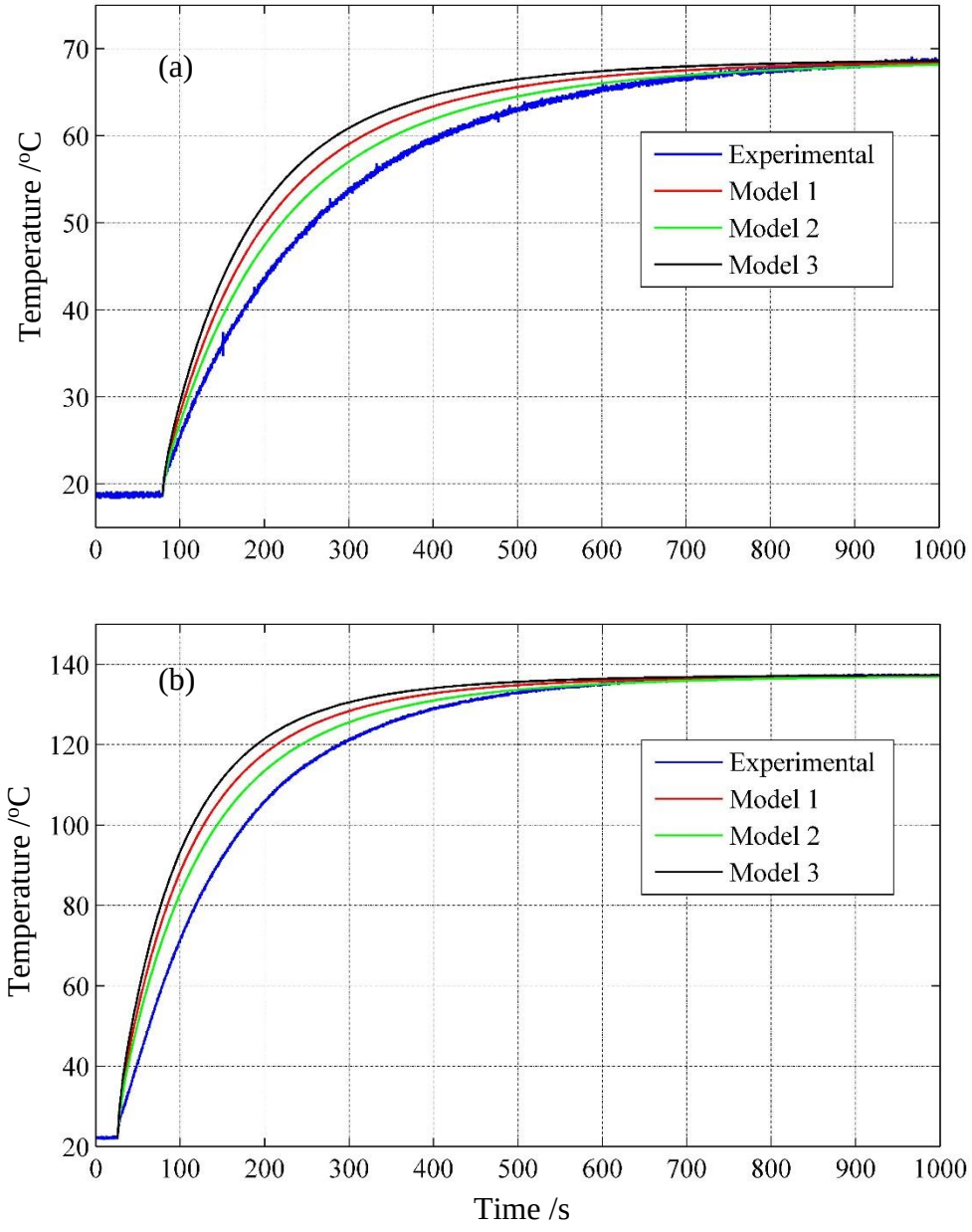

Figure 5.27: The measured temperature at 3 mm central below the surface during immersion tests at **(a)** 69 ºC, **(b)** 138 ºC. Modes l, 2 and 3 based on equations (5.2), (5.3), and (5.4) respectively.

It is apparent from Figure 5.27 that there is some difference in the temperature response obtained from the three models, in fact that is expected since those three models were chosen from different studies in the literature. However, compared to each of the models the experimental measurements display a lag in response. These results might explains the difficulties experienced in modelling the rapid temperature change in the EHL experiment discussed in 4.4.

In summary, according to the immersion tests and their modelling, the thermocouples dynamic response are consistent in terms of individual physical preparation and installation which were verified by the immersion experiments themselves. However, all of them have a systematic response lag when compared to theoretical models when the surrounding temperature is changing rapidly. There are different possible reasons for this lag of response:

- Thermocouple physical specifications like the wires diameter and the tip size.
- The cement used for installation.
- The holes made in the disks for the thermocouples.
- The electronic devices used in the data acquisition system.

Using the experimental and theoretical solution can be used to identify the measurement system characteristic, this will be described in the future work section 8.3

5.8. Additional hardware for temperature measurements

As part of the developments carried out on the test rig, the data acquisition system was enhanced by introducing hardware for additional temperature measurements. This

hardware is a National Instruments NI 9213 module which allows for using up to sixteen further thermocouples. It is fitted to a NI cDAQ-9174 4-slot USB chassis produced by National Instruments, these are shown in Figure 5.28. This allowed for various temperature measurements to be recorded during the current project such as of the oil in the tanks and the jets, the ambient and the bearings. The chassis was connected to the main computer via USB and was interfaced using the NI Labview software developed in conjunction with the existing hardware in the rig. Then the data acquired from all hardware are displayed and recorded together.

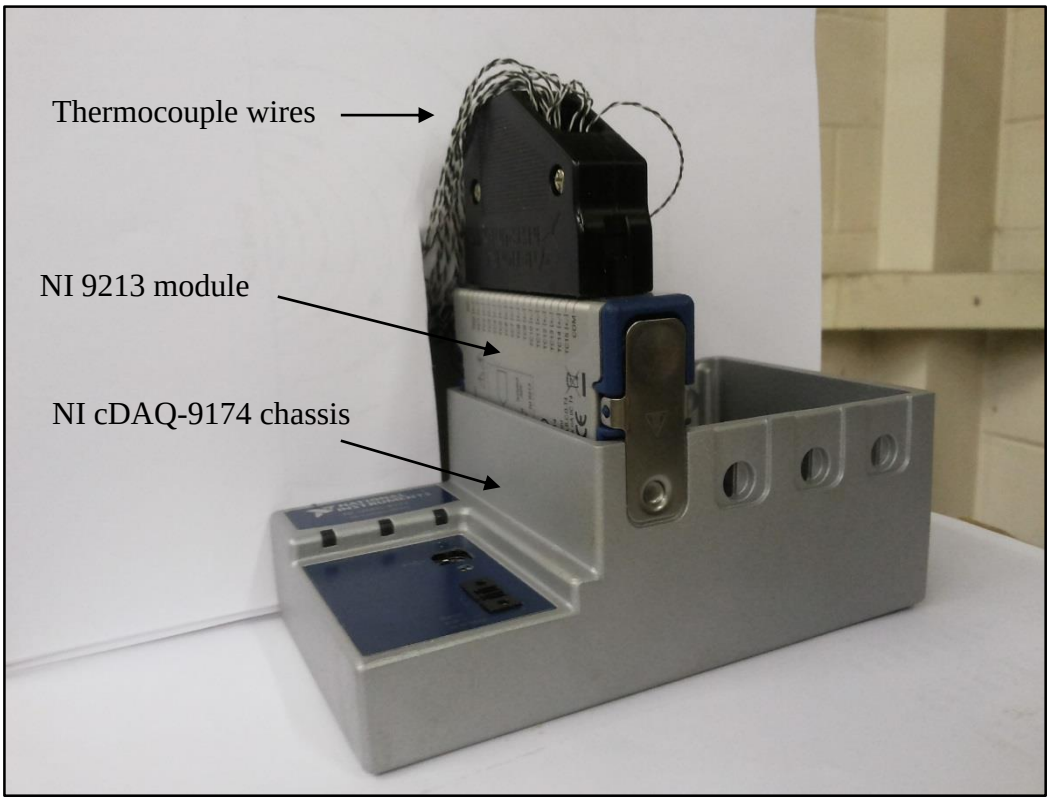

Figure 5.28: Sixteen channel thermocouple module (NI 9213) fitted on 4-slots (NI cDAQ-9174) chassis, both produced by National Instruments.

After all these developments and investigations that were carried out on the test rig, the fast shaft with the fitted instrumented disk are shown in Figure 5.29. A set of EHL experimental tests were then carried out, and these tests are described in the next chapter.

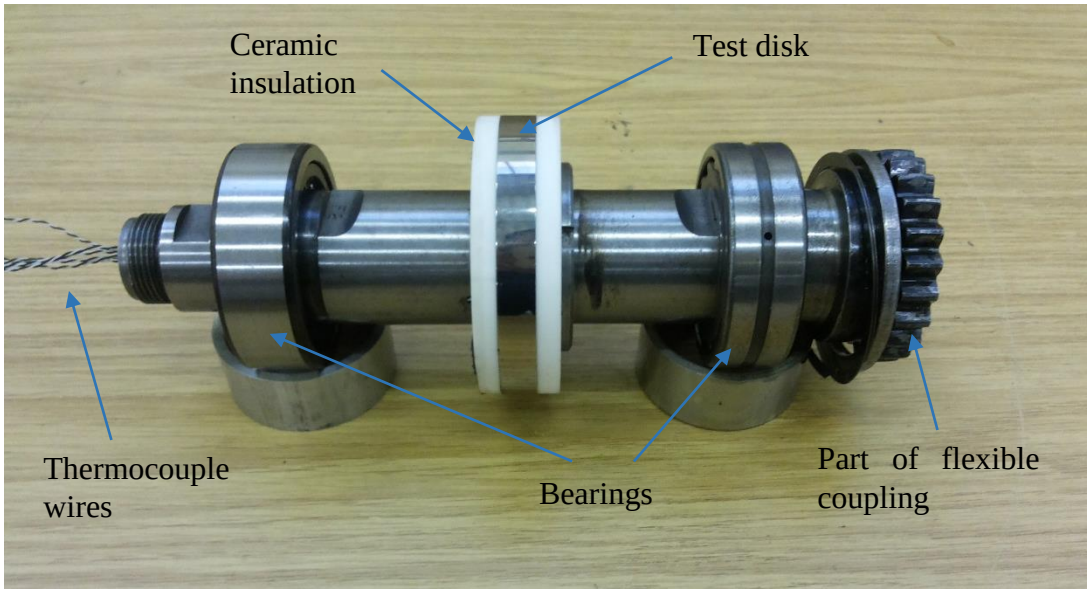

Figure 5.29: An instrumented test disk fitted on shaft prior to installation in the test rig

Chapter 6:
EHL Experimental Results

6.1. Introduction

In this chapter, the results of operating the test rig (that was described in chapter two) for a series of EHL tests are reported. These results involve the temperatures measured by the installed thermocouples in the test disks, the traction force generated at the EHL contact and the applied load. This chapter also includes an observations on the experimental results in addition to extensive investigations on some unexpected trends observed in these measurements.

6.2. EHL tests procedure

The experimental procedure that is used in this work is similar to that used in the work of Clarke (2009). In the current work, whilst this test rig was subject to several developments which are described in chapter five, the general function of the rig remained unchanged. The test series will be described in detail in the next section, however the general procedure which is carried out for all tests is described here.

Prior to carrying out an EHL test session, the oil in the tanks was heated to the desired temperature by heaters and stirrers which are built into each oil tank. The test head oil temperature was set to 60 ^{o}C and was monitored on the Labview software using a thermocouple immersed in the tank. The oil that supplies the hydraulic loading mechanism and the lubricant to the gearbox was adjusted to the normal supply temperature of 35 ^{o}C. When the oil reached the pre-set temperature, the oil pumps

were turned on to start the oil circulation. The circulated oil in the test head heats the test disks and the shafts while they are stationary. The jets are directed to the contact zone of the disks and the bearings which support the shafts. During this time, the oil jets were observed visually to make sure that the contact zone and the bearings were fed by the oil. Also during this time, the Labview software was used to monitor the temperatures in the test disks, the oil tank and the oil jet. Before the start of disk rotation, the load and friction force measurements were set to zero as described in sections 2.8 and 2.9, then the load was applied and set by the manual control to the required value for each individual test. The load then was removed by opening the dump valve whilst leaving the load control set at the desired load. During running, the disks will be loaded by closing the dump valve. This process of loading was followed to avoid controlling the load during the EHL contact which can give variable load during the test.

When steady temperatures were observed, the slip ring cooling air was turned on. Subsequently, the main drive motor was switched on and the disk speed adjusted to the planned speed of the test (the disks speed for each test will be reported in the next section). For this period, the disks were rotating whilst they were not in contact, this was continued until approximately steady temperatures were achieved for both disks, noting that the fast and slow disks rotate at different speeds.

At this time and after the warm-up process described, the actual EHL test was started. The Labview software was directed to write the acquired data in an output spread sheet file. After approximately 50 seconds, the pre-set load was applied and maintained by closing the dump valve. At the time of applying the load, the temperature of the disks was raised significantly, the constant loading process was continued until an approximately steady state temperature of the disks was achieved. It was observed that

this process takes approximately 1000 seconds, after which the disks were unloaded and separated rapidly by opening the dump valve. During this period, the disks were cooled while they were still rotating and the data were recorded continuously until the disks returned to steady temperatures. At this point the data acquisition software was stopped and the full EHL test had been conducted.

6.3. EHL tests programme

A series of 16 EHL tests were carried out using the developed test rig. These tests were varied according to a range of sliding speeds and loads similar to those used previously in the work of Clarke (2009). The tests were designed to investigate the thermal aspects of the EHL contact problem avoiding the conditions which might lead to scuffing. In this work, the load was limited to produce a maximum Hertzian pressure of 1.4 GPa as the disks were developed to have new thermocouples closer to the surface. Table 6.1 shows the conditions that were applied in running the EHL tests.

Note that the table gives the velocities of the disks relative to the contact point in terms of the mean (entrainment) velocity, u_m, and the sliding velocity, u_s. These are key kinematic parameters for any EHL analysis. For the gear ratio of 1.24 used in the experiments, these velocities were achieved with the stated rotational speeds w_{slow} and w_{fast}

Table 6.1: The EHL test conditions

Tests	Load /N	p_{HZ} /GPa	u_s /ms^{-1}	u_m /ms^{-1}	ω_{slow} rpm	ω_{fast} rpm
A1	850	1.0	10	8.06	774	3282
A2	1460	1.2	10	8.06	774	3282
A3	1850	1.3	10	8.06	774	3282
A4	2320	1.4	10	8.06	774	3282
B1	850	1.0	13	10.5	1005	4261
B2	1460	1.2	13	10.5	1005	4261
B3	1850	1.3	13	10.5	1005	4261
B4	2320	1.4	13	10.5	1005	4261
C1	850	1.0	16	12.9	1238	5249
C2	1460	1.2	16	12.9	1238	5249
C3	1850	1.3	16	12.9	1238	5249
C4	2320	1.4	16	12.9	1238	5249
D1	850	1.0	20	16.3	1546	6555
D2	1460	1.2	20	16.3	1546	6555
D3	1850	1.3	20	16.3	1546	6555
D4	2320	1.4	20	16.3	1546	6555

The results of these 16 tests are shown in Figure 6.1 to Figure 6.16. Each figure involves three parts; (a), (b) and (c). In part (a), the temperature measurements versus the whole time of the test are plotted for the central thermocouples (***e, a*** and ***b***) for both fast and slow disks. The data are recorded for a total of 2000 seconds, approximately 50 seconds before loading, then the disks are loaded for a time of approximately 1000 seconds at which point the load is removed for the rest of the test. In part (b) of the results figures, the load and traction force are plotted, they showing the loading and unloading phases. Part (c) of the test results figures shows the temperature map of the 12 thermocouples installed in both disks at the end of loading phase which is approximately steady state

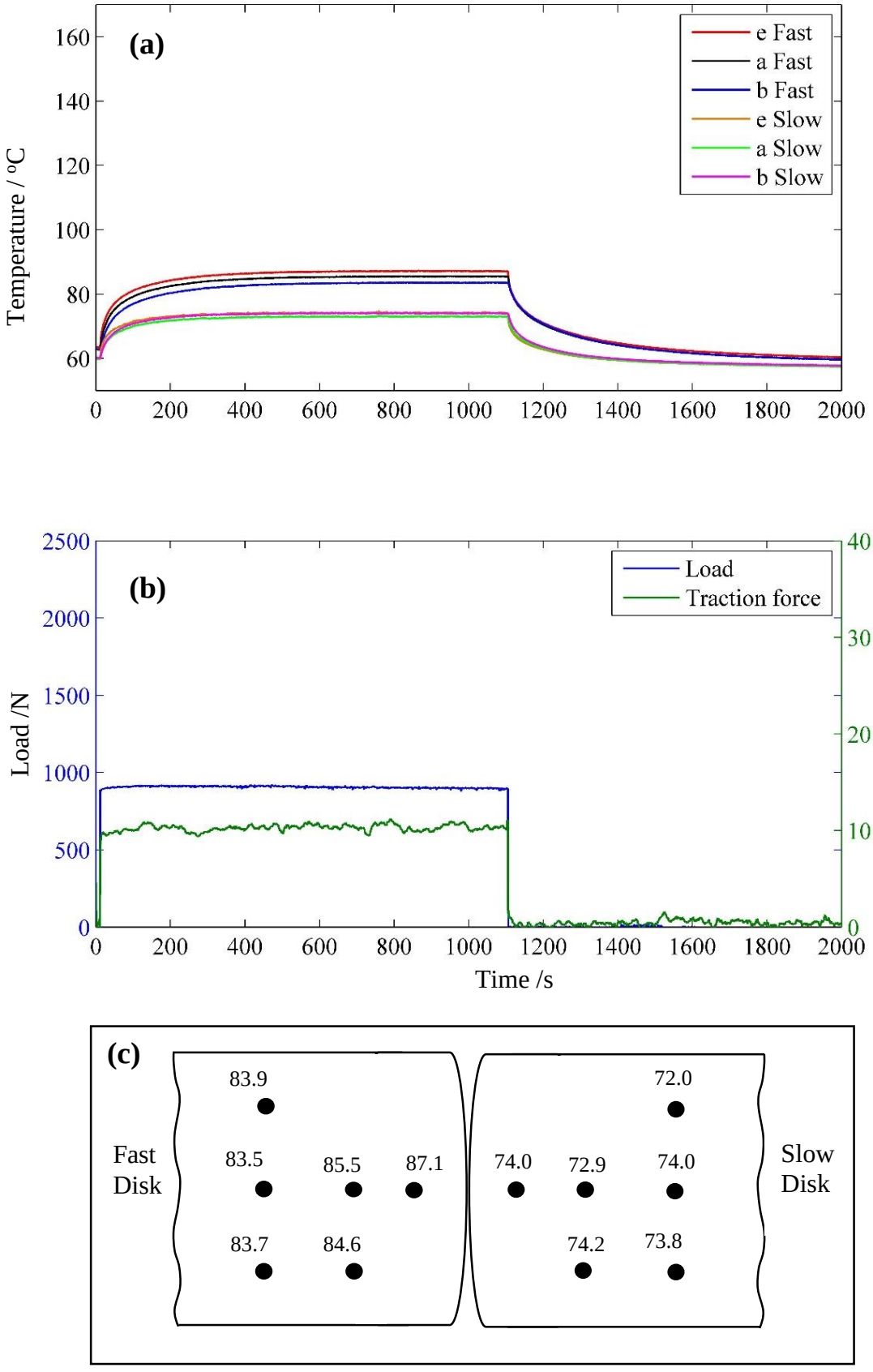

Figure 6.1:A1 test results**, (a)** the temperature of the central thermocouples, **(b)** the load and traction forces, **(c)** the temperature map °C at the approximately steady state.

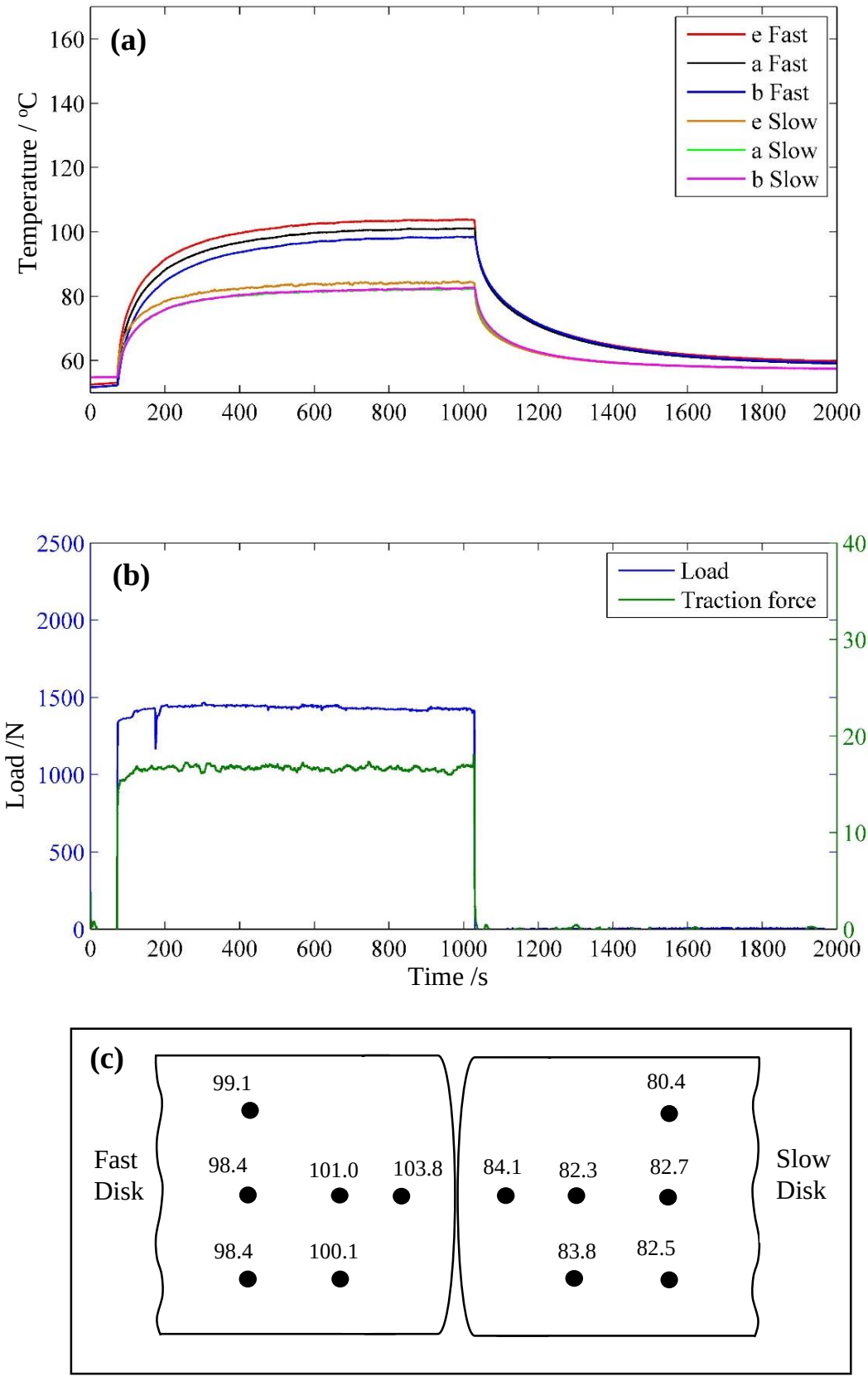

Figure 6.2: A2 test results**, (a)** the temperature of the central thermocouples, **(b)** the load and traction forces, **(c)** the temperature map °C at the approximately steady state.

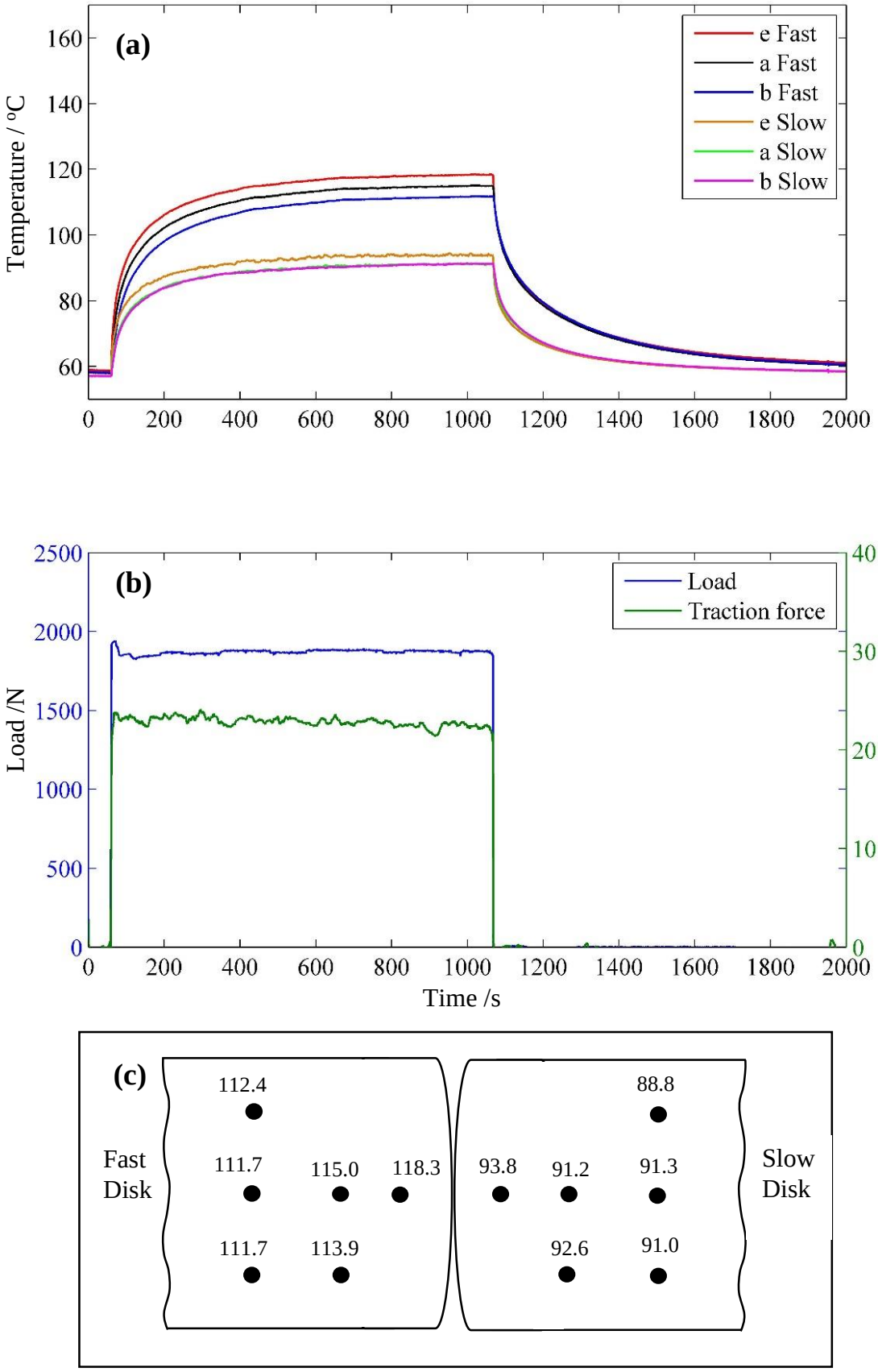

Figure 6.3: A3 test results**, (a)** the temperature of the central thermocouples, **(b)** the load and traction forces, **(c)** the temperature map °C at the approximately steady state.

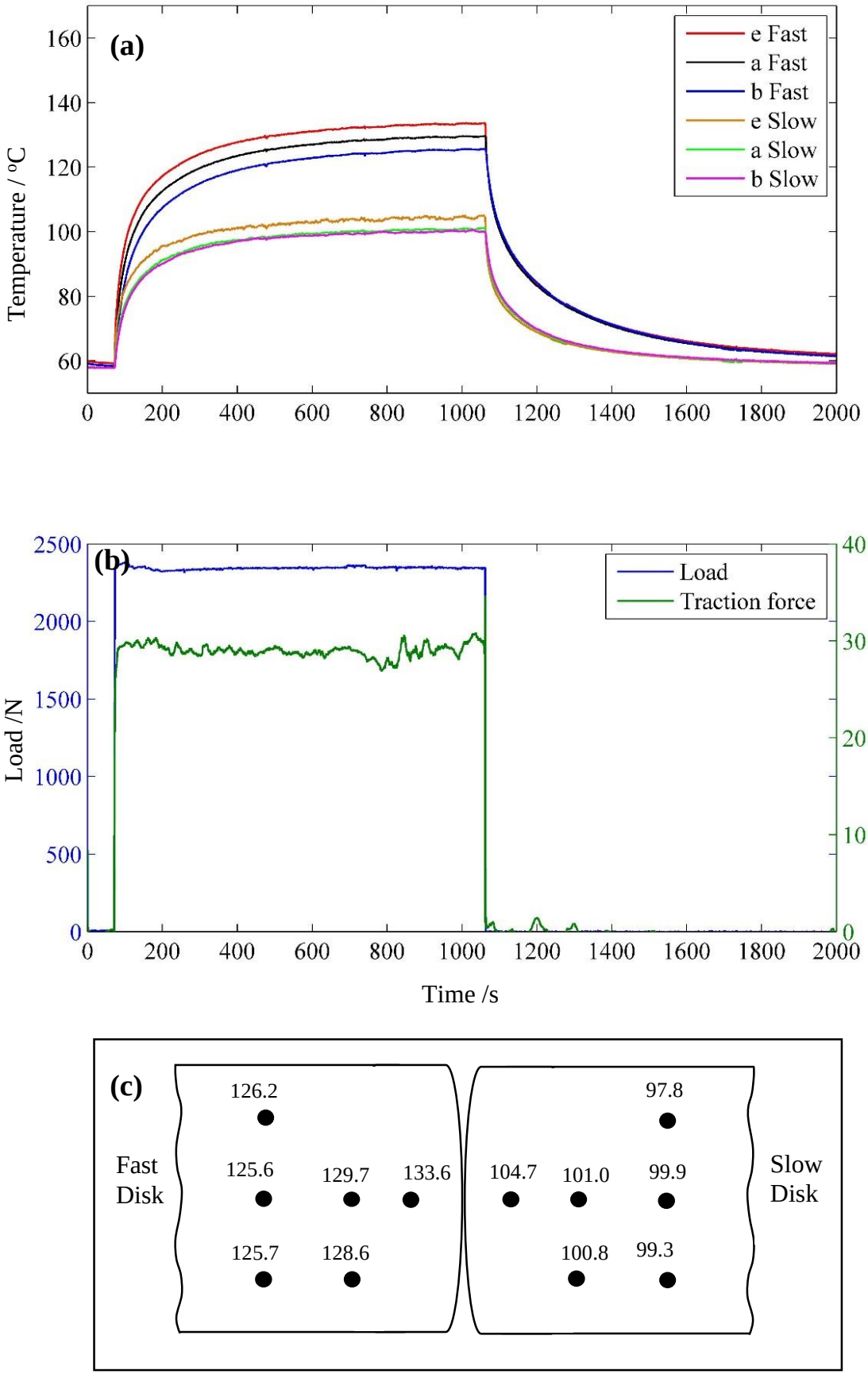

Figure 6.4: A4 test results**, (a)** the temperature of the central thermocouples, **(b)** the load and traction forces, **(c)** the temperature map °C at the approximately steady state.

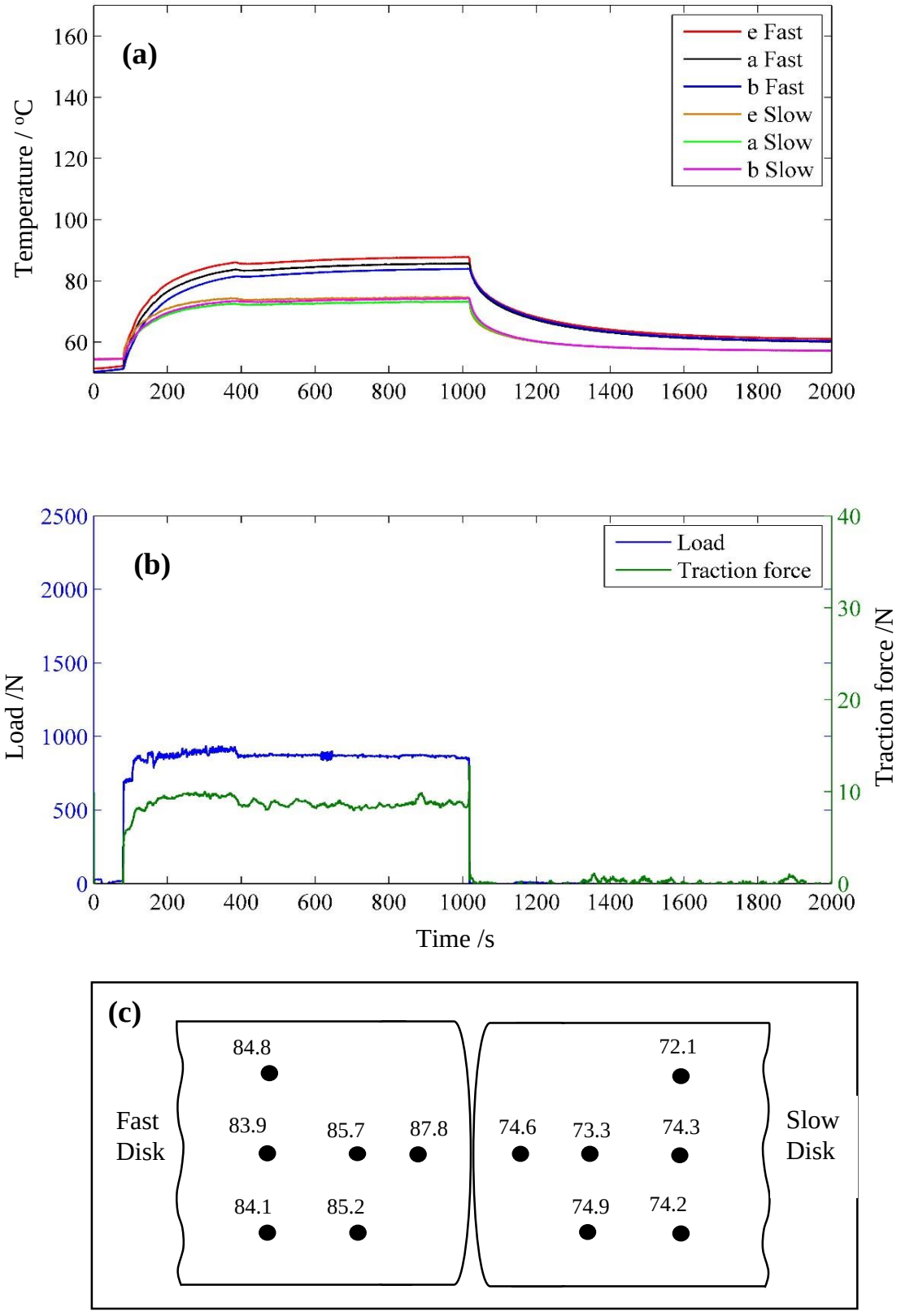

Figure 6.5: B1 test results**, (a)** the temperature of the central thermocouples, **(b)** the load and traction forces, **(c)** the temperature map °C at the approximately steady state.

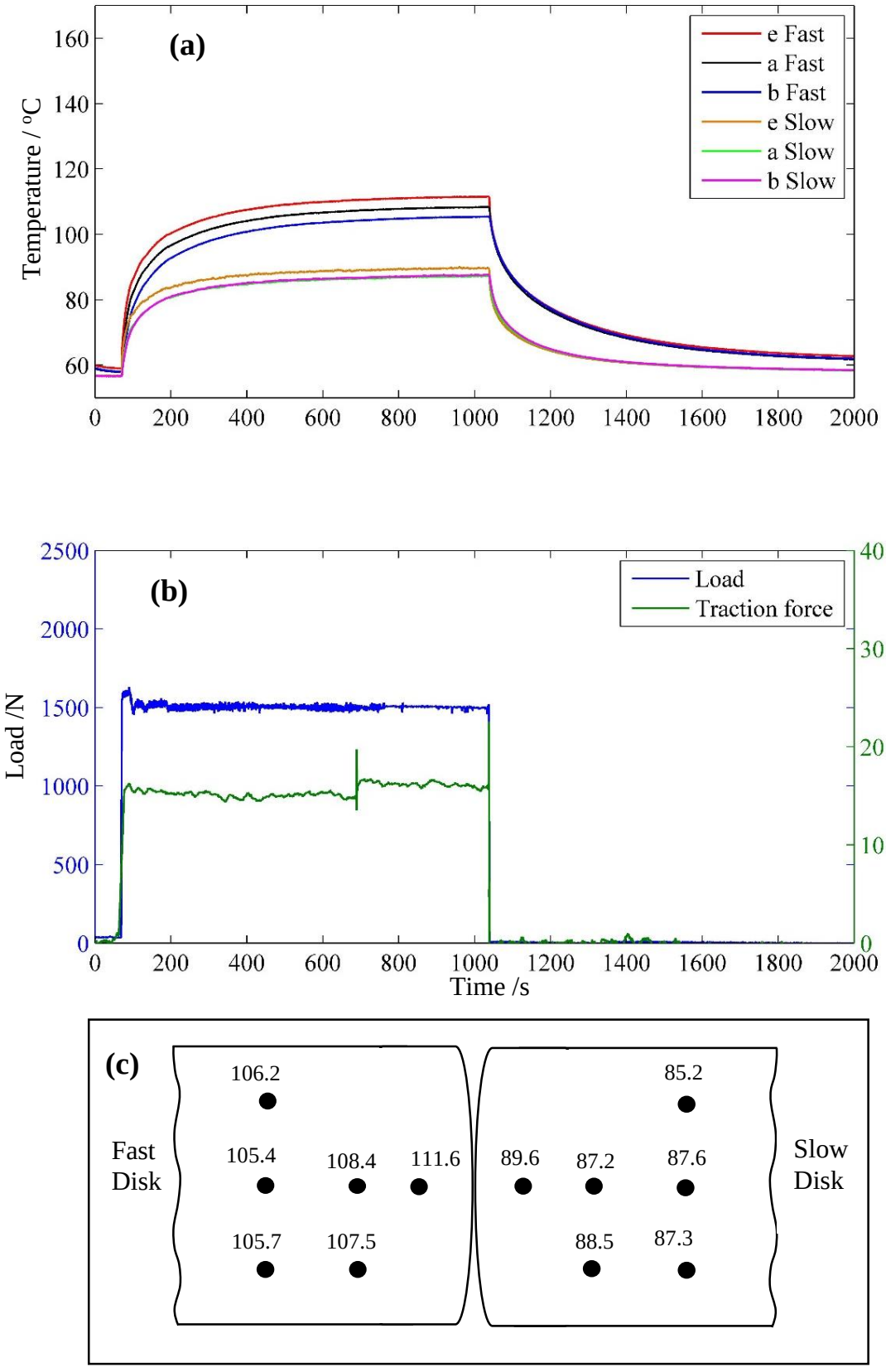

Figure 6.6: B2 test results**, (a)** the temperature of the central thermocouples, **(b)** the load and traction forces, **(c)** the temperature map °C at the approximately steady state.

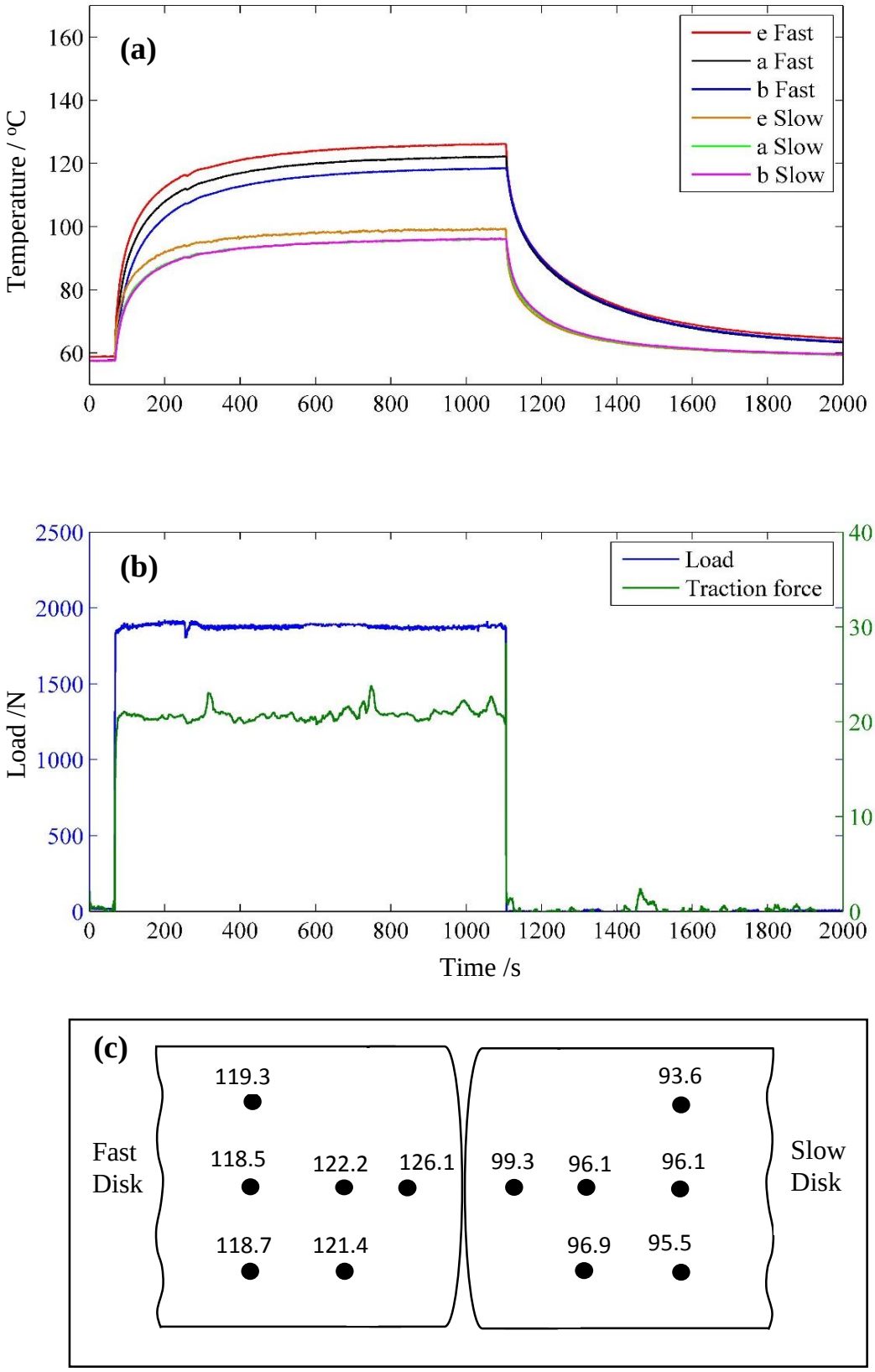

Figure 6.7: B3 test results**, (a)** the temperature of the central thermocouples, **(b)** the load and traction forces, **(c)** the temperature map °C at the approximately steady state.

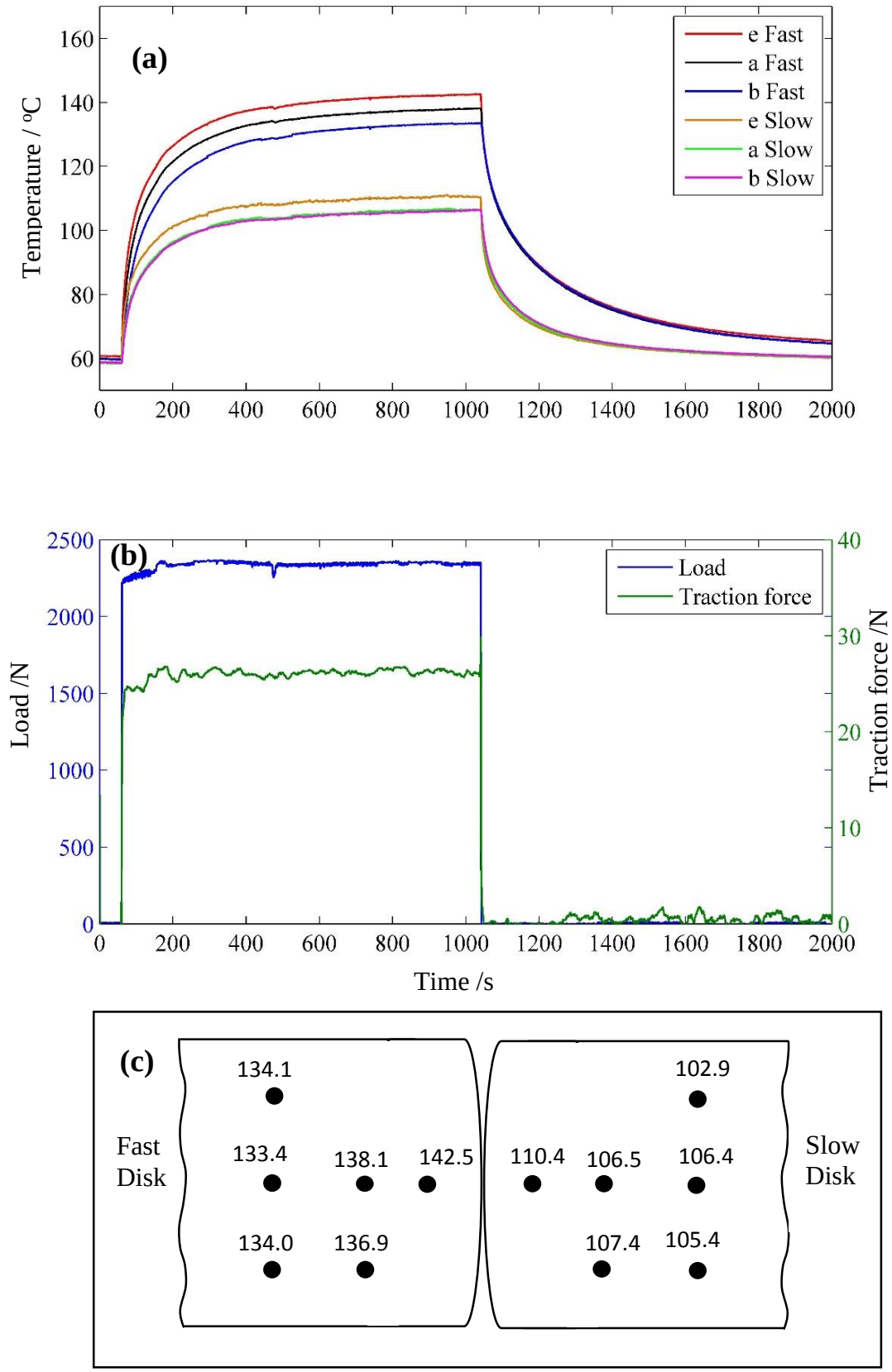

Figure 6.8: B4 test results**, (a)** the temperature of the central thermocouples, **(b)** the load and traction forces, **(c)** the temperature map °C at the approximately steady state.

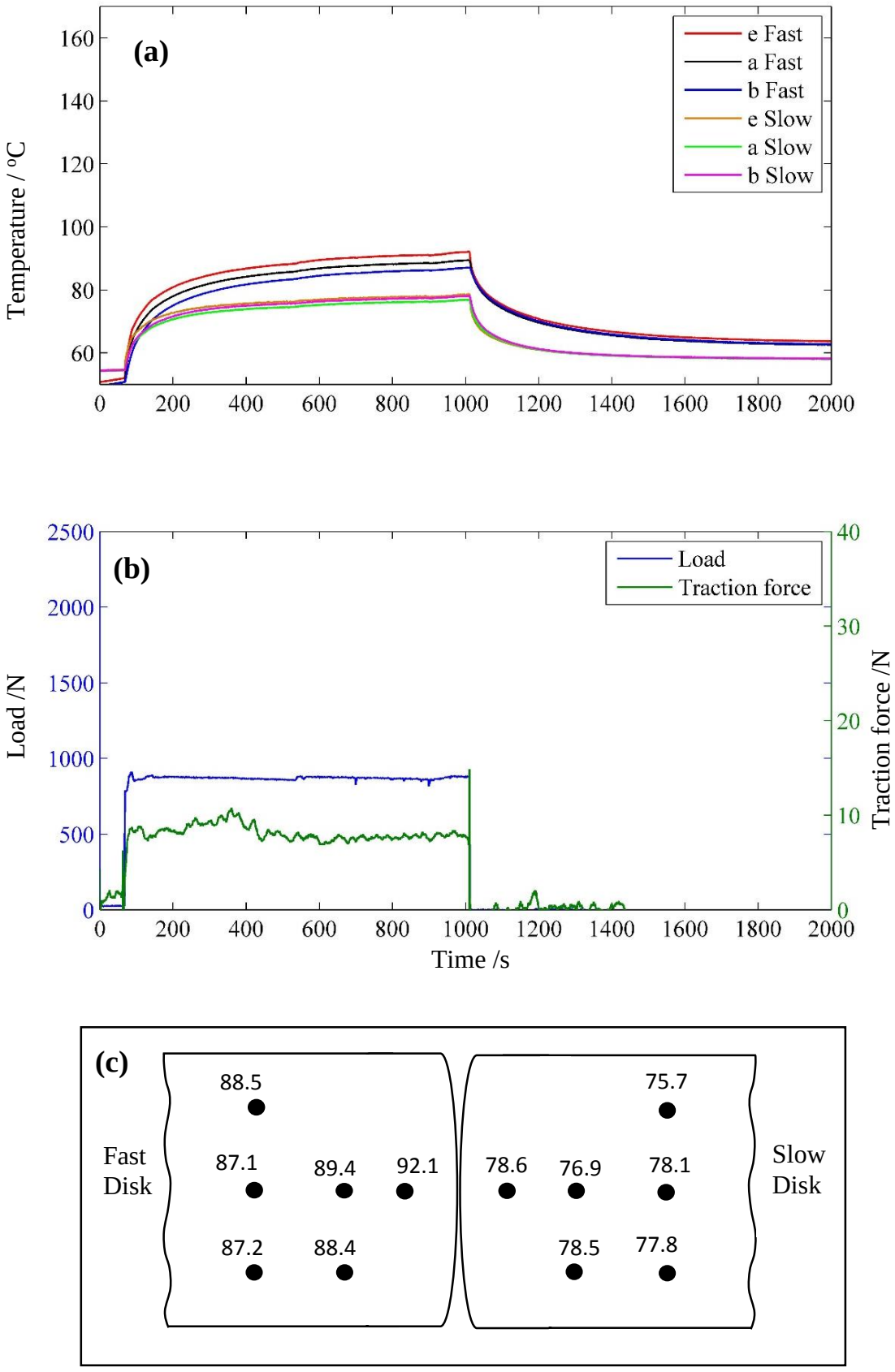

Figure 6.9: C1 test results**, (a)** the temperature of the central thermocouples, **(b)** the load and traction forces, **(c)** the temperature map °C at the approximately steady state.

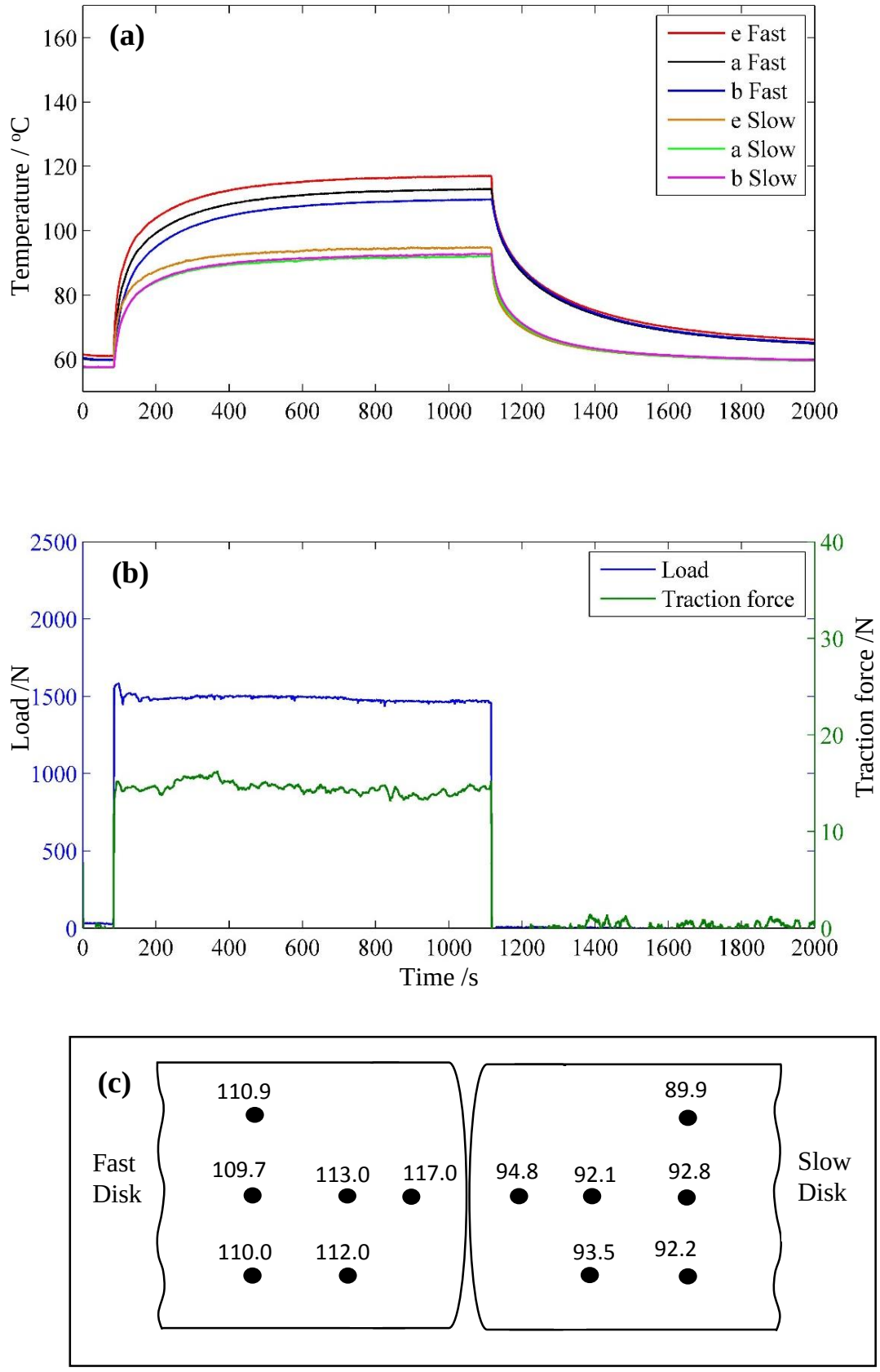

Figure 6.10: C2 test results**, (a)** the temperature of the central thermocouples, **(b)** the load and traction forces, **(c)** the temperature map °C at the approximately steady state.

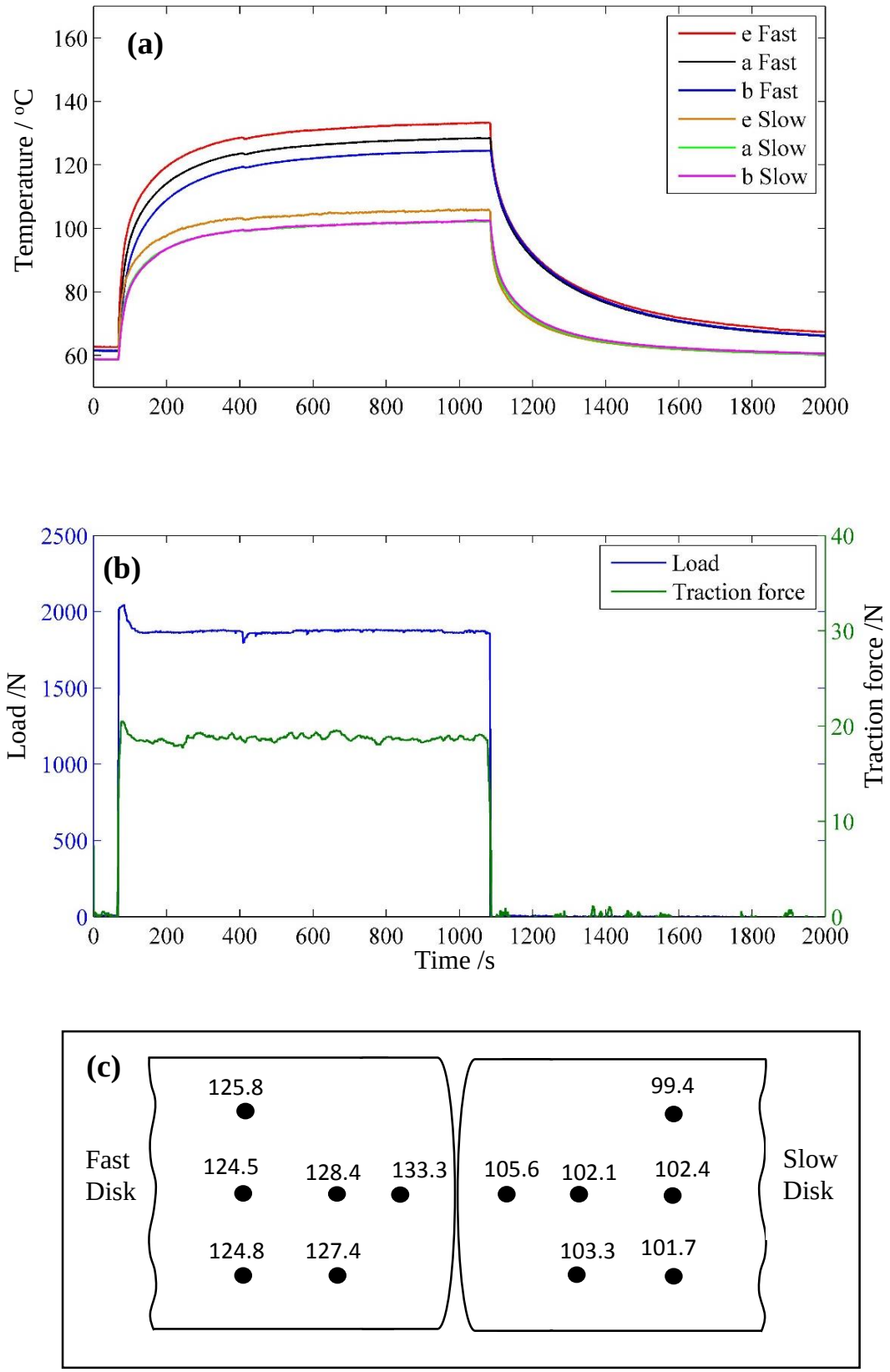

Figure 6.11: C3 test results**, (a)** the temperature of the central thermocouples, **(b)** the load and traction forces, **(c)** the temperature map °C at the approximately steady state.

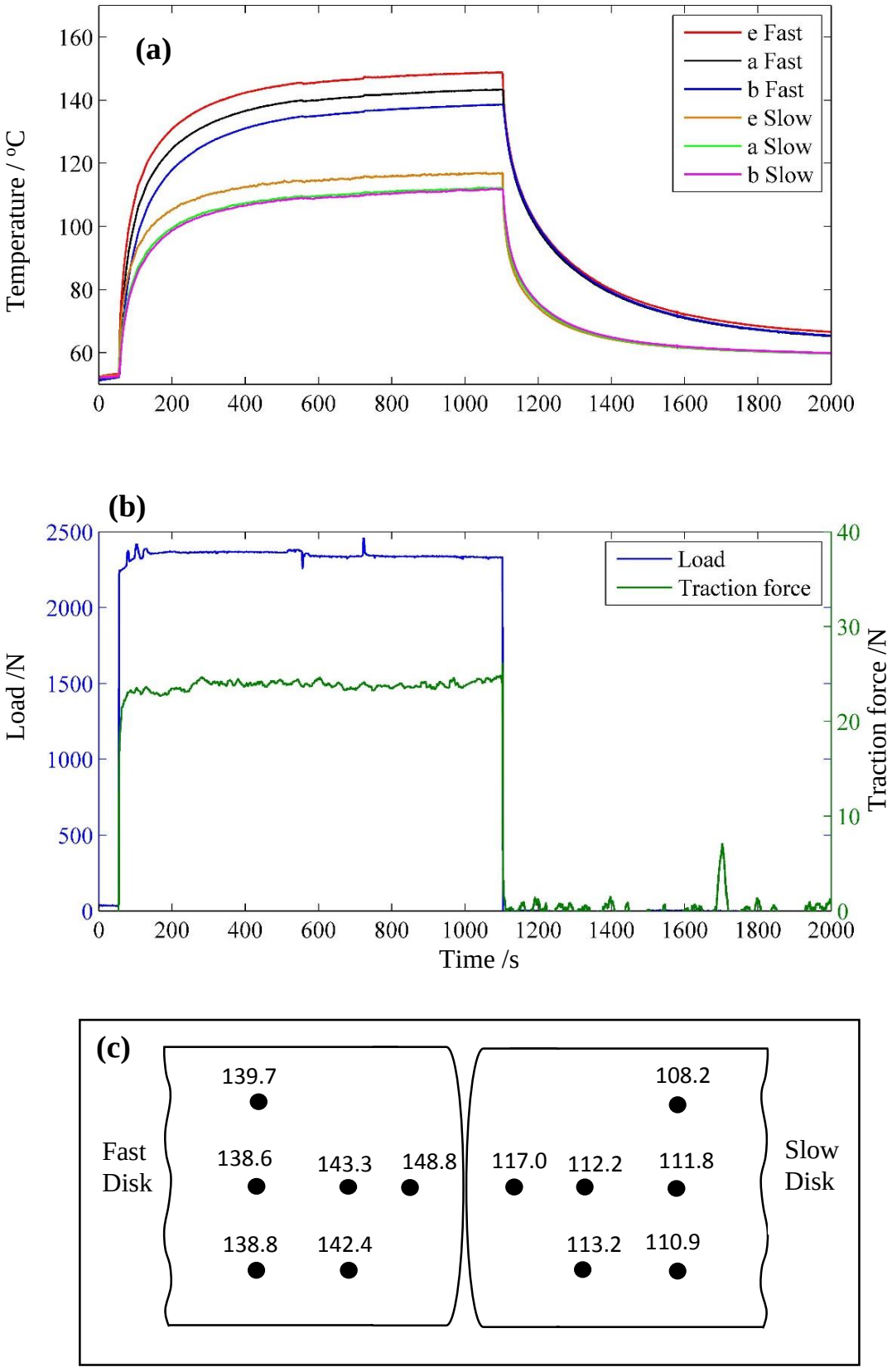

Figure 6.12: C4 test results**, (a)** the temperature of the central thermocouples, **(b)** the load and traction forces, **(c)** the temperature map °C at the approximately steady state.

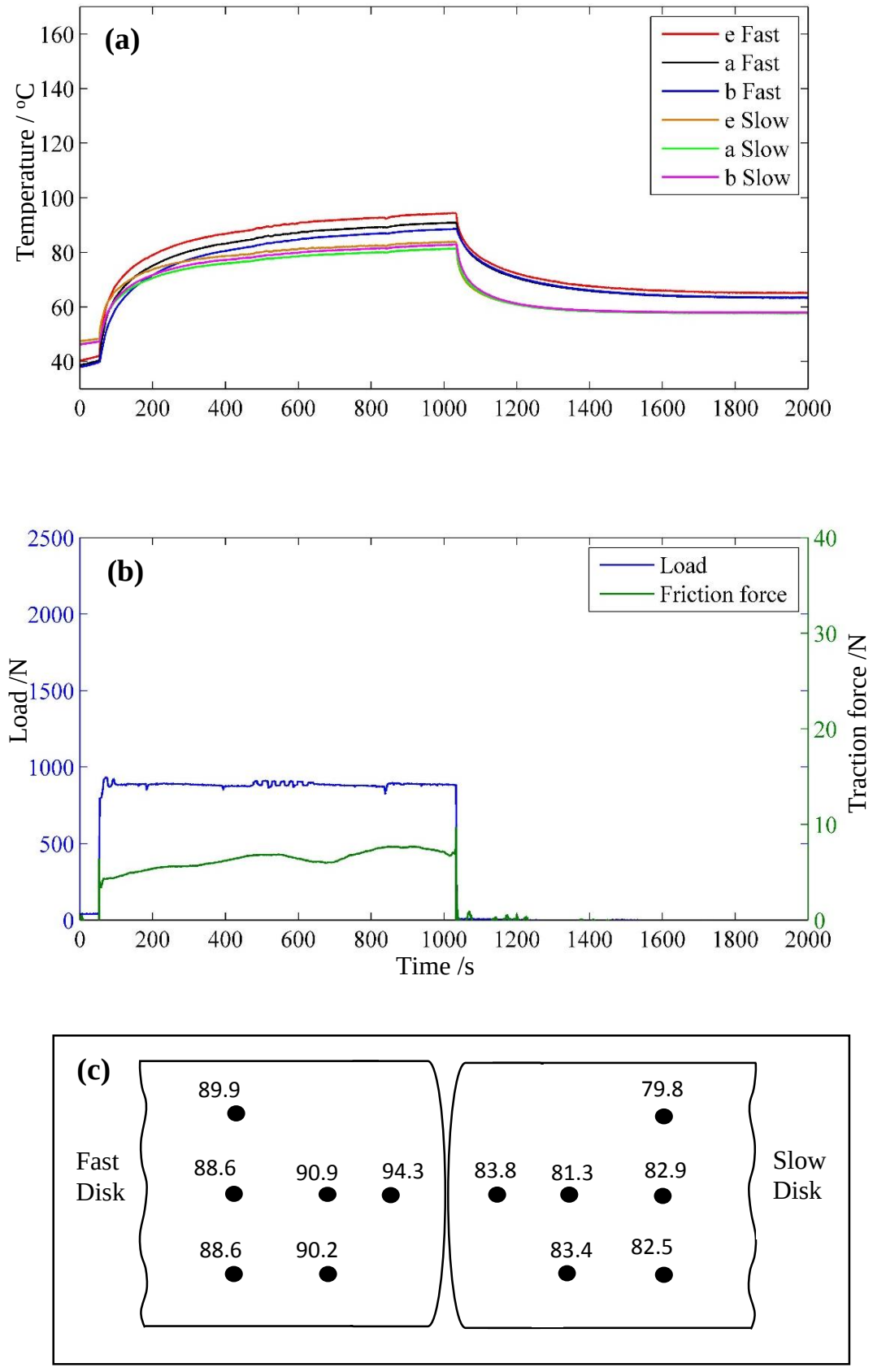

Figure 6.13: D1 test results**, (a)** the temperature of the central thermocouples, **(b)** the load and traction forces, **(c)** the temperature map °C at the approximately steady state.

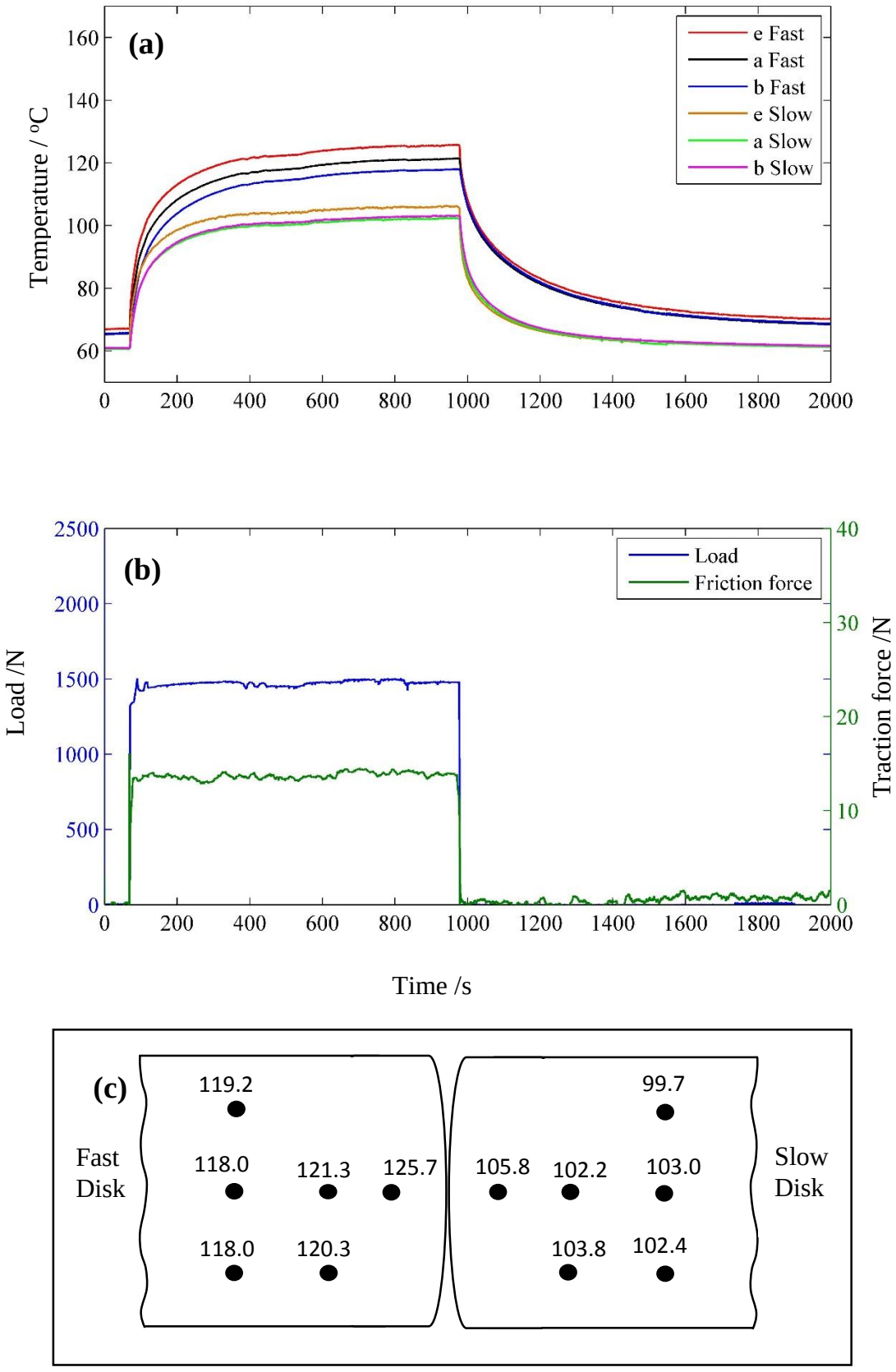

Figure 6.14: D2 test results**, (a)** the temperature of the central thermocouples, **(b)** the load and traction forces, **(c)** the temperature map °C at the approximately steady state.

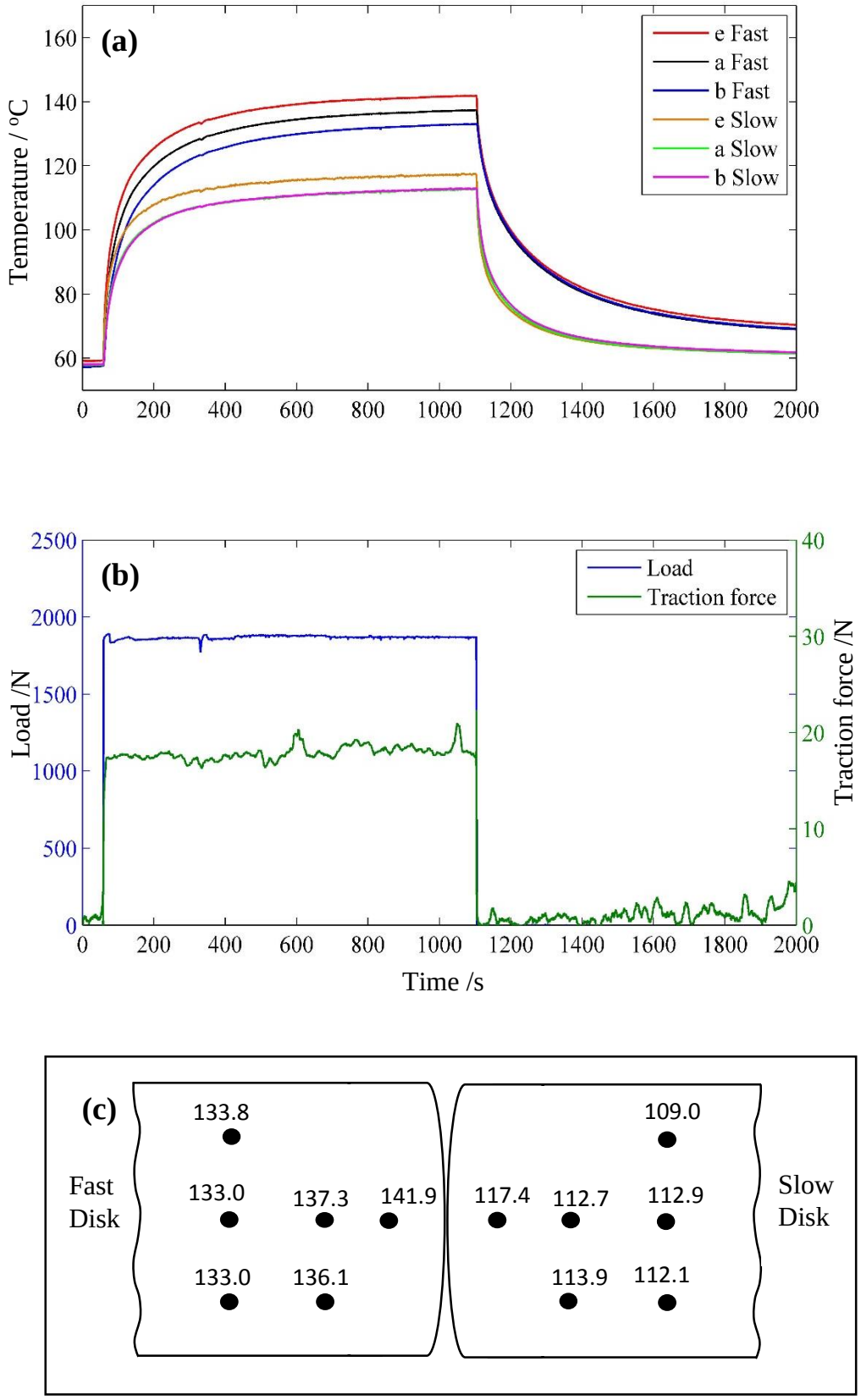

Figure 6.15: D3 test results**, (a)** the temperature of the central thermocouples, **(b)** the load and traction forces, **(c)** the temperature map °C at the approximately steady state.

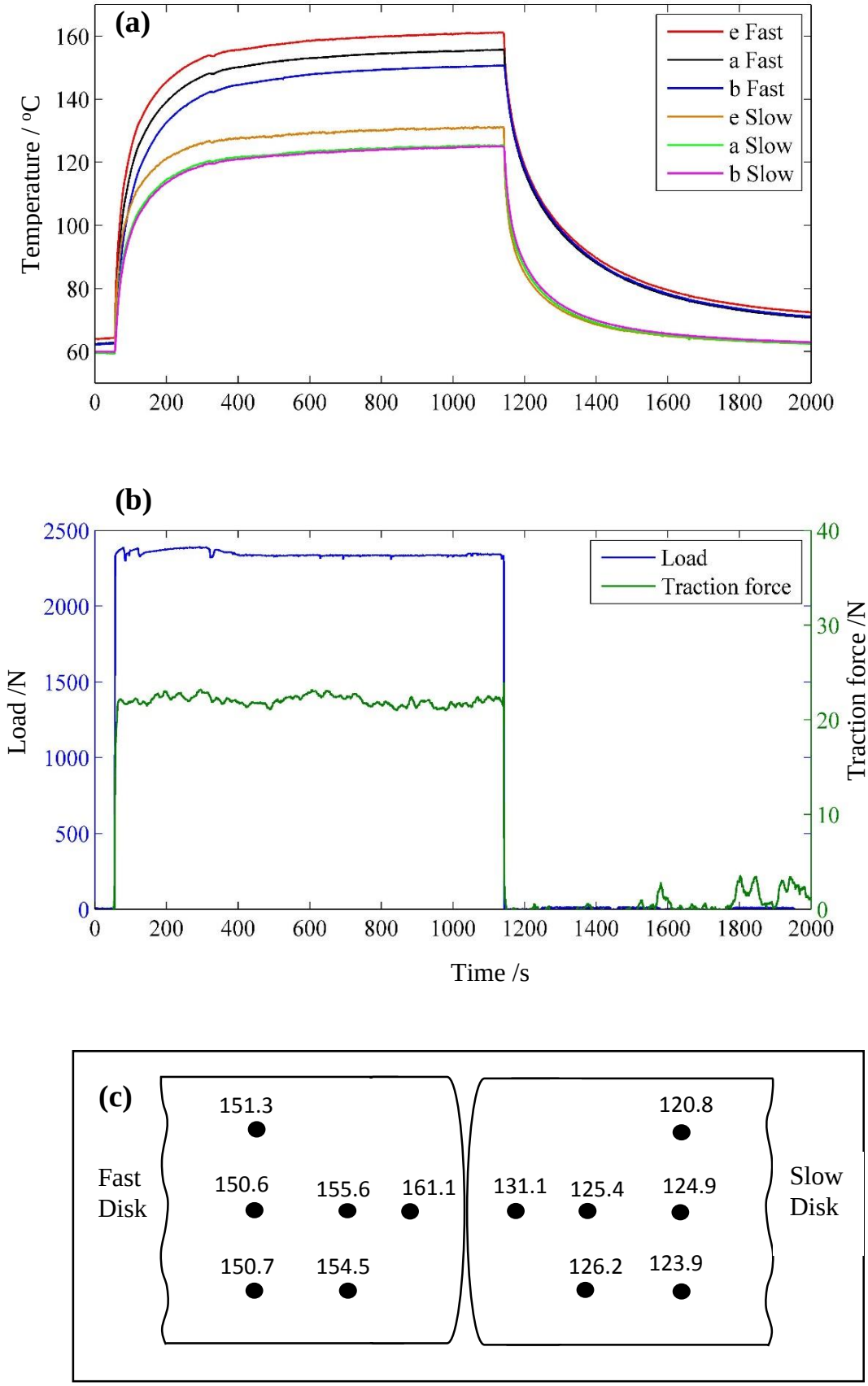

Figure 6.16: D4 test results**, (a)** the temperature of the central thermocouples, **(b)** the load and traction forces, **(c)** the temperature map °C at the approximately steady state.

6.4. Assessments of the measured temperature

6.4.1. The bulk temperature of the disks

The previous experimental results carried out on the same test rig in the work of Patching (1994) and Clarke (2009) showed that the fast disk reached significantly higher temperature than the slow disk. This phenomenon is repeated again in the current work, as can be seen for 16 EHL tests which are shown in Figure 6.1 to Figure 6.16. The results also confirm the expected trend of increased temperature in both disks with increasing load and sliding speed. Figure 6.17 shows the bulk temperature which is the mean temperature of the six thermocouples versus the applied load in each disk at the approximately steady state. In this figure, the results of the 16 tests are arranged into 4 groups according to the sliding speeds which are 10 m/s, 13 m/s, 16 m/s and 20 m/s in Figure 6.17 a, b, c, and d respectively.

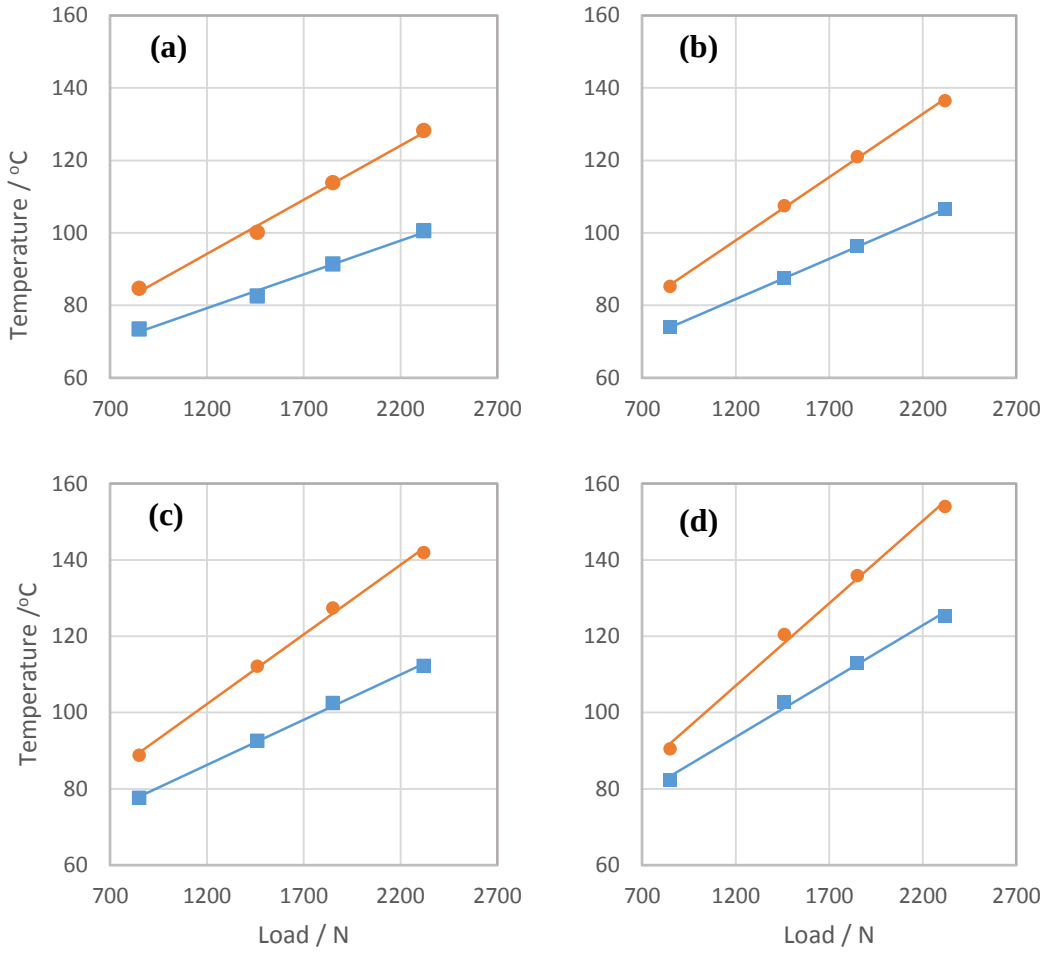

Figure 6.17: The bulk temperature versus load of the test disks at the end time of loading (approximately steady state), where orange indicates the fast disk and blue for the slow disk. Results are shown for sliding speeds of **(a)** 10 m/s, **(b)** 13 m/s, **(c)** 16 m/s and **(d)** 20 m/s

In Figure 6.17 the data are plotted with least square trend lines and it can be seen that the data follow these lines broadly in all the 16 tests. This indicates that the instrumented test rig and the experimental programme produce reliable EHL thermal results.

However, some uncertainties appear in the measured temperature for the individual thermocouples especially in the case of the slow disk. This was investigated extensively and will be reported in the next section.

6.4.2. Investigations on results uncertainties

The generated heat within the contact zone during the EHL test is conducted to both fast and slow disk. The contact zone is of an elliptical Hertzian shape which is located on the centre of the running track of both disks. During the EHL tests, the disk contact is centred at the middle of the running track around the circumferential of the disks. Hence, the temperatures that are measured by the central thermocouples are expected to be higher than those measured by the thermocouples on both sides of the disk at the same radial level. It is also expected that the centreline thermocouples measure higher temperatures the nearer they are to the heated surface. The slow disk results show significant asymmetry in the temperature map which is shown in part c of Figure 6.1 to Figure 6.16. In these figures, it can be seen that the significant asymmetry leads to higher temperatures being measured by the ***c*** and ***b*** thermocouple than the temperature measured by the ***a*** thermocouple. This un-expected temperature measurement led to several steps of investigation to understand this matter, which are now described in turn:

6.4.2.1. Thermocouple locations and wiring

The first step was an inspection of the thermocouple positions and wiring. This was to check that every thermocouple was installed in its correct place and connected to the appropriate channel of the data acquisition system. This inspection was carried out by applying a heated soldering iron to the disk surface adjacent to each thermocouple position and observing their responses on the Labview software. The soldering iron was applied only for a short period (for approximately two seconds) in order not to change the mechanical properties of the running surface. After carrying out these

investigations, it was concluded that the installation and wiring of the thermocouples was correct configuration. Figure 6.18 shows the temperature measured by the six thermocouples in the slow disk during six point heating tests. The figure parts (a) to (f) are for testing the thermocouples ***a*** to ***f*** respectively.

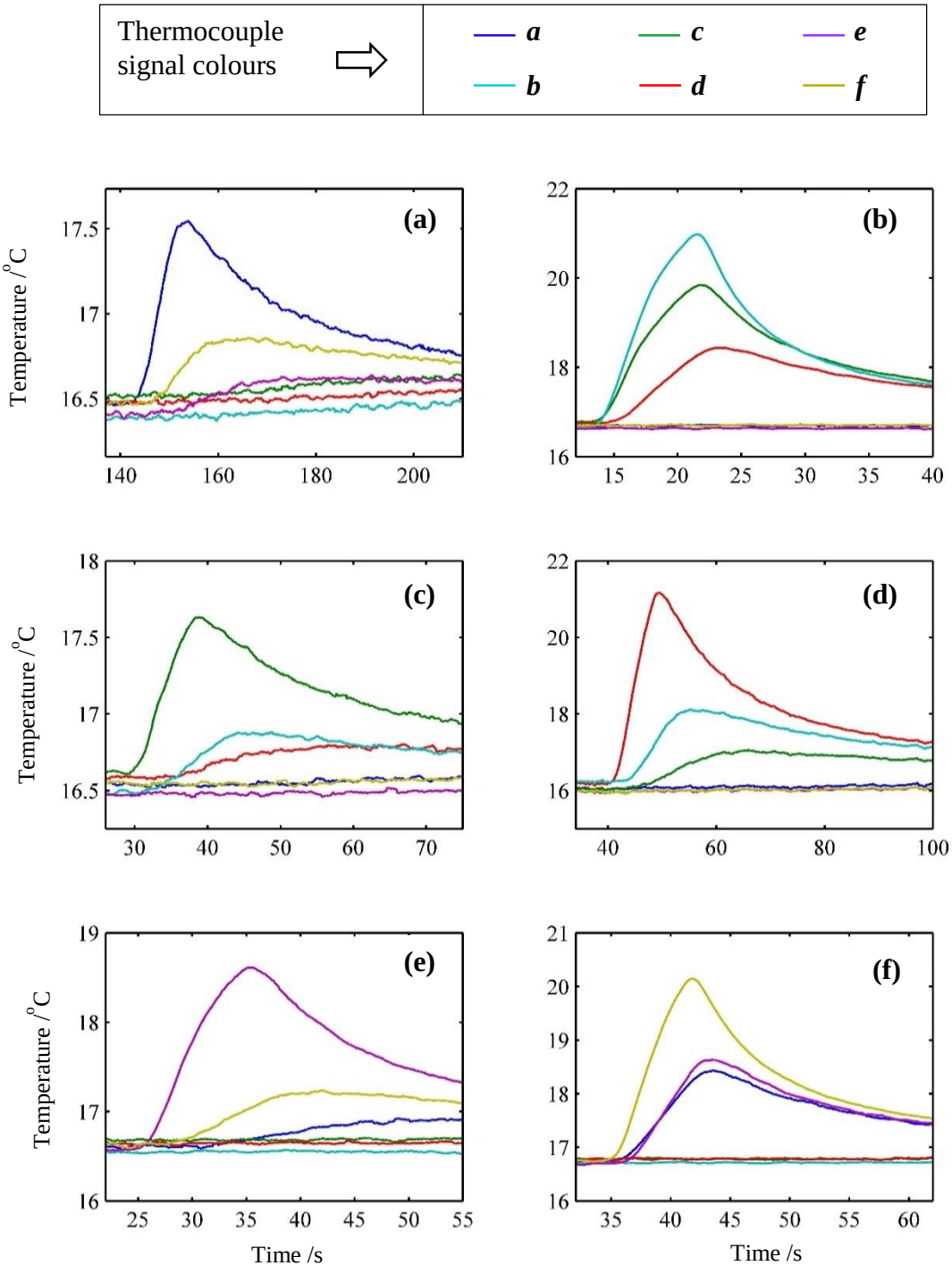

Figure 6.18: The thermocouple installation and wiring examination of the slow disk by applying a heated soldering iron, figures.**(a)** to **(f)** corresponds to positioning the iron at the position of thermocouples ***a*** to ***f*** respectively.

Figure 6.18 shows that at each inspection process, the temperature rises significantly for one thermocouple in comparison with the others which clearly establishes its identity. In each inspection process, it can also see that a further two thermocouples show a lesser response, whilst three of thermocouples do not show any response. This is because the thermocouples are located as two groups, each of three thermocouples located close to each other, and the two groups are well separated.

6.4.2.2. Location of the point of contact

Further investigation was carried out to determine if the disks axes were parallel to each other after installation in the rig. As the disks are crowned, they contact at an elliptical point contact when loaded. If their axes were not parallel, this point of contact would not be located at the centre of the disk width and the generated heat within the zone would not be conducted symmetrically into the disk. This was examined by applying a temporary coating material (engineer's blue) on the surface of the fast disk. Consequently, the stationary disks were loaded to the same load stage values used in the current work. After each loading, the marks on the slow disk were observed and showed that the contact zones were broadly at the centre of the disk width. Figure 6.19 shows photographs of the marks of the coating material on the slow disk after the four loading stages. This situation is difficult to photograph but it is clear that the blue ellipses are central on the disk whose whole axial width is shown in the photograph.

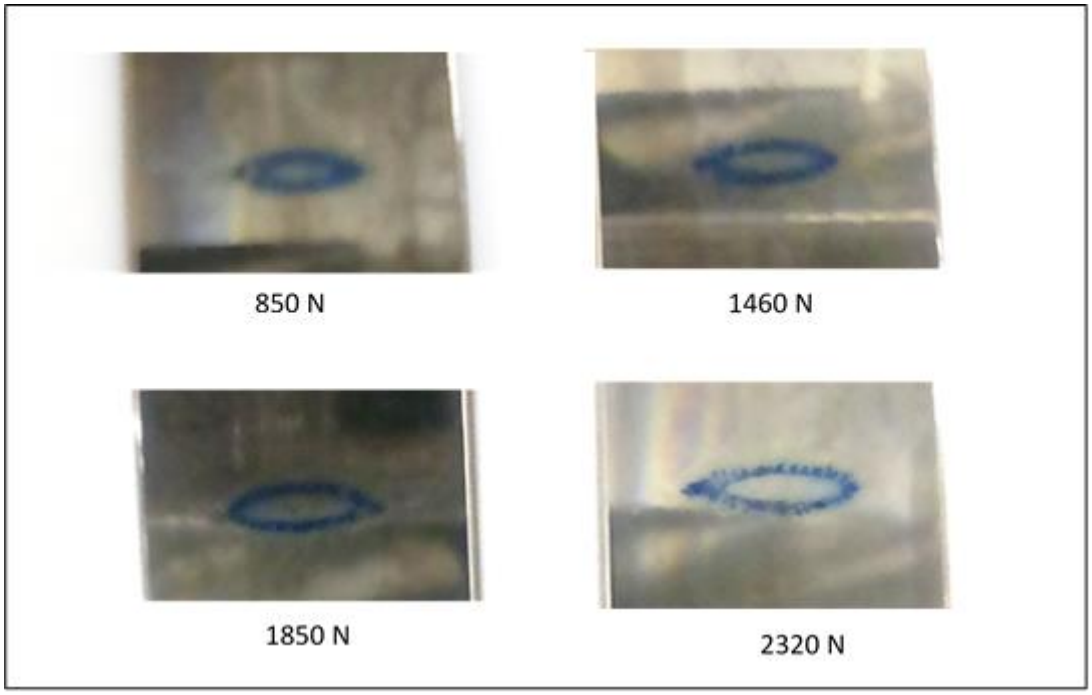

Figure 6.19: Photographs show the marks of the point of contact locations by loading the stationary disks with the existence of temporary coating material for four load stages shown.

6.4.2.3. Long term test

In order to make sure that the observed uncertainties in the measured temperatures are not due to a lag of response in the measurements, it was decided to carry out a test with a longer time of loading. A D4 test was carried out for 2250 s in the heating phase which is more than twice the typical time used usually during the EHL tests. Figure 6.20 shows the temperatures that are measured by the ***a*** and ***c*** thermocouples. It can be seen that the temperature at ***c*** continues to have a higher value than that at ***a***. Hence, it can be concluded that the uncertainties are not due to lag in response of measurements.

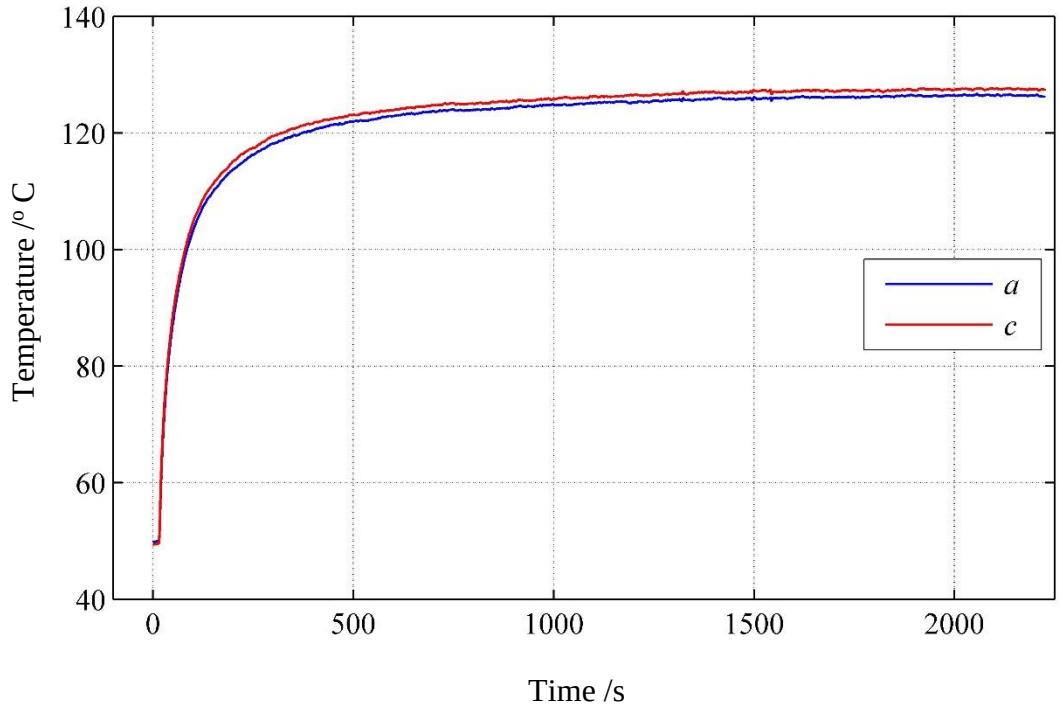

Figure 6.20: The temperatures measured by the thermocouples ***a*** and ***c*** of the slow disk for long time running of D4 EHL test.

6.4.2.4. Slip ring investigation

As described previously in section 2.2.1, the thermocouple wires were connected through slip rings in order to transfer signals from the rotating shafts to the other instruments for amplifying and conditioning. The thermocouples generate milli-volt low voltage signals which go through the slip rings and are then amplified and conditioned. Hence the error introduced at the slip ring might affect the low voltage signals and cause the unexpected results. Accordingly, the slip ring channels of thermocouples ***a*** and ***c*** were swapped. A D4 test was carried out with this interchange of slip rings and the corresponding temperature map is shown in Figure 6.21 along with the original temperature map. In this figure, it can be seen that the channel swap

did not make noticeable changes and the temperature at ***c*** was remains higher than the temperature at ***a***.

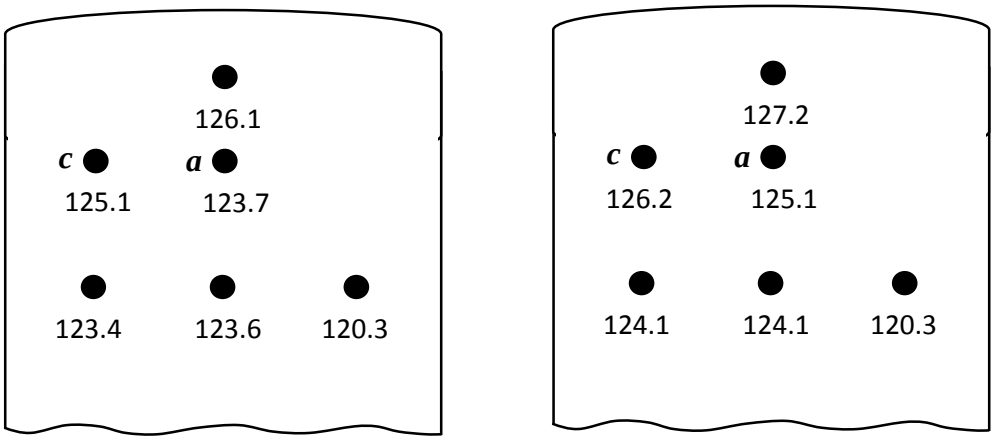

Figure 6.21: Temperature map ^{o}C for the slow disk; left with original slip ring arrangement, right with repeat experiment with slip ring channel interchanged.

6.4.2.5. Disk heating by using oil

In order to check the reliability of the thermocouples in measuring high temperatures, it was decided to run the rig without loading whilst the temperature of the oil in the tank was set to 150 ^{o}C. The purpose of this experiment was to check the measurement hardware and software function at a temperature of uniform heating unlike the heating in the EHL tests which is concentrated at the small area of the contact. The temperature was observed and recorded. Figure 6.22 shows the temperature map of the slow disk at approximately steady state after heating by the hot oil from the oil jet. It can be seen that all thermocouple measurements are very similar indicating an approximately uniform temperature distribution within the disk, which is compatible with the oil heating test. It should mentioned that the tank oil temperature is 150 ^{o}C but the disk temperature is approximately 125 ^{o}C, this is because the oil loses heat through the

pipes before reaching the oil jet. Again, the finding of this investigation suggest that the measurement system including the hardware and the software with the embedded calibration curves are reliable.

Figure 6.22: The temperature map ^{o}C of the slow disk when heated by high temperature oil.

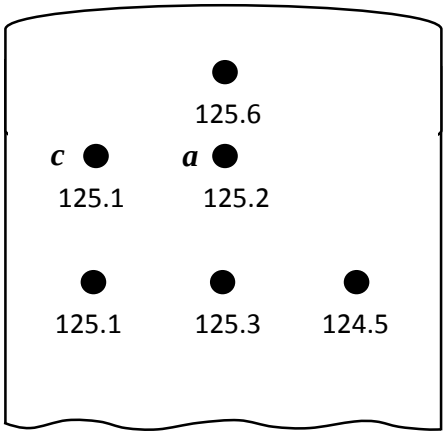

6.4.2.6. Bearing effects

As was described previously in section 2.2.1, each shaft is supported by a double row spherical roller bearing on the flexible coupling side and a cylindrical roller bearing on the slip ring side. These bearings are expected to be heated as a result of loading and high speed rotation. As a result, heat is conducted from the bearing into the shaft and might contribute to temperature asymmetry in the test disks. Consequently, four thermocouples were fixed on the housing of each bearing of the fast and slow disk. The temperatures at the bearing housings were recorded during a normal D4 test, these are shown in Figure 6.23.

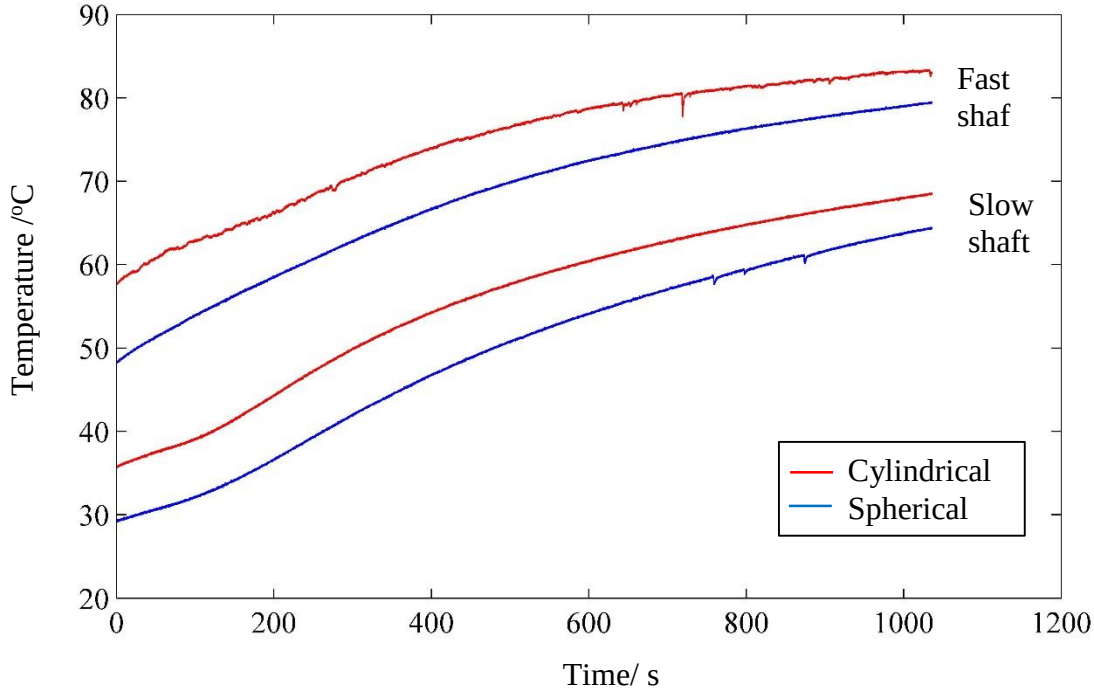

Figure 6.23: The temperature of the bearing housings during D4 experiment

Figure 6.23 shows several interesting aspects of the behaviour of the bearing. Firstly, for each bearing the temperature rose to approximately twice the value at the end of the test as compared with the temperature at the beginning of the test. Secondly, the temperature of the bearings of the fast shaft are significantly higher than these of the slow shaft. This is due to the fact that the fast shaft rotates at an angular speed four times that of the slow disk. The last important observation on Figure 6.23 is that the generated heat in the cylindrical bearing (which is at the ***c*** thermocouple side) is higher than that generated in the spherical bearing, the difference is more than 5 °C for both the slow and the fast shaft over the whole interval of the test. This temperature difference at both sides of the shaft, was thought to be a possible reason behind the temperature asymmetry of the slow disk. It also should be mentioned that the slow shaft is shorter than the fast shaft, i.e. the bearings in the slow shaft are closer to the disk and any temperature asymmetry on the part of the bearings might be reflected in

the temperature distribution in the slow shaft test disk. Further investigation was carried out to examine the bearing effects on the temperature distribution. A pure rolling test was conducted to observe the temperature rise in the test disks as a results of conducted heat from the bearings through the shafts. The fast shaft was uncoupled in order to achieve pure rolling as a result of the slow disk rotation when the disks were loaded in contact. During this test, the disks were loaded to the highest load (2320 N) to maximize the generated heat in the bearings, the temperature map of the slow disk is shown in Figure 6.24 at the end of the pure rolling test.

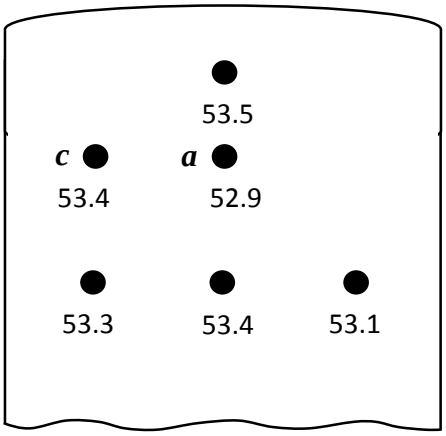

Figure 6.24: The temperature map ^{o}C of the slow disk at the end of the pure rolling test, the disks were loaded to 2320 N

Figure 6.24 shows that the bearing temperatures are not sufficient to change the temperature distribution within the slow disk and is not expected to be the reason behind the temperature asymmetry in the slow disk.

6.4.2.7. Convection coefficient and ambient temperature asymmetries

The effect of any possible asymmetry in the convection heat transfer coefficient over the running track of the disk, and ambient temperature asymmetry on the disk sides are investigated in this section. In the thermal model of the test disks constructed in chapter three, the convection heat transfer coefficient was assumed to be uniform over the width of the running track. If the supplied oil is not distributed uniformly over the width of the disk, the temperature map within the disks might be affected by this non uniformity. A temporary oil jet was installed to feed a large amount of oil in more symmetric mode across the running track. This jet is an oil pipe with two slots that deliver a wide stream of oil on both disks adjacent to the contact zone. The temperature map of the slow disk is shown in Figure 6.25 at the end of the loading stage of D4 test.

Figure 6.25: The Temperature map ^{o}C of the slow disk for D4 experiment after adding temporary oil jet.

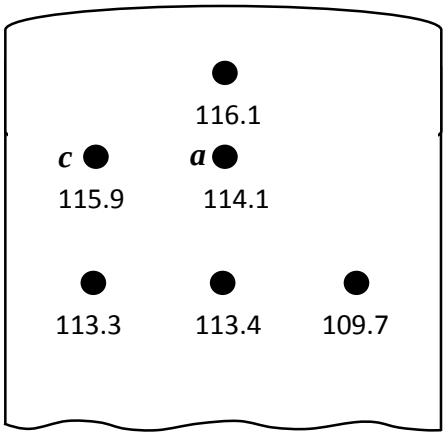

Figure 6.25 shows that the overall temperature is approximately 10 ^{o}C lower than the temperature map in the tests without the additional oil jet which is due to the enhanced cooling of the higher oil jet flow. However, the asymmetry in the temperature map

still exists which suggests that the original oil jet is not the reason behind the uncertainties in the results.

Further theoretical investigations were also carried out on the effects of possible asymmetries in the convection heat transfer coefficient and the ambient temperature. In the model, the convection heat transfer coefficient was distributed by two step uniform values, 200 $Wm^{-2}K^{-1}$ and 400 $Wm^{-2}K^{-1}$ on the disk surface as shown in Figure 6.26 . The aim of this analysis is to study the effect of the variation of the convection heat transfer coefficient on the temperature distribution within the disk. After modelling, the temperature distribution within the disk is shown in Figure 6.26. In this figure, the temperature at the positions of the thermocouples ***a*** and ***c*** is shown. This case can be compared with the normal case of uniform convection coefficient (300 $Wm^{-2}K^{-1}$) shown in Figure 6.27

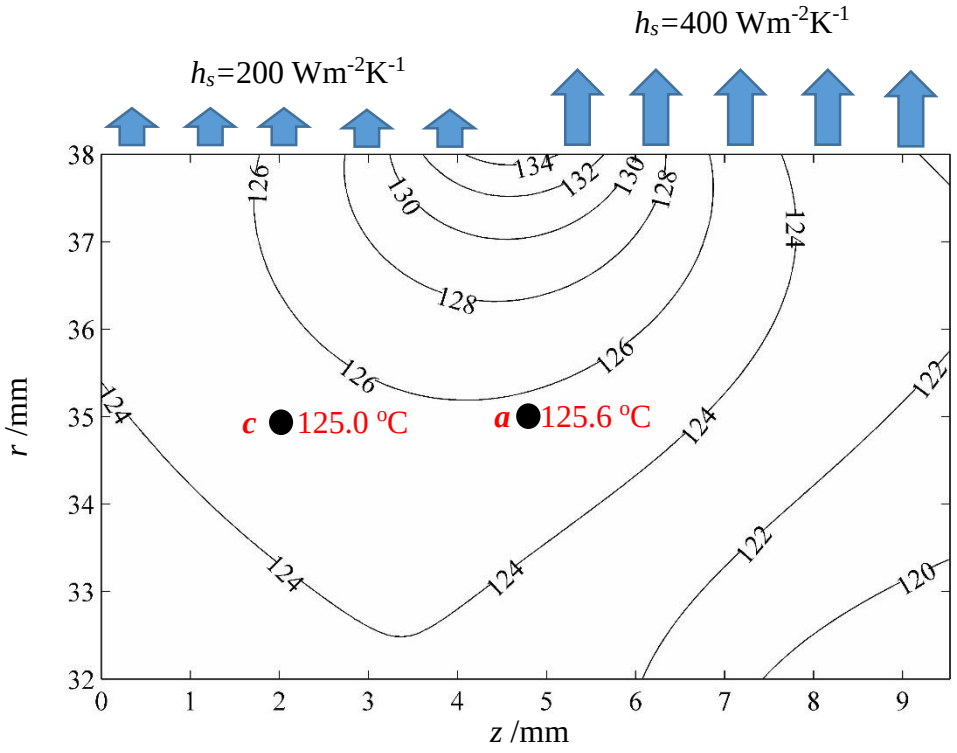

Figure 6.26: The effect of imposing non-uniform convection heat transfer coefficient on the temperature distribution within the slow disk.

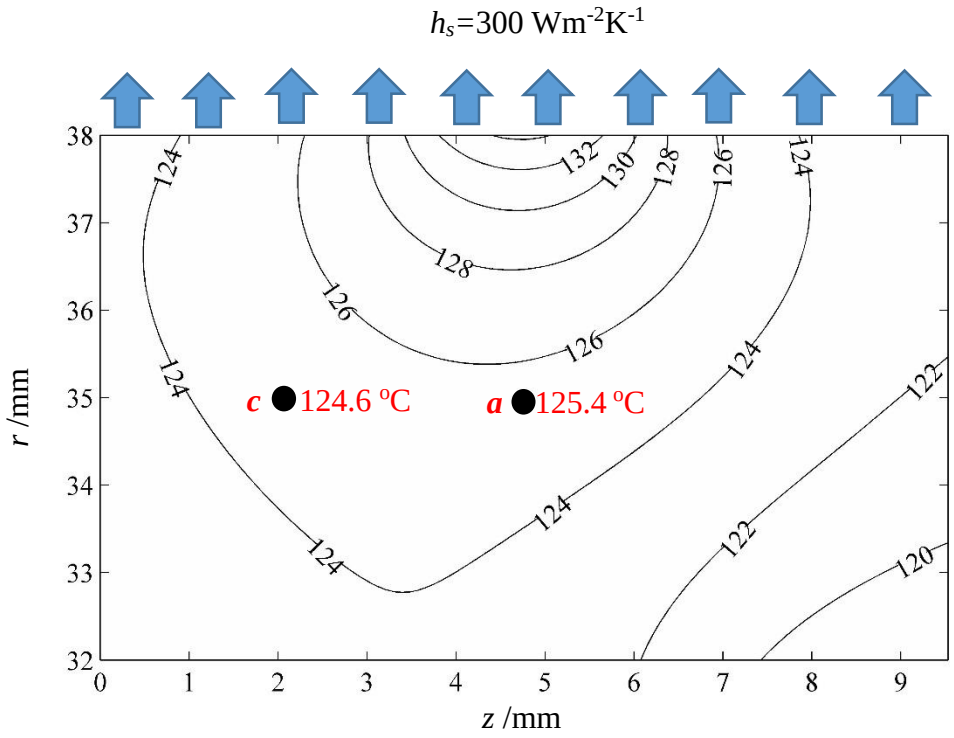

Figure 6.27: The temperature distribution within the slow disk for normal D4 test.

By comparing the temperature distribution in the normal case in Figure 6.27 with the case having a huge asymmetry in the convection coefficient of Figure 6.26, it can be seen that the temperature does became higher at the left hand side of the disk, but not to the extent of making the temperature at ***c*** higher than that at ***a,*** which is the case in the experiments.

To study the effect of a possible asymmetry in the ambient temperature on the sides of the disk a simulation was run with 70 °C on the left hand side of the disk and the right hand side was kept at 60 °C (i.e. outside the ceramic insulations). The resulting temperature distribution is shown in Figure 6.28

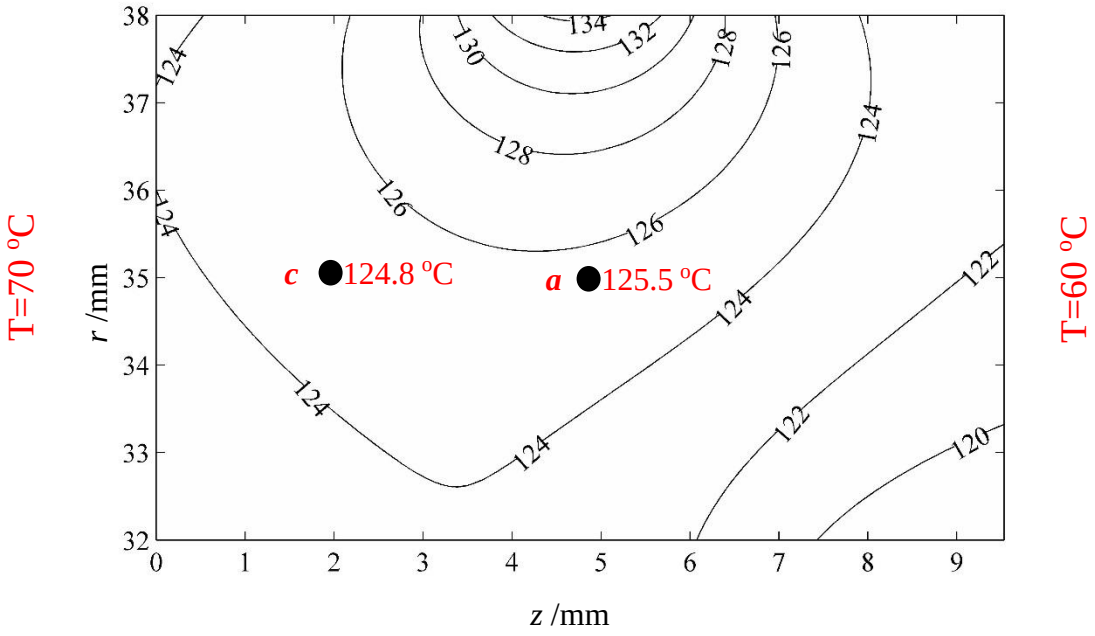

Figure 6.28: The temperature distribution within the slow disk for normal D4 test by assuming asymmetry of the ambient temperature so the side surfaces, noting that the ambient temperature is outside the ceramic insulation.

It can be seen again that the temperature distribution is changed by the effect of the ambient temperature asymmetry but not to the extent of making the temperature at ***c*** higher than that at ***a***, as found in the experimental results.

6.4.3. Circumferential temperature variation

The previous investigations on the un-expected temperature measurements were based on a possible asymmetry in the axial direction within the disks. In this section, the possibility of temperature variation in the circumferential direction is investigated. The two dimensional thermal model that was derived in section 3.4 is based on the assumption of no temperature variation in the circumferential direction. This assumption was verified in terms of the heat conduction from the contact zone in section 3.4.1. It was concluded that the circumferential temperature change penetrates

to a short distance below the surface without reaching to the position of the thermocouples. As a result, the conducted heat into the disk was imposed uniformly in the circumferential direction. However, the heat that leaves the disks was also assumed to be uniform around the circumferential direction. This is discussed in the current section.

The installed thermocouples are located at different angular positions on the test disks as shown in Figure 6.29. In general, they are concentrated in two groups at 180° apart, whilst in each group the thermocouples are 15° apart from each other. Accordingly, if there is an angular variation in the way that heat leaves the disk, the temperature at the location of one group will vary from the temperature at the location of the other group. An inspection was conducted in terms of this aspect on the current experimental work, and the experiments of Voller (2010) and Clarke (2009).

For the current work, Figure 6.29 shows a schematic diagram of the thermocouples' angular arrangement and the temperature map in the slow disk during the low load test A1.

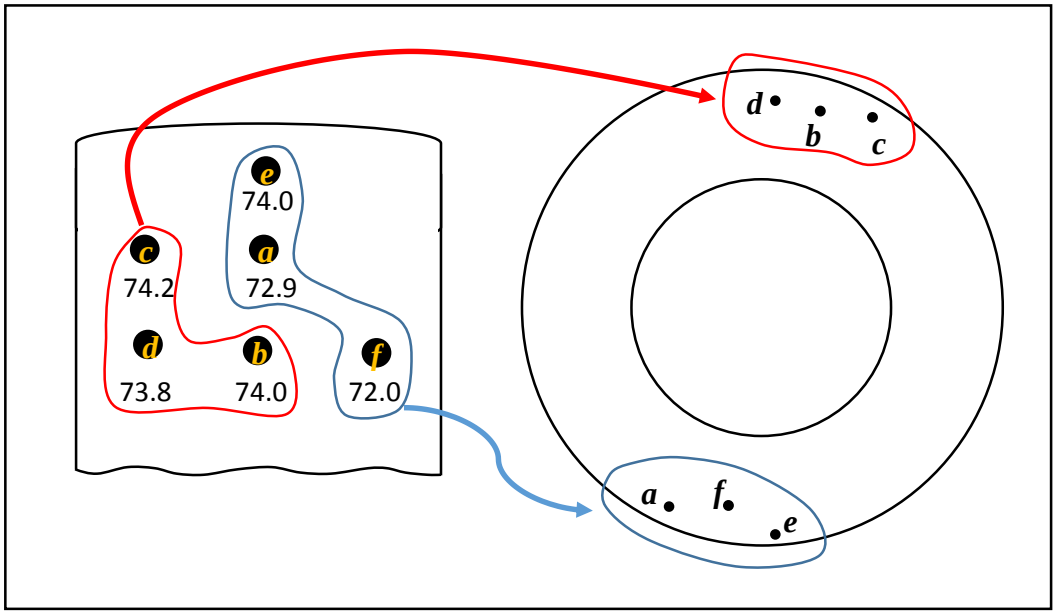

Figure 6.29: The temperature map °C (left), and the thermocouple circumferential positions (right) in the slow disk of test A1 of the current work.

By observing the temperature map in Figure 6.29, it can be seen that the thermocouples enclosed by the red curve generally have higher temperatures than those which is enclosed by the blue curve. Regarding the centreline thermocouples ***e***, ***a*** and ***b***, T_b T_e are equal and higher than T_a which is illogical. Thermocouple ***e*** is also much closer to the surface and must have the highest temperature. It can be noticed that comparing the measurements inside each group are logically related, however un-expected measurement behaviour is noticed when comparing a measurement in one group with a measurement in the other group. This uncertainty was found also in the work of Clarke (2009) and Voller (2010) in the fast disk for the tests mentioned in Figure 6.30 and Figure 6.31 respectively. In Figure 6.30, it can be seen that T_b and T_e are higher than T_a which is illogical and in Figure 6.31, T_e is higher than T_a which is also illogical.

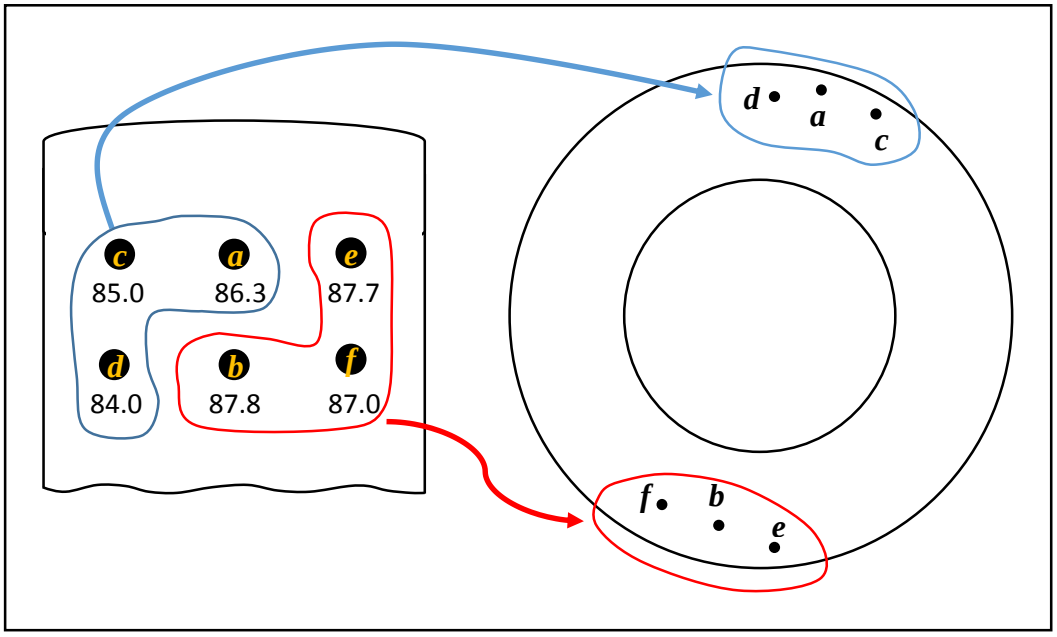

Figure 6.30: The temperature map °C (left), the thermocouple circumferential positions (right) in the fast disk of A1 test from Clarke (2009).

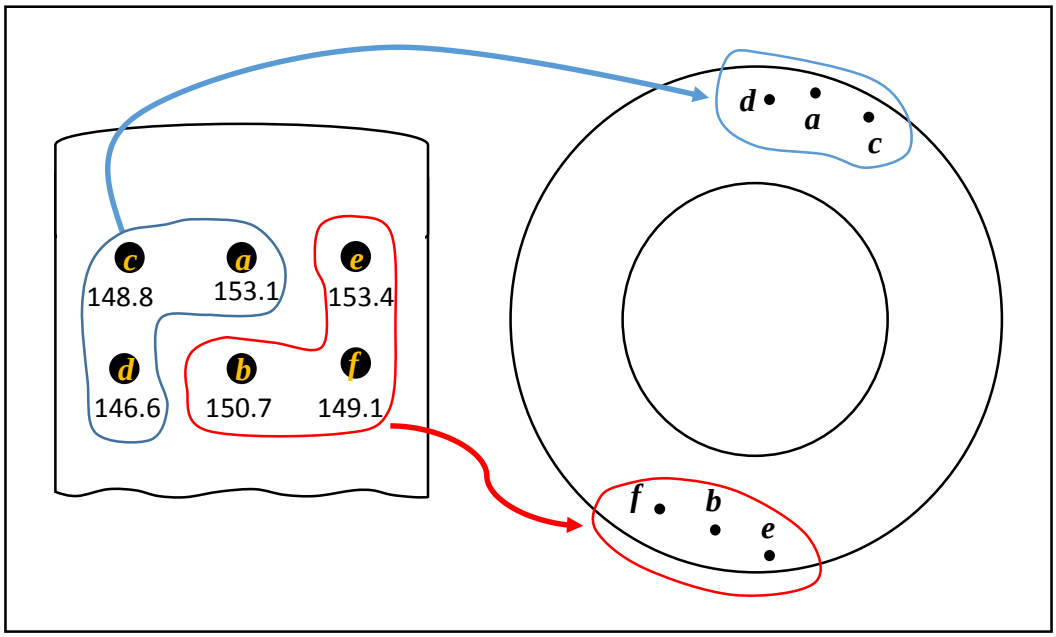

Figure 6.31 The temperature map (left), the thermocouple circumferential positions (right) in the fast disk of D4 test from Voller (2010).

A basic evaluation was conducted to consider the probability of systematic circumferential temperature variation in comparison with the probability of usual random measurement errors. The probability is based on comparing each thermocouple measurement with the rest of the thermocouple measurements. The results of these comparisons are shown in Tables 6.2, 6.3, 6.4 and 6.5. In these tables the thermocouples are arranged in their groups, the terminology meanings are:

- Logical: when the temperature of the thermocouple relates logically to its position if compared with another thermocouple temperature and position.
- Illogical: when the temperature of thermocouple does not relates logically to its position if compared with another thermocouple temperature and position.
- Weak: When the comparison is less reliable than the logical, for instance, big temperature asymmetry on both sides of the disk.
- N.A.: When the comparison is not applicable for these basic comparisons.

Table 6.2: The results of comparison of the thermocouples in A1 test of the current work.

	a	***e***	***f***	***b***	***c***	***d***
a		logical	logical	illogical	illogical	illogical
e			logical	illogical	illogical	weak
f				logical	N.A.	weak
b					N.A.	logical
c						logical
d						

Table 6.3: The results of comparison of the thermocouples in A1 test of the work of Clarke (2009).

	a	***c***	***d***	***b***	***e***	***f***
a		logical	logical	illogical	illogical	illogical
c			logical	weak	weak	illogical
d				weak	N.A.	weak
b					N.A.	logical
e						logical
f						

Table 6.4: The results of comparison of the thermocouples in D4 test of the work of Voller (2010).

	a	***c***	***d***	***b***	***e***	***f***
a		logical	logical	logical	illogical	logical
c			logical	N.A.	weak	illogical
d				logical	N.A.	weak
b					N.A.	logical
e						logical
f						

Table 6.5 : Summary of the results from Tables (6.2), (6.3) and (6.4).

	Logical	Weak	Illogical	N.A.	Total
Different group	4	8	11	4	27
Same group	15	-	-	3	18

From Table 6.5, it can be concluded that the probability of circumferential temperature variation is much higher than a random measurement error resulting in measurement discrepancies. The possible reasons behind the circumferential temperature variation is the variation of heat leaving the disk through the interface area. As described previously in section 2.2.1 the disk is pressed onto the shaft with an interference fit and locked by a nut. This makes the disk be in contact with three interface zones, these are the inner annular surface with the shaft, the shaft shoulder with the side face and the nut with the other side face of the disk. If the pressure varies along these interface surfaces, this will lead to thermal conductance variation at the contacting surface and hence non uniform heat transfer around the disk.

Consequently, an examination on the contact between the shaft and the disk was carried out. A typical shaft and disk were used for this examination, the shaft interface was coated with a highly pigmented paste (Engineer's blue) for assessing the mating of the contact. The disk was pressed onto the shaft and locked by the locking nut and disassembled again. Figure 6.32 are two photographs show the residual of the coating material on the shaft after disk disassembling.

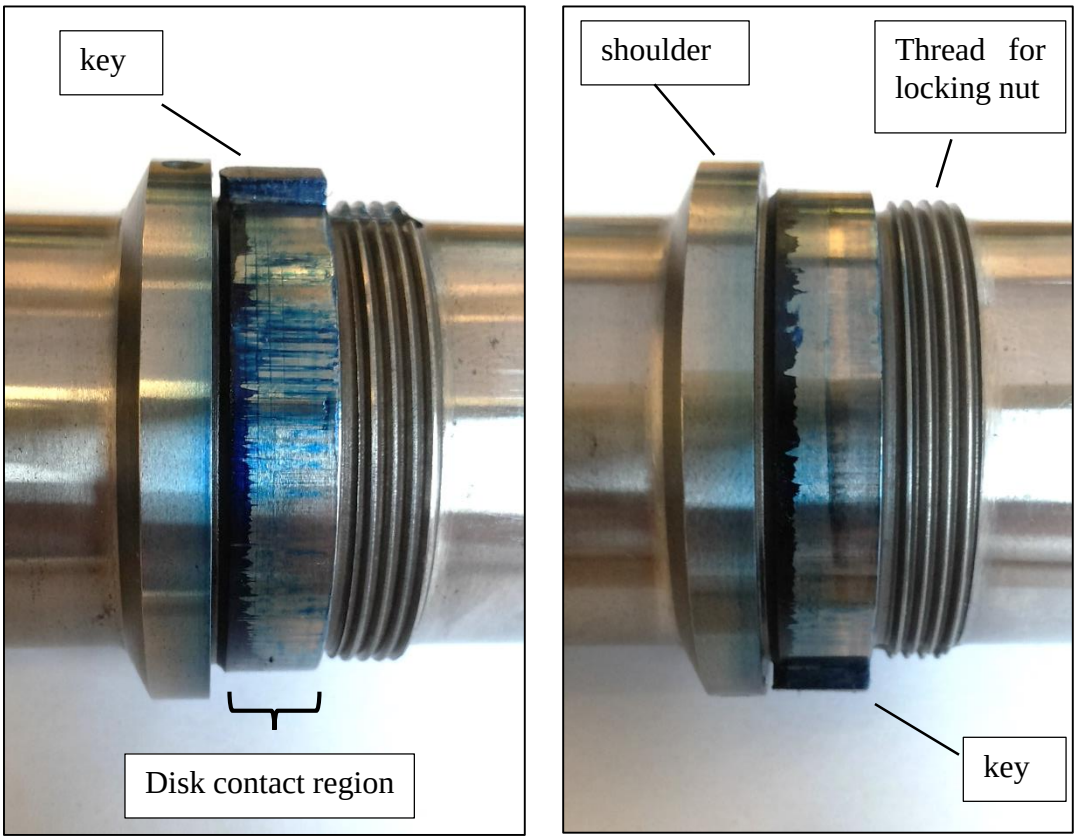

Figure 6.32: Photographs shows the residual of the coating test material (Engineer's blue) on a typical shaft after disk disassembly, the photos on two sides of the shaft.

The two photos in Figure 6.32 (which are from two sides) show clearly that the residual coating material is not distributed uniformly along the contacting region and hence neither is the contact pressure. The ideal pressure between the disk and the shaft may calculated from the interference fit conditions which is in the range of 0.0152 mm to 0.0254 mm in diameter (Patching 1994). The theoretical pressure in the contact may calculated according to the formula (Shigley J. E. 2001)

$$P = \frac{E\delta}{R}\frac{(r_o^2 - R^2)(R^2 - r_i^2)}{2R^2(r_o^2 - r_i^2)} \tag{6.1}$$

Where:

δ is the radial interference between the shaft and the disk

R is the nominal radius of the fit.

E is the Young's modules of the members which is assumed to be the same.

ν is the Poissos ratio of the members which is assumed to be the same.

r_i is the inner radius of the inner member (equal to zero for the shaft).

r_o is the outer radius of the outer member (the disk).

According to equation (6.1), the calculated contact pressure then is in the range of 27.3 MPa to 45.6 MPa. In fact, this pressure range is for ideal fit design. However the residual of coating material shown in Figure 6.32 demonstrates poor contact at some areas on the fit that might well have zero or much reduced local pressure in the contact. Furthermore, the fit includes two keys (one is blind) which in addition to the poor contact zone act to distort the fit pressure along the circumferential direction. The aim of studying pressure variation along the fit is to examine the variation of conduction of heat across the interface in the circumferential direction that direction. A considerable amount of work in the literature has been carried out on investigating the thermal contact conductance between contacting bodies, see (Fletcher 1988) and (Yovanovich 2005) for example. The experimental and theoretical work has shown that the thermal conductance is governed by the contact pressure. A correlation relation representing the contact thermal conductance in (Leung et al. 1998):

$$h^* = 0.170\ P^{*0.693} \tag{6.2}$$

Where h^* and P^* are dimensionless quantities defined as:

$$h^* = \frac{h\sigma}{mk}$$

$$P^* = \frac{P}{H}$$

The terms in these expressions are:

H is Vickers micro-hardness

σ is the standard deviation of the surface roughness.

m is the asperity slope.

k is thermal conductivity.

P is the contact pressure.

h is the thermal contact conductance $= \frac{q}{A\Delta T}$

Now the effect of the pressure variation obtained for the contact between the shaft and the disk is examined. The features of SS303 specimen reported by (Leung et al. 1998) are used in equation (6.2) with pressure variation of 1MPa (low pressure), 27.3MPa and 45.6MPa to evaluate the thermal contact conductance. The results are shown in Table 6.6

Table 6.6: the thermal conductance against the contact pressure

P / MPa	1.0	27.3	45.6
h / kWm^{-2} K^{-1}	0.78	7.7	11.1

As a result, to keep the heat flow rate ($q = hA\Delta T$) for the condition of lower pressure (1 MPa) as in the higher pressure case (45.6 MPa), an approximate 14 times higher temperature difference ΔT is required. Remembering that Figure 6.32 shows potentially zero local pressures which reduce the heat flow rate to zero according to

(Leung et al. 1998). The change in conductance may be significant factor, however, it should be mentioned that Leung et al. (1998) carried out their study in vacuum, whilst in the current work, the gaps in the fit will be filed either with air or with the lubricant. This may permit low rate of heat transfer occur at these positions

6.5. Traction force results

In addition to the temperature measurements in the EHL test, the traction force within the contact is also measured. The traction force is used to calculate the total frictional heat generated within the EHL contact, which is equal to the traction force multiplied by the sliding speed. The total traction forces are shown in Figure 6.33 as a function of the applied load for each of the sliding speeds used in this work.

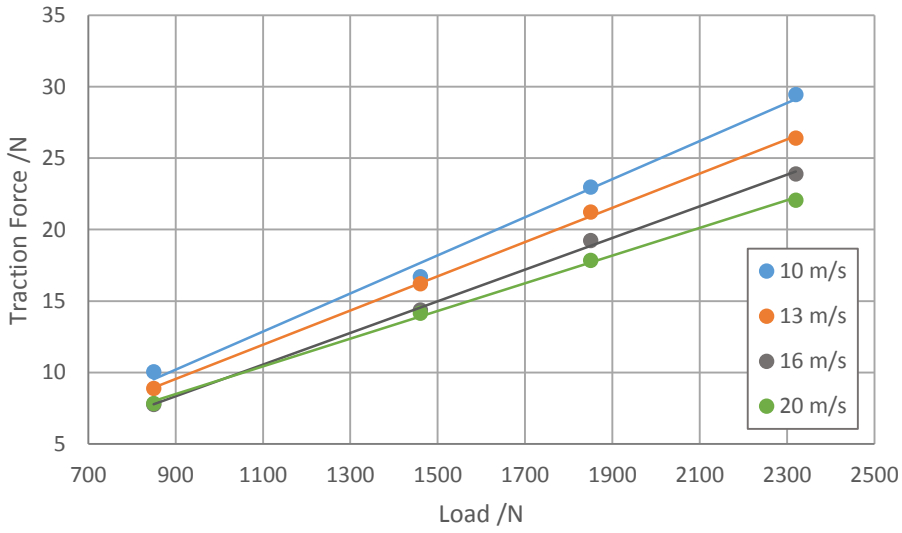

Figure 6.33: The traction force versus the load for the 16 EHL tests classified at four sliding speed families

From Figure 6.33, it can be observed that the measurements follow the linear trend lines in the four sliding speed groups. It can also be seen that as the load increases, the

traction force is increased. Figure 6.33 also shows that the traction force decreases as sliding speed increases for a particular load. This likely due to decrease in oil viscosity as the temperature increases resulting in lower coefficient of friction. This trend can be seen clearly in Figure 6.34 which shows the coefficient of friction versus the sliding speed for the EHL tests at load of 2320 N. The trend shown in this figure is compatible with the trend of the mean coefficient of friction that was measured in gear contact by Kleemola and Lehtovaara (2010), and is shown in Figure 1.6 (a).

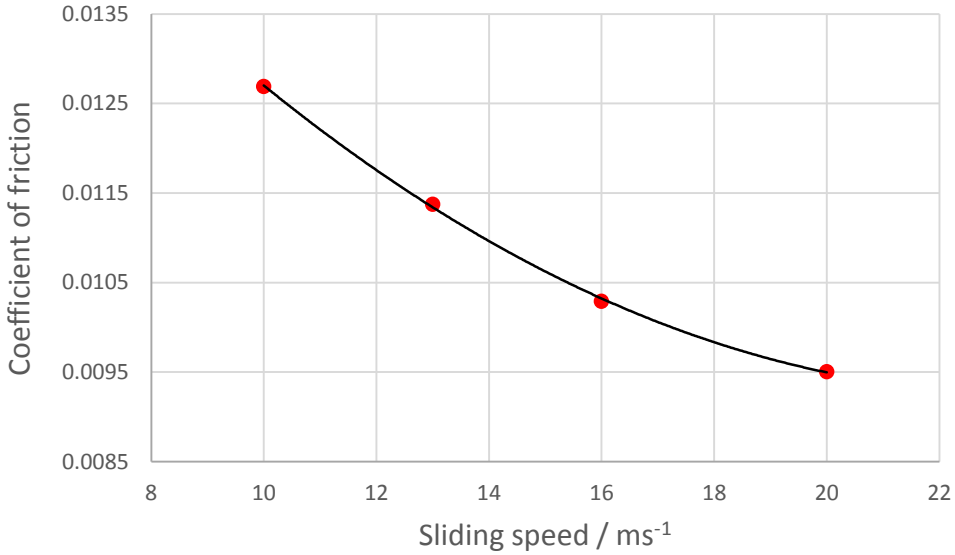

Figure 6.34: The coefficient of friction versus sliding speed in the EHL contact which is measured in the experimental tests under the condition of 2320 N load.

For further investigation of the traction force measurements, a comparison with the traction measurements in Clarke (2009) is shown in Figure 6.35. In this figures, the traction force is plotted versus load for the 13 m/s sliding speed series. It can be seen good agreement between both results.

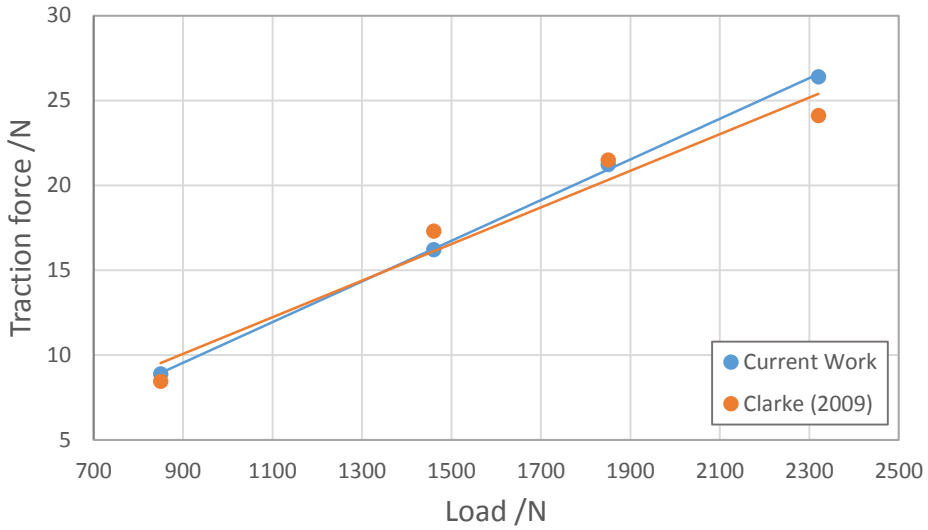

Figure 6.35: A comparison of the measured traction force between the current work and the work of Clarke (2009) at 13 m/s sliding speeds.

Chapter 7:
Modelling of the EHL Experimental Results

7.1. Introduction

In this chapter, the sixteen experimental EHL tests that were described in the previous chapter are modelled, by using the two dimensional numerical thermal model derived in chapter three. In addition, the EHL tests that were carried out by Clarke (2009) are also modelled using the current technique. In modelling of all tests, the steady state methodology which was described in section 4.3 is used for evaluating the heat partition factor β. The results of the current work are then compared with the experimental results in Clarke (2009) and (2006). The evaluated heat partition factor β values are also compared with the heat partition results taken from numerical thermal EHL point contact of the oil film developed by Cardiff Tribology group and used in Clarke (2009).

7.2. Modelling

The experimental data which were collected from the test rig during the EHL experimental results, were curve fitted using the Matlab curve fitting toolbox as described in section 4.2. The new smoothed fitted data were written to files that could be then imported to the numerical thermal model. The model was run using the range of heat partition factor $0.1 \leq \beta \leq 1$ with 0.1 step, and the range of heat transfer coefficients $100 \leq h \leq 1200$ $Wm^{-1}K^{-1}$ with 100 $Wm^{-1}K^{-1}$ step. Hence, 120 pairs of (β, h) combination values were used in the modelling of the full transient heating phase

(loading phase) of the EHL tests. As described in section 3.5 and 4.3, in order to evaluate the realistic (β, h) combination, the calculated temperatures at the location of the thermocouples ***a, c*** and ***e*** were compared with the measured temperatures taken from the experiment. In order to evaluate the realistic value of β at the steady state EHL contact, comparisons were conducted over the last 150 second interval prior to unloading with an error criteria :

$$\varepsilon = \frac{1}{n}\sum_{1}^{n}\left(\frac{\varepsilon_a + \varepsilon_c + \varepsilon_e}{3}\right) \tag{7.1}$$

Where, ε_a, ε_c, and ε_e are the absolute values of the difference between the calculated and measured temperatures at the thermocouple positions ***a, c,*** and ***e*** respectively, and n is the number of data points over the last 150 seconds. The error formulation in equation (7.1) is used for the thermocouple arrangement developed in this work which includes two central and one side thermocouples as described in section 5.6. On the other hand, the EHL tests carried out in the work of Clarke (2009) used one central and two side thermocouples. Hence, the error criteria for modelling these test needs to give a higher weight for the central thermocouple ***a*** as it has higher temperature discrimination, the criteria adopted is:

$$\varepsilon = \frac{1}{n}\sum_{1}^{n}\left(\frac{2\varepsilon_a + \varepsilon_c + \varepsilon_e}{4}\right) \tag{7.2}$$

The full range of the EHL experiments (16 tests) carried out in this work were modelled in addition to the 16 experimental tests carried out in the work of Clarke (2009) for which the raw experimental data were available. The β value was evaluated for both using error criteria in equation (7.1) for the current results and equation (7.2) for the previous results. Table 7.1 shows the calculated β values and the corresponding

heat transfer coefficients for the fast and slow disks obtained from modelling the 32 EHL experimental tests. Having quantified the effect of uncertainty in the Reynolds number exponent, as discussion in chapter four, the calculated β values shown in Table 7.1 are estimated to have an uncertainty of ±0.015

Table 7.1: The calculated β factors and corresponding heat transfer coefficients at the approximately steady state for the EHL experimental tests of the current work and the work of Clarke (2009)

Tests	Load / N	u_s /ms^{-1}	Modelling of the Current results			Modelling of tests of Clarke (2009)		
			β	h_f / Wm^{-2}K^{-1}	h_s / Wm^{-2}K^{-1}	β	h_f / Wm^{-2}K^{-1}	h_s / Wm^{-2}K^{-1}
A1	850	10	0.77	616	235	0.71	921	352
A2	1460	10	0.70	550	210	0.75	830	317
A3	1850	10	0.69	617	235	0.73	860	328
A4	2320	10	0.67	643	245	0.73	661	252
B1	850	13	0.75	731	279	0.75	950	363
B2	1460	13	0.70	714	272	0.76	946	361
B3	1850	13	0.70	734	280	0.75	927	354
B4	2320	13	0.67	772	295	0.74	746	285
C1	850	16	0.73	609	232	0.77	1287	491
C2	1460	16	0.70	705	269	0.76	1085	414
C3	1850	16	0.69	752	287	0.77	843	322
C4	2320	16	0.67	730	279	0.76	873	333
D1	850	20	0.68	632	241	0.72	1251	478
D2	1460	20	0.67	777	297	0.75	1110	424
D3	1850	20	0.66	746	285	0.76	929	355
D4	2320	20	0.65	721	275	0.75	886	338

Table 7.1 shows that the β results are in the range of 0.65 to 0.77 for the current work and 0.71 to 0.77 for the tests in the work of Clarke (2009). This indicates clearly that the majority of generated heat in the EHL contact is conducted to the fast disk. This outcome is compatible with the results of the tests of Patching (1995) which were modelled by Clarke et al. (2006). It is also compatible with the slow disk modelling conducted by Clarke (2009) who found the majority of heat was conducted to the fast disk. The calculated heat transfer coefficients in each experiment are related to each other by the relation $h_f / h_s = 2.62$ as the gear ratio is fixed and the power in equation (4.6) also fixed. Figures 7.1 to 7.16 show the modelling results of the experimental tests carried out in this work. Each figure is composed of four parts (a), (b), (c) and (d). Parts (a) and (b) show the error map contours of the fast and the slow disk respectively as defined in equation (7.1), and parts (c) and (d) of the figures shows the two dimensional temperature distribution contours of the fast and the slow disk respectively based on the specific calculated β and h for minimum error. Figure 7.17 shows the results of modelling the D4 test from the experimental work of Clarke (2009).

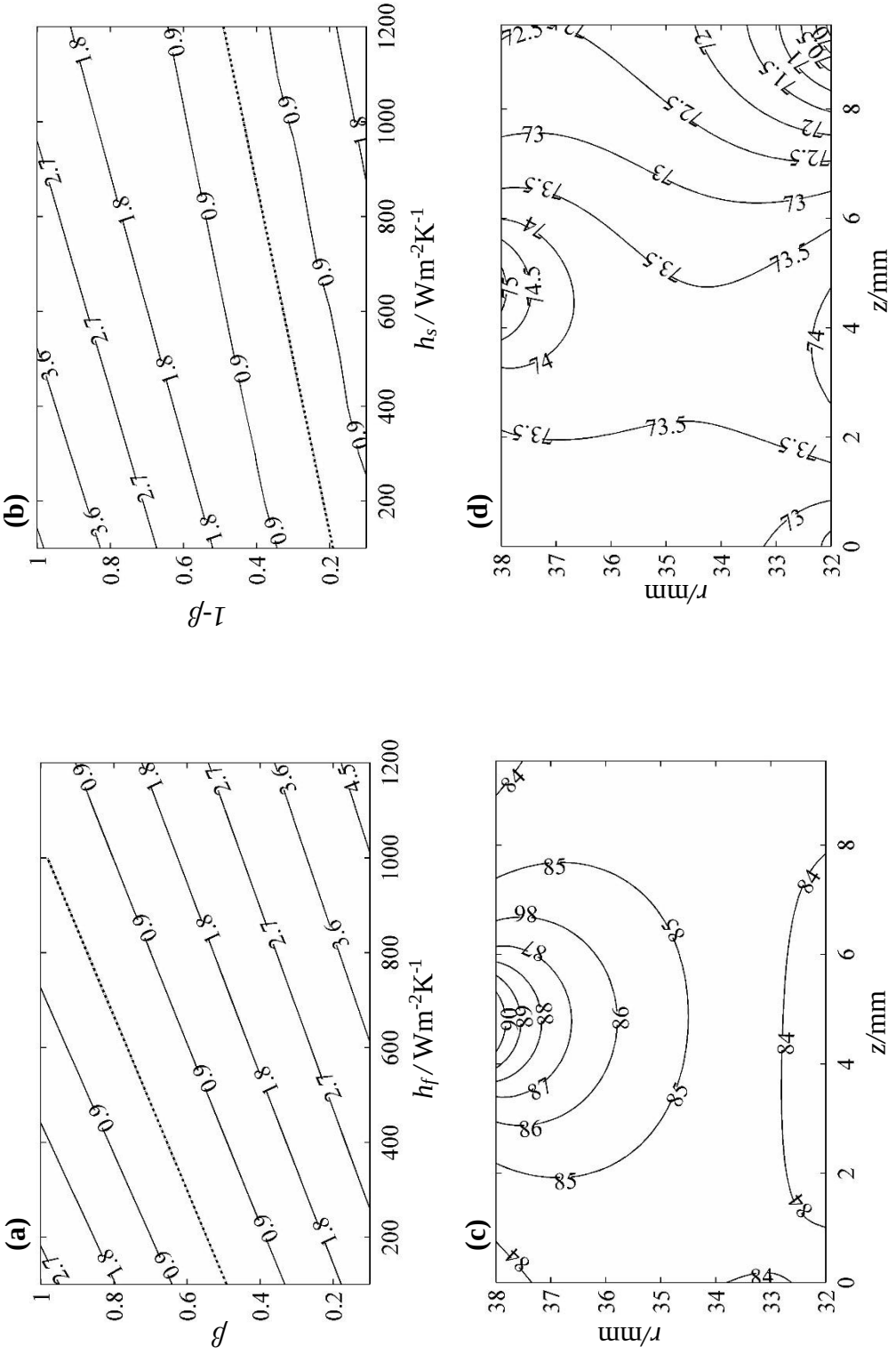

Figure 7.1: The results of modelling test A1, **(a)** The error map of the fast disk, **(b)** The error map of the slow disk, **(c)** The temperature distribution in the fast disk ^{o}C, **(d)** The temperature distribution in the slow disk ^{o}C

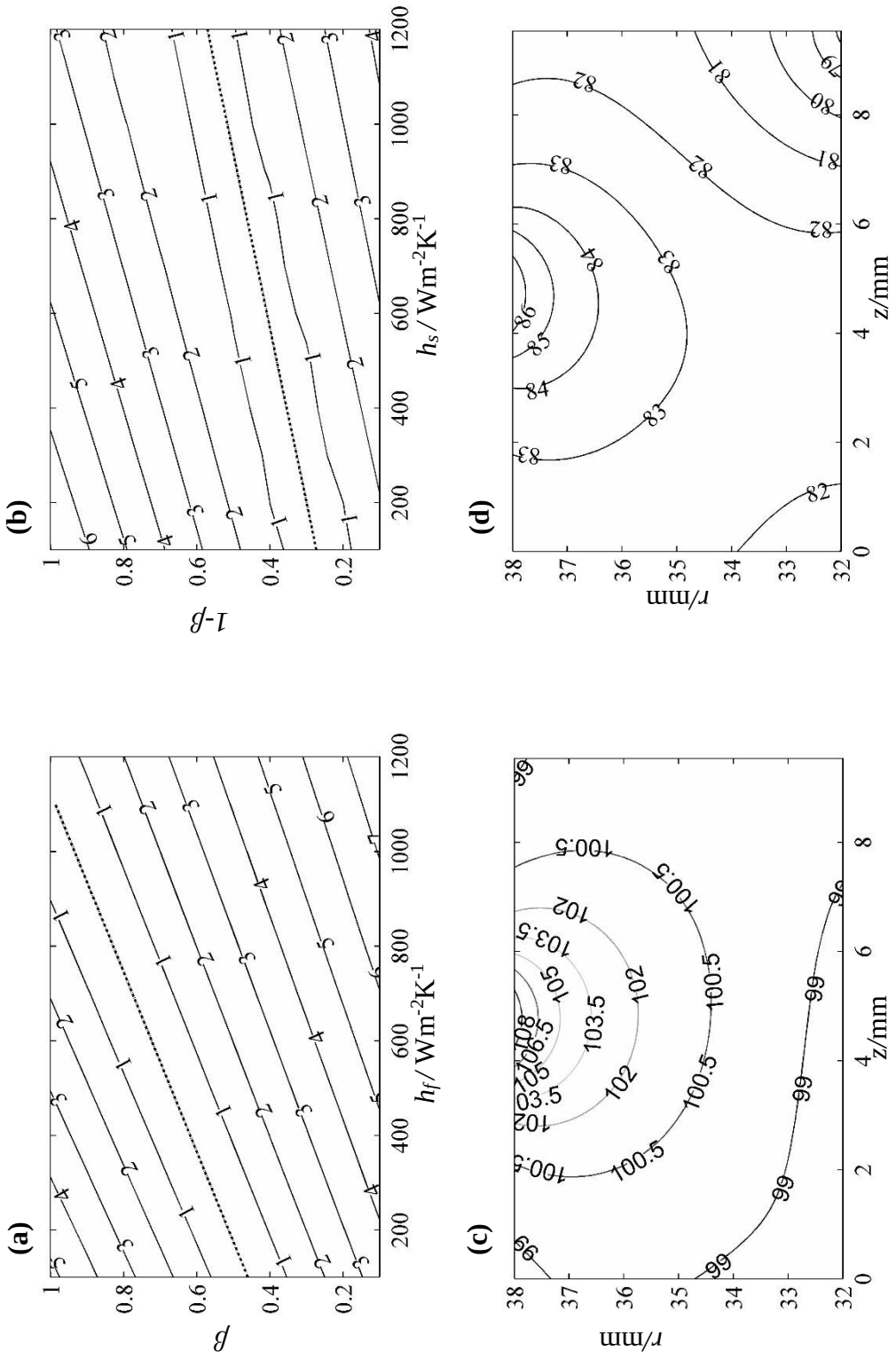

Figure 7.2: The results of modelling test A2, **(a)** The error map of the fast disk, **(b)** The error map of the slow disk, **(c)** The temperature distribution in the fast disk ^{o}C, **(d)** The temperature distribution in the slow disk ^{o}C

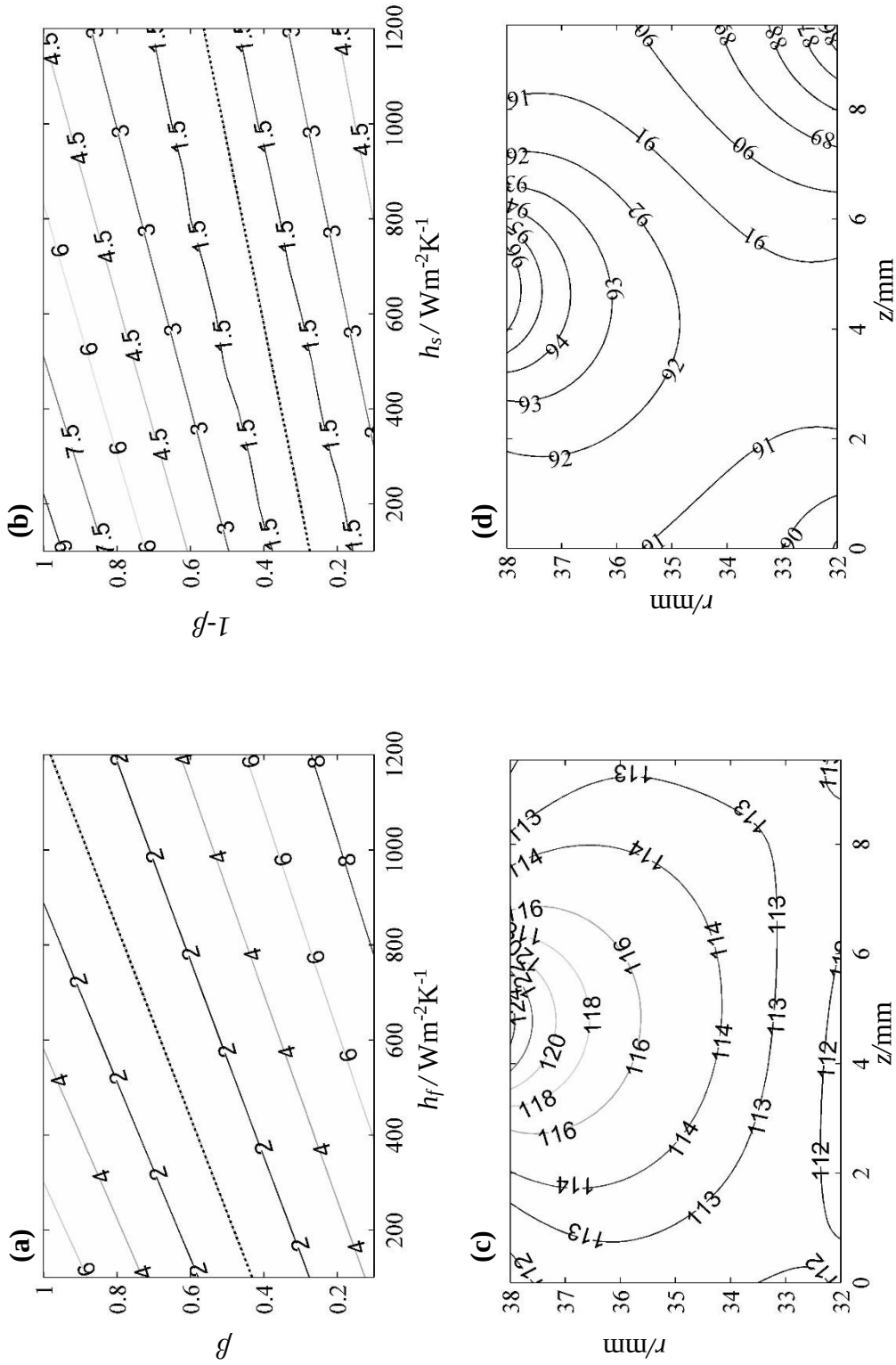

Figure 7.3: The results of modelling test A3, **(a)** The error map of the fast disk, **(b)** The error map of the slow disk, **(c)** The temperature distribution in the fast disk ^{o}C, **(d)** The temperature distribution in the slow disk ^{o}C

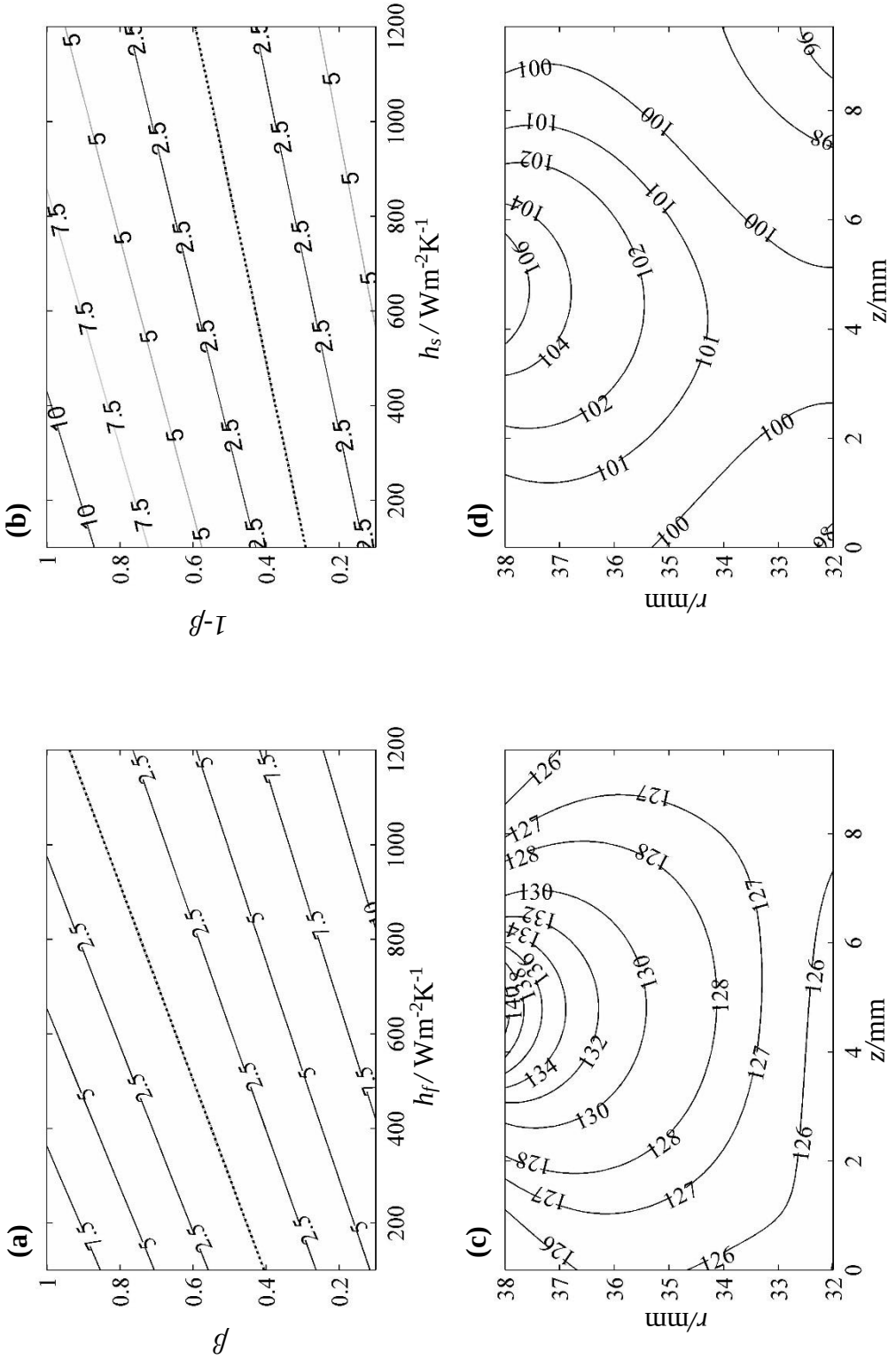

Figure 7.4: The results of modelling test A4 **(a)** The error map of the fast disk, **(b)** The error map of the slow disk, **(c)** The temperature distribution in the fast disk ^{o}C, **(d)** The temperature distribution in the slow disk ^{o}C

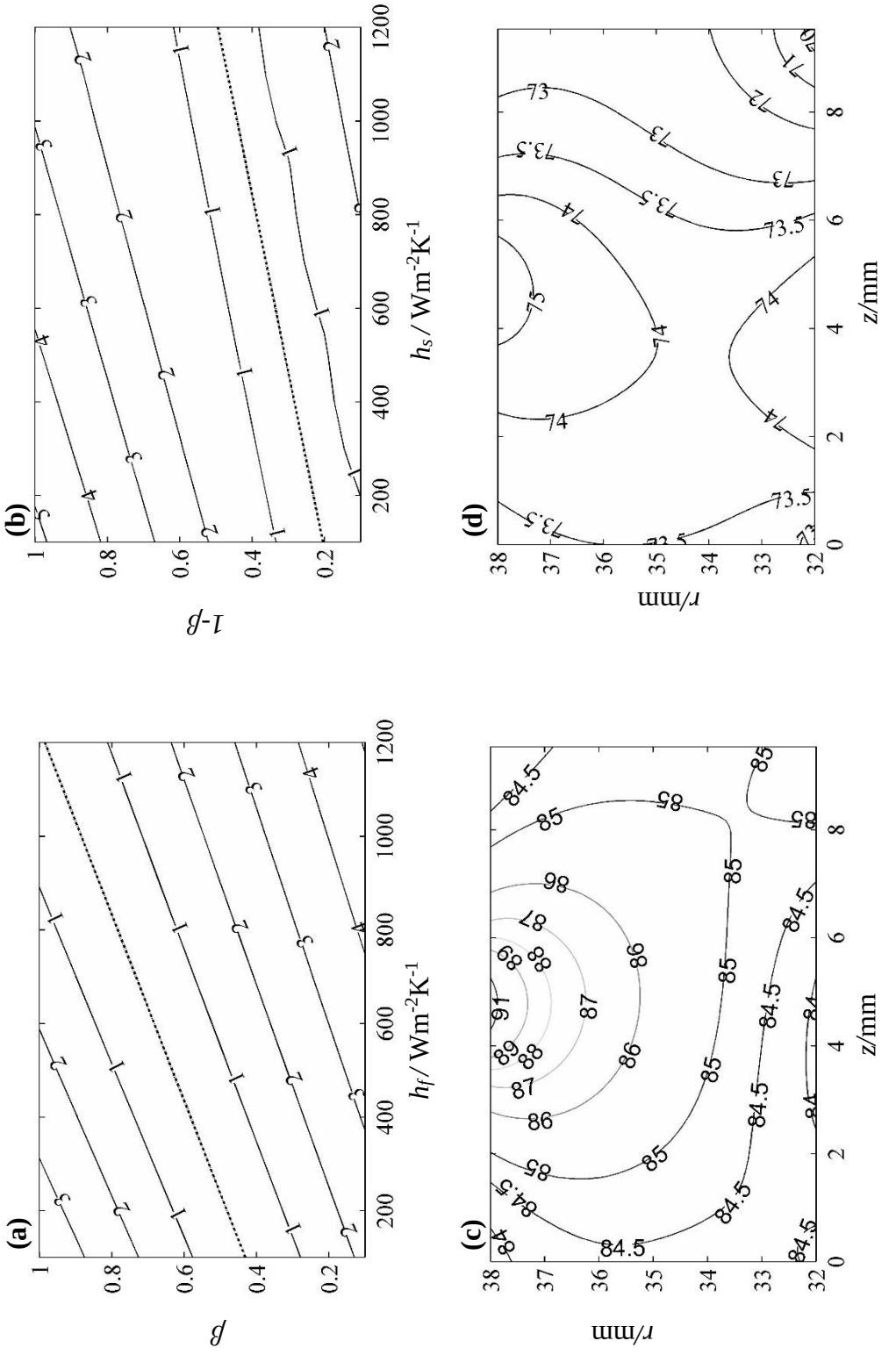

Figure 7.5: The results of modelling test B1, **(a)** The error map of the fast disk, **(b)** The error map of the slow disk, **(c)** The temperature distribution in the fast disk ^{o}C, **(d)** The temperature distribution in the slow disk ^{o}C

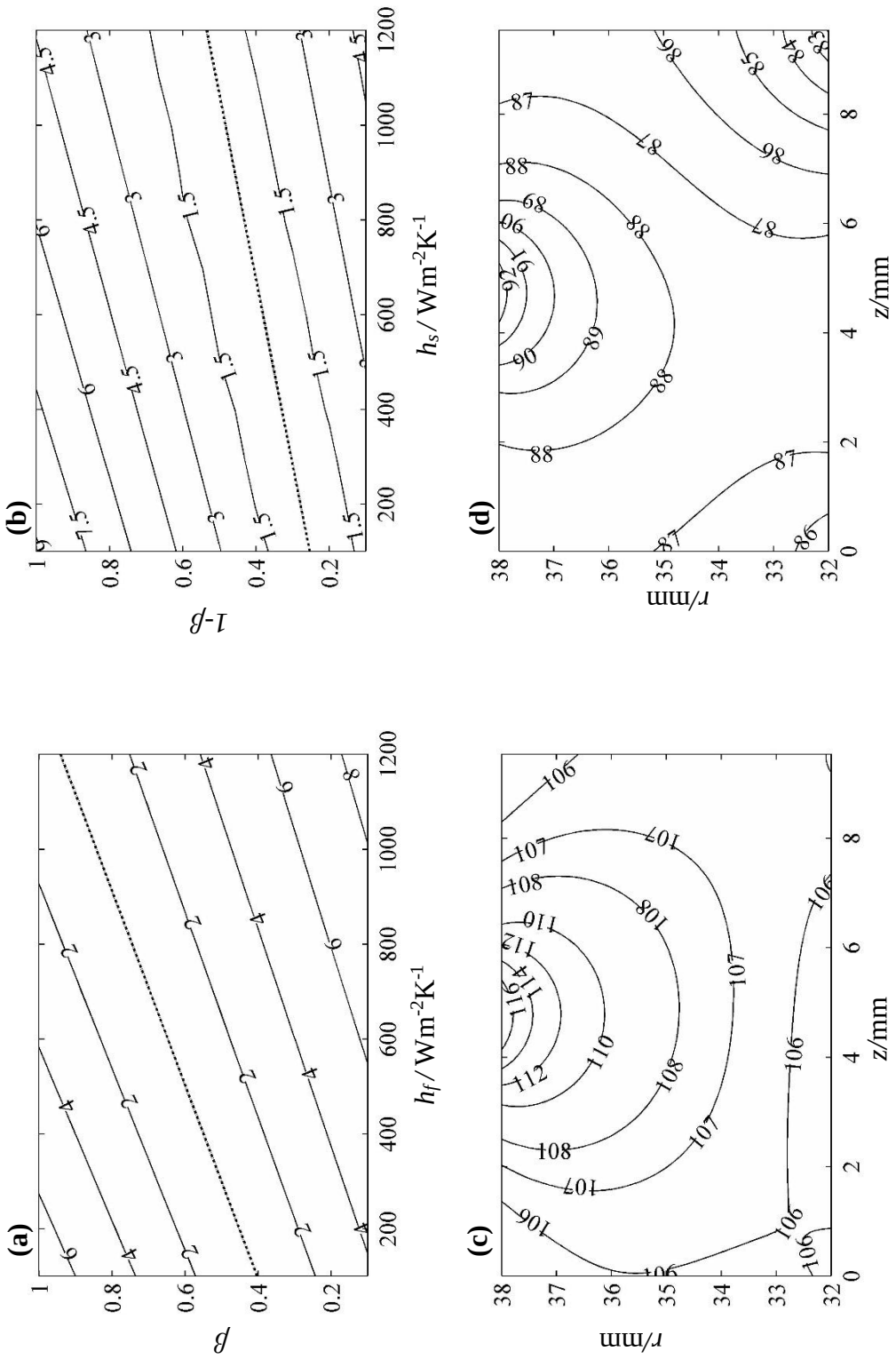

Figure 7.6: The results of modelling test B2, **(a)** The error map of the fast disk, **(b)** The error map of the slow disk, **(c)** The temperature distribution in the fast disk ^{o}C, **(d)** The temperature distribution in the slow disk ^{o}C

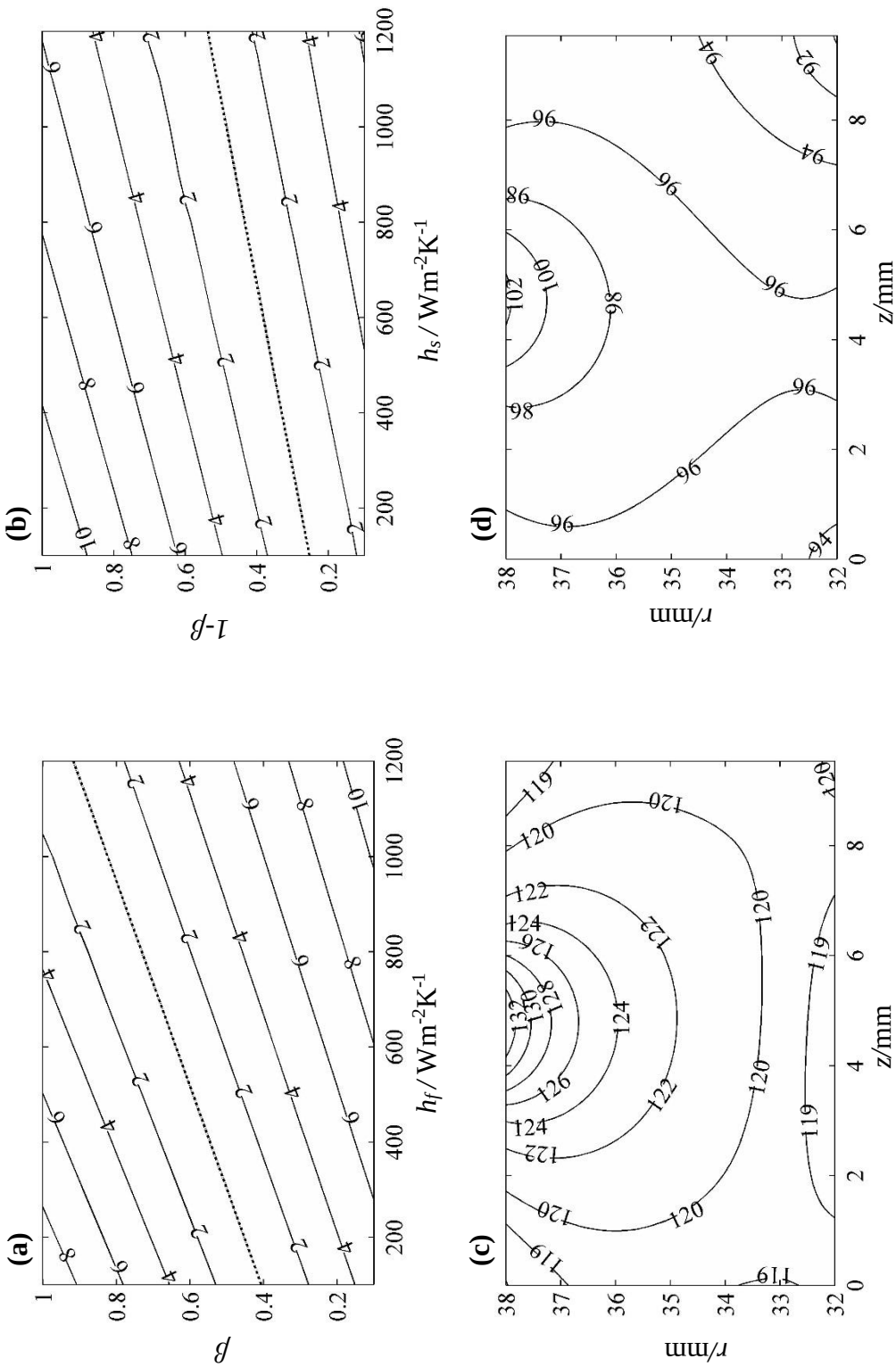

Figure 7.7: The results of modelling test B3, **(a)** The error map of the fast disk, **(b)** The error map of the slow disk, **(c)** The temperature distribution in the fast disk ^{o}C, **(d)** The temperature distribution in the slow disk ^{o}C

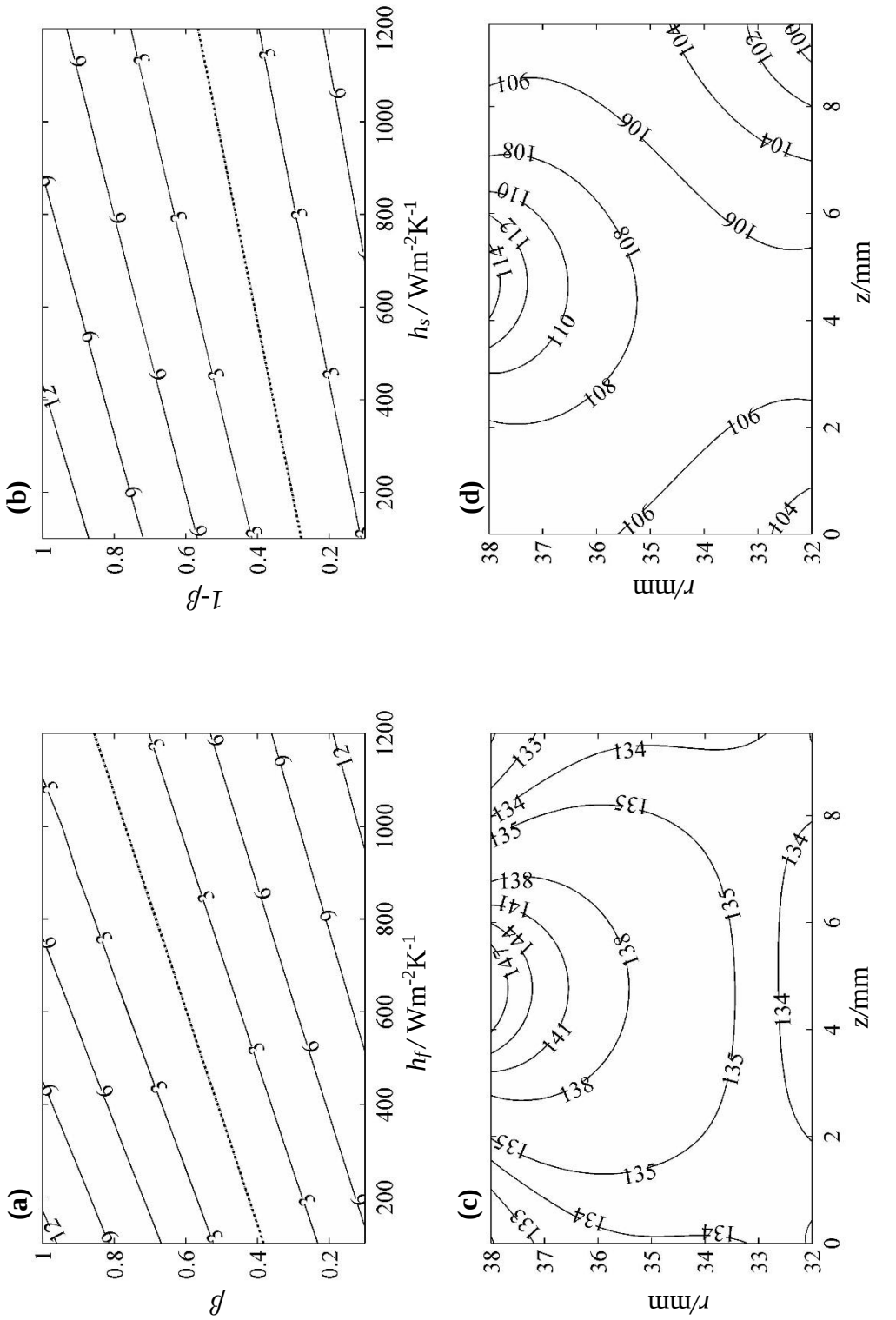

Figure 7.8: The results of modelling test B4, **(a)** The error map of the fast disk, **(b)** The error map of the slow disk, **(c)** The temperature distribution in the fast disk ^{o}C, **(d)** The temperature distribution in the slow disk ^{o}C

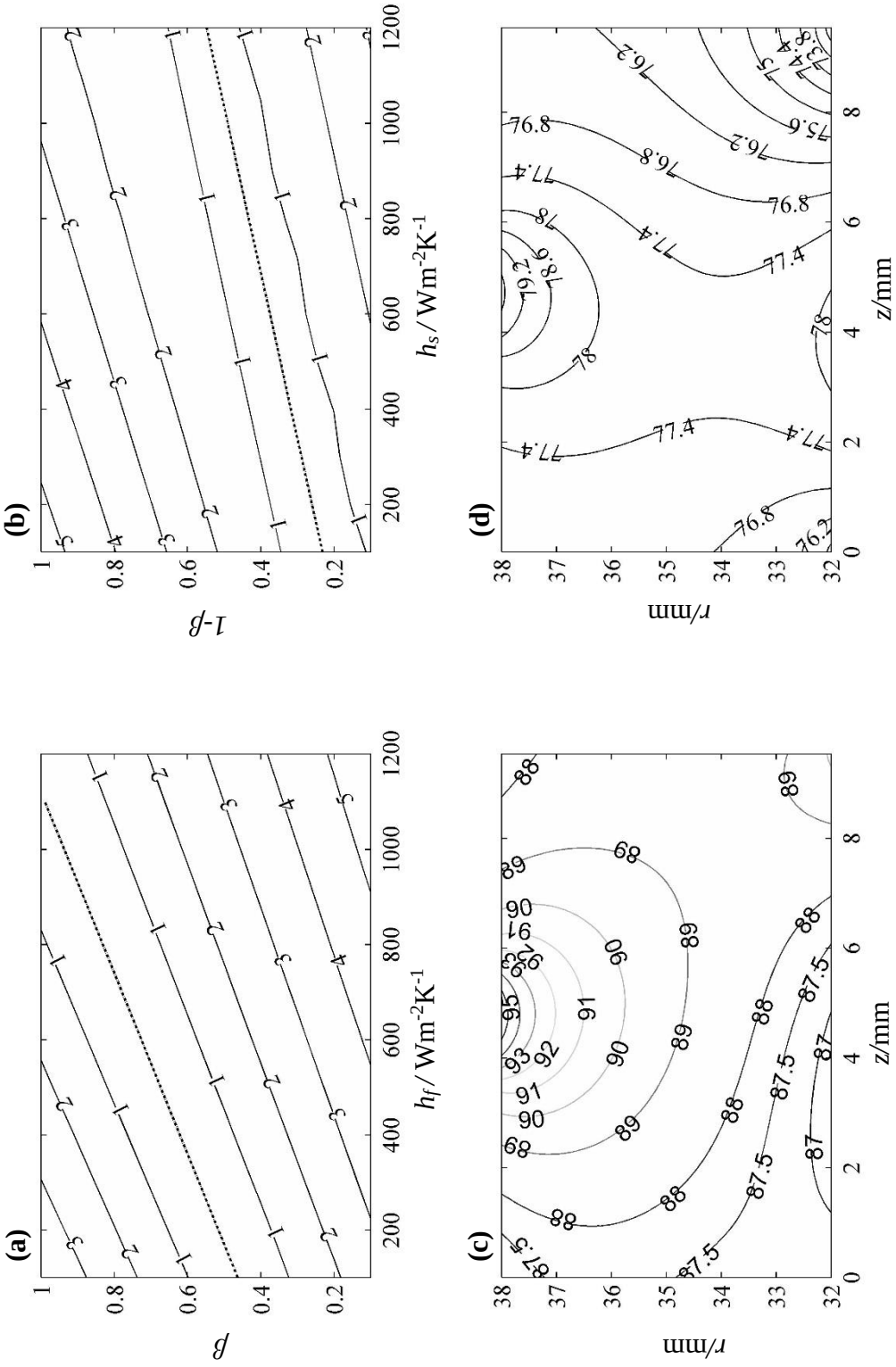

Figure 7.9: The results of modelling test C1, **(a)** The error map of the fast disk, **(b)** The error map of the slow disk, **(c)** The temperature distribution in the fast disk ^{o}C, **(d)** The temperature distribution in the slow disk ^{o}C

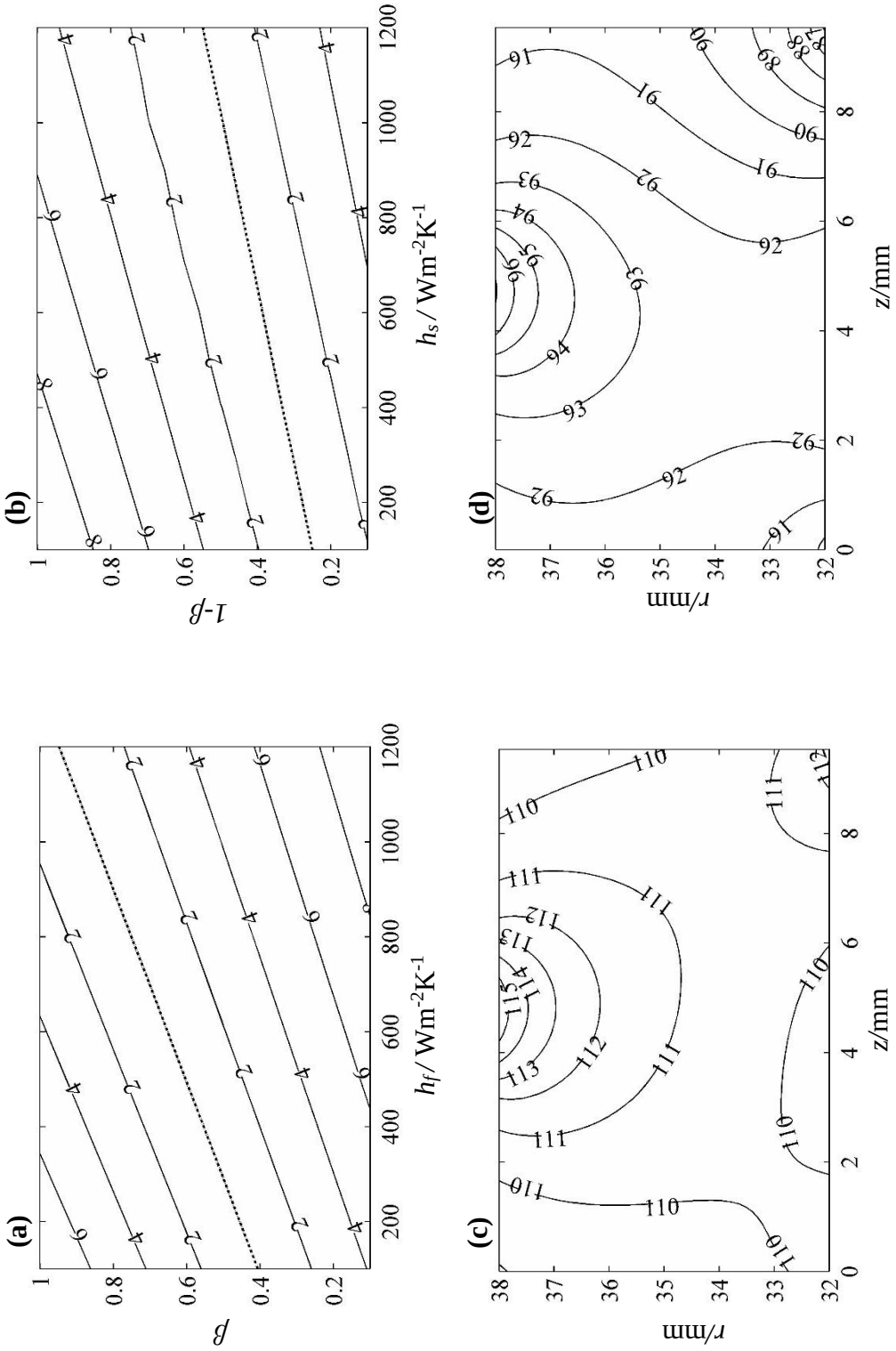

Figure 7.10: The results of modelling test C2, **(a)** The error map of the fast disk, **(b)** The error map of the slow disk, **(c)** The temperature distribution in the fast disk ^{o}C, **(d)** The temperature distribution in the slow disk ^{o}C

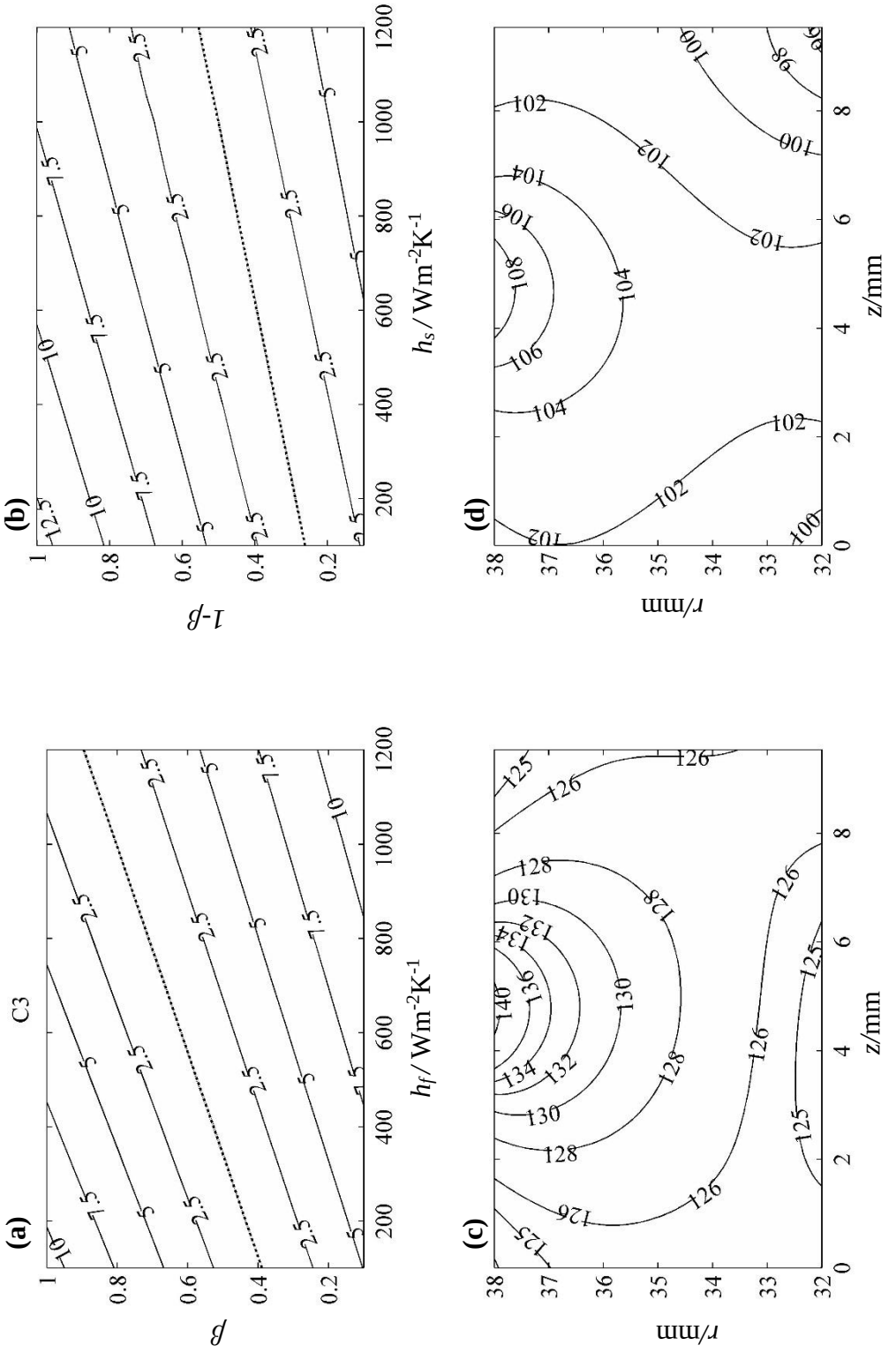

Figure 7.11: The results of modelling test C3, **(a)** The error map of the fast disk, **(b)** The error map of the slow disk, **(c)** The temperature distribution in the fast disk ^{o}C, **(d)** The temperature distribution in the slow disk ^{o}C

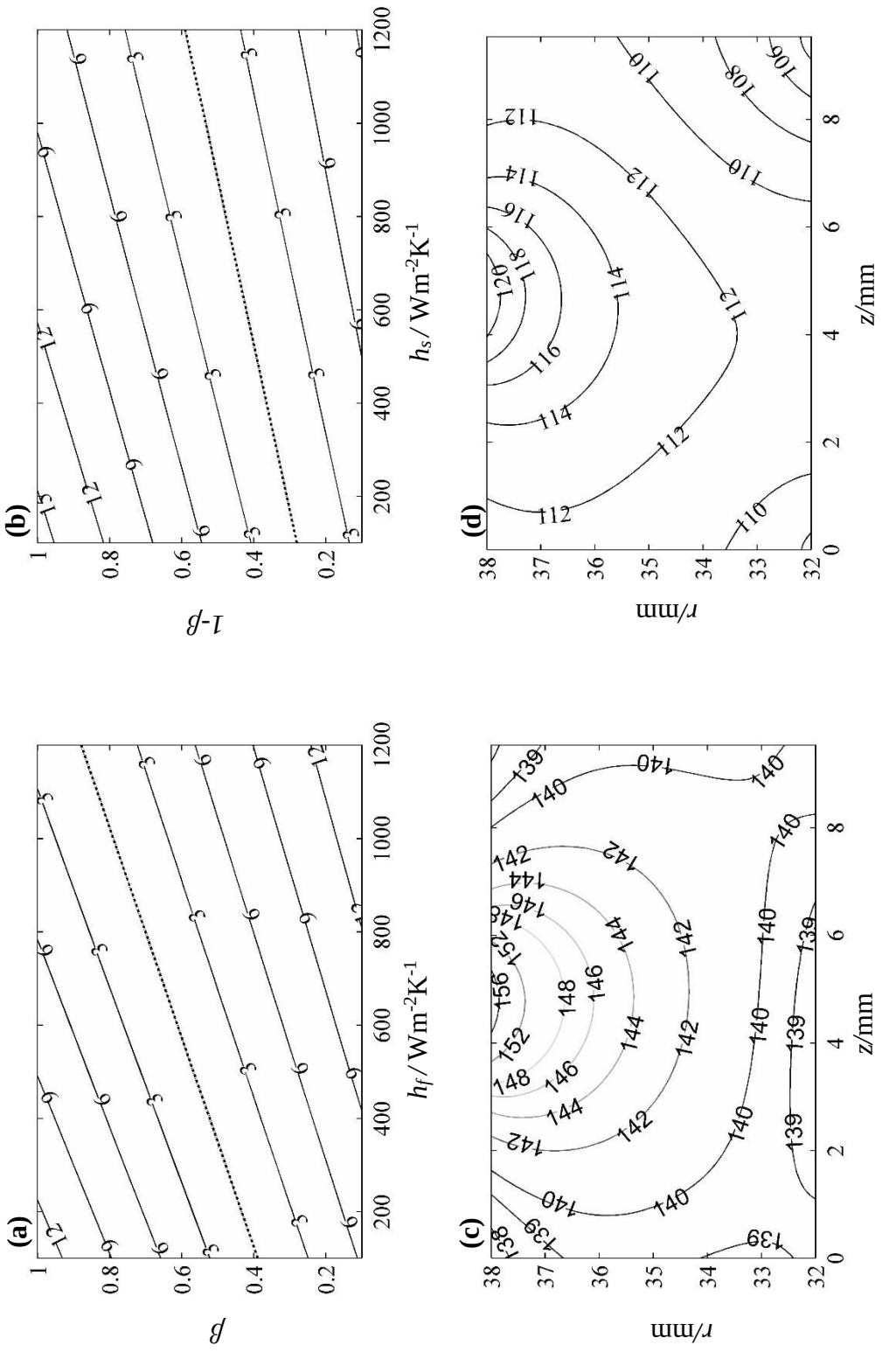

Figure 7.12: The results of modelling test C4, **(a)** The error map of the fast disk, **(b)** The error map of the slow disk, **(c)** The temperature distribution in the fast disk ^{o}C, **(d)** The temperature distribution in the slow disk ^{o}C

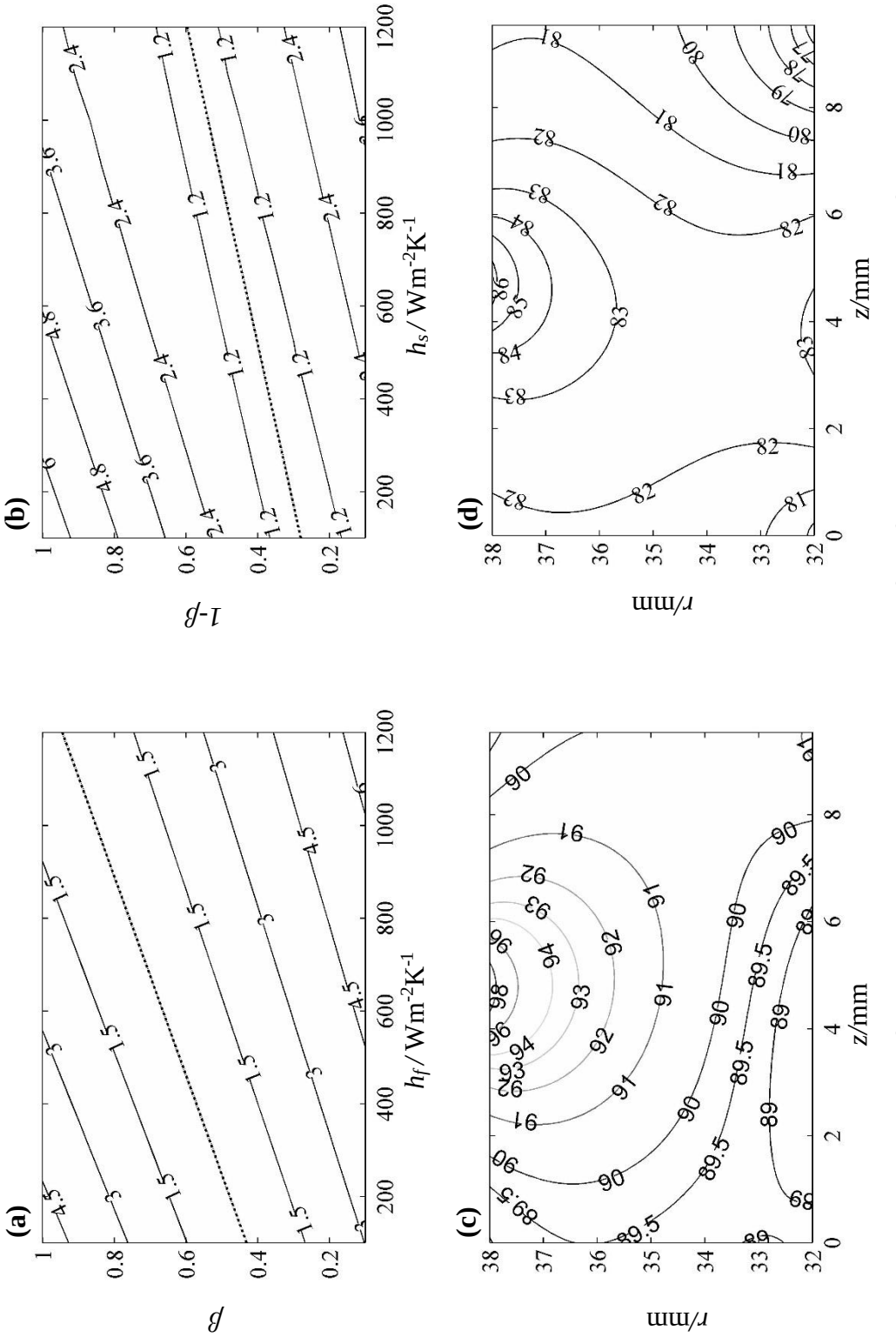

Figure 7.13: The results of modelling test D1, **(a)** The error map of the fast disk, **(b)** The error map of the slow disk, **(c)** The temperature distribution in the fast disk ^{o}C, **(d)** The temperature distribution in the slow disk ^{o}C

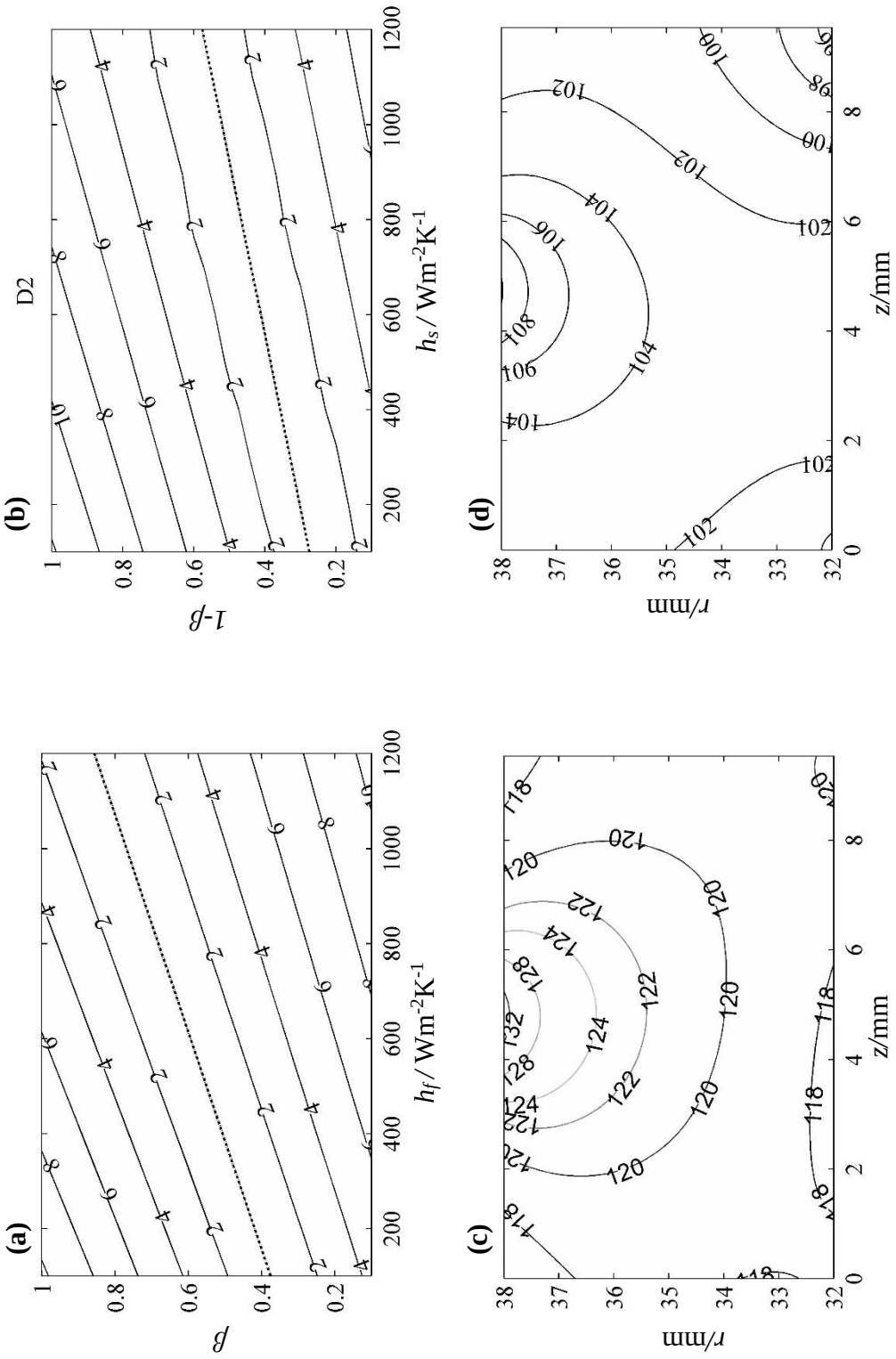

Figure 7.14: The results of modelling test D2, **(a)** The error map of the fast disk, **(b)** The error map of the slow disk, **(c)** The temperature distribution in the fast disk ^{o}C, **(d)** The temperature distribution in the slow disk ^{o}C

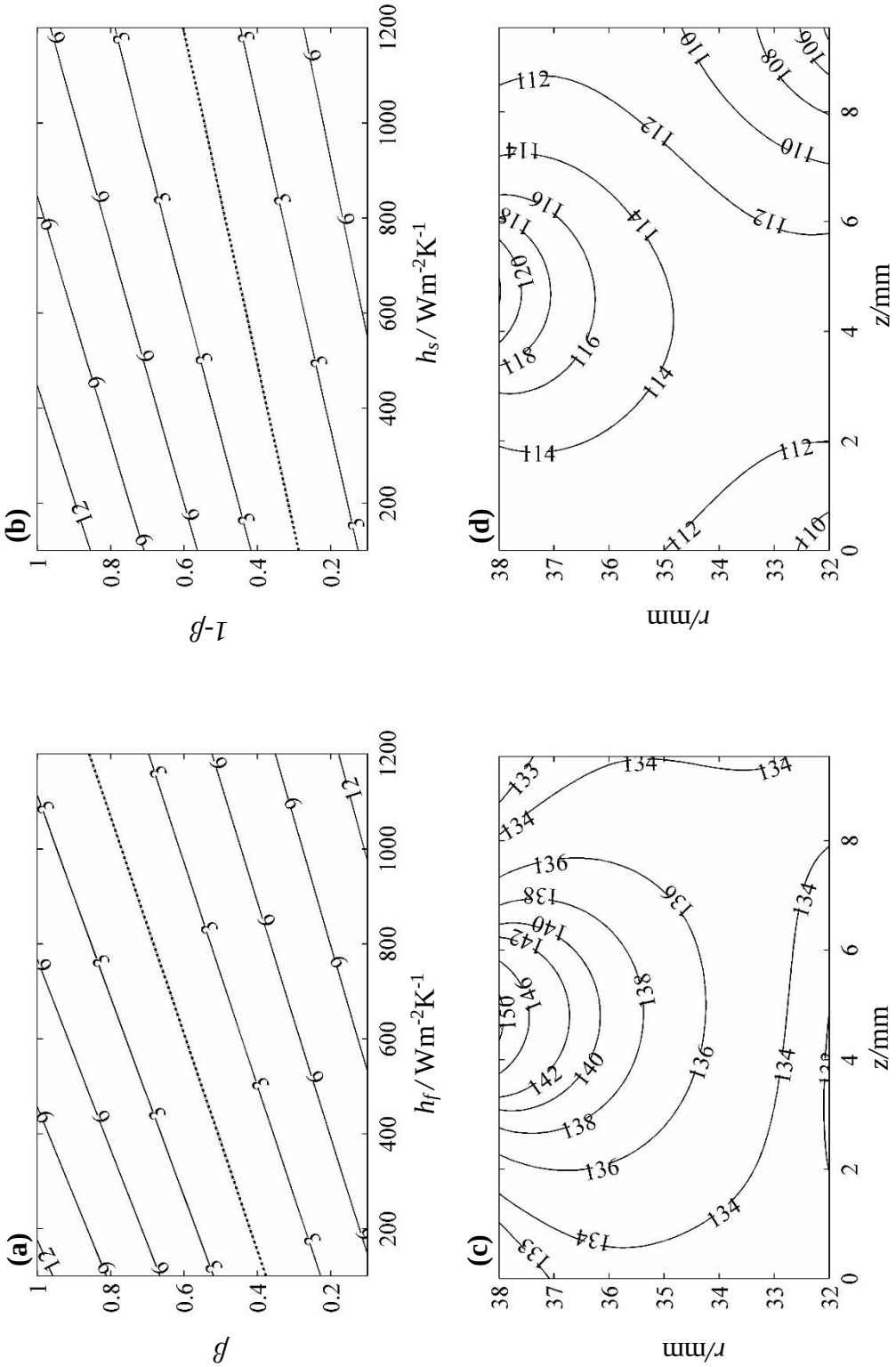

Figure 7.15: The results of modelling test D3, **(a)** The error map of the fast disk, **(b)** The error map of the slow disk, **(c)** The temperature distribution in the fast disk ^{o}C, **(d)** The temperature distribution in the slow disk ^{o}C

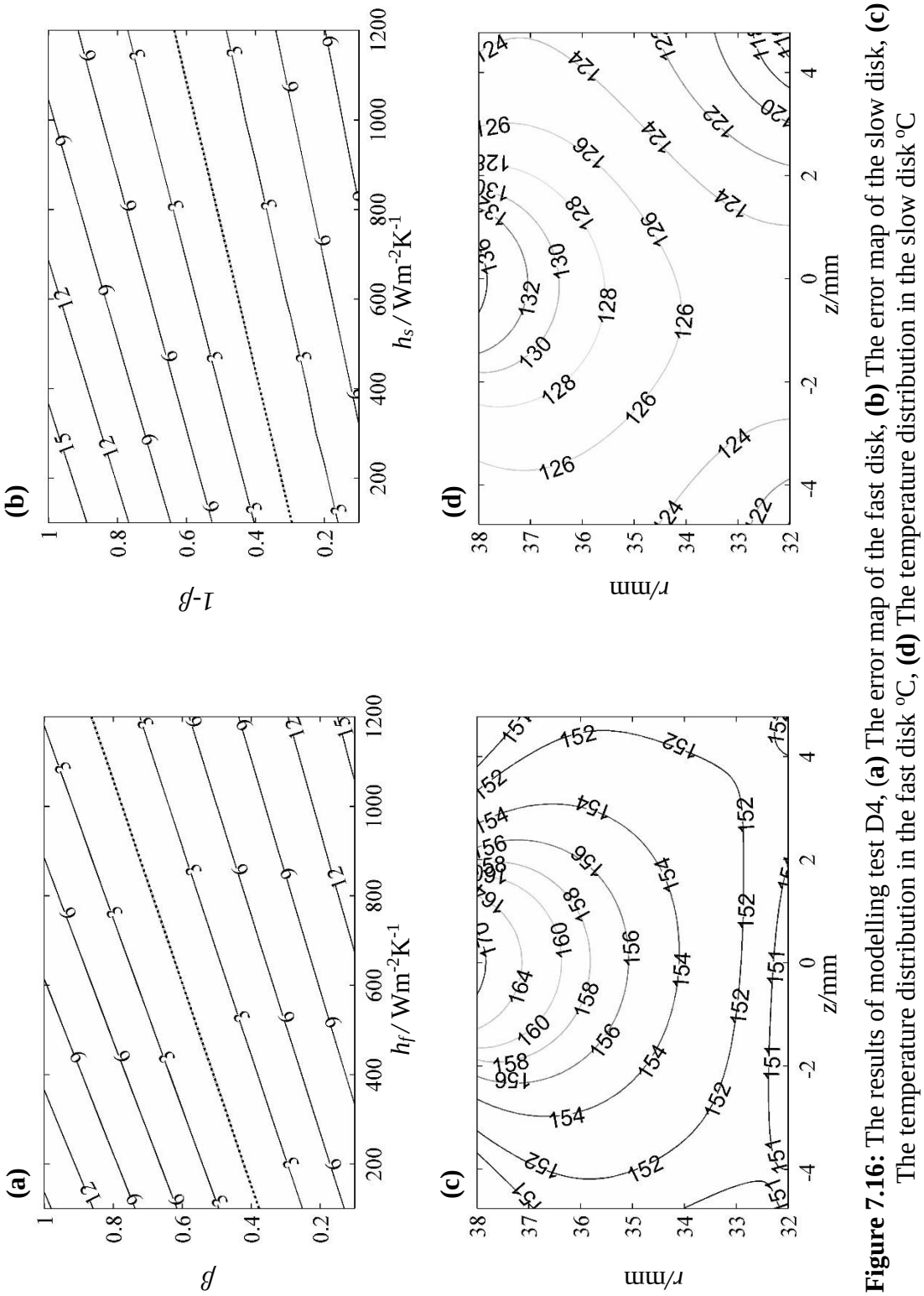

Figure 7.16: The results of modelling test D4, **(a)** The error map of the fast disk, **(b)** The error map of the slow disk, **(c)** The temperature distribution in the fast disk ^{o}C, **(d)** The temperature distribution in the slow disk ^{o}C

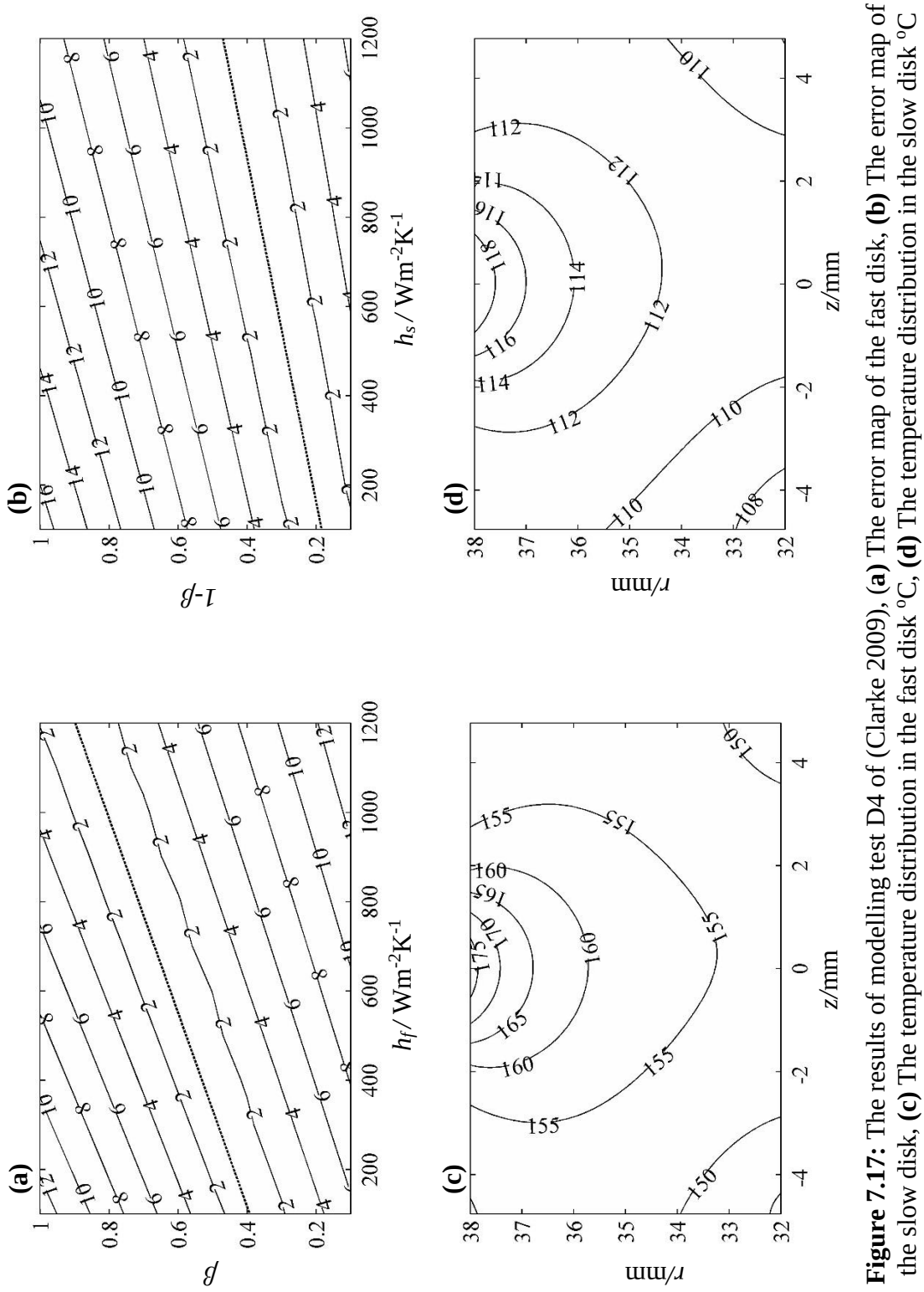

Figure 7.17: The results of modelling test D4 of (Clarke 2009), **(a)** The error map of the fast disk, **(b)** The error map of the slow disk, **(c)** The temperature distribution in the fast disk °C, **(d)** The temperature distribution in the slow disk °C

Parts (a) and (b) in Figures 7.1 to 7.17 show consistent and repeatable trend of the lines representing minimum error for each disk. The main features of these lines is that for the range of h values considered, β values for that disk are at a higher level than the 1- β values for the slow disk. This feature has led to calculated values of β in the range of 0.65 to 0.77 for the series of the EHL experimental tests. Remembering that the solution which was used to evaluate β was based on solving simultaneously the equations of the lines of the minimum error shown in (a) and (b) of the Figures 7.1 to 7.17. Another consistent and repeatable feature in the error contours is that the calculated temperatures above the line of minimum error is higher than the corresponding measurement whilst below this line the calculated temperature are always lower. This can be seen in the typical calculations in Figure 4.4. The trends of temperature shown in parts (c) and (d) of Figures 7.1 to 7.16 are considered in the discussion of maximum surface temperature in section 7.4.

Figure 7.17 represents the solution of the D4 test carried out in the work of Clarke (2009). The calculated β value for this D4 test is 0.75 whilst it is 0.65 for the current D4 experiment in spite the fact that they were run under the same load and sliding speed. This difference in results might be due to noticeably higher temperatures occurring in the slow disk of the current work as compared with the tests of Clarke (2009) with broadly similar measured fast disk temperatures and friction force values. Table 7.2 shows the temperature measurements at the approximately steady state of thermocouple ***a*** and the friction force for the current work and the work of Clarke (2009).

Table 7.2: A comparison between the temperature measurements of thermocouple ***a*** at steady state and the measured friction force of the current tests and the tests of Clarke (2009)

Tests	T_a (fast disk) /^{o}C		T_a (slow disk) /^{o}C		Friction force /N	
	Current results	Clarke (2009)	Current results	Clarke (2009)	Current results	Clarke (2009)
A1	84.6	79.4	73.0	65.9	10.0	10.5
A2	100.8	101.6	82.0	77.3	16.7	18.5
A3	114.7	110.3	91.1	81.3	22.9	23.4
A4	129.2	125.3	100.6	89.9	29.4	26.5
B1	85.5	86.2	73.1	70.8	8.9	8.5
B2	108.8	110.1	87.0	82.6	16.2	17.3
B3	121.8	121.9	95.8	88.4	21.2	21.5
B4	137.6	136.4	106.3	96.9	26.4	24.1
C1	88.4	89.9	76.3	74.2	7.7	8.9
C2	112.6	115.6	91.8	87.1	14.3	16.0
C3	128.0	130.3	101.9	94.1	19.2	19.4
C4	142.9	146.9	111.8	103.7	23.9	25.0
D1	89.9	90.9	80.5	76.2	7.8	7.8
D2	121.0	118.2	102.1	91.3	14.1	14.9
D3	136.8	139.0	112.3	101.6	17.8	19.1
D4	155.4	157.7	125.2	112.8	22.0	23.4

Table 7.2 shows generally higher temperature in the slow disk for the current tests with an average differences of 7.3 ^{o}C while the faster disk has slightly lower temperatures with 0.1 ^{o}C average error. The current friction forces are generally slightly lower than the tests of Clarke (2009) having an average error of 0.3 N. There was no clear reason for this variation in the slow disk measurements for the same load and speed conditions. The most likely reason is the issue related to the contact conductance in the disk-shaft interface as discussed in section 6.4.3. Another reason

probably related to the configuration of the oil feed pipes as it was subjected to some experimental work. Additional possible reasons are using a new oil filter and fresh oil that can have led to differences in the properties of the oil between the two sets of experiments

7.3. Results gathering

In the previous work of Clarke (2006), the heat partition factors β for the series of tests were found to be represented best in a trend if plotted against the product of sliding speed and the maximum calculated temperature difference between the disks as shown in Figure 1.14. Hence, the results of modelling the experiments of the current work and the results of the current modelling of the experiment of Clarke (2009) are gathered in Figure 7.18 together with the trend curve

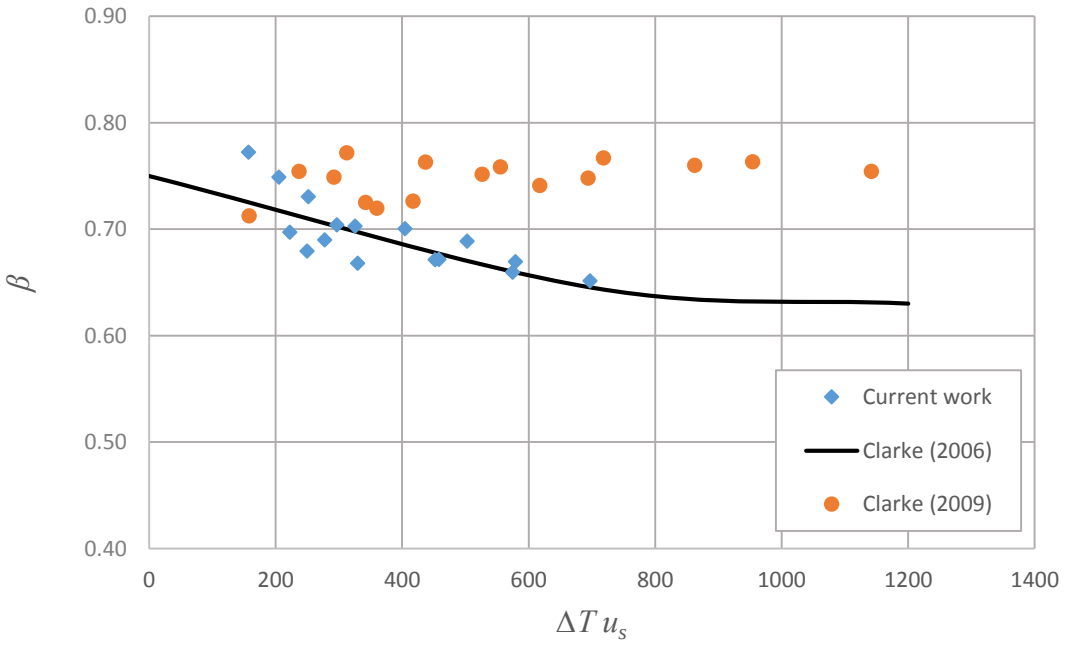

Figure 7.18: Comparisons of the experimental results modelling of the current work, the current modelling of the experiments of Clarke (2009) and the results of Clarke (2006)

In Figure 7.18 the trend curve is that obtained by Clarke (2006) in analysing the Patching (1995) data where only one subsurface temperature was measured and the thermal model included both support shafts and associated different heat transfer coefficients based on those available in the literature. It can be seen in Figure 7.18 that the current work and the trend curve of the results of Clarke (2006) are close to each other in β values which have a decreasing trend as the $\Delta T\, u_s$ product increases. The results of modelling the experiments of Clarke (2009) has a broadly uniform trend. However, in general the three sets of results confirm that the majority of generated heat in the EHL contact is conducted to the fast disk. It should also be noted that the current approach includes an additional thermocouple near to the disk running track and therefore more effectively measures the centre-line temperature gradient.

Another important comparison is now made between the current results and the results of the thermal EHL numerical point contact solver used by Clarke (2009). In that work, different combinations of rheological and viscosity models were investigated to compare the model predictions of heat partition with those derived from the experimental results of Patching (1995) to find the most realistic model. The combination which includes Bair and Winer (1979) rheology and Barus viscosity (Clarke's model F) was found to be the only combination that displayed the phenomena of which the fast surface receive the majority of the generated heat. The other models (A to E) indicated that the majority of the generated heat is conducted to the slow surface. Figure 7.19 shows the trend lines of the current experimental work, Model F and Model C used in Clarke (2009), the trend line for model C included in the figure is typical of the others (A, B, D and E).

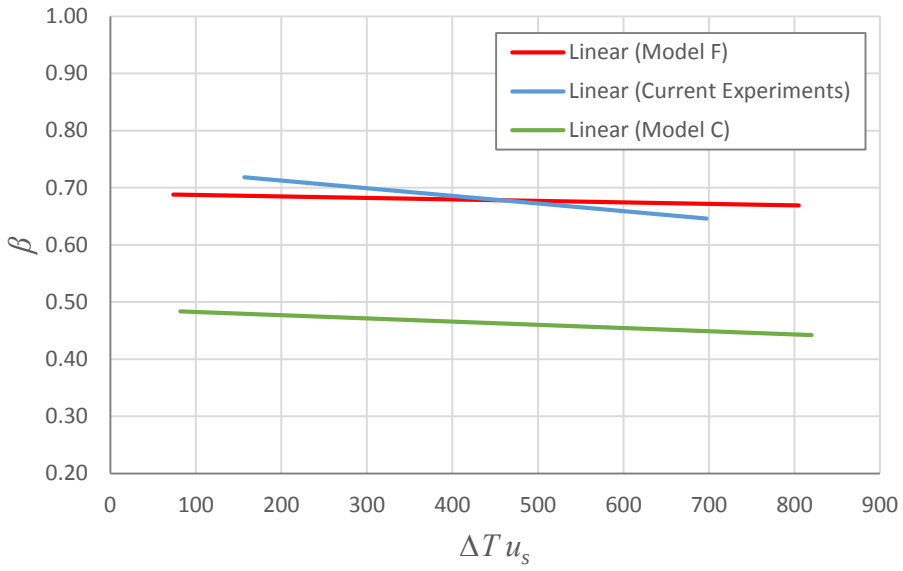

Figure 7.19: A comparison between the calculated β from the current experimental work with the EHL thermal modelling (Models C and F) for the comparable tests used in Clarke (2009)

Figure 7.19 shows good agreements between the current experimental work and model F used in the work of Clarke (2009).The linear trends for models C and F shown in Figure 7.19 have been applied to the results for the current experimental work given in Table 7.1 and the corresponding β values are given in Table 7.3. For these calculations, the values of ΔT were obtained from the thermal analysis presented in Figures 7.1 to 7.16 using maximum temperatures at the centre of the disk surface

Table 7.3: The calculated β factors for the current experimental work, Model (C and F) from the thermal EHL point contact modelling of Clarke(2009).

Tests	$\Delta T\, u_s$ $ms^{-1}\,{}^{o}C$	$\boldsymbol{\beta}$		
		Current Experimental results	Based on the trend line of Model F	Based on the trend line of Model C
A1	156.6	0.77	0.69	0.48
A2	222.0	0.70	0.68	0.48
A3	277.4	0.69	0.68	0.47
A4	329.6	0.67	0.68	0.47
B1	204.8	0.75	0.68	0.48
B2	325.4	0.70	0.68	0.47
B3	404.4	0.70	0.68	0.47
B4	452.0	0.67	0.68	0.46
C1	251.3	0.73	0.68	0.47
C2	296.5	0.70	0.68	0.47
C3	502.5	0.69	0.68	0.46
C4	578.8	0.67	0.67	0.46
D1	249.6	0.68	0.68	0.47
D2	458.2	0.67	0.68	0.46
D3	574.4	0.66	0.68	0.46
D4	697.1	0.65	0.67	0.45

7.4. Surface temperature

Now the trend of the fully modelled tests are represented by plotting the maximum calculated temperature for both disks versus the applied load in groups according to the sliding speeds as shown in Figure 7.20.

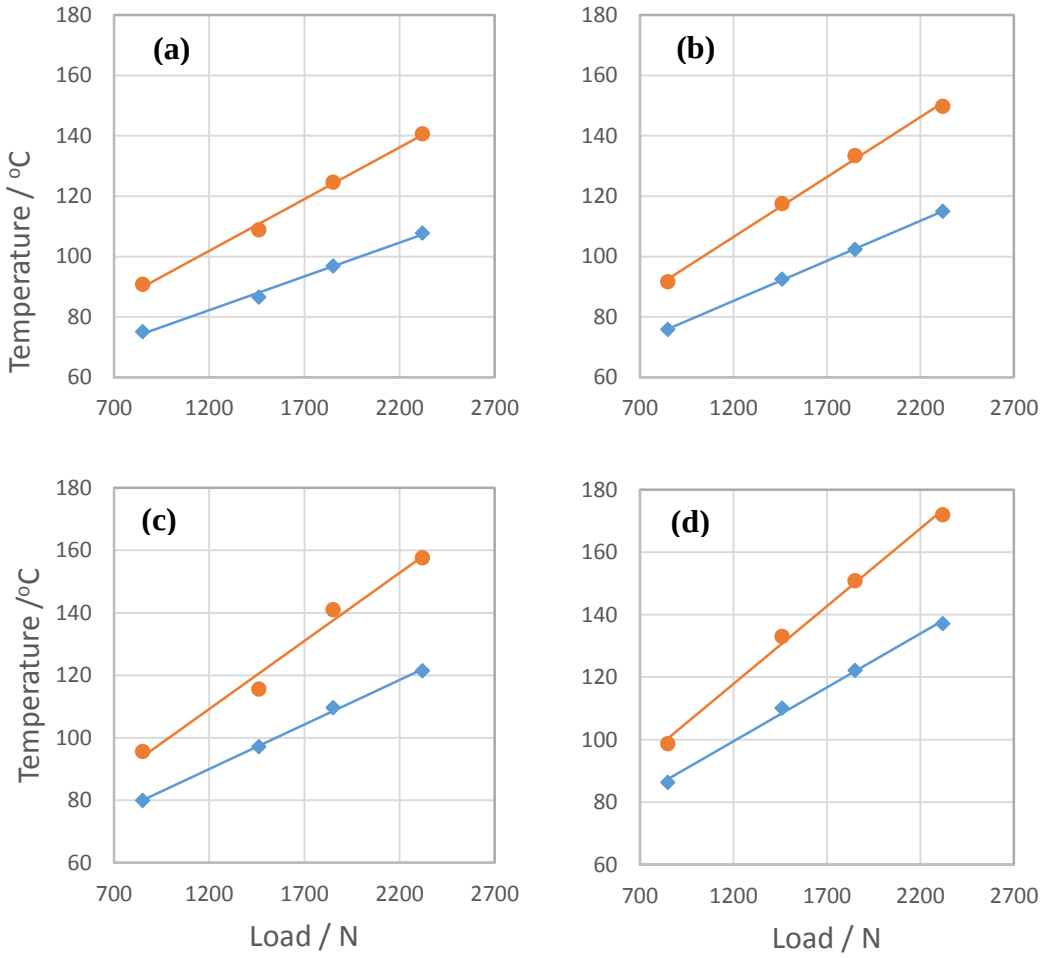

Figure 7.20: The maximum calculated surface temperature versus load of the test disks at the end time of loading (approximately steady state): orange points, fast disk; blue points, slow disk. The figure correspond to different sliding speeds of: (**a)** 10 m/s, (**b)** 13 m/s, (**c)** 16 m/s and (**d)** 20 m/s.

Figure 7.20 shows that the maximum surface temperatures of all experiments follow a linear trend for both fast and slow disks at each sliding speed. The temperature also increases when the sliding speed increased at particular load. The most important fact

that Figure 7.20 represents is that the temperature of the fast disk is higher than the slow disk, and they both follow linear trends. This is compatible with the measured bulk temperatures shown in Figure 6.17. From these observations, it can be concluded that the experimental method and the modelling technique are consistent to a good extent in spite of the uncertainties described in section 6.4.2.

The calculated surface temperature sensitivity to β in a particular test was also examined. The D4 experiment was selected for this investigation. The β factor was varied over the range of 0.42 to 0.68 with heat transfer coefficients values corresponding to the lines of minimum error in Figure 7.16 (a) and (b). Figure 7.21 shows the maximum surface temperature for both fast and slow disks from these thermal analysis together with the heat transfer coefficient ratio (h_f/h_s) variation over the β range considered.

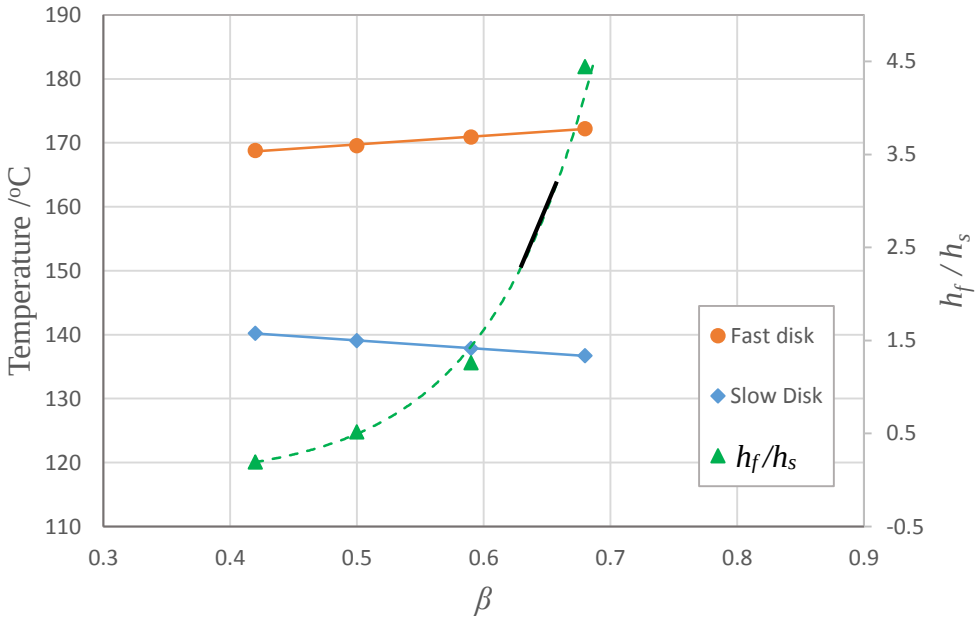

Figure 7.21: The ratio of the heat transfer coefficients and the maximum calculated surface temperature for the disks versus the assumed heat partition factor (β) in modelling the D4 test, black solid line indicates range of h_f/h_s corresponding to $0.57 \leq n \leq 0.8$

Over the β range considered, Figure 7.21 shows that the maximum temperature is increased by approximately 4^{o}C for the fast disk whilst for the slow disk it is decreased by approximately the same value.

However, significant variation is noticed for the heat transfer coefficient ratio (h_f/h_s) in Figure 7.21 over the range of β. As described in section 4.3, the ratio of the convection heat transfer coefficients is governed by the speed ratio between the disks raised to the power *n*. The value of this power was found in the literature to be typically 0.667 and varied between 0.57 to 0.8 for the literature review considered. Over this range and at constant speed ratio of 4.25, the (h_f/h_s) ratio is limited to the range of 2.3 to 3.2 which is shown as the solid h_f/h_s line in Figure 7.21 and corresponds to β value of the range 0.63 to 0.66 (approximately). Hence, the calculated β value using the technique of heat transfer coefficient speed dependence is robust to good extent.

7.5. Transient error minimization

As described in chapter four, in order to achieve full thermal modelling of the EHL experimental tests, two methods were proposed for evaluating the heat partition factor, β; in the tests. The first was to apply the speed dependence convection heat transfer coefficient relation for a horizontal rotating cylinder. This relation was used to link the lines of minimum error of both disks, and hence evaluate the values of β and the convection heat transfer coefficients, see section 4.3. The second method was to minimize the error over a short time (about one second) following the un-loading. In this case, the relation between the speed and the convection heat transfer coefficient is not involved and each disk is solved individually. Several challenges were associated with this method, such as the delay in the separation of the disks after

unloading, monitoring of the actual time of the separation, the thermocouple arrangement and installation in the disks and the lag in the dynamic response of the thermocouples. Most of these limitations were eliminated or reduced as described in chapter five. The lag in the thermocouples' dynamic response would be compensated before conducting this type of solution. Figure 7.22 shows the measured and calculated temperatures of a typical D4 test for the fast disk over a short time prior and following un-loading the disks. These temperatures are at the ***e*** and ***b*** thermocouples which are 1.25 mm and 6 mm below the surface respectively. In this figure, the dark zone would be used for the solution, when the ***e*** thermocouple measurement shows sufficient variation before the temperature measured by the ***b*** thermocouple shows any significant change. This was one of the goals for locating a thermocouple near the surface. It can also be seen clearly that all the calculated temperatures at ***e*** using a range of β values show a response in advance of the measurements which is due to system lag of response (including thermocouple lag). As a result, a response compensation method is required in order to complete this solution, noting that in the selected dark zone in Figure 7.22, the boundary thermocouples typically ***b*** measures the actual temperature at steady state, which lead to realistic calculated temperature at ***e***. So that this realistic calculated temperature can be used in the compensation especially if it is compensated to match the experimental measurements.

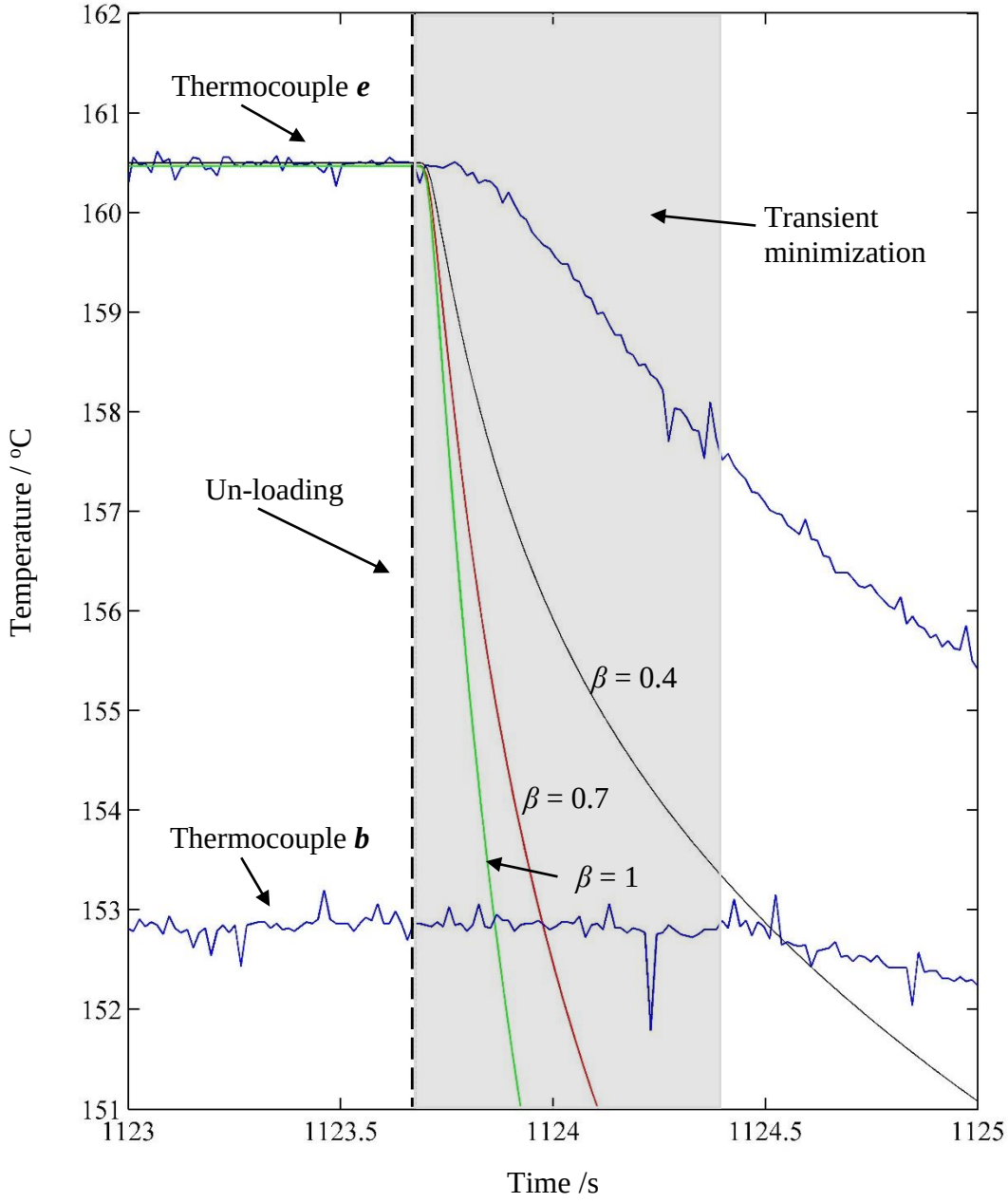

Figure 7.22: Typical calculated and measured temperature for the fast disk in D4 test showing the solution method based on transient error minimization.

In summary, this chapter reported the results of modelling the EHL tests carried out in the current work and in the work of Clarke(2009) based on error minimization over the approximately steady state. The results show that the majority(65 % to 77 %) of heat is conducted to the fast disk for both sets of experiments. This is in agreement with the previous findings of Clarke (2009, 2006). This also agrees with model F used in the thermal EHL point contact solver by Clarke (2009). Finally, the test rig developments have led to improvements in the modelling based on transient error minimization. However, compensation of the transient temperature measurements is required.

Chapter 8:

Conclusions and Recommendations for Future Works

8.1. Summary of the work

A twin disk test rig for the investigation of elastohydrodynamic lubrication (EHL) was re-commissioned and instrumented. Labview software was constructed for the test data acquisition. The temperature and heat partition between the super-finished test disks during rolling/sliding EHL contact were investigated using this rig.

The test rig was subjected to many developments:

- The loading mechanism was modified to ensure rapid disk separation during the unloading phase. The disk unloading time was monitored using a microswitch connected to the data acquisition software.
- The arrangement of the thermocouple locations and installation technique were studied and developed. The dynamic response of the thermocouples were studied by using disk immersion tests in a baths of hot oil and water.
- New data acquisition hardware (NI 9213) was installed in conjunction with the original hardware. This allows for the use of up to 16 additional thermocouples to measure and investigate further important temperatures. The oil jets, the ambient, the oil tank and the bearing housings were measured using this additional hardware.

A series of experimental EHL tests were carried out after this rig development program was completed. Furthermore, extensive investigation were carried out to study some experimental uncertainties.

A thermal numerical model was constructed to calculate the transient two dimensional temperature distribution within the test disks based on the experimental EHL tests. Electrical noise in the experimental data was eliminated by curve fitting the data before modelling it. A transient conduction analysis of the disks was developed and used in two ways. Firstly, an analysis of the heating phase leading to detailed evaluation of the temperature distribution with error minimization are applied over the approximately steady state interval over the last 150 seconds of the loading phase. Secondly, the transient solution where an attempt was made to optimize the error at the rapid temperature drop just after un-loading the test disks.

8.2. Conclusions

- During the series of EHL experimental tests conducted, higher bulk temperatures of the faster disk were achieved, which is in agreement with the previous work on the same test rig.
- The bulk temperature of the disks increases as the load is increased and they follow a linear trend at each equal sliding speed group. This consistency of the results indicates a robust experimental scheme.
- Asymmetry in the measured thermocouple temperatures was investigated at length and the following possible causes were ruled out:
    - Thermocouple wiring.
    - Misalignment of the disk contact.

  - Thermocouple dynamic response.
  - Slip ring error.
  - Bearing temperature asymmetry.
  - Possible asymmetry in heat transfer convection.
  - Possible ambient temperature asymmetry.

- The most likely cause behind the measurement uncertainties is thought to be circumferential variation in the contact pressure along the interference fit between the disks and the shafts. This pressure variation leads to significant circumferential change in the thermal conductance along the fit.
- The unloading mechanism developments led to realistic temperature measurements having continuous smooth trends within the cooling phase.
- Accurate time of disk separation was achieved using a microswitch connected to the data acquisition system.
- The thermocouples installed in the test disks undergo consistent lag in their dynamic response during rapid temperature change. This was noticed in modelling the cooling phase of the EHL tests and was confirmed by modelling the disk immersion tests in a hot oil bath. A mathematical model is required to compensate for the thermocouples dynamic response.
- The radial centreline temperature variation within the disks is much larger than that at and near the side faces, especially close to the outer diameter. This led to moving one of the side thermocouples at 3 mm below the surface to a centreline location at 1.25 mm below the outer surface in both disks.
- The new thermocouple position is also important in the cooling phase modelling. It measures a significant temperature drop before the boundary thermocouples (6 mm below the surface) experience a temperature change.

This allows the modelling to be based on realistic boundary temperatures as they are at steady state.

- Error minimization over near steady conditions state cannot give a clear position to determine the heat partition factor β (or 1- β for the slow disk) and the convection heat transfer. The minimum error construct a linear relationship between the heat partition factor and the convection heat transfer for both disks.
- The loading phase of the experimental data was modelled and the error was optimized over the approximately steady state interval. The heat partition factor was determined by relating the lines of minimum error of both disks and the speed dependence of the convection heat transfer coefficients. The calculated β values are in the range of 0.65 to 0.77 for the current work and 0.71 to 0.77 for modelling the previous experiments of (Clarke 2009) which were taken with different disks.
- The β results confirm that the majority of the generated heat within the EHL contact is conducted to the fast disk which is compatible with the previous finding in (Merritt 1962; Clarke et al. 2006; Clarke 2009).
- The calculated β results agree with the numerical EHL outcome in (Clarke 2009) and (Clarke et al. 2006) based on Bair and Winer rheology and Barus viscosity model of the lubricant, indicating that slip occurs at or near the faster surface.
- The measured traction force increases with load increase at constant sliding speed following a linear trend.
- The coefficient of friction decreases with sliding speed increase.

8.3. Recommendations for future work

- **Temperature measurement uncertainties**: Developing a three dimensional thermal numerical model for the test disk and including the effect of variable contact conductance with the shaft along the circumferential direction to assess the temperature variation according to the expected variation of the conductance due to pressure fit variation. If this effect was confirmed, the thermocouples arrangement should be redesigned making them in closer circumferential proximity. Alternatively, an integral disk and shaft should be designed and manufactured from solid. This will remove the conductance variation, furthermore, the disk and the shaft will be symmetric which allows for symmetric temperature distribution.
- **The compensation of the transient measured temperature:** The measured and calculated temperature obtained from immersion test could be used as input and output of un known dynamic system. The characteristic equation of this dynamic system can be determined using system identification techniques. The system is treated as a black box of known input and output. A useful computer software for this application is the Matlab System Identification Toolbox. This software allows for importing discrete input output data to be examined with many built in dynamic models. The user would select the best model that represents the input output data. The software also offers assessment technique to examine the identified system. Consequently, the identified system would be used to compensate the thermocouple measurements. This technique has the potential to offer proper compensation as all the possible factors that can contribute in the lag of response are included. These factors are: the thermocouple junction mass, the effect of the fixing

cement, the holes in which thermocouples are installed and the electronic devices. Alternatively, there are many studies to assess and compensate the dynamic response of thermocouples, for instance: (Segall 2001), (Asay et al. 2005) and (Yang and Meng 2014), these might be beneficial in the compensation in this work.

- **EHL heat flux:** A parabolic heat flux was imposed in this work in representing the heat input to the disks at the EHL contact. This was based on the correlation with the Hertzian pressure distribution. An alternative heat flux distribution might be applied based on the correlation with the lubricant viscosity.
- **Thermocouple fixing:** for better dynamic thermocouple response, an alternative fixing method could be used instead of the best available cement that has a thermal conductivity that is much lower than the conductivity of the disk material.
- **Oil type**: In addition to the Mobil jet II used in the current work, investigating different types of oil in the EHL experiments would give more insight on the thermal aspect of the elastohydrodynamic lubrication.
- **Heat flux measurements**: In modelling the running surface of the disk, the convection heat leaving the disks depends on the heat transfer coefficient and the ambient temperature which are complex to evaluate or measure. Alternatively, if the convection heat flux is measured, the heat transfer coefficient and the ambient temperature will not be involved in the modelling. This measurement could be achieved by fixing small element containing a heater and thermocouple on the ceramic washer running surface as shown in Figure 8.1. Measuring the electric current that provides the heater gives the amount of heat generated and leaving the heater at steady temperature. The

heat flux from this spot should be the same as that from the disks surface for the same temperature. A heat flux-temperature relation could be obtained and used for the disks surface model.

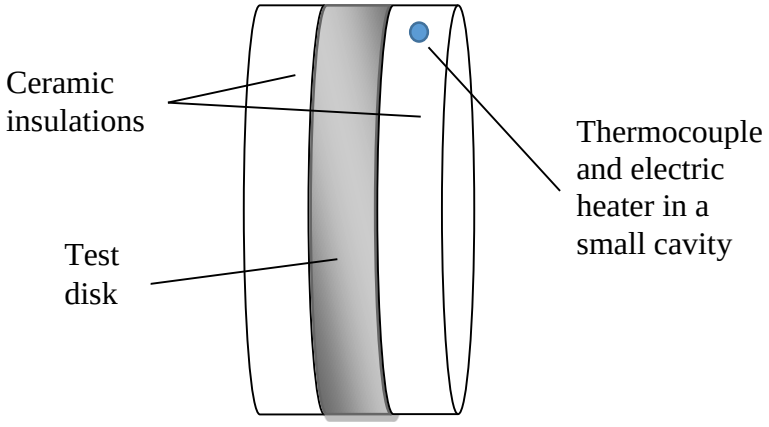

Figure 8.1: Schematic diagram of the proposed technique for measuring convected heat flux from the disk surface during EHL tests.

References

Al-Hamood, A., Clarke, A. and Evans, H. 2015. Experimental determination of heat partition in elastohydrodynamic contacts. *Proceedings of the Institution of Mechanical Engineers, Part J: Journal of Engineering Tribology* 0(0), pp. 1–10. Available at: http://pij.sagepub.com/lookup/doi/10.1177/1350650115587036.

Anderson, J.T. and Saunders, O.A. 1953. Convection from an Isolated Heated Horizontal Cylinder Rotating about Its Axis. *Proceedings of the Royal Society A: Mathematical, Physical and Engineering Sciences* 217, pp. 555–562.

Archard, J.F. 1959. The temperature of rubbing surfaces. *wear* 2(6), pp. 438–455.

Asay, B.W., Son, S.F., Dickson, P.M., Smilowitz, L.B. and Henson, B.F. 2005. An investigation of the dynamic response of thermocouples in inert and reacting condensed phase energetic materials. *Propellants, Explosives, Pyrotechnics* 30(3), pp. 199–208.

Ausherman, V.K., Sanborn, D.M., Winer, W.O. and Nagaraj, H.S. 1975. Infrared temperature mapping in elastohydrodynamic lubrication. *Trans. ASME* (April), pp. 236–242.

Bair, S. and Winer, W.O. 1979. A rheological model for elastohydrodynamic contacts based on primary laboratory data. *Journal of Tribology* 101(3), pp. 258–264.

Bently, J. 1995. *Principles of measurement systems*. Longman Group Limited.

Blok, H. 1937. Theoretical study of temperature rise at surfaces of actual contact under oilness lubricating conditions. In: *Proceedings of the IMechE-general discussion on lubrication 2*. pp. 222–235.

Bolton, W. 1996. *Measurement and instrumentation systems*. Butterworth-Heinemann.

Cameron, A. 1985. Righting a 40-year-old wrong. *Tribology International* 18(30), p. 92.

Cann, P.M. and Spikes, H.A. 1989. Determination of the shear stresses of lubricants in elastohydrodynamic contacts. *Tribology Transactions* 32(3), pp. 414–422.

Cardone, G., Astarita, T. and Carlomagno, G.M. 1997. Heat transfer measurements on a rotating disk. *International Journal of Rotating Machinery* 3(1), pp. 1–9.

Chang, L. 1992. Traction in Thermal Elastohydrodynamic Lubrication of Rough Surfaces. *Journal of Tribology* 114(January), p. 186.

Churchill, S.W. and Chu, H.H.S. 1975. Correlating equations for laminar and turbulent free convection from a vertical plate. *International journal of heat and mass transfer* 18(11), pp. 1323–1329.

Clarke, A., Sharif, K., Evans, H.P. and Snidle, R.W. 2006. Heat partition in rolling/sliding elastohydrodynamic contacts. *Journal of Tribology* 128(January), pp. 67–78. Available at: http://orca.cf.ac.uk/7688/.

Clarke, A., Sharif, K., Evans, H.P. and Snidle, R.W. 2007. Elastohydrodynamic modelling of heat partition in rolling-sliding point contacts. *Proceedings of the Institution of Mechanical Engineers, Part J: Journal of Engineering Tribology* 221, pp. 223–235. Available at: http://orca.cf.ac.uk/7689/.

Clarke, A., Weeks, I.J.J., Evans, H.P. and Snidle, R.W. 2014. An investigation into mixed lubrication conditions using electrical contact resistance techniques. *Tribology International*, pp. 1–8. Available at: http://linkinghub.elsevier.com/retrieve/pii/S0301679X14003661.

Clarke, A. 2009. Heat partition in elastohydrodynamic sliding contacts under full film lubrication conditions. PhD Thesis. Cardiff University

Croft, D.R., Stone, J.A.R. and Lilley, D.G. 1977. *Heat transfer calculations using finite difference equations*. Applied Science Publishers London.

Deolalikar, N., Sadeghi, F. and Marble, S. 2008. Numerical Modeling of Mixed Lubrication and Flash Temperature in EHL Elliptical Contacts. *Journal of Tribology* 130(January), p. 011004.

Department of Education and Scince. 1966. Lubrication (Tribology) Education and Research A Report on the Present Position and Industries' Needs. HMSO. London.

Dinç, O.S., Ettles, C.M., Calabrese, S.J. and Scarton, H. A. 1993. The Measurement of Surface Temperature in Dry or Lubricated Sliding. *Journal of Tribology* 115(January), p. 78.

Dow, T.A. and Kannel, J.W. 1979. Evaluation of rolling/sliding EHD temperatures. In: *Proc. 6th Leeds-Lyon Symposium on Tribology*. pp. 228–241.

Dowson, D. 1998. *History of Tribology*. 2nd ed. Professional Engineering Publishing Limited, London, UK

Dowson, D. and Higginson, G.R. 1959. A numerical solution to the elasto-hydrodynamic problem. *Journal of Mechanical Engineering Science* 1(1), pp. 6–15.

Dowson, D., Higginson, G.R. and Whitaker, A. V 1962. Elasto-Hydrodynamic Lubrication: A Survey of Isothermal Solutions. *Journal of Mechanical Engineering Science* 4(2), pp. 121–126.

Dropkin, D. and Carmi, A. 1957. Natural convection heat transfer from a horizontal cylinder rotating in air. *Trans. ASME* 79(4), pp. 741–749.

Evans, H.P. and Snidle, R.W. 2009. The future of engineering tribology in concentrated contacts. *Proceedings of the Institution of Mechanical Engineers, Part C: Journal of Mechanical Engineering Science* 223(12), pp. 2939–2948.

Evans, R.D., Cogdell, J.D., Richter, G. A. and Doll, G.L. 2008. Traction of Lubricated Rolling Contacts between Thin-Film Coatings and Steel. *Tribology Transactions* 52(September 2014), pp. 106–113.

Fletcher, L.S. 1988. Recent Developments in Contact Conductance Heat Transfer. *Journal of Heat Transfer* 110(November 1988), p. 1059.

Glovnea, R.P. and Spikes, H.A. 1995. Mapping shear stress in elastohydrodynamic contacts. *Tribology transactions* 38(4), pp. 932–940.

Gohar, R. 2001. *Elastohydrodynamics*. World Scientific.

Grubin, A.N. 1949. *Investigation of the Contact of Machine Components*. Central Scientific Research Institute for Technology and Mechanical Engineering, Book No.30, Moscow, DSIR Translation No. 337.

Habchi, W. and Vergne, P. 2015. On the compressive heating/cooling mechanism in thermal elastohydrodynamic lubricated contacts. *Tribology International* 88, pp. 143–152. Available at: http://linkinghub.elsevier.com/retrieve/pii/S0301679X15001152.

Hamrock, B.J., Schmid, S.R. and Jacobson, B.O. 2004. *Fundamentals of fluid film lubrication*. CRC press.

Handschuh, R.F. and Gargano, L.J. 2014. Test Facility Simulation Results for Aerospace Loss-of-Lubrication of Spur Gears. *Nasa Technical Reports Server (NTRS)* (October).

Henning, F.E.K.A.K., Frusescu, D., Caballero, L.M., Tian, X. and Cook, T.M. 1995. TEMPERATURE SENSORS FOR DETECTING FAILURE OF TRIBOLOGICAL COMPONENTS. *Vibration Institute*, p. 281.

Hertz, H. 1881. On the contact of elastic solids. *J. reine angew. Math* 92(156-171), p. 110.

Holman, J.P. 2010. *Heat Transfer*. Tenth Edit. McGraw-Hill.

Horng, J.H. 1998. True Friction Power Intensity and Scuffing in Sliding Contacts. *Journal of Tribology* 120(October), p. 829.

Iliuc, I. 1980. *Tribology of thin layers*. Elsevier.

Ishikawa, J., Hayashi, K. and Okoyama, M. 1974. Surface Temperature and Scoring Resistance of Heavy-Duty Gears. *Engineer* 96(72), pp. 385–390.

Jaeger, J.C. 1942. Moving sources of heat and the temperature at sliding contacts. *Proceedings of the Royal Society of NSW* 76, pp. 203–224.

Jarvio, O. and Lehtovaara, A. 2002. Experimental study of influence of lubricants on friction in spur gear contacts. *TRIBOLOGIA-TAMPERE-* 21(2/3), pp. 22–29.

Johnson, K.L. and Johnson, K.L. 1987. *Contact mechanics*. Cambridge university press.

Kim, H.J., Ehret, P., Dowson, D. and Taylor, C.M. 2001a. Thermal elastohydrodynamic analysis of circular contacts Part 1: Newtonian model. *Proceedings of the Institution of Mechanical Engineers, Part J: Journal of Engineering Tribology* 215(January 2000), pp. 339–352. Available at: http://pij.sagepub.com/lookup/doi/10.1243/1350650011543592.

Kim, H.J., Ehret, P., Dowson, D. and Taylor, C.M. 2001b. Thermal elastohydrodynamic analysis of circular contacts Part 2: non-Newtonian model. *Proceedings of the Institution of Mechanical Engineers, Part J: Journal of Engineering Tribology* 215(January 2000), pp. 353–362. Available at: http://pij.sagepub.com/lookup/doi/10.1243/1350650011543592.

Kleemola, J. 2010. Experimental Methods for the Evaluation of Lubrication Conditions in Gear Contacts. Tampere University of Technology.

Kleemola, J. and Lehtovaara, A 2008. An approach for determination of lubricant properties at elliptical elastohydrodynamic contacts using a twin-disc test device and a numerical traction model. *Proceedings of the Institution of Mechanical Engineers, Part J: Journal of Engineering Tribology* 222, pp. 797–806. Available at: http://pij.sagepub.com/lookup/doi/10.1243/13506501JET447.

Kleemola, J. and Lehtovaara, A 2010. Evaluation of lubrication conditions in gear contacts using contact resistance and bulk temperature measurements. *Proceedings of the Institution of Mechanical Engineers, Part J: Journal of Engineering Tribology* 224, pp. 367–375. Available at: http://pij.sagepub.com/lookup/doi/10.1243/13506501JET675.

Kleemola, J. and Lehtovaara, A. 2006. Development of a high pressure twin disc test device for the simulation of gear contact. *Tribologia, Finnish Journal of Tribology*.

Kleemola, J. and Lehtovaara, A. 2007. Experimental evaluation of friction between contacting discs for the simulation of gear contact. *Tribo Test* 13(December 2006), pp. 13–20.

Kleemola, J. and Lehtovaara, A. 2009. Experimental simulation of gear contact along the line of action. *Tribology International* 42(10), pp. 1453–1459. Available at: http://dx.doi.org/10.1016/j.triboint.2009.06.007.

Lehtovaara, A. 2002. Calculation of Sliding Power Loss in Spur Gear Contacts. *Tribologest*. 2002, pp. 23–34.

Leung, M., Hsieh, C.K. and Goswami, D.Y. 1998. Prediction of Thermal Contact Conductance in Vacuum by Statistical Mechanics. *Journal of Heat Transfer* 120, p. 51.

Lugt, P.M. and Morales-Espejel, G.E. 2011. A Review of Elasto-Hydrodynamic Lubrication Theory. *Tribology Transactions* 54(April 2015), pp. 470–496.

Manton, S.M., O'Donoghue, J.P. and Cameron, A. 1967. Temperatures at lubricated rolling/sliding contacts. *Proceedings of the Institution of Mechanical Engineers* 182(1), pp. 813–824.

Martin, H.M. 1916. Lubrication of gear teeth. *Engineering (London)* 102, pp. 119–121.

Matlab curve fitting toolbox user's guide [Online] Available at: www.mathworks.co.uk/help/pdf_doc/curvefit/curvefit.pdf.

McGee, T.D. 1988. *Principles and methods of temperature measurement*. John Wiley & Sons.

Merritt, H.E. 1962. Gear- tooth contact phenomena. *Proceedings of the Institution of Mechanical Engineers 1847-1982 (vols 1-196)* 176(7), pp. 141–163.

Okamoto, Y., Kitahara, K., Ushijima, K., Aoyama, S., Xu, H., Jones, G.J. 2000. Study for wear and fatigue on engine bearings by using EHL analysis. *JSAE review* 21, pp. 189–196. Available at: http://papers.sae.org/1999-01-0287.

Olver, A.V. 1991. Testing transmission lubricants: the importance of thermal response. *ARCHIVE: Proceedings of the Institution of Mechanical Engineers, Part G: Journal of Aerospace Engineering 1989-1996 (vols 203-210)* 205, pp. 35–44. Available at: http://archive.pepublishing.com/openurl.asp?genre=article&id=doi:10.1243/PIME_PROC_1991_205_235_02.

Olver, A.V. and Spikes, H. A. 1998. Prediction of traction in elastohydrodynamic lubrication. *Proceedings of the Institution of Mechanical Engineers , Part J : Journal of Engineering Tribology* 212(May), pp. 321–332.

Özerdem, B. 2000. Measurement of convective heat transfer coefficient for a horizontal cylinder rotating in quiescent air. *International Communications in Heat and Mass Transfer* 27(3), pp. 389–395.

Patching, M.J. 1994. The effect of surface roughness on the microelastohydrodynamic lubrication and scuffing performance of aerospace gear tooth contacts. University of Wales College of Cardiff.

Patching, M.J., Kweh, C.C., Evans, H.P. and Snidle, R.W. 1995. Conditions for Scuffing Failure of Ground and Superfinished Steel Disks at High Sliding Speeds Using a Gas Turbine Engine Oil. *Journal of Tribology* 117(July), p. 482.

Popova, E. and Popov, V.L. 2014. On the history of elastohydrodynamics: The dramatic destiny of Alexander Mohrenstein-Ertel and his contribution to the theory and practice of lubrication. *ZAMM Zeitschrift fur Angewandte Mathematik und Mechanik* 12, pp. 1–12.

Qiao, H. 2005. Prediction of contact fatigue for the rough surface elastohydrodynamic lubrication line contact problem under rolling and sliding conditions. PhD Thesis.Cardiff University.

Reddyhoff, T., Spikes, H.A. and Olver, A.V. 2009. Improved infrared temperature mapping of elastohydrodynamic contacts. *Proceedings of the Institution of Mechanical Engineers, Part J: Journal of Engineering Tribology* 223, pp. 1165–1177. Available at: http://pij.sagepub.com/content/223/8/1165.abstract.

Reynolds, O. 1886. On the Theory of Lubrication and Its Application to Mr. Beauchamp Tower's Experiments, Including an Experimental Determination of the Viscosity of Olive Oil. *Proceedings of the Royal Society of London* 40(242-245), pp. 191–203.

Le Rouzic, J. and Reddyhoff, T. 2013. Development of Infrared Microscopy for Measuring Asperity Contact Temperatures. *Journal of Tribology* 135(April), p. 21504. Available at: http://dx.doi.org/10.1115/1.4023148.

Sadeghi, F. and Dow, T.A. 1987. Thermal Effects in Rolling/Sliding Contacts: Part 2—Analysis of Thermal Effects in Fluid Film. *Journal of Tribology* 109(July), p. 512.

Sadeghi, F. and Sui, P.C. 1990. Thermal Elastohydrodynamic Lubrication of Rolling/Sliding Contacts. *Journal of Tribology* 112(April), p. 189.

Sanborn, D.M. and Winer, W.O. 1971. Fluid Rheological Effects in Sliding Elastohydrodynamic Point Contacts With Transient Loading: 1—Film Thickness. *Journal of Lubrication Technology* 93, pp. 262–270 (a).

Sanborn, D.M. and Winer, W.O. 1971. Fluid Rheological Effects in Sliding Elastohydrodynamic Point Contacts With Transient Loading: 2—Traction. *Journal of Lubrication Technology* 93(70), pp. 342–346 (b).

Segall, A. E. 2001. Solutions for the correction of temperature measurements based on beaded thermocouples. *International Journal of Heat and Mass Transfer* 44, pp. 2801–2808.

Sharif, K., Evans, H.P., Snidle, R.W. and Newall, J.P. 2004. Modelling of film thickness and traction in a variable ratio traction drive rig. *Journal of Tribology* 126(January). Available at: http://orca.cf.ac.uk/21294/.

Sharif, K.J., Kong, S., Evans, H.P. and Snidle, R.W. 2001. Contact and elastohydrodynamic analysis of worm gears, Part 1: Theoretical formulation. *Journal of Mechanical Engineering Science* 215, pp. 817–830. Available at: http://orca.cf.ac.uk/2106/.

Shigley, J E. C.R.M. 2001. *Mechanical Engineering Design*. sixth. McGraw-Hill.

Smith, G.D. 1985. *Numerical solution of partial differential*. Clarendon Press. Oxford.

Spikes, H.A., Anghel, V. and Glovnea, R. 2004. Measurement of the rheology of lubricant films within elastohydrodynamic contacts. *Tribology Letters* 17(3), pp. 593–605.

Stachowiak, G. and Batchelor, A.W. 2004. *Experimental methods in tribology*. Elsevier.

Sui, P.C. and Sadeghi, F. 1991. Non-Newtonian Thermal Elastohydrodynamic Lubrication. *Journal of Tribology* 113(April), p. 390.

Turchina, V., Sanborn, D.M. and Winer, W.O. 1974. Temperature measurements in sliding elastohydrodynamic point contacts. *Trans. ASME* (July), pp. 464–469.

Vizintin, J., Kalin, M., Dohda, K. and Jahanmir, S. 2004. Tribology of Mechanical Systems. *ASME, New York*.

Voller, L. 2010. Development of heat partition test rig. Final year project. Cardiff University.

Wang, S.H. and Zhang, H.H. 1987. Combined effects of thermal and non-Newtonian character of lubricant on pressure, film profile, temperature rise, and shear stress in EHL. *Journal of tribology* 109(4), pp. 666–670.

Williams, J. 2005. *Engineering tribology*. Cambridge University Press.

Wolff, R., Nonaka, T., Kubo, A. and Matsuo, K. 1992. Thermal Elastohydrodynamic Lubrication of Rolling/Sliding Line Contacts. *Journal of Tribology* 114(October), p. 706.

Wymer, D.G. and Macpherson, P.B. 1975. An infra-red technique for the measurement of gear tooth surface temperature. *ASLE TRANSACTIONS* 18(4), pp. 229–238.

Yang, Z. and Meng, X. 2014. Research on the Dynamic Calibration of Thermocouple and Temperature Excitation Signal Generation Method Based on Shock-Tube Theory. *Journal of Engineering for Gas Turbines and Power* 136(37), p. 071602. Available at: http://gasturbinespower.asmedigitalcollection.asme.org/article.aspx?doi=10.1115/1.4026547.

Yovanovich, M.M. 2005. Four decades of research on thermal contact, gap, and joint resistance in microelectronics. *IEEE Transactions on Components and Packaging Technologies* 28(2), pp. 182–206.

Zhu, D. and Hu, Y.-Z. 2001. A computer program package for the prediction of EHL and mixed lubrication characteristics, friction, subsurface stresses and flash temperatures based on measured 3-D surface roughness. *Tribology Transactions* 44(3), pp. 383–390.

Appendix A: Macor machinable ceramic brochure.

Corning Incorporated
Lighting & Materials
Houghton Park CB-08
Corning, New York 14831
tel: 607-974-4331
fax: 607-974-7618

www.corning.com
e-mail: macor@corning.com

MACOR 01

Printed in the U.S.A

MACOR®

CORNING
Discovering Beyond Imagination

Lighting &
Materials

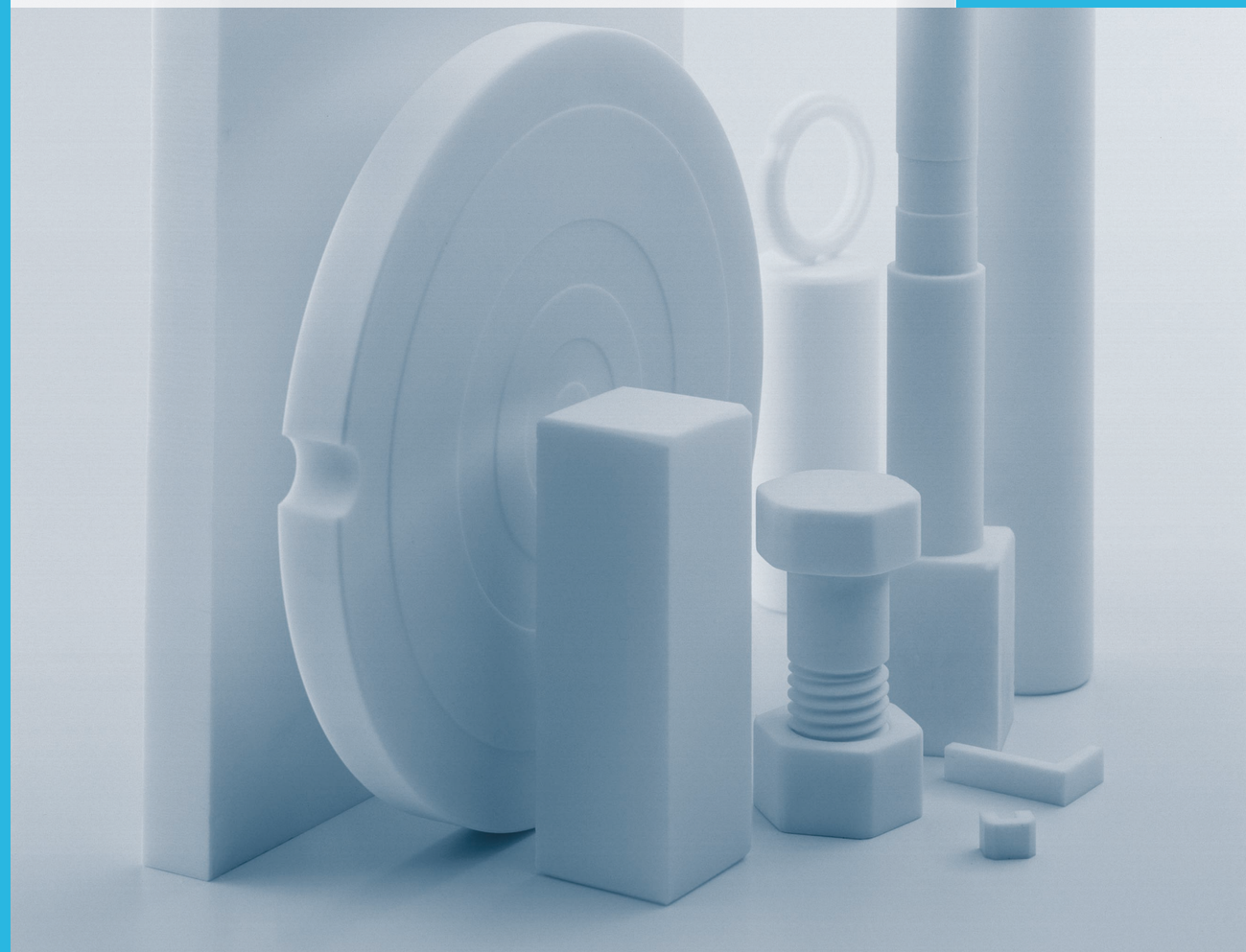

MACOR®
Machinable Glass Ceramic

- is MACHINABLE with ordinary metal working tools
- allows FAST TURNAROUND, no post firing required
- holds TIGHT TOLERANCES, up to .0005”
- withstands HIGH TEMPERATURE, up to 1000°C (no load)
- is CLEAN, no outgasing and zero porosity

With MACOR® Machinable Glass Ceramic (MGC), fabrication is fast because it can be machined into complicated shapes and precision parts with ordinary metal working tools, quickly and inexpensively, and it requires no post firing after machining. That means no frustrating delays, no expensive hardware, no post fabrication shrinkage, and no costly diamond tools to meet specifications.

Properties

MACOR® Machinable Glass Ceramic has a continuous use temperature of 800°C and a peak temperature of 1000°C. Its coefficient of thermal expansion readily matches most metals and sealing glasses. It is nonwetting, exhibits zero porosity, and unlike ductile materials, won't deform. It is an excellent insulator at high voltages, various frequencies, and high temperatures. When properly baked out, it won't outgas in vacuum environments.

Machining

Machining tolerances are surprisingly tight, up to .0005". It can be machined to a surface finish of less than 20µin. and polished to a smoothness of 0.5µin.-AA. Configurations are limited only by available equipment and the experience of the machinist.

Sealing, Joining and Metalizing

MACOR MGC can also be joined or sealed - both to itself and to other materials - in a number of ways: metalized parts can be soldered together and brazing has proven an effective method of joining the material to various metals; epoxy produces a strong joint, and sealing glass creates a vacuum tight seal. Even a straight-forward mechanical joint is possible.

It can be thick film metalized using metal inks, or thin film metalized by sputtering.

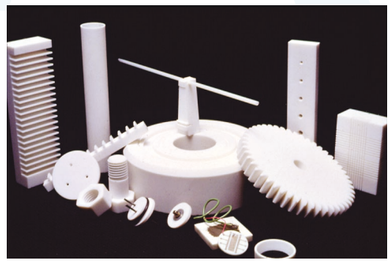

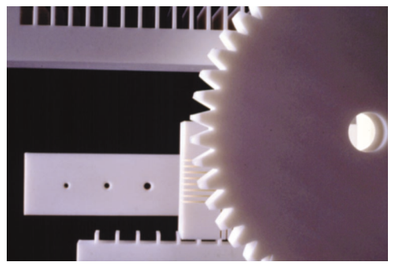

Applications

Ultra-High Vacuum Environments

MACOR® Machinable Glass Ceramic is used as an insulator or coil support and for vacuum feed-throughs. In these applications, the conductive materials are supported by the MACOR MGC part and a compatible sealing glass is used to produce a vacuum-tight, hermetic seal.

Constant Vacuum Applications

MACOR MGC parts are found in spacers, headers and windows for microwave tube devices and as sample holders in field ion microscopes.

Aerospace Industry

Over 200 distinctly shaped MACOR MGC parts can be found on America's reusable Space Shuttle Orbiter. Retaining rings of MACOR MGC are used at all hinge points, windows and doors.

Also, large pieces of MACOR glass ceramic are used in a NASA spaceborne gamma radiation detector. For this application, frame corners are joined by a combination of machined (butt-lap) mechanical joints and a sealing glass.

Nuclear-Related Experiments

Since MACOR MGC is not dimensionally affected by irradiation, small cubes of the material are machined to a tolerance of one micron and used as a reference piece to measure dimensional change in other materials.

Welding Nozzles

Welding equipment manufacturers are using MACOR MGC as a nozzle on the tips of oxyacetylene torches. The material's nonwetting characteristic means molten particles won't adhere to and decrease the effectiveness of the nozzle.

Fixtures

MACOR MGC is used as an electrode support and burner block in several industrial high heat, electrical cutting operations due to its low thermal conductivity and excellent electrical properties.

Medical Equipment

Producers of medical components are intrigued by MACOR MGC's inertness, precise machinability and dimensional stability.

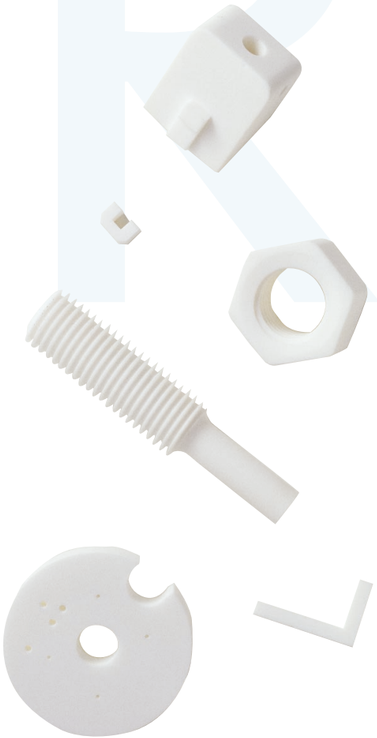

The Point is this:

When you need the performance of a technical ceramic (high use temperature, electrical resistivity, zero porosity) and your application demands the ready fabrication of a complicated shape (quickly, precisely, privately), look at MACOR MGC. It will lower costs and substantially reduce the time between design and actual use.

Properties

I. Thermal

	SI/Metric	English
Coefficient of Expansion		
-200 - 25ºC	$74x10^{-7}$/ºC	$41x10^{-7}$/ºF
25 - 300ºC	$93x10^{-7}$/ºC	$52x10^{-7}$/ºF
25 - 600ºC	$114x10^{-7}$/ºC	$63x10^{-7}$/ºF
25 - 800ºC	$126x10^{-7}$/ºC	$70x10^{-7}$/ºF
Specific Heat, 25ºC	.79 KJ/kgºC	0.19 Btu/lbºF
Thermal Conductivity, 25ºC	1.46 W/mºC	10.16 $\frac{\text{Btu in}}{\text{hr ft}^2\text{ºF}}$
Thermal Diffusivity, 25ºC	$7.3x10^{-7}m^2/s$	0.028 ft^2/hr
Continuous Operating Temperature	800ºC	1472ºF
Maximum No Load Temperature	1000ºC	1832ºF

II. Mechanical

	SI/Metric	English
Density	2.52 g/cm^3	157 lbs/ft^3
Porosity	0%	0%
Young's Modulus, 25ºC (Modulus of Elasticity)	66.9 GPa	$9.7x10^6$psi
Poisson's Ratio	0.29	0.29
Shear Modulus, 25ºC	25.5GPa	$3.7x10^6$psi
Hardness, Knopp, 100g	250	250
Rockwell A	48	48
Modulus of Rupture, 25ºC (Flexural Strength)	94 MPa	13,600 psi (minimum specified average value)
Compressive strength	345 MPa	50,000 psi
Fracture Toughness	1.53 MPa $m^{0.5}$	1,390 psi $in^{0.5}$

III. Electrical

		SI/Metric	English
Dielectric Constant, 25°C			
	1 KHz	6.03	6.03
	8.5 GHz	5.67	5.67
Loss Tangent,	25°C		
	1 KHz	$4.7x10^{-3}$	$4.7x10^{-3}$
	8.5 GHz	$7.1x10^{-3}$	$7.1x10^{-3}$
Dielectric Strength (AC) avg. (at 12 mil thickness and 25°C)		9.4 KV/mm	785 V/mil
Dielectric Strength (DC) avg. (at 12 mil thickness and 25°C)		62.4 KV/mm	5206 V/mil
DC Volume Resistivity, 25°C		$>10^{16}$ ohm-cm	$>10^{16}$ ohm-cm

IV. Chemical

Solution	pH	Time	Temp.	Results Weight Loss (mg/cm^2) Gravimetric
	Tests			
5% HCL (Hydrochloric Acid)	0.1	24 hrs.	95ºC	~ 100
0.002 N HNO_3 (Nitric Acid)	2.8	24 hrs.	95ºC	~ 0.6
0.1 N $NaHCO_3$ (Sodium Bicarbonate)	8.4	24 hrs.	95ºC	~ 0.3
0.02 N Na_2CO_3 (Sodium Carbonate)	10.9	6 hrs.	95ºC	~ 0.1
5% NaOH (Sodium Hydroxide)	13.2	6 hrs.	95ºC	~ 10
Resistance to water over time				
H_2O	7.6	1 day*	95ºC	0.01
		3 days*	95ºC	0.07
		7 days*	95ºC	9.4
		3 days**	95ºC	0.06
		6 days**	95ºC	0.11

*Water not freshened daily
**Water freshened daily

Technical Data

The general characteristics of this material described below were derived from laboratory tests performed by Corning from time to time on sample quantities. Actual characteristics of production lots may vary.

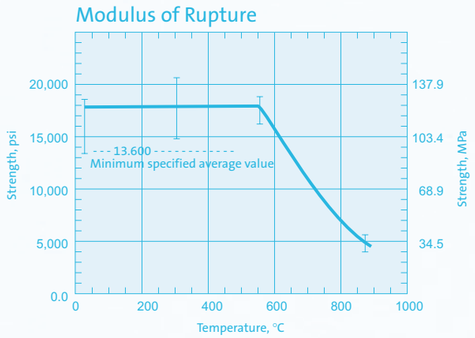

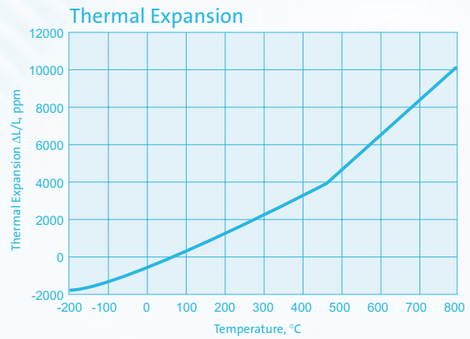

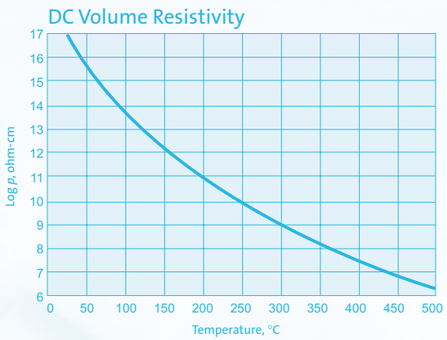

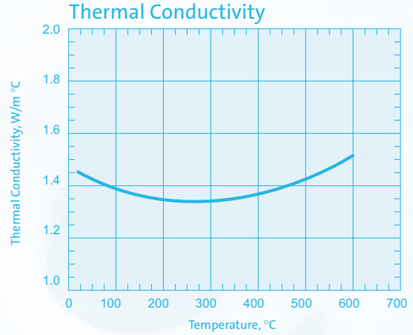

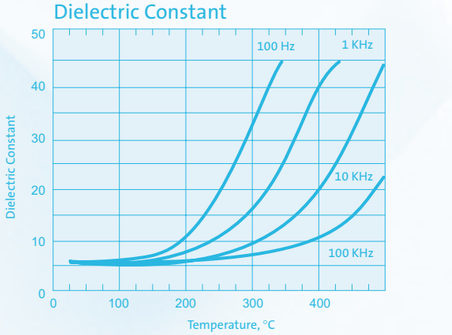

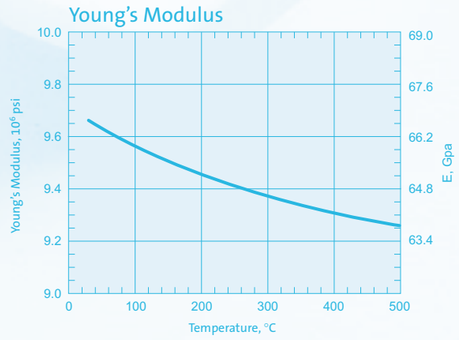

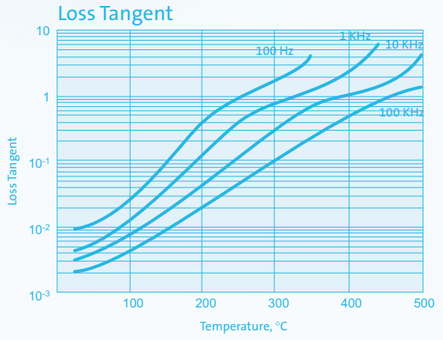

Machining

Key factors for successful machining are proper machining speeds and coolant.

MACOR Machinable Glass Ceramic can be machined with high speed steel tools, but carbide tools are recommended for longer wear.

Achieve the best results by using a water-soluble coolant, such as Cimstar 40 - Pink, especially formulated for cutting and grinding glass or ceramics.

No post firing is required after machining.

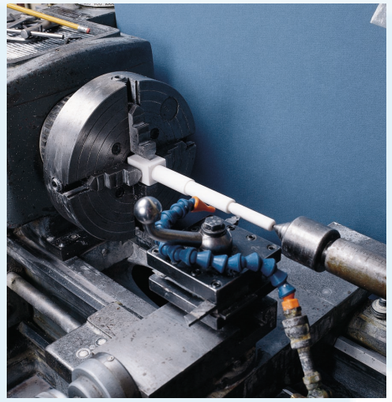

Grinding

Diamond, silicon-carbide or aluminum-oxide grinding wheels can be used.

Sawing

Use a carbide grit blade at a band speed of 100 fpm. An alternative is a silicon carbide or diamond cut-off wheel.

Milling

Cutting speed	20-35 sfm
Chip load	.002 ipt
Depth of cut	.150-.200 in.

Polishing

Start with loose 400-grit silicon carbide on a steel wheel. For the final polish, use cerium oxide or alumina on a polishing pad for glass or ceramics. A 0.5µin.-AA finish can be achieved.

Turning

Cutting speed	30-50 sfm
Feed rate	.002-.005 ipr
Depth of cut	.150-.250 in.

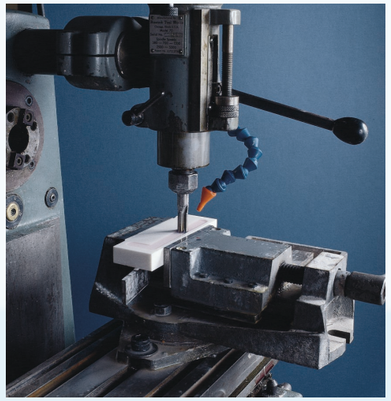

Drilling

Drill size	Spindle Speed	Feed Rate
1/4 in.	300 rpm	.005 ipr
1/2	250	.007
3/4	200	.010
1	100	.012
2	50	.015

Allow at least .050" of extra material on the back side for breakout. This excess can be removed after drilling.

Tapping

Make clearance holes one size larger than those recommended for metals. Chamfer both ends of the hole to reduce chipping. Run the tap in one direction only. (Turning the tap back and forth can cause chipping.) Continuously flush with water or coolant to clear chips and dust from the tap.

Composition

MACOR Machinable Glass Ceramic is a white, odorless, porcelain-like (in appearance) material composed of approximately 55% fluorophlogopite mica and 45% borosilicate glass. It has no known toxic effects; however, the dust created in machining can be an irritant. This irritation can be avoided by good housekeeping and appropriate machining techniques. The material contains the following compounds:

	Approximate Weight %
Silicon - SiO_2	46%
Magnesium - MgO	17%
Aluminum - Al_2O_3	16%
Potassium - K_2O	10%
Boron - B_2O_3	7%
Fluorine - F	4%

Randomly oriented mica flakes in the microstructure of MACOR MGC are the key to its machinability.

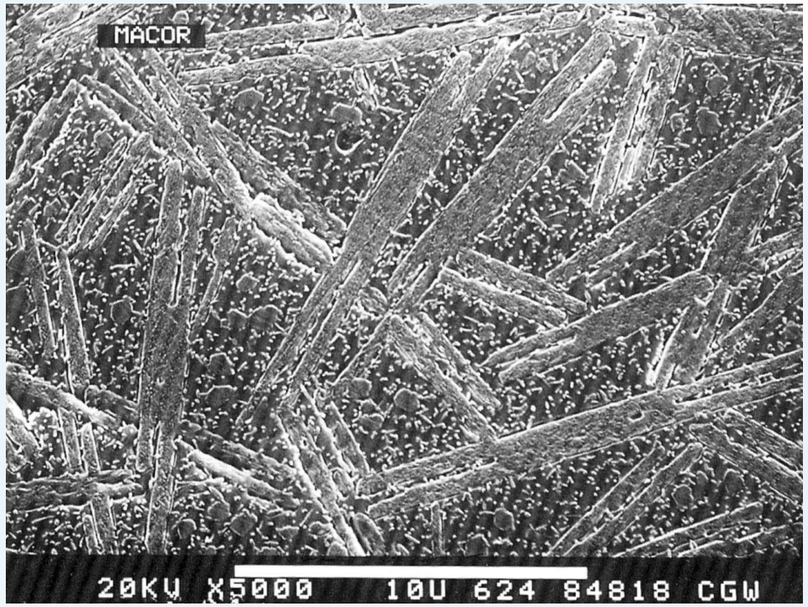

Microstructure of MACOR MGC 5000X magnification.

Appendix B. Extract from (Al-Hamood et al. 2015)

In order to relate the measured disk temperatures to the amount of heat entering the disks a heat partition parameter, β, is introduced. This is defined as the fraction of the total heat dissipated at the contact that enters the fast disk. The fraction of the dissipated heat entering the slow disk is then 1-β as the amount of heat convected out of the contact by the lubricant film separating the surfaces is orders of magnitude smaller than that conducted into the disks. This can be easily verified as the rate at which heat is convected out of the Hertzian contact area by motion of the oil in the lubricant film can be approximated by the expression

$$Q_{film} = bH_c(u_f + u_s)\rho \ c\Delta T \tag{1}$$

where ΔT is the mean temperature rise of the lubricant in passing through the Hertzian contact area, while the rate at which heat is dissipated at the contact is

$$Q_{fr} = F\left(u_f - u_s\right) \tag{2}$$

Evaluating Q_{film} and Q_{fr} for the contacts used in the experiment using data for film temperature and thickness from [11] and [12] shows that Q_{fr} exceeds Q_{film} by a factor of between 500 and 1200, and consequently that Q_{film} can be disregarded as being negligible.

Notation

b	Hertzian contact dimension transverse to the entrainment direction	M
c	Lubricant specific heat	J $kg^{-1}K^{-1}$
F	Friction force	N
H_c	Film thickness at centre of contact	M
ΔT	Lubricant temperature ris in crossing contact area	K
u_f	Velocity of the fast surface relative to the contact	ms_{-1}
u_s	Velocity of the slow surface relative to the contact	ms_{-1}
Q_{film}	Rate at which heat is convected out of the Hertzian contact area by motion of the oil in the lubricant film	W
Q_{fr}	Rate of dissipation of heat in the contact.	W
ρ	Fluid density	kgm^{-3}

Appendix C: The CC-High temperature cement data sheet.

1 YEAR
WARRANTY

OMEGA®
User's Guide

Shop online at omega.com®

e-mail: info@omega.com
For latest product manuals:
www.omegamanual.info

CC Cement
High Temperature Cement

General

OMEGA® CC High Temperature Cement is a zircon base, two-part ceramic cement which has many exceptional characteristics including:

- Resists temperatures to 1550°F (843°C) as well as cryogenic conditions (-200°C).
- Resists water, oil, electricity, most solvents and all acids (except hydrofluoric).
- Heat conductive and thermal shock resistant.
- Excellent electrical insulator.
- Adheres to metals, ceramics, glass, porcelain, and most other surfaces.
- Excellent mechanical strength.
- Ceramic-like body.

CC High Temperature Cement is an inorganic cement used for embedding heating elements; insulating thermocouples; coating resistors and coils; sealing and assembling parts which require high resistance to electricity, chemicals, and thermal shock.

Handling

CAUTION

- Avoid prolonged breathing of vapors - work in well ventilated area
- Protect skin against contamination
- Protect eyes against contamination
- Do not take internally

CC Cement Liquid Binder is an alkaline material and may irritate eyes and skin. Avoid contact with eyes and skin by wearing gloves and goggles or a face shield. CC Cement powder Filler is a harmful dust. Avoid breathing dust by wearing respirators. Wash thoroughly with soap and water after handling the liquid Binder and/or the powder Filler before eating and smoking.

Shelf Life

The CC High Temperature Cement has a shelf life of one (1) year when stored in closed, tightly sealed containers in a dry location at 70°F.

Application

The CC High Temperature Cement is supplied in two containers-one being the powder, Zirconium Silicate, the other being the liquid, Sodium Silicate. These two components are mixed together as needed. **The usual mixture is 80% powder Filler to 20% liquid Binder by weight. CC Cement may be mixed to a thinner consistency by regulating the amount of liquid Binder used; however, the use of excess liquid will reduce mechanical strength, increase shrinkage and delay the set time.** CC may be used in a vacuum, depending on application, without out-gasing. The mixture may be applied by brushing, dipping, pouring molding or by mechanical dispenser.

Curing

CC Cement hardens with an internal chemical-setting action with an initial set in approximately 30 minutes. The final set is reached in 18 to 24 hours when cured at room temperature. If it is desired to accelerate the curing time, set the drying oven to 65°C (150°F) and the cement will cure in 4 hours. If the drying oven is set to 104°C (220°F), the cement will cure in 3 hours.

Solvent

To remove cured cement, soak it with Sodium Hydroxide. The cement should soften with time. Wipe clean with cloth.

NOTE

Material safety information (in the Material Safety Data Sheet) can be obtained by contacting OMEGA Engineering and asking 6r MSDS-0103.

Specifications

Color:	Tan
Maximum Service Temperature:	843°C (1550°F)
Thermal Conductivity (K Factor) at 260°C (500°F):	8 Btu·in/ft^2-hr.°F
Curing Time:	(2.7 x 10^3 Cal·cm/cm^2·sec·°C)
At Room Temperature:	18 to 24 hours
At 65°C (150°F):	4 hours
At 104°C (220°F):	3 hours
Absorption (Water):	10 to 12%
Shrinkage:	0.50%
Coefficient of Thermal Expansion:	4.6 x 10^{-6}in/in/°F
Density:	141 lb/ft^3 (pcf) 2.26 g/cm^3
Specific Gravity:	1.92 ±0.05g/cc
Dielectric Strength ASTM D-149	
At 21°C (70°F):	25.0 to 51.0 Volts/mil (980 to 2000 Volts/mm)
At 399°C (750°F):	12.5 to 25.0 Volts/mil (490 to 980 Volts/mm)
At 801°C (1475°F):	≤1.3 Volts/mil (51 Volts/mm)
Compressive Strength:	3900 PSI (274 kg/cm^2)
Tensile Strength:	425 PSI (29 kg/cm^2)
Volume Resistivity ASTM D-1829	
At 21°C (70°F):	10^7 to 10^9 ohm-cm
At 399°C (750°F):	10^4 to 10^6 ohm-cm
At 801°C* (1475°F):	10^2 to 10^3 ohm-cm
Dielectric Constants:	5.0 to 7.0

omega.com info@omega.com

Servicing North America:

U.S.A.: Omega Engineering, Inc., One Omega Drive, P.O. Box 4047
Stamford, CT 06907-0047 USA
Toll-Free: 1-800-826-6342 (USA & Canada only)
Customer Service: 1-800-622-2378 (USA & Canada only)
Engineering Service: 1-800-872-9436 (USA & Canada only)
Tel: (203) 359-1660 Fax: (203) 359-7700
e-mail: info@omega.com

For Other Locations Visit omega.com/worldwide

WARRANTY/DISCLAIMER

OMEGA ENGINEERING, INC. warrants this unit to be free of defects in materials and workmanship for a period of **13 months** from date of purchase. OMEGA's WARRANTY adds an additional one (1) month grace period to the normal **one (1) year product warranty** to cover handling and shipping time. This ensures that OMEGA's customers receive maximum coverage on each product.

If the unit malfunctions, it must be returned to the factory for evaluation. OMEGA's Customer Service Department will issue an Authorized Return (AR) number immediately upon phone or written request. Upon examination by OMEGA, if the unit is found to be defective, it will be repaired or replaced at no charge. OMEGA's WARRANTY does not apply to defects resulting from any action of the purchaser, including but not limited to mishandling, improper interfacing, operation outside of design limits, improper repair, or unauthorized modification. This WARRANTY is VOID if the unit shows evidence of having been tampered with or shows evidence of having been damaged as a result of excessive corrosion; or current, heat, moisture or vibration; improper specification; misapplication; misuse or other operating conditions outside of OMEGA's control. Components in which wear is not warranted, include but are not limited to contact points, fuses, and triacs.

OMEGA is pleased to offer suggestions on the use of its various products. However, OMEGA neither assumes responsibility for any omissions or errors nor assumes liability for any damages that result from the use of its products in accordance with information provided by OMEGA, either verbal or written. OMEGA warrants only that the parts manufactured by the company will be as specified and free of defects. OMEGA MAKES NO OTHER WARRANTIES OR REPRESENTATIONS OF ANY KIND WHATSOEVER, EXPRESSED OR IMPLIED, EXCEPT THAT OF TITLE, AND ALL IMPLIED WARRANTIES INCLUDING ANY WARRANTY OF MERCHANTABILITY AND FITNESS FOR A PARTICULAR PURPOSE ARE HEREBY DISCLAIMED. LIMITATION OF LIABILITY: The remedies of purchaser set forth herein are exclusive, and the total liability of OMEGA with respect to this order, whether based on contract, warranty, negligence, indemnification, strict liability or otherwise, shall not exceed the purchase price of the component upon which liability is based. In no event shall OMEGA be liable for consequential, incidental or special damages.

CONDITIONS: Equipment sold by OMEGA is not intended to be used, nor shall it be used: (1) as a "Basic Component" under 10 CFR 21 (NRC), used in or with any nuclear installation or activity; or (2) in medical applications or used on humans. Should any Product(s) be used in or with any nuclear installation or activity, medical application, used on humans, or misused in any way, OMEGA assumes no responsibility as set forth in our basic WARRANTY/DISCLAIMER language, and, additionally, purchaser will indemnify OMEGA and hold OMEGA harmless from any liability or damage whatsoever arising out of the use of the Product(s) in such a manner.

RETURN REQUESTS / INQUIRIES

Direct all warranty and repair requests/inquiries to the OMEGA Customer Service Department. BEFORE RETURNING ANY PRODUCT(S) TO OMEGA, PURCHASER MUST OBTAIN AN AUTHORIZED RETURN (AR) NUMBER FROM OMEGA'S CUSTOMER SERVICE DEPARTMENT (IN ORDER TO AVOID PROCESSING DELAYS). The assigned AR number should then be marked on the outside of the return package and on any correspondence.

The purchaser is responsible for shipping charges, freight, insurance and proper packaging to prevent breakage in transit.

FOR **WARRANTY** RETURNS, please have the following information available BEFORE contacting OMEGA:

1. Purchase Order number under which the product was PURCHASED,
2. Model and serial number of the product under warranty, and
3. Repair instructions and/or specific problems relative to the product.

FOR **NON-WARRANTY** REPAIRS, consult OMEGA for current repair charges. Have the following information available BEFORE contacting OMEGA:

1. Purchase Order number to cover the COST of the repair,
2. Model and serial number of the product, and
3. Repair instructions and/or specific problems relative to the product.

OMEGA's policy is to make running changes, not model changes, whenever an improvement is possible. This affords our customers the latest in technology and engineering. OMEGA is a registered trademark of OMEGA ENGINEERING, INC.

M0080/0511